



## City Research Online

### City, University of London Institutional Repository

---

**Citation:** Lu, Y. (2023). Numerical and Experimental Study of Screw Machines with Large Helix Angle. (Unpublished Doctoral thesis, City, University of London)

This is the accepted version of the paper.

This version of the publication may differ from the final published version.

---

**Permanent repository link:** <https://openaccess.city.ac.uk/id/eprint/31052/>

**Link to published version:**

**Copyright:** City Research Online aims to make research outputs of City, University of London available to a wider audience. Copyright and Moral Rights remain with the author(s) and/or copyright holders. URLs from City Research Online may be freely distributed and linked to.

**Reuse:** Copies of full items can be used for personal research or study, educational, or not-for-profit purposes without prior permission or charge. Provided that the authors, title and full bibliographic details are credited, a hyperlink and/or URL is given for the original metadata page and the content is not changed in any way.



# **Numerical and Experimental Study of Screw Machines with Large Helix Angle**

**Yang Lu**

This dissertation is submitted for the degree of  
*Doctor of Philosophy*

School of Science and Technology

Centre for Compressor Technology  
Northampton Square, London, EC1V 0HB, U.K.

July 2023

---



---

## **Dedication**

This work is dedicated to my beloved wife and cherished family, whose boundless support has been the cornerstone of my journey.

---



## Acknowledgement

When the word of acknowledgement is typed, it signifies that my four and half years of PhD study are coming to an end, and life is like ascending a staircase, entering the next stage of life. Throughout the journey, I am thankful for my parents, grateful for my supervisor, and appreciative of my friends. Thank you for walking alongside me and being with me throughout my journey of PhD.

First and foremost, I want to express my gratitude to Professor Kovacevic, Professor Stosic, Dr Read and Dr Rane. Professor Kovacevic accepted me as his student and guided me through pursuing a PhD degree, starting a new chapter in my life. The research for this thesis and the writing of the paper were accomplished under Professor Kovacevic's meticulous and rigorous guidance. I also want to thank Professor Stosic, Dr Read and Dr Rane, who always provided insightful feedback during our meetings, helping me clarify the direction of my research and avoiding unnecessary detours.

Secondly, I extend my sincere thanks my friends and colleagues. Nausheen, Brijesh, Afia, Suraj, Sunny, Aamir are few of them to mention. They offered me tremendous support and assistance in my academic life. brought warmth to my life. Each one of you having become an integral part of my life. I hope our paths may cross again.

I am deeply grateful to City, University of London, Mayekawa, and Vert Rotors for their financial assistance during my PhD, which has been instrumental in enabling me to focus on my research and academic pursuits.

Lastly, I want to express my profound gratitude to my parents and my wife. The love and support I have received from my parents go beyond words. and they have been my pillar of strength, providing the motivation and confidence to keep moving forward. I am also immensely thankful to my wife, Lijuan, for bringing sweetness and warmth to my life.

**Yang Lu**

Edinburgh

July,2023

---



# Table of Contents

<b>Table of Contents .....</b>	<b>ii</b>
<b>List of Figures.....</b>	<b>v</b>
<b>List of Tables .....</b>	<b>ix</b>
<b>Abstract .....</b>	<b>xi</b>
<b>Nomenclature .....</b>	<b>xii</b>
<b>Publications .....</b>	<b>xiv</b>
<b>Chapter 1 – Introduction.....</b>	<b>1</b>
1.1 Roots blower .....	2
1.2 Twin Screw Machines.....	5
1.2.1 Twin screw compressors.....	6
1.2.2 Twin screw vacuum pumps .....	7
1.3 Computational fluid dynamics .....	8
<b>Chapter 2 – Literature Review .....</b>	<b>13</b>
2.1 Introduction .....	13
2.2 Mesh generation methods.....	13
2.3 CFD analysis of screw machines .....	16
2.3.1 Review of CFD studies of rotatory compressors and pumps .....	21
2.3.2 Performance study .....	23
2.4 Stand-alone software for twin screw machines.....	24
2.5 Summary .....	25
<b>Chapter 3 Research Aims and Contribution to Knowledge.....</b>	<b>26</b>
3.1 Aims of research.....	26
3.2 Methodology .....	26



3.3	Expected contribution to knowledge.....	27
<b>Chapter 4 Suitability of cut-cell cartesian grid generation method for twin screw machines. ....</b>		
		<b>28</b>
4.1	Introduction .....	28
4.2	Governing equations .....	28
4.3	Evaluation of the cut-cell method .....	30
4.3.1	Timestep independence study .....	32
4.3.2	Mesh independence study .....	33
4.4	Comparison between aligned and non-aligned mesh.....	36
4.4.1	Comparison with increased number of cycles .....	38
4.5	Conclusion.....	41
<b>Chapter 5 Case studies of Alternative grid generation methods for twin screw machines</b>		
		<b>43</b>
5.1	Introduction .....	43
5.2	The simulation of the hook claw pump .....	43
5.2.1	Rotor geometry .....	44
5.2.2	Experimental setup .....	45
5.2.3	ANSYS Forte solver setup.....	46
5.2.4	Mesh independence study .....	46
5.2.5	Study with varying fluids and operating conditions .....	48
5.2.6	Conclusion .....	56
5.3	The simulation of the Roots blower .....	57
5.3.1	Working conditions.....	57
5.3.2	Setup of the ANSYS Forte and ANSYS CFX models.....	58
5.3.3	Simulation results and discussion .....	61
5.3.4	Conclusion .....	65
5.4	Analysis of the twin screw compressors .....	65
5.4.1	Oil injection with flow rate boundary condition .....	71
5.4.2	Oil injection with pressure boundary condition .....	72
5.4.3	Oil free cases.....	74
5.4.4	Other cases.....	75
5.4.5	PV power calculated at different rotor length positions.....	75
5.4.6	Investigation of the rotor torque power and PV power in CFD .....	77
5.4.7	Conclusion .....	80

5.5	Analysis of a twin screw vacuum pump with large helix angle using Body-fitted mesh .....	81
5.5.1	Rotor geometry .....	81
5.5.2	Grid generation for twin screw vacuum pump.....	83
5.5.3	Simulation.....	85
5.5.4	Conclusion .....	89
5.6	Analysis of a twin screw vacuum pump with large helix angle using Cut-cell cartesian mesh .....	90
5.6.1	ANSYS Forte solver setup.....	92
5.6.2	Mesh generation.....	92
5.6.3	Results and discussion .....	95
5.6.4	Conclusion .....	100
5.7	Closure .....	100
<b>Chapter 6 Grid Generation in a normal plane for Screw Machines with Large Helix Angles .....</b>		<b>103</b>
6.1	Introduction .....	103
6.2	Fluid domain decomposition.....	103
6.2.1	Coordinate systems .....	104
6.2.2	Normal rack and normal rotor profile .....	111
6.3	Algebraic Grid generation.....	120
6.3.1	Outer boundary regularisation .....	121
6.3.2	Transfinite interpolation .....	123
6.3.3	3D mesh generation .....	124
6.4	Summary .....	126
<b>Chapter 7 Summary and Recommendation for Future Work .....</b>		<b>128</b>
7.1	Conclusions of the research.....	128
7.2	Recommendations for future work.....	129
<b>Appendix A. Profile and rack generation.....</b>		<b>137</b>
A.1	Coordinate transformation.....	137
A.2	Rack generation.....	138
A.3	Derivation of meshing equation .....	140
A.4	Calculation of meshing angle.....	142

<b>Appendix B. Algebraic approach for Grid Generation of Twin Screw Rotors.....</b>	<b>144</b>
B.1 Coordinate transformation of the interlobe rotor space .....	144
B.2 Outer boundary regularisation.....	144
B.3 Transfinite interpolation.....	148
<b>Appendix C. Mesh quality evaluation standard .....</b>	<b>149</b>

## List of Figures

Figure 1-1 Compressor Categories. ....	1
Figure 1-2 Typical application ranges of compressors (adapted from [1]). ....	2
Figure 1-3 Cutaway of a Roots blower .....	3
Figure 1-4 Working process of roots blower. ....	4
Figure 1-5 Three different types of rotor profiles of roots blower .....	5
Figure 1-6 Helix angle. ....	5
Figure 1-7 Structure of the twin screw compressor. ....	6
Figure 1-8 Operating stages in a twin-screw compressor. ....	7
Figure 1-9 Structure of twin-screw compressor-expander.....	7
Figure 1-10 Twin-screw vacuum pump. ....	8
Figure 1-11 Framework of CFD analysis. ....	10
Figure 1-12 Basic grid generation techniques [23]. ....	12
Figure 2-1 Meshing techniques comparison. ....	15
Figure 2-2 Transverse rack as a splitting curve .....	17
Figure 2-3 Differential division line as a splitting curve .....	17
Figure 2-4 The vacuum pump rotors with different helix angle [31]. ....	20
Figure 2-5 Domain decomposition in the transverse plane .....	21
Figure 2-6 Comparison of the flow direction .....	21
Figure 2-7 The experimental result of twin screw vacuum pump .....	24
Figure 3-1 Research methodology .....	27
Figure 4-1 Cylinder model.....	31
Figure 4-2 The cylinder cross-section mesh with different size. ....	34
Figure 4-3 Cyclic chamber volume variation. ....	35
Figure 4-4 Pressure variation and error. ....	35
Figure 4-5 Temperature variation and error.....	36
Figure 4-6 Mesh of aligned and non-aligned case.....	37

---

Figure 4-7 Comparison of calculated pressure for first three cycles .....	37
Figure 4-8 Volume variation and error. ....	38
Figure 4-9 Pressure variation and error. ....	39
Figure 4-10 Temperature variation and error.....	39
Figure 4-11 Volume Error. ....	40
Figure 4-12 Pressure Error.....	41
Figure 4-13 Temperature Error.....	41
Figure 5-1 The twin screw vacuum pump rotor profile.....	44
Figure 5-2 Test rig of claw pump. ....	46
Figure 5-3 The mesh and velocity distribution results of varying mesh sizes.....	47
Figure 5-4 The Volume flow rate .....	48
Figure 5-5 Location of the seven pressure monitor points .....	50
Figure 5-6 The Pressure variation with angle and volume .....	50
Figure 5-7 The gas pressure contour in the mid plane.....	51
Figure 5-8 The velocity distribution in the middle plan .....	52
Figure 5-9 The velocity distribution comparison.....	53
Figure 5-10 Comparison of the Temperature distribution in mid plane .....	54
Figure 5-11 Comparison of the Pressure distribution in mid plane .....	56
Figure 5-12 Rotor profile .....	57
Figure 5-13 Cut-cell cartesian mesh from ANSYS Forte.....	59
Figure 5-14 Body-fitted mesh for ANSYS CFX .....	59
Figure 5-15 Pressure variation at Point1 .....	62
Figure 5-16 Temperature variation at outlet .....	62
Figure 5-17 Inlet Mass flow rate.....	63
Figure 5-18 Outlet Mass flow rate .....	63
Figure 5-19 Torque .....	64
Figure 5-20 Power.....	64
Figure 5-21 Velocity vector in different position from two solvers .....	65
Figure 5-22 Boundary condition of oil return port .....	70

---

Figure 5-23 Integrated PV power .....	71
Figure 5-24 Torque constitution .....	71
Figure 5-25 Comparison of Oil Volume Fraction.....	72
Figure 5-26 Pressure distribution.....	74
Figure 5-27 Oil Free Cases .....	74
Figure 5-28 Pressure Variation along the rotor.....	75
Figure 5-29 Position of pressure transducer .....	76
Figure 5-30 Position of probes.....	76
Figure 5-31 Oil free $V_i = 1.6$ .....	77
Figure 5-32 Case6 New4 $V_i = 1.6$ .....	77
Figure 5-33 Oil free case comparison .....	78
Figure 5-34 Pressure contour of oil free case .....	79
Figure 5-35 Pressure contour of oil free case .....	80
Figure 5-36 Twin screw rotor profile.....	81
Figure 5-37 Monitor points.....	82
Figure 5-38 Volume angle curve .....	83
Figure 5-39 Mesh of casing to rotor non-conformal.....	84
Figure 5-40 Mesh of casing to rotor conformal .....	84
Figure 5-41 Grid distribution on the rotor .....	84
Figure 5-42 Comparison of the aspect ratio and orthogonality .....	85
Figure 5-43 Pressure contour of -0.5 barg inlet pressure.....	86
Figure 5-44 Pressure variation in the compression with -0.5 barg .....	87
Figure 5-45 Pressure variation in the compression with -0.3 bar. ....	87
Figure 5-46 Comparison of torque and power .....	88
Figure 5-47 Comparison of the mass flow rate.....	89
Figure 5-48 The twin screw vacuum pump rotor profile. ....	90
Figure 5-49 3D rotor geometry. ....	91
Figure 5-50 Schematic diagram of the test rig .....	92
Figure 5-51 Mesh at XY AND XZ cross section.....	93

---

Figure 5-52 XY cross section of scaled rotor. ....	94
Figure 5-53 Set up of scale factor. ....	95
Figure 5-54 Pressure contour at YZ cross section of scaled rotor. ....	96
Figure 5-55 YZ cross section with different gap scale factors. ....	100
Figure 5-56 Comparison of analysed geometries ....	101
Figure 6-1 Two sub-domain between the rotors. ....	105
Figure 6-2 The flow chart of grid generation subroutine.....	106
Figure 6-3 Transverse plane and normal plane. ....	107
Figure 6-4 Global coordinate system. ....	107
Figure 6-5 Main rotor local <i>coordinate</i> system. ....	109
Figure 6-6 Gate rotor local coordinate system.....	110
Figure 6-7 Local coordinate system of main rotor.....	111
Figure 6-8 Input Profile. ....	112
Figure 6-9 Main rotor profile transformation. ....	113
Figure 6-10 Rotor profile and rack relative position. ....	114
Figure 6-11 Line-plane intersection.....	116
Figure 6-12 The main rotor sub-domain and rack in LNCS.....	118
Figure 6-13 The gate rotor sub-domain and rack in LNCS. ....	120
Figure 6-14 The sub-domain coordinate in the normal plane.....	121
Figure 6-15. Computational coordinate systems ....	122
Figure 6-16 Transform the casing form circle to ellipse.....	123
Figure 6-17 Numerical mesh generated by TFI.....	123
Figure 6-18 Flow chart of grid generation. ....	125
Figure 6-19 3D mesh of one interlobe. ....	126
Figure 6-20 3D mesh of one rotor.....	126

## List of Tables

Table 1-1 Commercial CFD packages for twin screw compressors.....	11
Table 4-1 Terms in the generic transport equation .....	29
Table 4-2 Fluid properties.....	32
Table 4-3 Timestep independence study.....	33
Table 4-4 Mesh independence analysis .....	34
Table 4-5 Comparison between aligned and non-aligned mesh .....	37
Table 4-6 Comparison between cycles .....	38
Table 5-1 Rotor geometry .....	45
Table 5-2 Operating conditions and solver setup parameters .....	46
Table 5-3 Mesh independence analysis .....	47
Table 5-4 Cycle comparison .....	48
Table 5-5 Simulation results comparison .....	49
Table 5-6 Comparison of volume flow rate and power .....	56
Table 5-7 Rotor dimensions.....	57
Table 5-8 Working conditions .....	58
Table 5-9 Number of mesh for solver Forte and CFX.....	60
Table 5-10 Numerical setup for Forte and CFX .....	60
Table 5-11 Calculation time comparison of Forte and CFX.....	61
Table 5-12 Numerical setup for Forte and CFX .....	61
Table 5-13 Rotor Geometry .....	66
Table 5-14 Working conditions and fluid properties .....	66
Table 5-15 The CFX setup.....	67
Table 5-16 Comparison between PV power and Torque Power.....	68
Table 5-17 Oil Drag Power.....	72
Table 5-18 The PV power and Torque Power .....	72
Table 5-19 Other Cases.....	75



---

Table 5-20 PV Power and Torque Power .....	77
Table 5-21 PV Power and Torque Power .....	78
Table 5-22 PV Power and Torque Power of Oil free case.....	79
Table 5-23 Rotor configuration .....	81
Table 5-24 Fluid domain grid set-up .....	83
Table 5-25 Working condition.....	85
Table 5-26 Rotor configuration .....	90
Table 5-27 Operating conditions and solver setup parameters .....	92
Table 5-28 Comparison between simulation and experimental results .....	97
Table 6-1 Unit vector of global coordinate system.....	108
Table 6-2 Unit vector of rotor coordinate systems .....	108
Table 6-3 Unit vector of rotor local transverse coordinate systems .....	109
Table 6-4 Unit vector of rotor local normal coordinate systems .....	110
Table 6-5 Unit vector of rack normal coordinate system .....	111
Table 6-6 The input rotor profile coordinates.....	112

# Abstract

An effective and efficient CFD simulation is of high importance to accelerate the design activities of twin screw machines. However, mesh generation for screw machines with large helix angles can produce highly skewed numerical cells which can make simulation unreliable. From the established literature, the two main approaches to generate structured deforming mesh for CFD analysis of twin screw machines are algebraic and differential. The purpose of this thesis is to explore grid generation techniques suitable for 3D numerical modelling of rotatory positive displacement machines with large helix angles. Both cut-cell cartesian and body-fitted grid generation methods are investigated for analysis of machines with different profiles and helix angles.

The conservation and simulation accuracy of cut-cell cartesian method was first evaluated using a simple piston cylinder example and a hook and claw rotor profile used in vacuum pump which is difficult to set by a body fitted mesh. It was shown that even with coarse initial mesh, such profiles could have been analysed using a cut-cell cartesian mesh, but it required special model to account for leakage flows. Secondly, screw machines with low helix angle are used to examine the capability of both grid generation methods. ANSYS CFX was used for analysis of body fitted mesh produced by SCORG grid generator, while ANSYS Forte was used for evaluation of cut-cell cartesian method. Thirdly, oil-injected twin screw compressor with intermediate helix angle was explored using body-fitted method. In addition, a case study of a twin-screw vacuum pump with higher helix angle of 62 degree was studied using SCORG and FLUENT to further explore the body-fitted method. Lastly, a twin-screw vacuum pump with variable pitch and cusp points was analysed using cut-cell cartesian method. These five case studies demonstrated advantages and disadvantages of body-fitted and cut-cell cartesian methods for low, intermediate, and large helix angles.

This thesis then proposes development of an alternative method called a normal grid generation method which is expected to improve mesh quality of a body fitted mesh for screw machine with large helix angles and in turn could improve accuracy of flow calculation.

# Nomenclature

$A_c$	-	Axis distance between main and gate rotor
$Z_k$	-	Number of lobes
$L$	-	Rotor length
$M$	-	Number of points along the rotor profile
$N$	-	Number of cross sections
$i_k, j_k, k_k$	-	Unit vector of the local coordinate system
$ri_k$	-	Radius of the inner circle
$ro_k$	-	Radius of the outer circle
$rp_k$	-	Radius of the pitch circle
$rx_k$	-	Anticlockwise rotation matrix along x-axis
$ry_k$	-	Anticlockwise rotation matrix along y-axis
$rz_k$	-	Anticlockwise rotation matrix along z-axis
$S(X, Y, Z)$	-	Global coordinate system
$S_k(X_k, Y_k, Z_k)$	-	Rotor coordinate system
$S_{0k}(X_{0k}, Y_{0k}, Z_{0k})$	-	Transverse coordinate system
$S_{1k}(X_{1k}, Y_{1k}, Z_{1k})$	-	Normal coordinate system

## Greek symbols

$\theta_k$	-	Rotation angle
$\alpha_k$	-	Angle corresponding to the cross section
$\beta$	-	Helix angle
$\omega_k$	-	Wrap angle
$\Omega_k$	-	Wrap angle

## Subscripts

- 1 - Male rotor
- 2 - Female rotor
- 3 - Rack

#### Abbreviations

- PDM - Positive Displacement Machines
- CFD - Computational Fluid Dynamics
- RANS - Reynolds Averaged Navier-Stokes
- ALE - Arbitrary Lagrangian-Eulerian
- TFI - Transfinite Interpolation
- PDE - Partial Differential Equation
- AMG - Automatic Mesh Generation
- AMR - Adaptive Mesh Refinement
- SCORG - Screw Compressor Rotor Grid Generator

# Publications

## Journal publications:

1. Lu, Y., S. Rane, and A. Kovacevic. 2022. Evaluation of cut cell cartesian method for simulation of a hook and claw type hydrogen pump. *International Journal of Hydrogen Energy* 47 (54):23006-23018.
2. Lu, Y., A. Kovacevic, M. Read, and N. Basha. 2019. Numerical Study of Customised Mesh for Twin Screw Vacuum Pumps. *Designs* 3 (4).

## Conference papers:

1. Theofanidis, K., Y. Lu, and A. Kovacevic. 2021. CFD analysis on the effect of discharge port geometry of the hook and claw vacuum pumps. In *IOP Conference Series: Materials Science and Engineering*: IOP Publishing, 012063.
2. Yang, L., A. Kovacevic, B. Nausheen, and M. Read. 2019. CFD Analysis of Twin Screw Vacuum Pump. Paper read at 9th International Conference on Compressor and Refrigeration, ICCR2019, at Xi'an.
3. Yang, L., A. Kovacevic, and M. Read. 2019. Normal Rack Grid Generation Method for Screw Machines with Large Helix Angles. In *IOP Conference Series: Materials Science and Engineering*. London.
4. Yang, L., A. Kovacevic, and M. Read. 2018. Numerical study on screw machines with large helix angles. In *IOP Conference Series: Materials Science and Engineering*. Dortmund.

# Chapter 1 – Introduction

According to their working principle, compressors are divided into two main categories: positive displacement (volume changing) and dynamic compressors (velocity changing), as shown in Figure 1-1. Positive displacement compressors can be further divided into rotatory and reciprocating compressors. These machines have been widely used in many applications including air, process gas compression and refrigeration. The reciprocating compressor is possibly the best known and the most widely used of all compressors [1].

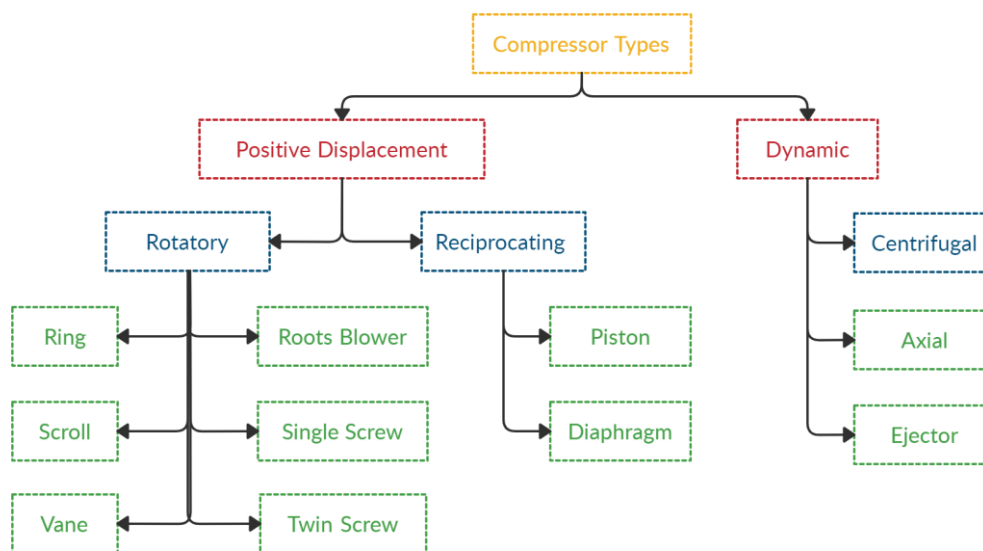


Figure 1-1 Compressor categories.

There are many different types of rotatory compressors. The selection of appropriate compressor types for a certain application can be performed on the basis of the required pressure rise and flow rate. A simple illustration of this is shown in Figure 1-2. The positive displacement compressors are commonly considered for high-pressure ratios while centrifugal and axial compressors are mostly for the high-volume flow rates. Rotatory positive displacement compressors are frequently used for intermediate pressure ratios and flow rates. However, with improvements in their designs and manufacturing, twin screw compressors are able to provide discharge pressures up to 45 bar and differential pressures of 15 bar and are capable of flows up to 92,000 m<sup>3</sup>/h [2]. The subject of research in this thesis are twin-screw

machines and roots blowers which have some common features. Twin-screw compressors are positive displacement machines that use two intermeshing screws to compress gas. They are widely used in various industrial applications such as refrigeration, air conditioning systems, petrochemical industry for processes such as gas compression, vapor recovery, and hydrogen compression. They can handle a wide range of gases and provide reliable compression in demanding environments. These compressors are also used in food and beverage production processes, pneumatic conveying, gas boosting, and packaging applications where a clean and oil-free operation is required.

Roots blowers, also known as rotary lobe blowers, are dynamic compressors that use two or three lobed rotors to generate airflow. They are commonly used for applications that require low-pressure, high-volume flow rate. Some relevant applications of roots blowers are wastewater treatment, pneumatic conveying and industrial processes.

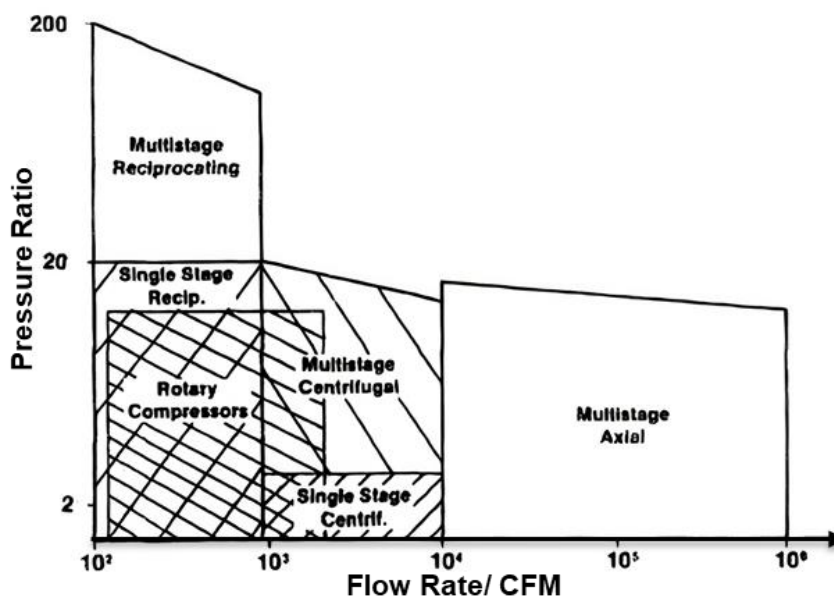


Figure 1-2 Typical application ranges of compressors (adapted from [1]).

## 1.1 Roots blower

Roots blower is a positive displacement compressor that was initially invented as a gas pump for use in blast furnaces in 1860 by Philander H. Roots and Francis M. Roots two brothers from Connersville Indiana [1]. Roots blowers consist of two straight-lobe rotors which rotate in a casing as shown in Figure 1-3. Two rotors intermesh with each other and rotate in opposite directions synchronized by timing gears. There is a small clearance between two rotors. Roots

blowers have simple structure, high reliability as well as low manufacturing and maintenance costs. The biggest advantage of roots blower compared to twin-screw compressor is that the rotors are easier for manufacturing. However, contrary to screw compressors that have internal compression within the rotors, roots blowers have just external compression which is less efficient.

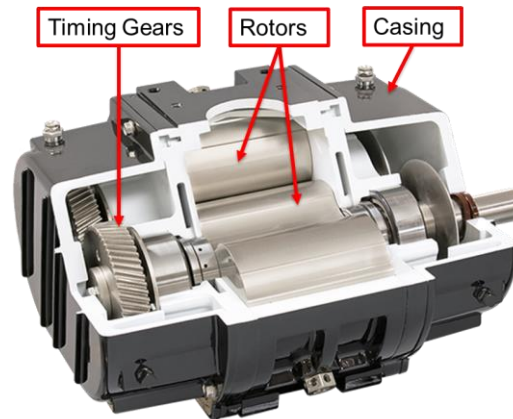


Figure 1-3 Cutaway of a Roots blower

Since the clearance between two rotors and no internal compression, roots blower can achieve only limited pressure ratio, typically 1.4 - 2.0. However, it can compress large volumes of gas at efficiencies up to 70 % [1]. Therefore, roots blowers are typically used in applications where a large volume of air must be moved across a relatively small pressure differential such as supercharger [3], vacuum pump [4], and boosters in various compression applications. With the increase in number of fuel cell electrical vehicles, by adapting its rotor profile, Roots blower can also be used as hydrogen recirculation pump in fuel cell battery [5].

The working process of 2/2 rotor combination roots blower is shown in Figure 1-4. With the rotating of two rotors, the air is trapped between rotors and casing and separated to low pressure and high-pressure regions. The pressure increases inside the chamber due to high pressure air back flow. In one revolution, this positive displacement of air trapped between rotor and casing from suction to discharge shall occur four times in case of two lobe rotor.



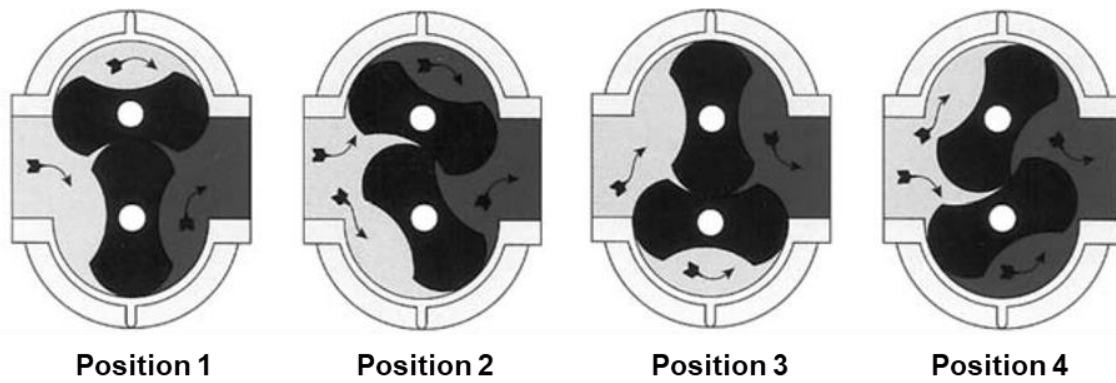
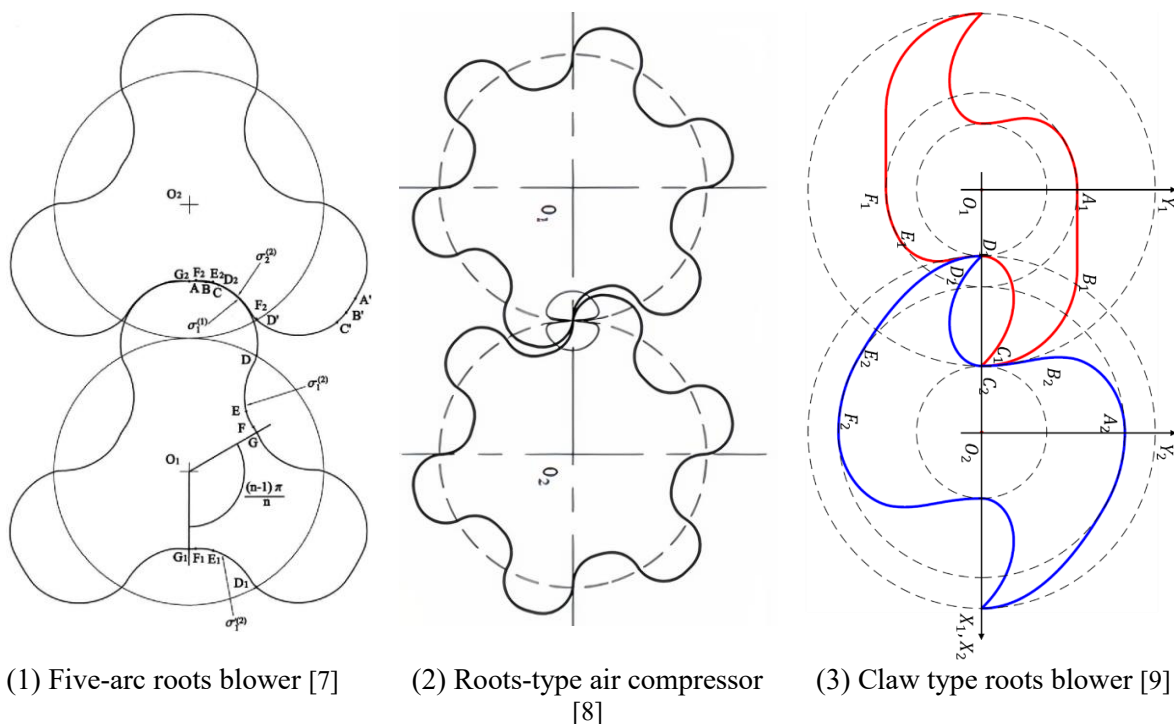


Figure 1-4 Working process of roots blower.

Initial roots blower design consists of two figure-eight rotors. Two rotors usually have same profile which consists of eccentric arcs, epicycloid and hypocycloid or involute profiles [6]. Typical three-lobe rotor tooth profile is shown in Figure 1-5 (a). With increased popularity of hydrogen as energy source, the rotor profile and structure of roots blower are adapted to hydrogen recirculation pump. Roots-type compressors with fixed internal compression ratio and claw pump with a discharge port are used for compression of air in fuel cell vehicles. Two examples of roots blowers used for fuel cell system are shown in Figure 1-5(b) and Figure 1-5 (c). There is internal compression in the latest one because of the twist of rotors and the position and geometry of the discharge port.



(1) Five-arc roots blower [7]

(2) Roots-type air compressor [8]

(3) Claw type roots blower [9]

Figure 1-5 Three different types of rotor profiles of roots blower

## 1.2 Twin Screw Machines

Twin-screw machines are positive displacement machines comprising of a meshing pair of helical rotors contained in a casing. The main difference between roots blower and twin-screw compressors is the feature of the rotors which are twisted and the helix angle. The angle between normal plane and transverse is the helix angle  $90 - \beta$  as shown in Figure 1-6. Helix angle can be defined according to the lead and the radius of the pitch circle with equation  $\beta = \text{atan} \left( 2 * \pi * \frac{r_{pitch}}{Lead} \right)$ .

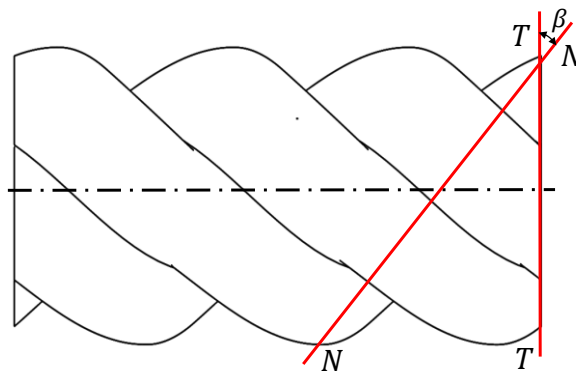


Figure 1-6 Helix angle.

One of the earliest twin-screw compressors was developed in Germany in 1878 by Heinrich Krigar [1]. The rotor profile resembles the roots blower rotor with the exception that the wrap angle is in the range of  $250^{\circ}$ – $310^{\circ}$  while roots blower has  $0$  degree. Wrap angle of the rotors is a geometric parameter that denotes the rotational angle of the helix from starting to end. In 1935, Alf Lysholm from Sweden improved the screw compressor with asymmetric 4/5 lobe combination profile that is still in use today.

Currently, the main development of twin-screw machines is in improving rotor profile designs, rotor manufacturing, oil or water injection to increase efficiency of the working process in various industrial applications in high-pressure gases, energy recovery and vacuum conditions. The improvements in performance and efficiency of screw machines are mostly associated with efficient rotor profiles and machining precision.

### 1.2.1 Twin screw compressors

Twin-screw compressor is one of the most common used machines for industrial refrigeration, gas processing and other industries. Typical twin-screw compressor is shown in Figure 1-7.

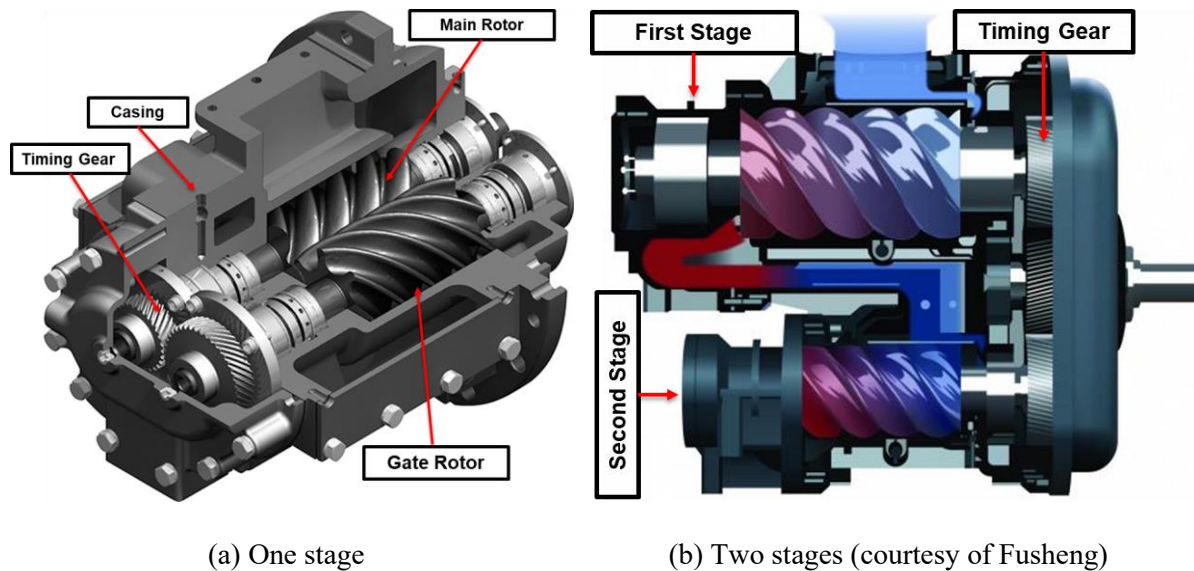


Figure 1-7 Structure of the twin screw compressor.

Twin screw machines are positive displacement rotary machines comprising a meshing pair of rotors contained in a casing, which together form a working chamber whose volume depends on the angle of rotation. Screw compressors can be classified as oil free and oil injected machines. The oil free compressors require additional timing gears on the rotor shafts to maintain contactless operation whereas in oil injected compressors the motor drives the main rotor then the main rotor drives the gate rotor. The operating principle of screw machines has been known for over 100 years. The main rotor meshes with the gate rotor in a fix casing together forming different working chambers which volume depends on the rotation angle, as shown in Figure 1-8. The working process can be divided into suction, compression, and discharge.

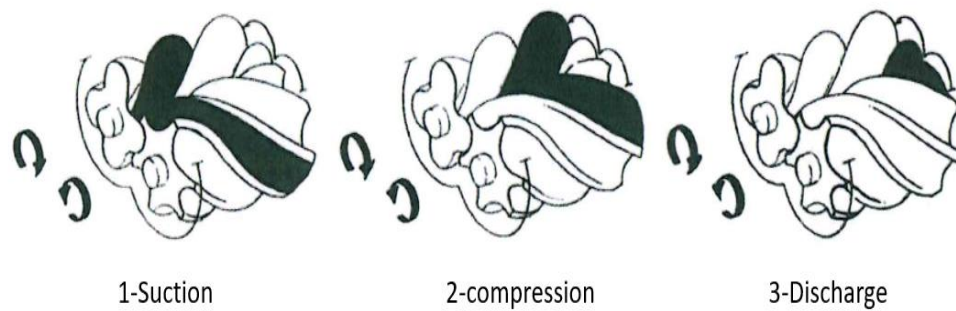


Figure 1-8 Operating stages in a twin-screw compressor.

Recently, fuel cells developed for various applications, such as fuel cell vehicles (FCV), have a high thermodynamic efficiency. A compressor can be used to improve the cell working pressure and more importantly, Smith and Stosic [10] proposed a combined compressor-expander unit which can be used in the automobile as shown in Figure 1-9. The machine consists of a compressor and expander in separate chambers within same casing. Compressor is directly driven by expander to reduce low power consumption of the main drive.

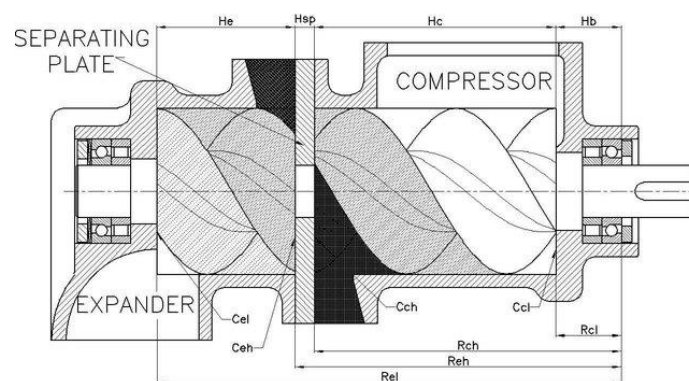


Figure 1-9 Structure of twin-screw compressor-expander.

### 1.2.2 Twin screw vacuum pumps

The first vacuum dry pumps based on the roots blower principle were introduced in 1984 in Japan [1]. The typical twin screw vacuum pump is shown in Figure 1-10. Nowadays, the vacuum pumps are widely used in many different industries such as nanotechnology, microelectronics, medicine, pharmaceuticals, thermonuclear power, food and packaging industry and others [2]. The semiconductor industry is one of the largest and most rapidly developed market for twin-screw vacuum pumps. They are specifically designed for clean and dry vacuum processes including water processing and film deposition. Overall, twin screw

vacuum pumps provide reliable, efficient, and clean vacuum solutions for various semiconductor manufacturing processes. They contribute to maintaining the required vacuum levels, minimizing contamination, and ensuring the high-quality production of semiconductor devices. To minimize contamination, twin-screw vacuum pumps are normally oil-free. Their screw rotors are synchronized using timing gears to prevent any contact between them. Main and gate rotor commonly have same profile comprising of single lobe in order to reduce manufacturing cost as well as to achieve higher volumetric efficiency.

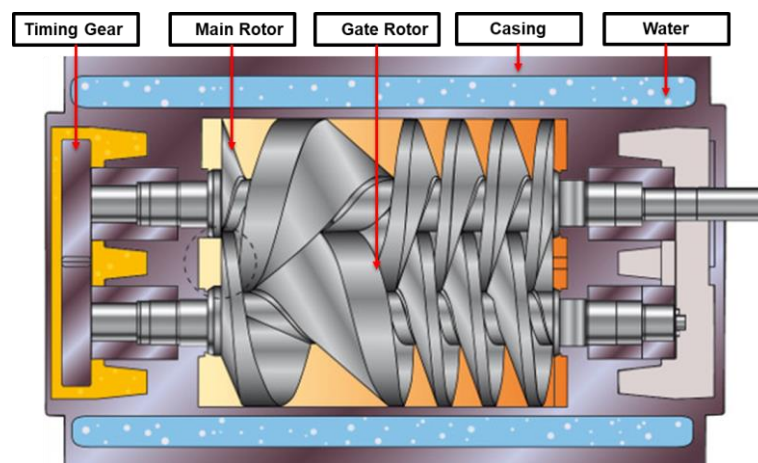


Figure 1-10 Twin-screw vacuum pump.

Twin screw vacuum pumps are designed with large helix angles to reduce the leakage losses and variable lead to increase internal compression ratio. In addition, hook and claw rotor profile is commonly utilised for profile design of twin screw vacuum pumps to increase area utilisation coefficient.

### 1.3 Computational fluid dynamics

Computational fluid dynamics (CFD) is the branch of fluid mechanics, which is used to investigate fluid flow through numerical simulations. CFD is one of the three basic approaches to solve problems of fluid dynamics and heat transfer [11]. Two additional approaches emerged in the study of fluid dynamics: experimental fluid dynamics, which originated in the seventeenth century, and theoretical fluid dynamics, primarily developed in Europe during the eighteenth and nineteenth centuries. While computational fluid dynamics (CFD) complements these two approaches, it cannot fully replace either of them. However, CFD has the following advantages:

- CFD simulations are generally more cost-effective compared to conducting physical experiments. Experimental setups can be expensive due to the need for specialized equipment, materials, and skilled personnel.
- CFD allows for virtual testing and optimization of designs, reducing the need for physical prototypes and associated costs.
- CFD simulations enable easy exploration of a wide range of design and operating parameters.
- CFD simulations provide a safe and controlled environment for studying potentially hazardous or extreme flow conditions.
- With CFD, engineers have greater flexibility and control over the simulation setup. They can easily modify parameters, boundary conditions, and geometry, allowing for quick design iterations and optimization.

It is crucial to acknowledge that while CFD provides numerous advantages, it is not without limitations. Validating and verifying CFD results through experimental data remains essential, and there are scenarios where experimental or theoretical methods are still preferred. A combination of CFD, experiments, and theoretical analysis can provide a comprehensive understanding of fluid dynamics and yield reliable results.

Thanks to advancements in high-performance computer technology over the past three decades, CFD is now regularly employed to swiftly and accurately solve complex problems. However, substantial difficulties of numerical analysts exist for some practical fluid flow problems of which there are three main obstacles [12]:

- The physical complexity of the flow,
- The geometrical complexity of the flow domains,
- The limited accuracy, stability, and economy of numerical solution methods.

CFD has been used for simulation of the twin screw compressors since late 1990s. The CFD simulation [13] of twin-screw compressor are three dimensional, unsteady with turbulent flows and often multiphase. However, there are still some open questions to be answered:

1. Can improved leakage models allow further optimisation?
2. Improving the simulation efficiency and accuracy for multiphase machines.
3. Fluid structure interaction (FSI) between the fluid, rotor and casing.
4. The influence of conjugate heat transfer to the performance and reliability.

There are four steps of CFD analyses. Step 1 is to create the geometry of the simulation model. Step 2 is mesh generation. Step 3 is to select physics and fluid properties. The simulation could be transient or static flow and specify the boundary conditions. The last step is to solve the simulation. Tu [11] has presented a framework to illustrate the interconnectivity of the three modules as shown in Figure 1-11.

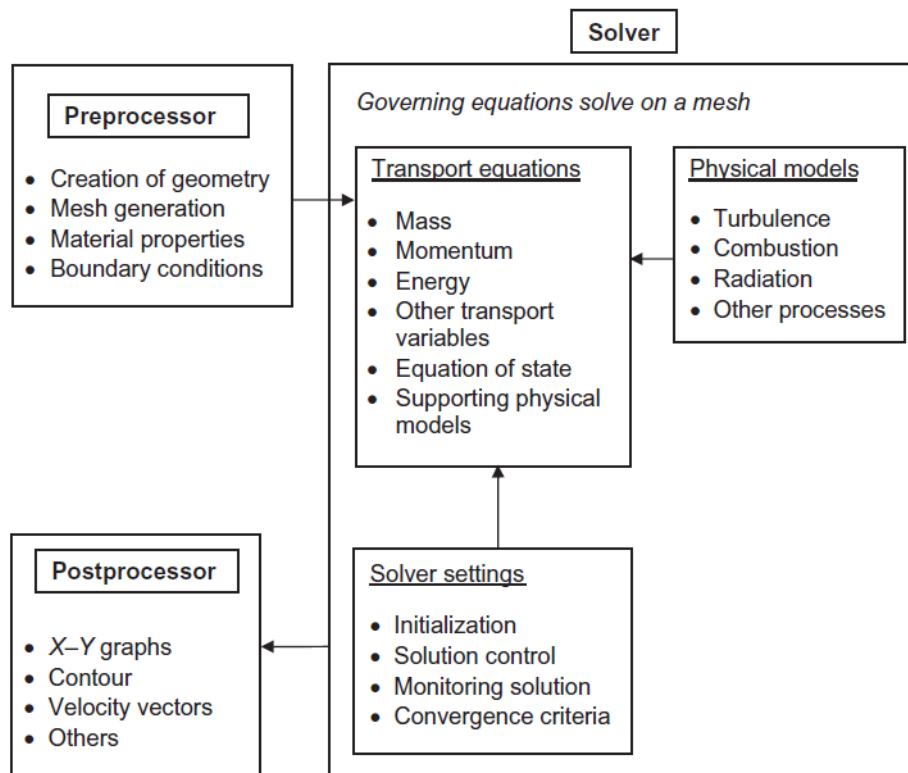


Figure 1-11 Framework of CFD analysis.

There are in general three modules of CFD analysis: pre-process, solver and postprocessor. Software has been developed regarding to each module. Commercial software packages have been successfully employed for the simulation of twin-screw compressor as presents in Table 1-1. The open source CFD software OpenFOAM has been developed primarily by OpenCFD Ltd since 2004 [14]. There are also many in-house CFD code commands which are confidential and only exclusively used within their companies or research centres. Software suits listed in Table 1-1 are capable to deal with moving boundaries in the condition when high quality mesh is updated correctly. Ansys Forte and Converge have built-in dynamic cut-cell cartesian mesh generation algorithm while other software needs to read external mesh files to update mesh position during simulation.

*Table 1-1 Commercial CFD packages for twin screw compressors*

<b>Company</b>	<b>Software</b>
ANSYS, Inc [15].	FLUENT, CFX & Forte
SIEMENS [16]	Simcenter STAR-CCM+
Simerics [17]	PumpLinx
CONVERGE [18]	CONVERGE
COMSOL, Inc [19]	COMSOL

Numerical grid or mesh generation is the process to discretize a fluid domain into a number of the points where the transport equations are solved based on the coordinates of the points. The types of grid generation can be classified into two basic categories which are structured and unstructured mesh. Structured mesh is typically all quad and hexahedral which have an equal number of adjacent elements [20]. A quad mesh consists of four adjacent elements, while a hexahedral mesh comprises six adjacent elements. In structured mesh algorithms, intricate iterative smoothing techniques are employed to align the distribution of the mesh along boundaries or the direction of flow. Structured meshes are extensively utilized in the field of CFD, primarily due to the critical significance of ensuring strict alignment among the elements [20]. Unstructured mesh, on the other hand, is featured with triangle mesh for 2D and hexahedral mesh for 3D. In general, the mapping methods such as transfinite interpolation and elliptic operator are used for structured mesh generation [21] while advancing front and Delaunay triangulation for unstructured mesh generation [22]. Figure 1-12 shows the basic grid generation techniques.



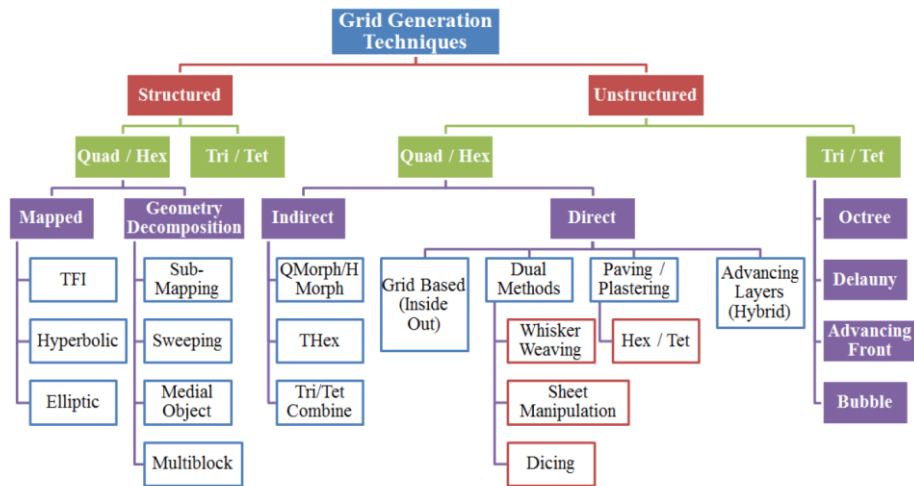


Figure 1-12 Basic grid generation techniques [23].

Overall, CFD has been successfully used for the analysis of twin screw compressors. Stand-alone grid generation software has been developed specifically for twin screw compressors [13]. However, grid generation for twin screw machines with large helix angle has not been studied and remains as a problem when hook and claw rotor profile is used for this type of machine. Hence, it becomes imperative to investigate the impact of the helix angle on grid generation and to develop grid generation methods specifically tailored for screw machines with significant helix angles.

# Chapter 2 – Literature Review

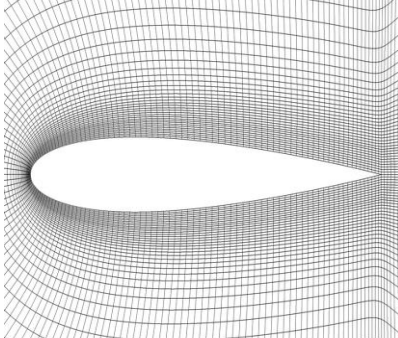
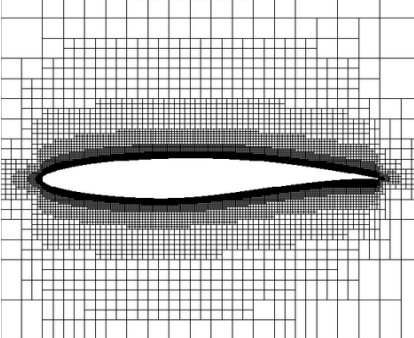
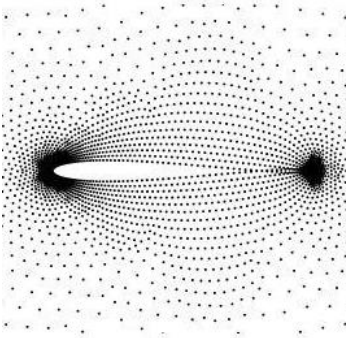
## 2.1 Introduction

Extensive research efforts have been dedicated to enhancing the performance of positive displacement machines, including diaphragm compressors [24], scroll compressors [25], roots blower [26,27], twin screw compressors [28] and claw pumps [29]. With the rapid growth of the screw compressor industry, screw machines have been studied from rotor profiles design [30-34], numerical simulation using lumped parameter models [35,36] or 3D CFD simulations [37-40] to experimental investigation [5,41-43]. The first step of the process is the design of the rotor profile. Many rotor profiles have been proposed [30,44,45]. The geometric parameters were subsequently compared. The chamber model was described in greater detail by Stosic [35] [46] and Peng et al [47] and validated by comparing it with experimental results. Furthermore, with the development of the computer performance, the computational fluid dynamics (CFD) is used to simulate the working process of the positive displacement machines (PDMs). However, the numerical simulation of screw machines is difficult because of the complex rotor geometry and the volume-changing chambers with very small clearances between the rotors and casing. In this chapter, the practice and application of grid generation method and computational fluid dynamics simulation of roots blower and screw machines has been critically reviewed.

## 2.2 Mesh generation methods

Grid generation involves discretizing the domain into multiple cells, enabling the solution of the partial differential equation that describes gas flow. This is accomplished through three primary discretization methods: finite difference method (FDM), finite volume method (FVM) [48] and finite element method (FEM). Other methods, such as the spectral schemes, the boundary element methods or the lattice Boltzmann method are used in CFD but their use is limited to special types of problems. In CFD, most of the methods solve the Navier-Stokes equations either in Eulerian or in Lagrangian approach. Apart from that, some methods solve the Boltzmann equations instead of Navier-Stokes equations [49]. The meshing process is time-consuming. Push-button automated meshing is the goal not only because this will benefit engineers who then can focus on the innovation and optimization of the products [22]. Fluid

domain discretization process is the first action for CFD simulation. The grid generation is challenging for the 3D simulation of the screw machine because the complex geometries of screw machine and boundary-fitted computational mesh and sufficient resolution are difficult to achieve. Thompson [50] has explained structure, unstructured and hybrid mesh generation through analytical or differential method. The current grid generation methods have been studied. There are two main grid generation methods that can be utilized for screw machines. The first method is the body-fitted mesh, which can generate a fixed number of hexahedral meshes. This method ensures full conservation and accuracy, although it may require some effort to obtain the desired mesh configuration. The second method is the cut-cell Cartesian method, which is compatible with automated mesh generation. This method is particularly well-suited for complex and moving geometries. To reduce the number of meshes and optimize simulation time, the mentioned method can incorporate gap models to account for leakage flow. However, a key concern in this approach is ensuring the conservativeness of spatial discretization. Commercial software like Converge and ANSYS Forte have implemented this method. There is another promising method called the meshless method. A comparison of the three mesh generation methods is presented in Figure 2-1.

			
	Body-fitted Mesh	Cut-cell Cartesian Method	Meshless Method
Advantages	Hexahedra Mesh Fixed number of neighbouring grids Fully conservative mesh	Meshing time Hexahedra Mesh Complex and moving geometries AMR (Adaptive Mesh Refinement) Gap models (ML)	Mesh free Complex and moving geometries High Knudson number
Disadvant	Complex Geometries Meshing time	Conservativeness of spatial discretisation	DBC's require special treatments Unstable and less accurate

Software	SCORG TwinMesh	ANSYS Forte Converge	Abaqus
----------	-------------------	-------------------------	--------

Figure 2-1 Comparison of various meshing techniques comparison of CFD analysis.

The cut-cell cartesian methods was firstly developed and adopted by Frymier [51]. The advantage of the cut cell Cartesian meshing is as following:

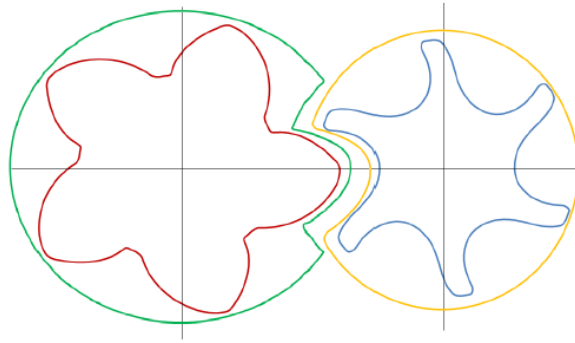
- Body-fitted – This method offers the advantage of fitting the geometry perfectly, making it easier and more accurate to handle complex and moving geometries. Rather than stretching and shrinking cells to accommodate the geometry, this method achieves accuracy by cutting the cells to fit the shape precisely.
- Independent resolution - Since this method cuts the volume cells at the wall, the mesh resolution becomes independent of the geometric resolution. In simpler terms, it is possible to achieve a high-fidelity geometric representation while using a coarse mesh. This characteristic can significantly accelerate run-time calculations and enhance computational efficiency.
- Clearance refinement and leakage model - The cut-cell Cartesian method incorporates cell refinement at the wall, which enhances accuracy. Unlike other methods where the entire grid needs to be provided as input and the surface geometry is lost, this method preserves the original surface information. Consequently, any grid refinement carried out during the simulation will accurately represent the near-wall flow predictions, as the resolution added near walls improves the representation of the actual geometry. In contrast, other methods may be limited in accurately capturing the surface location due to the resolution of the original grid.
- Automatic mesh generation - The meshing process is very straightforward and automatically distributed according to velocity gradient. Cut cell cartesian method is more suitable for moving boundary problems cause the cells update every time step is only happened to domain adjacent to moving boundary [52]. However, one major disadvantage of cut-cell Cartesian method is that accuracy could be compromised for finite volume method [52]. ANSYS Forte uses the Arbitrary Lagrangian-Euler (ALE) method [53,54] for spatial differencing of the governing equations.

### 2.3 CFD analysis of screw machines

CFD is applied to a wide range of research and engineering problems including aerodynamics and aerospace analysis, industrial system design and analysis, biological engineering and fluid flows, and engine and combustion analysis. Kovacevic made a major breakthrough of 3D CFD simulation of twin screw compressors [13,46,55-58]. The fundamental of the CFD calculation on twin screw compressor is based on the Navier-Stokes equations describing the general fluid flow. The application of conservation of mass, momentum, and energy, along with additional relationships, leads to a system of equations represented by partial differential equations (PDEs). These equations are time-dependent and tightly coupled. An example of such a relationship is the equation of state, which establishes a connection between pressure, density, and temperature as thermodynamic variables. To solve this system of equations, numerical methods like the finite difference method, finite volume method, and finite element method can be employed to approximate the PDEs on a discretized domain. The finite volume method involves partitioning the fluid domain into small, regular, and adjacent volumes, with the centroids of these volumes serving as integration points. One advantage of the finite volume method is its versatility, as it can be applied to grids of any type, making it well-suited for complex geometries. The primary concern in computational fluid dynamics (CFD) is ensuring the accuracy of the simulation results. Jasak [59] proposed three methods to estimate discretisation error which results from discretisation of the fluid domain and equation discretisation. Error from discretisation of fluid domain mainly caused by insufficient mesh resolution, mesh skewness and non-orthogonality. This error is very typical for screw machines with large helix angle. CFD simulation can help to understand the working detailed of the compressors including not only the integral performance quantities but also the pressure and pressure distribution and velocity field.

In order to enable calculation of the performance using CFD solvers, the working domain between the casing and the rotors has to be mapped with a numerical grid. The decomposition of the flow domain between the casing and two rotors consists of dividing it into number of 2D cross sections. Practically, three methods can be utilised to decompose a cross section of the flow domain, namely, differential division line, transverse rack and normal rack. Kovacevic [13] was the first to use the analytical rack in the transverse cross section for decomposition of the rotor cross section. Recently, as shown by Rane [60], algebraic grid generation are verified for variable profile rotors with parallel axis using transverse rack to split the rotor domain to

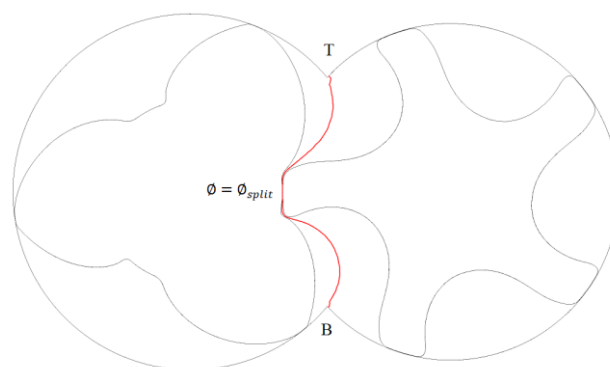
two O blocks as shown in Figure 2-2. In his case, each 2D cross section has a different rotor profile position at an instant due to helical rotors and they are related to each other by lead of the rotors. The two O blocks together form a composite grid. Some small non-aligned node movements are observed at the transition point from the inter-lobe region to the casing region on the rotor surface.



Reproduced from Kovacevic[13]

Figure 2-2 Transverse rack as a splitting curve

Vande Voorde et al [61] constructed a block structured mesh using the gradient lines and the equipotential lines in the transverse planes which also leads to the large differing volume around the CUSP. Figure 2-3 demonstrates the application this method. A dynamic boundary condition for the potential on the casing in order to get the iso-potential lines at top and bottom CUSP to be produced nearly tangential and coincide with CUSP points [61].



Reproduced from Vande Voorde[62]

Figure 2-3 Differential division line as a splitting curve

In the case of machines with non-parallel axis such as single screw compressors or twin-screw compressors with large helix angle, the cell skewness becomes prohibitively large in the transverse cross section mesh. The twist of the helical rotor in third dimension makes grid generation difficult. The proposed normal rack grid generation method [63,64] will decompose and generate grid be directly applicable for such machines. The rack generation procedure was firstly proposed to generate screw rotor profiles by Rinder [65], which means that the generating profile is rack and both the main and gate rotor profiles can be generated from the same rack in the same coordinate system. The rack line can mesh with the main rotor profile and gate rotor profile simultaneously. In addition to that convenience, a rack generation procedure offers the possibility to design various lobe combinations rotors using the same rack. The envelope method is the basis for the design of rotor profiles of screw rotors. The envelope gearing method of the screw rotors is similar to the method used for helical gears. The rack generation process and enveloping methods are introduced in Appendix A. Litvin [66] described the process of coordinate transformation in matrix representation and implemented it in the generation of gear and rack-cutter. Stosic [67] used the envelope gearing method to derive a general meshing condition for crossed helical gears which is then used to generate the profile of a hobbing tool. Stosic and Hanjalic [68] presented a rack based procedure to generate various lobe combination rotors. Refer to the rack-generated profile method of Stosic, Yu-ren [69] explicitly redefined the rack which including two normal-equidistant trochoids using at least one control parameter to each compound curve, which contributes to the flexible and adjustable rack. Then a method using a rack defined in the normal plane to design the twin screw rotor profiles was proposed. The advantage of this method is that the normal circular pitch does not change as the helix angle varies.

There are two primary methods to generate the numerical meshes: analytical transformations and algebraic grid generation. Analytical transformations are suitable for simple geometry. The algebraic grid generation is also called transfinite interpolation, which has good control over the placement of grid nodes. Algebraic grid generation is widely used for the discretization of the working domain of screw machines. However, it is important to further improve the quality and robustness of the computational grid to obtain fast solution of oil injection screw machines. A detailed review of the algebraic and differential approach of deforming grid for twin screw machines has been presented. For the modelling of the twin screw machines, the disadvantage of the structured meshes is that they can be very difficult to construct in complex geometries.

Even if the meshes can be constructed, the quality may not be desirable. As a result, there have been many attempts to optimise the grids distribution and improve the quality of grids.

Kovacevic [56] generated a fully structured hexahedral, block oriented numerical mesh for all parts of screw compressor domain using pre-specified rack coordinates. Boundary adaptation procedure has been developed to produce a regular boundary distribution on the mesh boundaries. Rane [40] used Elliptic PDE solver in a selective interlobe area bounded by the top and bottom cusp radial nodes of the mesh to convert the rack curve into a smooth transitioning curve across the specified number of angular positions of the rotor. A gradually changing partition between the two O grids of the main and gate rotors can be obtained through this smooth rack.

More recently, Rane [70] compared the simulation results of reversible adiabatic compression in a Piston Cylinder of three grid deformation methods: Diffusion Smoothing, User Defined Nodal Displacement and Key-Frame Re-meshing. It was concluded that customized tools for generation of CFD grids are required for complex screw machine. Rane[60] compared the advantages and disadvantages of algebraic grid generation method and differential decomposition method and then based on two methods proposed a new algebraic method which can be implemented to generate a single domain rotor grid in order to improve the accuracy of the CFD simulations. Rane [40,71,72] also proposed new developments of SCORG on the grid generation for variable geometry rotors, accurate representation of clearances and multiphase screw machines. Rane [60] proposed the algebraic grid generation method which combined the advantages of algebraic and differential method together. In this method, the boundary nodes are firstly distributed on the transverse rack and casing circle and these nodes remain steady with respect to the rotor. At the same time, Rane [73] verified that Casing to Rotor grid with a con-formal interface by comparing the simulation results from Rotor to Casing grid and refined Casing to Rotor grid and also the experimental results. The best performance prediction was achieved, especially for the oil injection and multiphase flows.

Kennedy et al [74] presented a study of an oil-free twin-screw compressor using SCORG<sup>TM</sup> to generate conformal numerical mesh and ANSYS CFX 3D CFD tool [75] to calculate performance. This was compared with the validated 1D Thermodynamic model. 1D thermodynamic models simplify complex flow and heat transfer processes, still allowing to predict important compressor performance parameters such as pressure and temperature variation, volumetric efficiency and power consumption. This model can be used for performance optimization, design evaluation, and understanding the behaviour of the twin



screw compressor under different operating conditions. The paper concludes that the difference between both models decrease as the compressor operating speed increases. This confirmed that numerical meshes generated by the method used in SCORG<sup>TM</sup> based on generation of series of 2D meshes in transverse planes either as rotor to casing or casing to rotor could be successfully used with a variety of CFD solvers. However, these meshes become difficult to use in calculation of the performance of vacuum pumps because large helix angle as shown in Figure 2-4. This type of rotor profile will make the rotor to casing numerical mesh extremely non orthogonal which in turn leads to difficulty in obtaining CFD results.

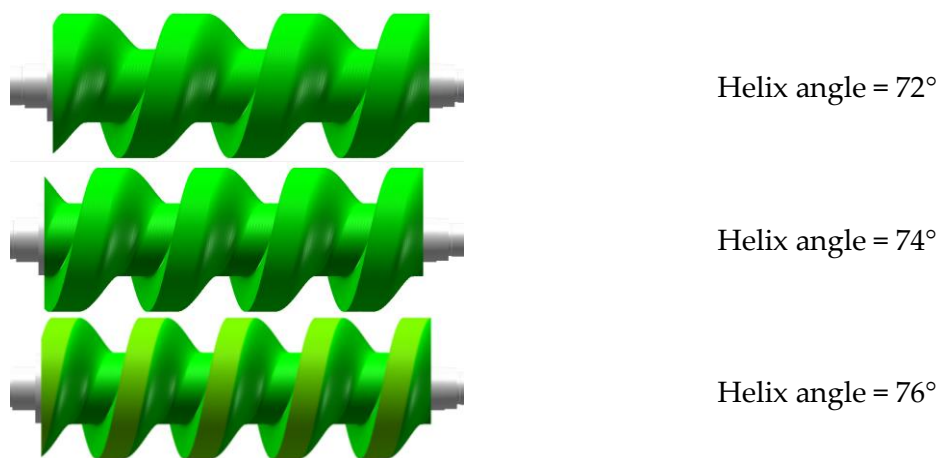


Figure 2-4 The vacuum pump rotors with different helix angle [31].

According to the CFD study of twin-screw machines [42,43], the main fluid direction is perpendicular to the helix line especially in the clearance area. Voorde et al [61] constructed a block structured mesh using the gradient lines and the potential lines to split the fluid domain in the transverse planes as shown in Figure 2-5 (b). This algorithm was applied to an oil-free screw compressor and was demonstrated on the applicability of this algorithm. For the vacuum pumps and oil-free compressors, the leakage loss is huge. The helix angle is relatively large to increase the sealing points. Then the 3-D cell skewness becomes large for this kind of machines which will introduces errors in numerical simulation.

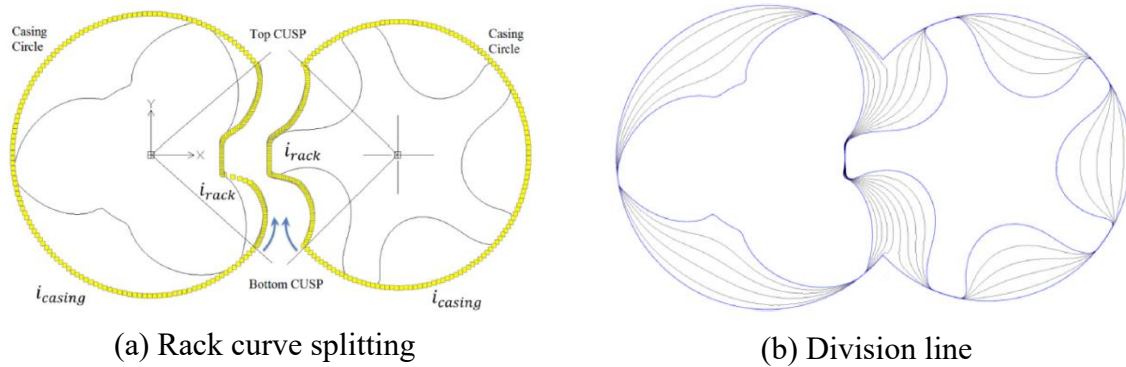


Figure 2-5 Domain decomposition in the transverse plane

The governing equations of the fluid domain can be defined by coupled and time dependent partial differential equations which are discretised across the grid. Vierendeels [76] compared two different velocity flows through a square discretised with structured grid. As shown in Figure 2-6, when the flow direction is not aligned to the grid direction, the interface between two flows is not distinctive. It is demonstrated that less numerical diffusion in the governing equation across streamlines produced by grid alignment.

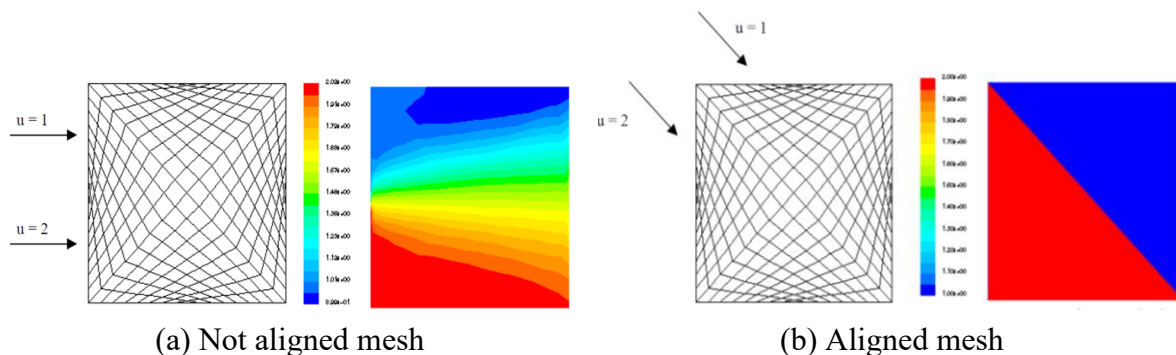


Figure 2-6 Comparison of the flow direction

### 2.3.1 Review of CFD studies of rotatory compressors and pumps

The structured body-fitted methods are traditionally used for the simulation of compressors and pumps. Casari [77] compared the state-of-the-art mesh generating methods: along with immersed boundaries, overset, dynamics remeshing and key frame remeshing and conclude that the custom predefined mesh generation strategy is the most suitable choice for the simulation of PDMs. SCORG is the mesh generation software for positive displacement

machines which has been successfully used for the analysis of roots blowers [78,79], air compressors [60,73], oil-injected compressors [80] and water injected compressors [81].

Gu [82] used TwinMesh software to generate the body-fitted structure mesh for the simulation of the hook and claw pump. The objective of this study was to investigate the influence of three clearances on volumetric efficiency so that the best combination of clearances could be selected. In addition, authors noticed vortices at the suction, control and discharge chambers. Dong [83] utilised a unstructured mesh for his CFD simulation and the numerical results matched well with the experimental results. Objective of this study was to explore volumetric efficiency and  $p - \theta$  diagram at different suction and discharge pressure. Over-compression is observed from  $p - \theta$  diagram. Many cases have been performed using body-fitted method which requires very high-resolution mesh to capture velocity distribution. Recently, the cut-cell based method for CFD modelling has been developed for simulation of twin-screw compressors. The method offers several advantages, notably its ability to handle complex moving geometries, which simplifies the simulation process through automated grid generation. Commercial software like Converge Science, Star CCM+ and ANSYS Forte have adopted this technology in their commercial CFD codes.

Rowinski [84,85] has also modelled a twin screw compressor and expander and validated simulation results against experimental measurements. However, the conservation and accuracy of the cut-cell method have not yet been thoroughly evaluated, and its application in simulating a claw pumps has not been explored. The main disadvantage of cut-cartesian grid generation method is that clearances cannot be simulated accurately and a separate model for leakage flows is required.

Yan [86] carried out the 3D CFD numerical analysis to investigate the flow characteristics and the formation process of cavitation in twin screw pumps using the SCORG grid generator and Star-CCM+. A conformal structured moving meshes was generated. The numerical simulation results were analysed and discussed on the influence between the cavitation and the performance parameters of twin screw pumps, such as the mass flow rate, pressure distribution, rotor torque and the shaft power. Another numerical modelling of twin screw pumps was conducted by Yan [87]. This novel approach of numerical conformal structured moving mesh developed by City University London was validated by full 3D CFD analysis of screw pump using Star-CCM+ commercial solver. At the same time, the numerical analysis of 2-3 type multiphase twin screw pumps was conducted. To compare the performance of A-type-involute-

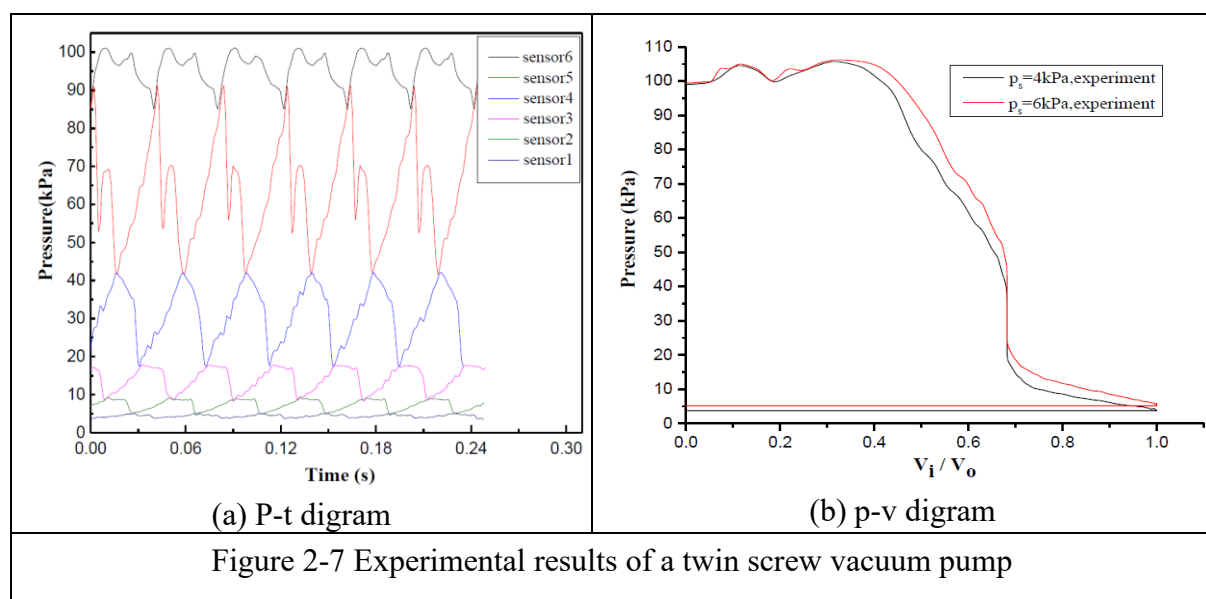
cycloid and D-type-cycloid based rotor profiles, a single domain structured moving mesh was generated using SCROG and full 3-D CFD simulation was carried out. Because of the complexity of the twin screw machines both in the geometric configuration and the flow problems, some CFD commercial solvers are not able to cope with the tangled screw compressor geometry. To get accurate simulation utilising a CFD solver effectively, user defined numerical mesh are required for complex geometry configuration. In 2000, Kovacevic [88] used an independent stand-alone CAD-CFD interface program written in FORTRAN to generate the numerical mesh of the suction, compression and discharge chambers of an oil-free screw compressor. To showcase the capabilities of the procedure, flow calculations were performed using Comet. Rainer [89] and Andreas [90] from CFX Berlin Software GmbH have published a few paper relating to CFD simulations of positive displacement machines like screw compressors or expanders, scroll compressors or expanders, roots blowers, lobe pumps, internal gear pumps and external gear pumps. They successfully demonstrated the high quality hexahedral meshes generated with TwinMesh could be employed for all rotor positions prior to the CFD solution. Furthermore, the CFD solver allows for the utilization of physical and numerical models without any limitations. The simulation results demonstrate excellent agreement with experimental data obtained from the literature. When considering the internal gear pump, notable cavitation phenomena are observed particularly at high rotational velocities. Kennedy [74] proposed a study of an oil-free twin screw compressor using 1-D thermodynamic chamber model which is inherited to SCORG<sup>TM</sup> and 3-D CFD model. The paper concludes that the difference between the models decreases as the compressor operating speed increase. Hsieh [78] compared the 3-D numerical results of cylindrical and screw type roots vacuum pumps using the CFD solver PumpLinx<sup>TM</sup>. The results show that the cylindrical type of pump has higher efficiency, and the screw type pump is steadier.

Despite a significant increase in the number of papers published recently concerning application of computational fluid dynamics to screw compressor, very few journal papers have been published on CFD simulation of twin screw machines with large helix angle and single screw machines.

### **2.3.2 Performance study**

Tuo [91] carried out an experimental study of a single tooth oil-free twin screw vacuum pump as shown in Figure 2-7. Six pressure transducers were installed along the casing to measure the pressure distribution under different working conditions. The pressure distribution and the

variation of pressure and volume are shown in the figure. The measured ultimate pressure can reach 0.7 Pa at the speed of 3000 rpm. Junemann [92] has built thermodynamic model to optimise the internal volume ratio, dimensionless rotor length  $L/D$  and rotor pitch. The working process of vacuum pump is approximated as series pumping stages. The biggest improvement occurs by an increase of the  $L/D$  ratio from 2 to 2:5. Huck [93] carried out the thermodynamical investigation of variable pitch cycloid tooth twin screw vacuum pumps using the simulation tool KaSim. Quimby profile has the feature of cycloid profile [93,94] as shown in Figure 1-5 (3). It has the advantage in the suction speed and inner power at the same rotational speed while cycloid profile has potential in energy savings when operating at variable rotational speeds.



## 2.4 Stand-alone software for twin screw machines

With the efficiency of the computer technology, a few software is developed for rotor profiling, basic thermodynamic calculation based on chamber model and grids generation solver. Kovacevic [13] has introduced a software called SCORG (Screw Compressor Rotor Grid Generator) which is a tool for constructing deforming grids in the rotor domain of a twin screw machine. TwinMesh [95] was developed by CFX Berlin Software GmbH to generate grids for PD machines. Xing [96] developed a software package called SCCAD which can be used to design rotor profile and calculate the geometrical characteristics, thermodynamic performance. A detailed description of the algebraic grid generation for twin screw rotors can be found in the thesis of Kovacevic [13].

## 2.5 Summary

From the literature review, the most efficient way of 3D CFD simulation of screw machines is the method involving customised grid generation used with the finite volume method. The numerical procedures explained in literature are based on the 3D numerical mesh generated by series of 2D numerical meshes in transverse cross sections which allows mesh to either follow the helix or be perpendicular to the axis. A significant number of research has been conducted to analysis roots blower and twin-screw compressors using this method. However, the modelling and performance calculation of the screw machines with large helix angles is challenging. If the rotor helix angle is large, the cell skewness becomes prohibitively large which introduces errors in numerical simulation. From the available techniques for deforming grid generation, no published works are available on the grid generation of screw machines with large helix angle and CFD practises have confirmed that it is necessary to further develop numerical models and grid generation techniques for screw machines with large helix angle.

# Chapter 3 Research Aims and Contribution to Knowledge

## 3.1 Aims of research

Improving the efficiency of screw machines through exploring novel methods in numerical simulation such as computational domain fidelity, mesh quality and numerical models are potentially significant for industry. The 3D computational fluid dynamic simulation provides a better insight into the flow parameters of screw machines ultimately leading to improvements rotor geometry design and performance. However, using current methods, it is difficult to generate the computational grids required for screw rotors with large helix angle.

The aim of this investigation is to establish a method to enable accurate and faster CFD performance analysis of screw machines with large helix angles and other complex geometries (like single screw or variable geometry machines). To achieve this, the following objectives are set:

- Evaluate accuracy of cut-cell cartesian methods for analysis of screw machines with large helix angle.
- Demonstrate and validate various grid generation technologies on different types of rotatory positive displacement machines such as hook and claw pumps, low Vi twin screw compressors and large helix angle twin screw vacuum pump and validate the results obtained from 3D CFD simulation using general commercial solvers with experimental measurements.
- Develop the algorithm for numerical grid generation in a plane normal to the helix of screw machine.

## 3.2 Methodology

The research methodology is illustrated by Figure 3-1. Cut-cell cartesian method is studied using piston cylinder case to investigate the challenge that grid is not aligned with clearance flow direction. Body-fitted mesh and cut-cell cartesian mesh are compared using four cases with different helix angle. The normal rack grid generation method is proposed to generate

flow aligned mesh for screw machines with large helix angle. The proposed methodology could provide guideline and reference for CFD simulation of positive displacement machines.

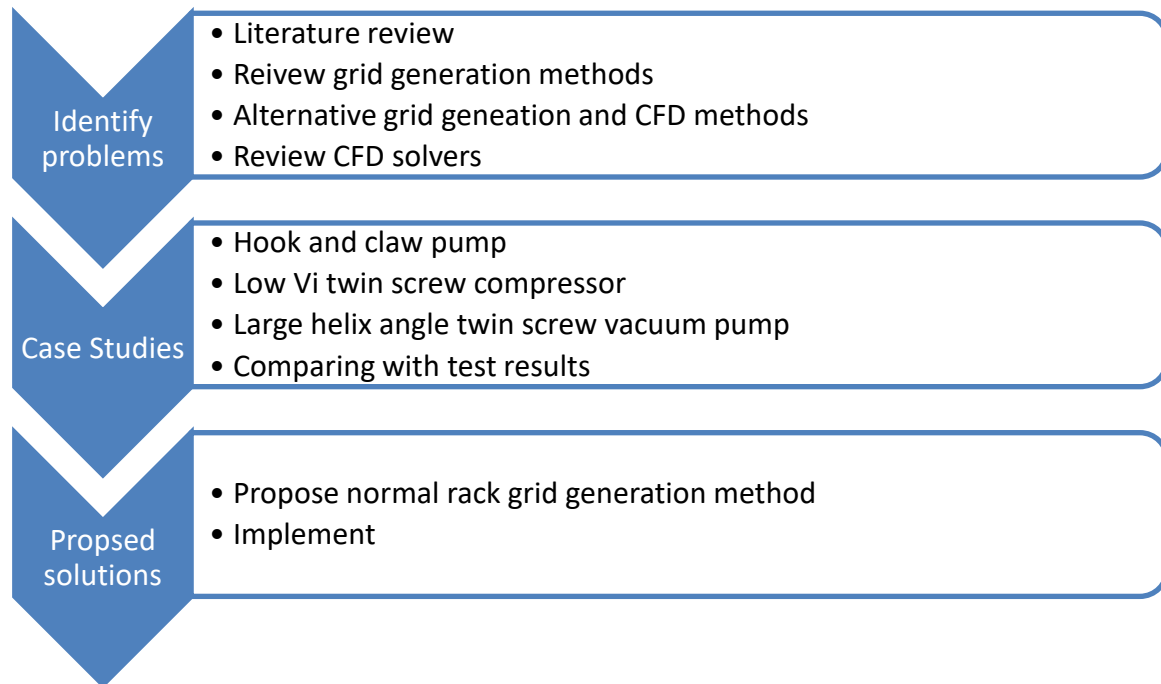


Figure 3-1 Research methodology

### 3.3 Expected contribution to knowledge.

The expected contribution to knowledge from this research is as follows.

- Comprehensive review of grid generation methods suitable for CFD analysis of large helix angle twin screw machines. Demonstrate accuracy of cut-cell cartesian method with piston cylinder case.
- Demonstrate most suitable methods for simulation of screw machines with large helix angle through case studies.
- The algorithms for numerical grid generation of screw machines with numerical cells aligned with leakage flows through clearances.



# Chapter 4 Suitability of cut-cell cartesian grid generation method for twin screw machines.

## 4.1 Introduction

The Cartesian cut cell method provides efficient and flexible alternative to traditional body fitted grid techniques. The Cartesian cut cell approach uses a background Cartesian grid for most of the flow domain with special treatments being applied to cells which are cut by solid bodies, thus retaining a boundary conforming grid. The Cartesian cut cell method has been used in the commercial solvers such like Converge, ANSYS Forte and some others. However, accuracy could be potentially compromised for the cut-cell cartesian method. In this chapter, ANSYS Fore is used to test the conservation and the leakage model of this method.

## 4.2 Governing equations

The conservation of mass, momentum, and energy equations, along with other properties, are applied to a discretized control volume (CV) of fluid, and they can be defined through coupled, time-dependent, partial differential equations. These equations serve as the foundation for solution using the Finite Volume Method. The general transport equation is represented as equation 4-1 [97].

$$\underbrace{\frac{\partial}{\partial t} \int_{\Omega} \rho \phi d\Omega}_{transient} + \underbrace{\int_S \rho \phi \mathbf{v} \cdot \mathbf{n} dS}_{convection} = \underbrace{\int_S \Gamma \text{grad } \phi \cdot \mathbf{n} dS}_{diffusion} + \underbrace{\int_{\Omega} q_{\phi} d\Omega}_{source} \quad 4-1$$

In the case of transient domains with moving boundaries, the calculation of convective fluxes requires the use of relative velocity components at the faces of the cells. If the velocity components are calculated in a fixed Cartesian system, all terms in conservation equation 4-1 remain unchanged, except for the relative velocity ( $\mathbf{v} - \mathbf{v}_b$ ), where  $\mathbf{v}_b$  is the velocity vector of the cell's face.

$$\frac{\partial}{\partial t} \int_{\Omega} \rho \phi d\Omega = \frac{d}{dt} \int_{\Omega} \rho \phi d\Omega - \int_S \rho \phi \mathbf{v}_b \cdot \mathbf{n} dS \quad 4-2$$

$$\frac{d}{dt} \int_{\Omega} \rho \phi d\Omega + \int_S \rho \phi (\mathbf{v} - \mathbf{v}_b) \cdot \mathbf{n} dS = \int_S \Gamma \text{grad } \phi \cdot \mathbf{n} dS + \int_{\Omega} q_{\phi} d\Omega \quad 4-3$$

*transient*                      *convection*                      *diffusion*                      *source*

When the cell face moves, the mass and other quantities may not be conserved if the grid velocities used to calculate the convective terms are explicitly calculated. To ensure mass conservation, it is necessary to satisfy the law of space conservation, as given by equation 4-4.

$$\frac{d}{dt} \int_{\Omega} d\Omega + \int_S \mathbf{v}_b \cdot \mathbf{n} dS = 0 \quad 4-4$$

This has been introduced for the finite difference calculation by Trulio [98]. The space conservation for the finite volume implement has been introduced by Demirdzic and Issa [99]. Table 4-1 presents the terms that correspond to a given intrinsic property in its respective conservation equation.

Table 4-1 Terms in the generic transport equation

			$q_{\phi}$	
Equation	$\phi$	$\Gamma$	$q_{\phi s}$	$q_{\phi v}$
Mass	1	0	0	0
Momentum	$v_i$	$\mu_{eff}$	$\left[ \mu_{eff} (\text{grad } \mathbf{v})^T - \left( \frac{2}{3} \mu_{eff} \text{div } \mathbf{v} + P \right) \mathbf{I} \right] \mathbf{i}_i$	$f_{b,i}$
Energy	e	$\frac{k}{\partial e / \partial T} + \frac{\mu_t}{\sigma_T}$	$-\frac{k}{\partial e / \partial T} \frac{\partial e}{\partial P} \text{grad } P$	$\mathbf{T}: \text{grad } \mathbf{v} + h$
Concentration	$c_i$	$\rho D_{i,eff}$	0	$S_{ci}$
Space	$\frac{1}{\rho}$	0	0	0
Turbulent kinetic energy	k	$\mu + \frac{\mu_t}{\sigma_k}$	0	$P - \rho \epsilon$

Dissipation of turbulent kinetic energy	$\varepsilon$	$\mu + \frac{\mu_t}{\sigma_\varepsilon}$	0	$C_1 P \frac{\varepsilon}{k}$ $- C_2 \rho \frac{\varepsilon^2}{k}$ $- C_3 \rho \varepsilon \operatorname{div} \mathbf{v}$
---	---------------	--	---	---

The following assumption and simplicity are considered for CFD simulations.

- Ideal gas

The working fluid satisfies the ideal gas equation  $pv = nRT$  which is a simple and straightforward equation that relates the pressure ( $p$ ), volume ( $v$ ), temperature ( $T$ ) Ideal gas law is a useful approximation for many practical applications, especially at moderate pressures and temperatures.

- Air viscosity is constant.

For the simulation in this chapter, air viscosity is considered as constant. The variation of air viscosity has negligible influence on the torque comparing with variation of oil viscosity. This assumption is widely used in many CFD applications due to their simplicity and computational efficiency, which implies that the dynamic viscosity of the fluid is independent of temperature, pressure, and strain rate.

- Reversible adiabatic compression process

An adiabatic process is considered for the piston cylinder case study. This assumption is convenient for error estimation of the mass conservation and the numerical accuracy of cut-cell method.

### 4.3 Evaluation of the cut-cell method

Automatic mesh generation (AMG) and adaptive mesh refinement (AMR) are used for the mesh generation in Ansys Forte [100]. The AMR option allows the software to automatically refine or coarsen the computational mesh based on specified criteria, such as gradients, cell size, or user-defined variables. By activating adaptive mesh refinement in ANSYS Forte, a more accurate and efficient simulation can be achieved by concentrating computational resources where they are most needed. This can help capture important flow features, resolve gradients, and enhance the overall accuracy of the simulation results. Gap flow models are employed for the under-resolution of the local gap size. The gap flow models consider the cell size and wall shear resistance effect which is derived based on an analytical solution of shear stress in Poiseuille flow [101].

The purpose of this section of the thesis is to evaluate conservativeness of the cut cell cartesian method by comparing the results from ANSYS Forte with the theoretical results in a simple adiabatic piston cylinder.

Liu [102] has performed the simulation of the piston-cylinder using the Large-eddy simulation and compared the results with the experimental and RANS approach. Dr Rane [70] has compared three grid deformation strategies, namely the diffusion equation mesh smoothing, user defined nodal displacement and key-frame remeshing. It was concluded that the key-frame remeshing has lower accuracy due to issues with conservation of calculated variables. Senecal [103] developed the CFD code which used the cut-cell Cartesian technique to eliminate the difficulty of the grid generation.

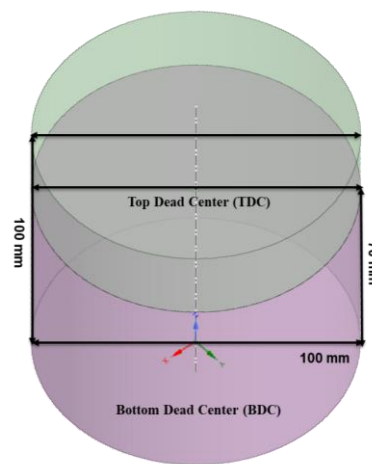


Figure 4-1 Cylinder model

An adiabatic compression and expansion process in a simple piston cylinder geometry is convenient for evaluation of the mass conservation and the numerical accuracy of cut-cell method for application to positive displacement machines.

A cylinder with diameter of 100 mm and length 100 mm was considered in this case as shown in Figure 4-1. The piston is highlighted with grey colour and moving along z-axis which is demonstrated as blue colour arrow. The cylinder is divided to two chambers by position which are shown with purple and green colours. Piston is moving inside the purple chamber as defined by equation 4-5. The rod length  $b$ , piston compression height  $s$ , crank radius  $r$  and crank angle  $\theta$  follow the relation:

$$s^2 + r^2 - 2rs * \cos(\theta) = b^2 \quad 4-5$$

The piston stroke is 70 mm and was changing sinusoidally with the frequency of 50 Hz. The piston at the top dead centre (TDC) position has the minimum volume of  $2.356 \times 10^{-4} \text{ m}^3$ . The maximum cylinder volume is  $7.854 \times 10^{-4} \text{ m}^3$  at the bottom dead centre (BDC). This gives the fixed volume ratio of 3.333 for the system. There are no leakages or flow boundaries present in the system.

The reversible adiabatic compression and expansion process in a piston cylinder without clearance was solved in this study by ANSYS Forte 2020R2. The simulation results of pressure and temperature are compared with the analytical results which are calculated by the polytropic process equation 4-6 while the polytropic index is 1.4.

$$\frac{p_2}{p_1} = \left(\frac{v_1}{v_2}\right)^\gamma = \left(\frac{T_2}{T_1}\right)^{\frac{\gamma}{\gamma-1}} \quad 4-6$$

The initial position of the piston was at TDC position i.e., minimum chamber volume. The initial conditions are 10.86 bar for absolute pressure and 482.35 K for temperature. The crank speed is set to 3000 rpm. Walls are considered adiabatic. The lowest pressure and temperature are 2.013 bar and 298 K respectively. The working fluid is air which satisfies the ideal gas equation  $pv = nRT$ . The fluid properties of air, nitrogen, oxygen, and hydrogen at 300 K are shown in Table 4-2.

Table 4-2 Fluid properties

	Unit	N2	O2	Air	H2
Molar mass	<i>g/mol</i>	28	32	29	2
Density	<i>kg/m<sup>3</sup></i>	1.142	1.301	1.176	0.082
Dynamic viscosity	<i>10<sup>-5</sup> Pa s</i>	1.76	2.04	1.849	0.88
Thermal conductivity	<i>W/(kg °C)</i>	0.0262	0.02676	0.02551	0.1820
Specific heat capacity	<i>J/(kg °C)</i>	1041	920	1007	14314

### 4.3.1 Timestep independence study

ANSYS Forte uses adaptive time step control to adjust the solver's time step size for each transient flow integration step. By setting the proper timestep not only can save the simulation time, but also capture the velocity and pressure variation. For rotary machines, the

recommended method for deciding the maximum simulation time step is to have at least 10-time steps per degree of rotation [104]. Using this guideline, the maximum time step can be calculated as  $60/(\text{RPM} \times 360 \times 10)$  which gives  $5.55\text{E-}6$  seconds per step for 3000 rpm. To test the time step setup in Forte, three different time steps are compared as shown in the Table 4-3. The simulation is run for 5 cycles corresponding to total of 1800 degree. The time step has an impact on the pressure and temperature. The calculation error decreased from 3.37 % to 0.35 % as calculated by the equation  $\text{Error} = \frac{P-10.86}{10.86} * 100$  and  $\text{Error} = \frac{T-482.35}{482.35} * 100$ . With the increasing of the time step, the pressure and temperature error decrease.

The Courant number otherwise called CFL number is a dimensionless parameter to determine the stability and accuracy of time-dependent simulations. The Courant number can be expressed as  $C = v * \Delta t / \Delta x$ . Maximum Courant number is compared for three timesteps as shown in Table 4-3.

Table 4-3 Timestep independence study

	Timestep 1	Timestep 2	Timestep 3
Time steps per degree	0.9	1.1	11
Maximum Courant number	1.95	0.91	0.19
Error in max pressure [%]	3.37	2.83	0.35
Error in max temperature [%]	3.39	2.83	0.33

### 4.3.2 Mesh independence study

The cut-cell cartesian method utilises global mesh size parameter to control the number of cells in the mesh. Ideally, the solution should be independent of the mesh size. Three cases with increasing number of elements were simulated to evaluate the mesh independence. The mesh number is adjusted by the global mesh size. The maximum number of elements of three cases are 10.3 k, 15.8 k, and 22.0 k elements respectively while the minimum number of elements are 3.5 k, 5.6 k and 8.1 k elements respectively for three analysed cases as shown in Figure 4-2. The presented section is the starting position of the piston motion, which shows the entire cylinder chamber.

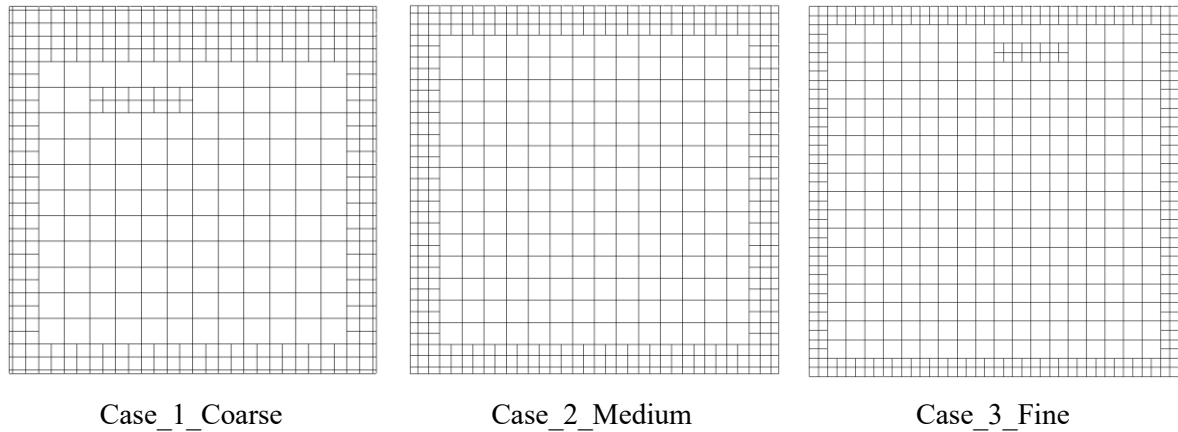


Figure 4-2 The cylinder cross-section mesh with different size.

As shown in Table 4-4, both pressure and temperature errors were very low of the order of 0.05 % for all the three mesh sizes. This can be considered as high numerical accuracy level. Therefore, the medium mesh size was used for further analysis since temperature error was the lowest for this mesh size. The global mesh size in this case is 0.6 cm, the local mesh size is half of the global mesh sizes with 3 layers of cells near the wall boundaries as shown in the Figure 4-2 Case\_2\_Medium.

Table 4-4 Mesh independence analysis

	Coarse	Medium	Fine
Element number	10.3k	15.8k	23k
Global Mesh Size	0.7	0.6	0.5
Error in max pressure [%]	-0.07	-0.04	0.03
Error in max temperature [%]	-0.04	-0.01	0.06

Firstly, the volume conservation is compared for three different mesh sizes as shown in the Figure 4-3. The maximum volume error of three cases is around 0.97 %. That means volume conservation is not sensitive to the mesh size. In addition, the change of volume error with cycles can be ignored because with the increasing of the cycle number, the maximum volume error is around 0.97 %. Figure 4-3 indicates that all mesh sizes are sufficiently accurate to describe the chamber volume's cyclic repetition.

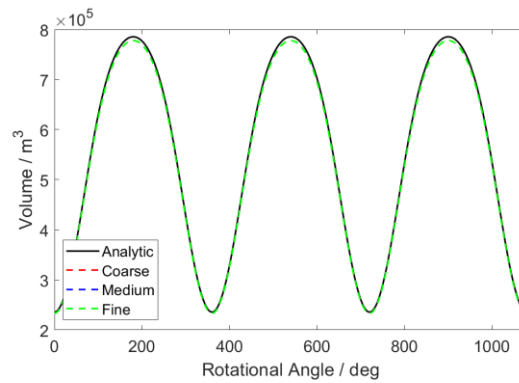
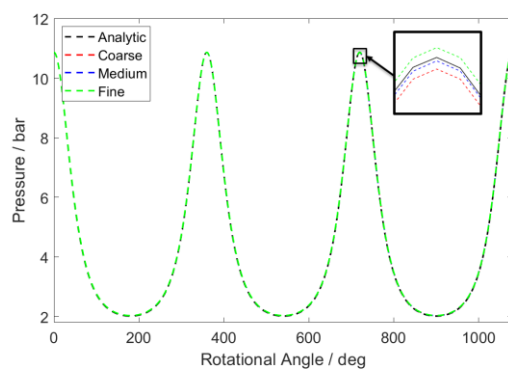
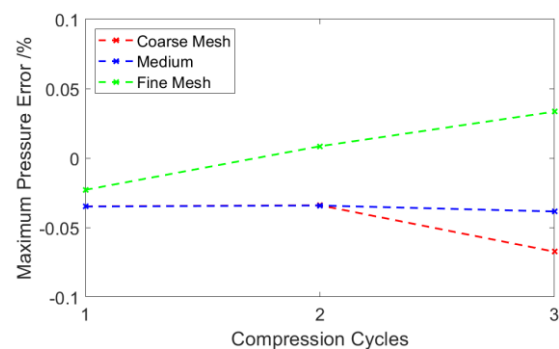


Figure 4-3 Cyclic chamber volume variation.

The pressure variation of three cases is shown in Figure 4-4 (a), the pressure matched well with the analytic solution for three continuous cycles. Figure 4-4 (b) shows the error in cyclic pressure predictions for three continuous cycles. The pressure error increased with the number of cycles because of the accumulated error. For the first two cycles of the coarse mesh, the error remained largely consistent, but it was increased in the third cycle. For the fine mesh, the maximum pressure error increased linearly with the progression of compression cycles. The medium mesh had the consistent error for the three cycles and was chosen for further study.



(a) Pressure variation



(b) Error in pressure predictions

Figure 4-4 Pressure variation and error.

The temperature variation and error of cyclic temperature prediction are shown in Figure 4-5 which has similar trend to pressure variations shown in Figure 4-3.



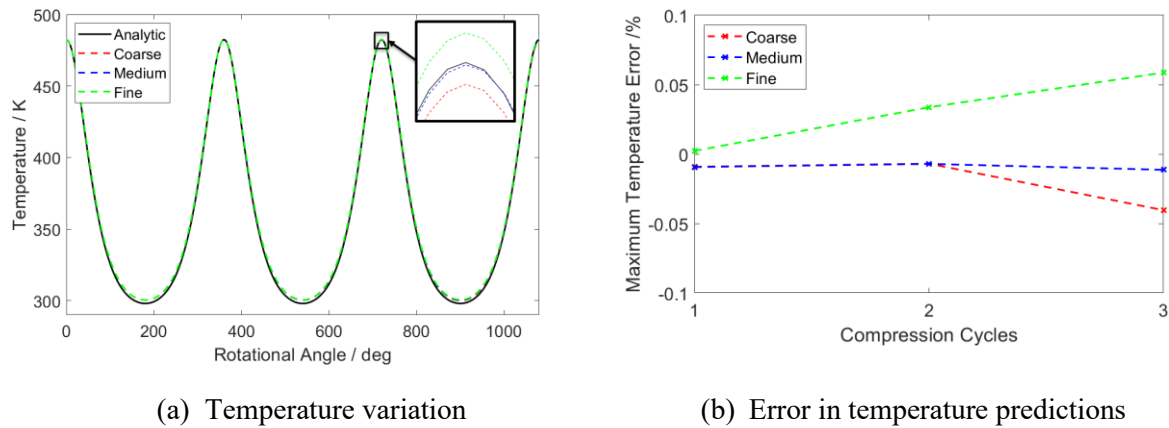


Figure 4-5 Temperature variation and error.

The numerical accuracy level of the cut-cell method was thus found to be suitable to use this technique for a practical pump application with complex rotor geometry.

According to the ideal gas law  $PV = nRT$ , the average molecular weight is 28.8 g/mol. The mass in the cylinder is 1.84 g while for all the case study, the mass is a constant which is 1.82 g. The error in mass is around 1.1 %. The error of max volume and min volume are both 0.97 %.

#### 4.4 Comparison between aligned and non-aligned mesh

The objective of the next exercise is to evaluate for conservativeness of the cut-cell cartesian method when the numerical mesh is not aligned to the to the direction of the piston movement. This is achieved by rotating the cylinder along the y-axis and then along the x-axis as shown in Figure 4-6. In this case, the mesh is aligned with the global coordinate system while the piston moving direction is along the cylinder axis.

All other simulation setups in ANSYS Forte are same for both cases.



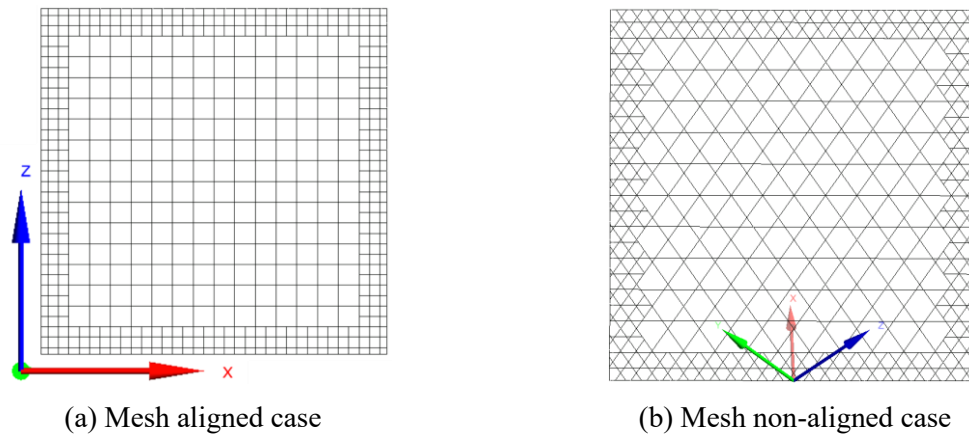


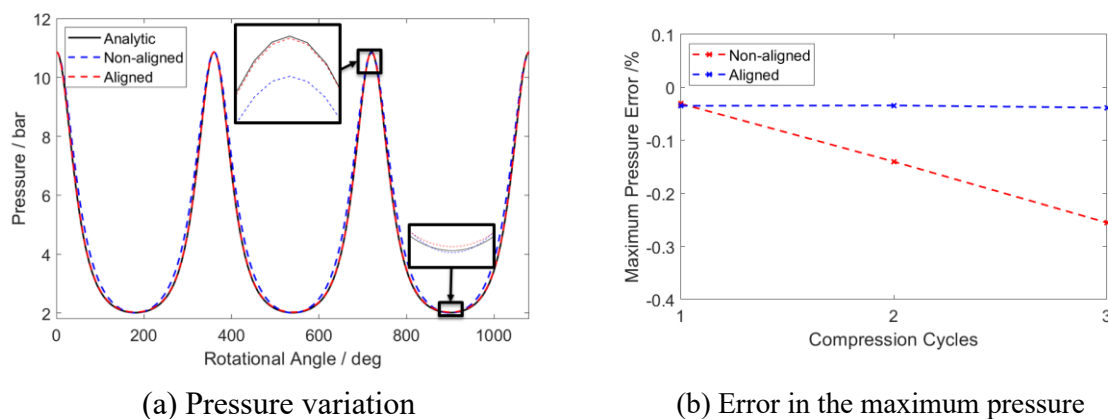
Figure 4-6 Mesh of aligned and non-aligned case

Table 4-5 shows the comparison between the aligned and non-aligned meshes. It can be observed that the error in mass is same for both cases.

Table 4-5 Comparison between aligned and non-aligned mesh

	Aligned mesh	Non-aligned mesh
Element number [k]	15.8	15.2
Global Mesh Size	0.6	0.6
Error in mass [%]	1.1	1.1
Error in max pressure [%]	-0.04	-0.26
Error in min pressure [%]	0.77	-0.4

Figure 4-7 shows that the pressure of the non-aligned case also matches well with the analytical solution. The Figure 4-7 (b) shows that the error in the maximum pressure is increasing with compression cycles.



(a) Pressure variation

(b) Error in the maximum pressure

Figure 4-7 Comparison of calculated pressure for first three cycles

#### 4.4.1 Comparison with increased number of cycles

In this section, taking the coarse aligned mesh as an example, the volume, pressure, and temperature variation of cycles 1 - 3 were compared with the values in cycles 101 - 103. After 100 cycles, the error of volume remains the same. However, the error of maximum and minimum pressures increased significantly to -12.58 % and -13.24 % respectively. The error in maximum and minimum temperatures also has the similar level, i.e., -12.55 % and -13.23 % respectively. The simulation is continuous, the next cycle of simulation used the results from last cycle as initial boundary conditions. The numerical error is accumulated with increased number of cycles.

Table 4-6 Comparison between cycles

	Cycle 3	Cycle 103
Error in Volume [%]	-0.97	-0.97
Error in max pressure [%]	-0.36	-12.58
Error in min pressure [%]	-0.72	-13.24
Error in max temperature [%]	-0.33	-12.55
Error in min temperature [%]	-0.71	-13.23

The volume variations in cycles 1-3 and cycles 101-103 are shown in Figure 4-8. After 100 cycles, the volume error remains small at -0.97 %.

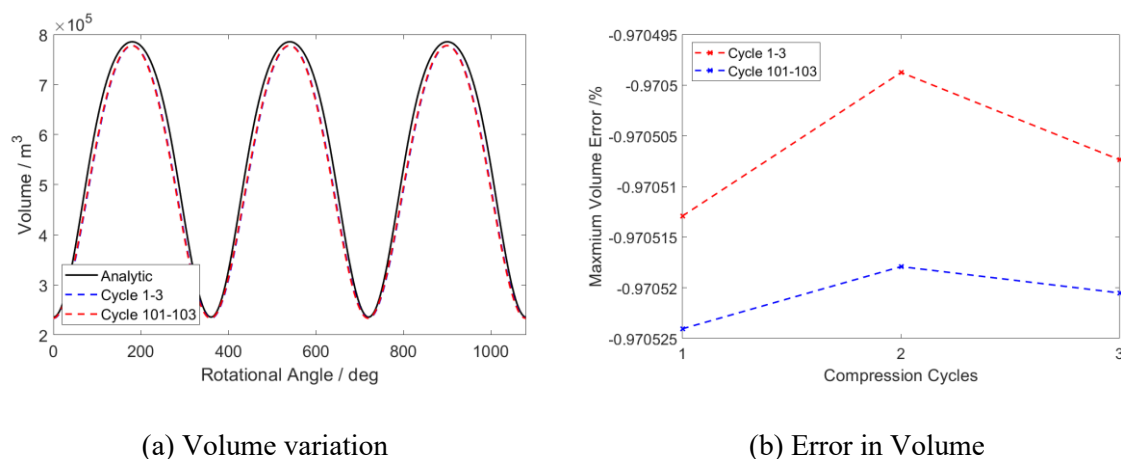


Figure 4-8 Volume variation and error.

The comparison of variation in pressure for cycles 1-3 and cycles 101-103 are shown in Figure 4-9. The maximum pressure error increased linearly with number of calculated cycles. The error is significantly higher after 100 cycles and will continue increasing with further simulation.

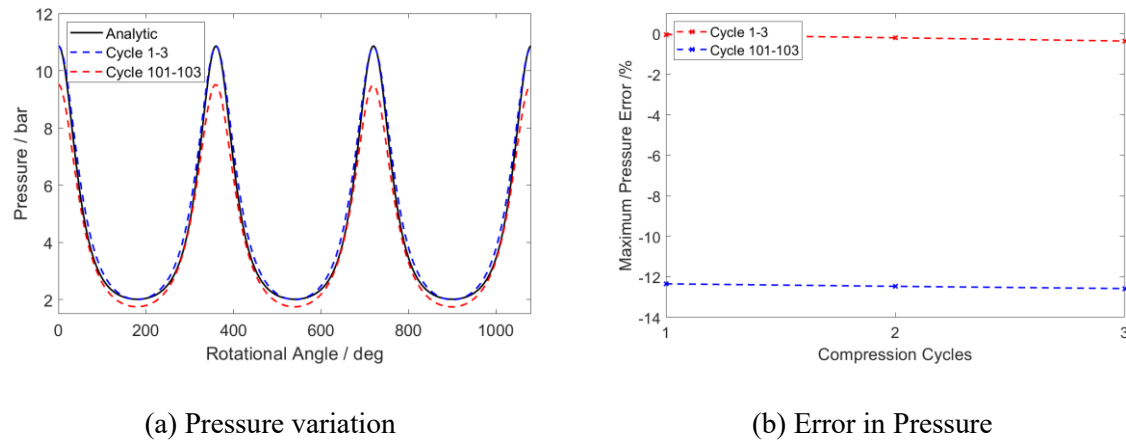


Figure 4-9 Pressure variation and error.

The temperature difference between cycles 1-3 and 100-103 is shown in Figure 4-10(a). The error of the maximum temperature is of the same level as pressure Figure 4-9(b).

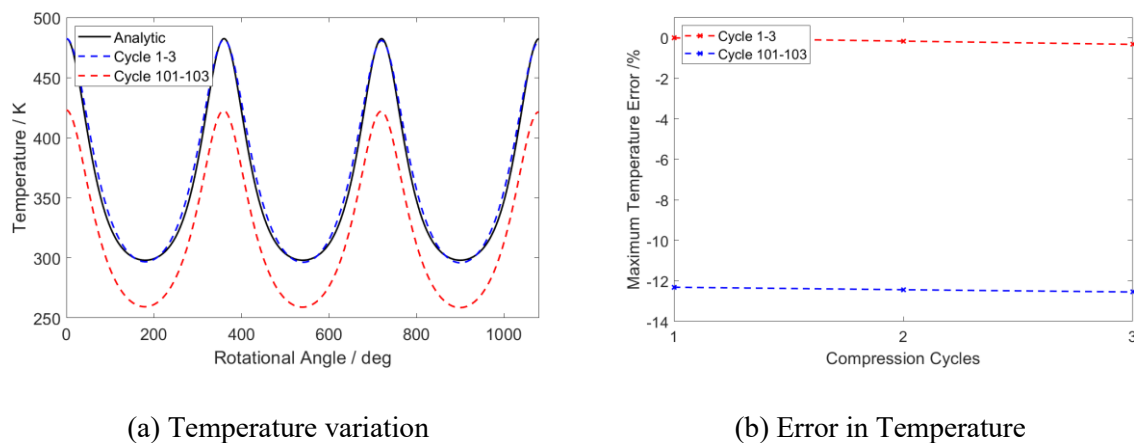
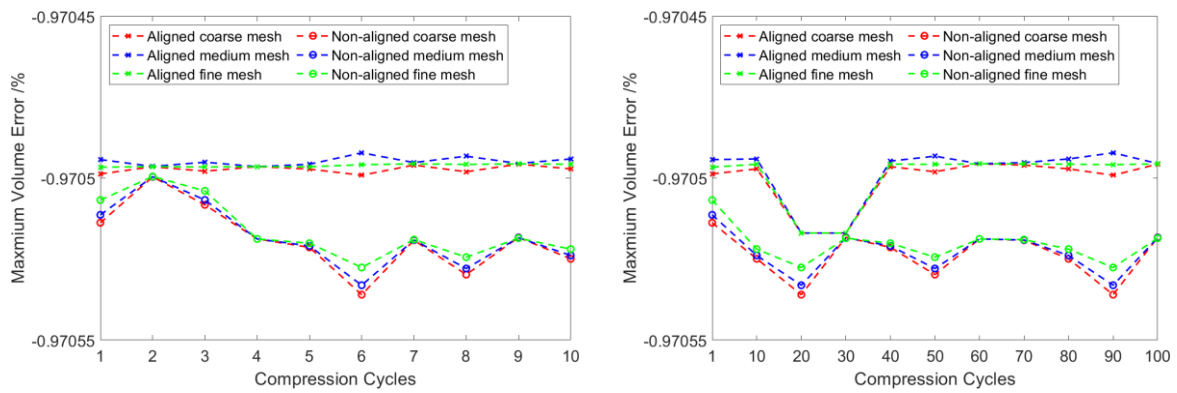


Figure 4-10 Temperature variation and error.

To further study the effect of the cycles to the coarse mesh, medium mesh and fine mesh, the volume error, temperature error and pressure error were calculated for 10 cycles and 100 cycles and show in Figure 4-11, Figure 4-12, Figure 4-13. The volume error for all mesh sizes remains small irrespective of the increase in the number of piston cycles. The mesh number does not

have large effect on the volume error. ANSYS Forte has good consistency of mesh generation for different mesh size. The error is within the range from -0.97055 % to -0.97045 %.



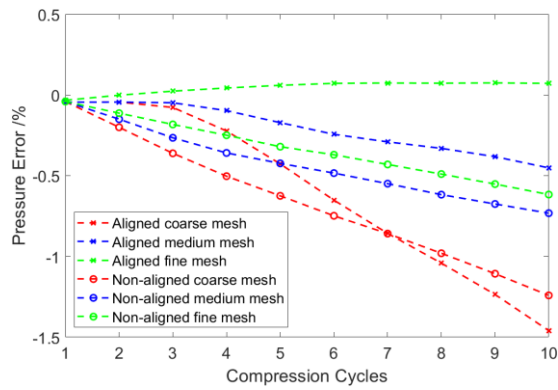
(a) Volume Error of 10 Cycles.

(b) Volume Error of 100 Cycles.

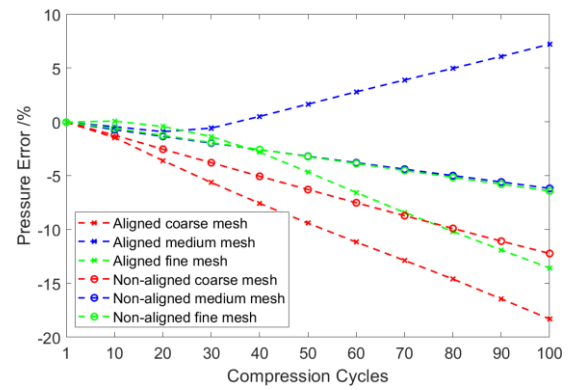
Figure 4-11 Volume Error.

Figure 4-12(a) shows the pressure error in the first 10 cycles. For all cases, the error increases with the increase in the number of cycles and the absolute error reaches 1.5 %. The aligned mesh shows better accuracy than a non-aligned mesh in the first 10 cycles. By increasing the number of mesh elements, the error decreases.

Figure 4-12(b) illustrates the pressure error in the 100 cycles with interval of 10 cycles. The pressure error increases with the number of cycles and reaches maximum of -13.24 %. The error shows linear trend after 30 cycles. Unexpectedly, the results obtained on a non-aligned meshes shows better accuracy after 30 cycles. Also, the increase in the number of cell elements shows reduction in calculation error.



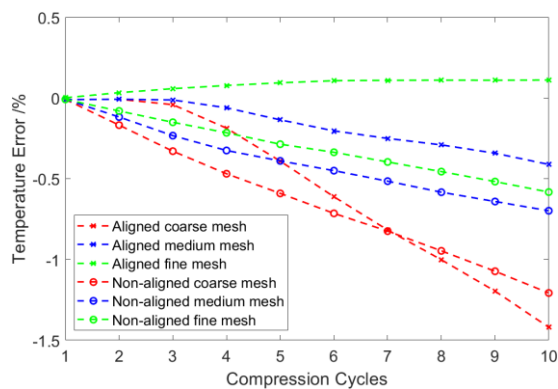
(a) Pressure Error of 10 Cycles.



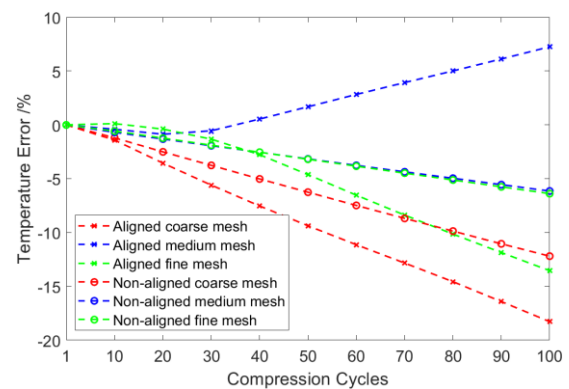
(b) Pressure Error of 100 Cycles.

Figure 4-12 Pressure Error.

The Figure 4-13 shows the error in temperature which remains similar to the error in pressure.



(a) Temperature Error of 10 Cycles



(b) Temperature Error of 100 Cycles

Figure 4-13 Temperature Error.

## 4.5 Conclusion

The simple piston cylinder case is used to evaluate the conservativeness of the cut-cell cartesian method. The time step independence study and the mesh independence study have been conducted for the mesh aligned with the direction of piston movement. Then, with the optimal timestep and mesh size, the aligned mesh and non-aligned mesh were compared in terms of the pressure, temperature, and mass conservation. The conclusions can be drawn as following:

- By continuing increasing the number of mesh elements, the overall accuracy will improve.
- The cut-cell cartesian mesh satisfied the volume conservation. The volume error remained low with the increase in the number of cycles.

- The error in pressure and temperature increased with the number of cycles. It is likely that the numerical error accumulates with the increase in the number of cycles. The pressure and temperature absolute errors of all the cases are within 1% in the first 3 cycles, within 1.5 % in the first 10 cycles and can reach as high as 13.24 % at 100 cycles.
- The aligned mesh shows better accuracy than the non-aligned mesh in the first 10 cycles. However, the non-aligned mesh shows better accuracy after 30 cycles. It is considered as an error cancellation for non-aligned mesh.
- The error shows linear relation to the number of cycles after 30 cycles.

# Chapter 5 Case studies of Alternative grid generation methods for twin screw machines

## 5.1 Introduction

Two of the most common grid generation methods which can be implemented for 3D simulation of twin screw machines are body-fitted method and cut-cell cartesian method. The cut-cell cartesian grid generation method has been explored in the previous chapter using piston cylinder. In this chapter, the body-fitted method was examined on the Roots blower case, low-Vi oil injected compressor case and twin screw vacuum pump case. The cut-cell cartesian method was examined on the Roots blower case and hook and claw pump case. The body-fitted mesh was generated by SCORG [105] and the cut-cell cartesian mesh was generated by ANSYS Forte. The solvers for two methods are ANSYS CFX, ANSYS Fluent and ANSYS Forte.

## 5.2 The simulation of the hook claw pump

Hook and claw positive displacement pumps are widely used for recirculation of excess hydrogen in fuel cells. The system throughput is sensitive to the efficiency of the pump at varying operating conditions and hence needs an optimisation of the pump design. 3D computational fluid dynamic analysis is an effective method to optimise the performance by design modifications. However, for the hook and claw pumps it is difficult to conduct 3D CFD (Computational Fluid Dynamics) simulation using body fitted deforming grids because of the sharp cusp of the rotor profile and the abrupt topology changes which pose problems for generation of structured meshes. With the availability of software like ANSYS Forte, Star CCM+, and Converge CFD, cut cell Cartesian mesh can be generated automatically from the CAD model, and solvers are capable to handle the complex and moving geometries. The aim of this chapter is to evaluate ANSYS Forte solver to simulate hook and claw pumps under different working conditions. In Chapter 4, the conservation accuracy of the cut-cell Cartesian mesh was checked using an adiabatic piston cylinder case and it was found out that the conservativeness for a closed system is not achieved. Since the hook and claw pump is an open system, this analysis will investigate conservativeness of the method for such system. The pump was simulated under different working condition and the results are validated with the



experimental data. Finally, operation with two working fluids, air and hydrogen are compared for velocity, temperature, and pressure variations. The results show that CFD simulation of positive displacement hook and claw type hydrogen pump using cut-cell cartesian mesh is an efficient and effective approach for the optimisation of the system.

Air and hydrogen supply systems play important role in the proton electrolyte membrane fuel cell (PEMFC) systems [106]. However, few research focus on the air and hydrogen supply systems' working parameters such as pressure, temperature and mass flow rate which have significant impact on the performance of PEMFC. Computational fluid dynamics combined with Taguchi method, as the optimization tool of the working parameters, have been utilized for the performance prediction of scroll-type hydrogen pump [25,107] and claw-type hydrogen pump [29,82].

### 5.2.1 Rotor geometry

The geometry of a typical hook and claw pump is shown in the Figure 5-1. The drive motor connects with the main rotor through synchronised gears. Hence there is a clearance between the main and gate rotors without their direct contact. Two rotors rotate in the opposite direction in the casing to accomplish the suction, transport, internal compression, and the discharge process. The main rotor rotates clockwise, and gate rotor rotates anti-clockwise in the configuration shown in Figure 5-1. The suction and discharge ports are on the same axial side. The internal compression ratio can be varied by adjusting the discharge port position and area.

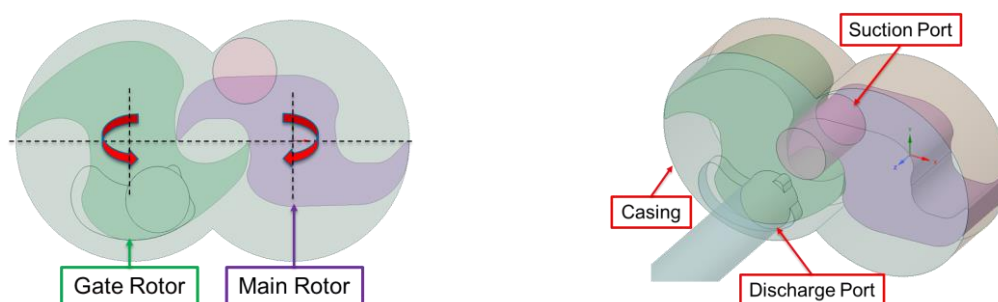


Figure 5-1 The twin screw vacuum pump rotor profile.

The claw pump rotor geometry parameters are listed in Table 5-1. The main rotor and gate rotors have the same outer and inner circle diameters. The clearance between the rotors and casing in axial direction is 0.08 mm. The clearance between the rotors and casing in the radial direction is 0.07 mm. The clearance between the main and gate rotor is 0.08 mm.

Table 5-1 Rotor geometry

Rotor Configuration	Value	Rotor Configuration	Value
Rotor combination	1by1	Inlet pipe length [mm]	20
Axis distance [mm]	45	Outlet pipe length [mm]	100
Rotor length [mm]	25	Axial clearance [mm]	0.08
Outer circle diameter [mm]	65.42	Radial gap [mm]	0.07
Inner circle diameter [mm]	24.42	Interlobe gap [mm]	0.08

ANSYS Forte solver's gap model has been used to calculate the leakage flow if the clearance is smaller than the surface proximity which is an input parameter defining the size of the clearance where leakage model was implemented. The leakage model considers the cell size effect and wall shear resistance effect. The gap resistance model is switched on in order to model the higher resistance caused by the smaller physical gap sizes if the gap sizes in the geometry are larger than the physical values. The gap shear resistance factor is defined as the ratio of decelerated velocity and the original velocity as shown in equation 5-1 [101]. In the equation  $h$  is the gap size,  $\nu$  is the kinematic viscosity, and  $\Delta t$  is the CFD time step [100]. The gap resistance model is based on the analytical solution of a shear flow between two parallel plates.

$$\frac{U_{decelerated}}{U_{original}} = f\left(\frac{1}{h^2}, \nu, \Delta t\right) \quad 5-1$$

### 5.2.2 Experimental setup

The test rig of the prototype of claw pump is shown in Figure 5-2. Claw pump is directly connected with variable speed motor. A yellow tank is connected with suction pipe in order to provide elevated suction pressure. Discharge pressure is controlled by a relieve valve which is connected to the discharge pipe. Volume flow rate is also measured in the discharge pipe. Electrical power is recorded from the power input cable.

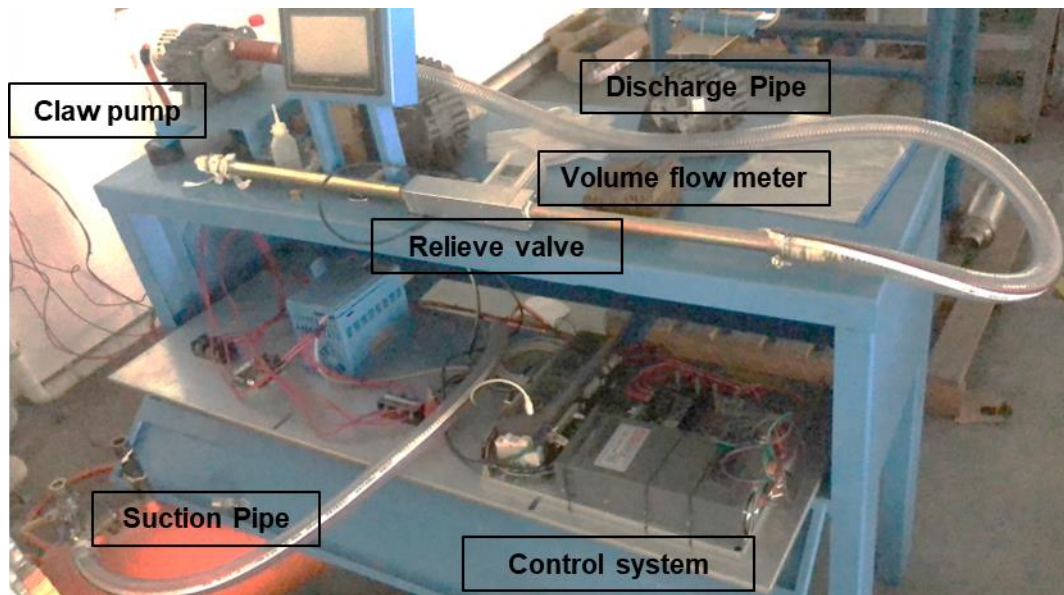


Figure 5-2 Test rig of claw pump.

### 5.2.3 ANSYS Forte solver setup

The pump's operating condition specifications are listed in Table 5-2. This case study did not consider the heat transfer between the casing wall and environment, the outlet wall and the environment, and the rotors and chamber. All boundary walls were thus set as adiabatic. The inlet pressure is set to 1.01 bar while the outlet pressure is varied in the range 1.01 – 1.31 bar as tested during the experiments. Based on the study in section 4.3.1, the time step 5.0E-6 was chosen for the simulation of this claw pump.

Table 5-2 Operating conditions and solver setup parameters

Parameters	Value	Parameters	Value
Speed [rpm]	6000	Turbulence Model	k-epsilon
Suction Temperature [K]	300	Suction Pressure [bar]	1.01
Discharge Temperature [K]	300	Discharge Pressure [bar]	1.01-1.31
Global mesh size	0.1	Time steps size	2.5E-06

### 5.2.4 Mesh independence study

Based on the preliminary study, three global mesh sizes were chosen as listed in Table 5-3. The suction and discharge pressure are same and set to 1.01 bar. The experimental inlet volume flow rate for that pressure is 361 L/min. The volume flow rate error was calculated based on

the equation  $Error = \frac{V-361}{361} * 100$ . The case with the fine mesh can reach high accuracy and suitable simulation time.

Table 5-3 Mesh independence analysis

Parameters	Units	Coarse	Medium	Fine
Global mesh size	[cm]	0.3	0.2	0.1
Element count	[/]	61,000	148,000	615,000
Simulation time for 5 cycles	[h]	15	26	42.5
Inlet volume flow rate	[L/min]	408.6	388.6	371.4
Volume flow rate error	%	13.19	7.65	2.88

The cartesian cut-cell mesh is generated automatically based on the global mesh size and adaptive mesh refining settings. The mesh is refined based on the temperature and velocity gradients as can be seen in Figure 5-3 with three different mesh size. Coarse mesh and medium mesh were not able to capture the details of flow vortices and higher-pressure gradients, but it was possible to observe these vortices in the Fine Mesh case. As shown in Figure 5-3 (c), the pressure gradient was observed in red squares 1 and 2 and the vortices were captured in red squares 3 and 4.

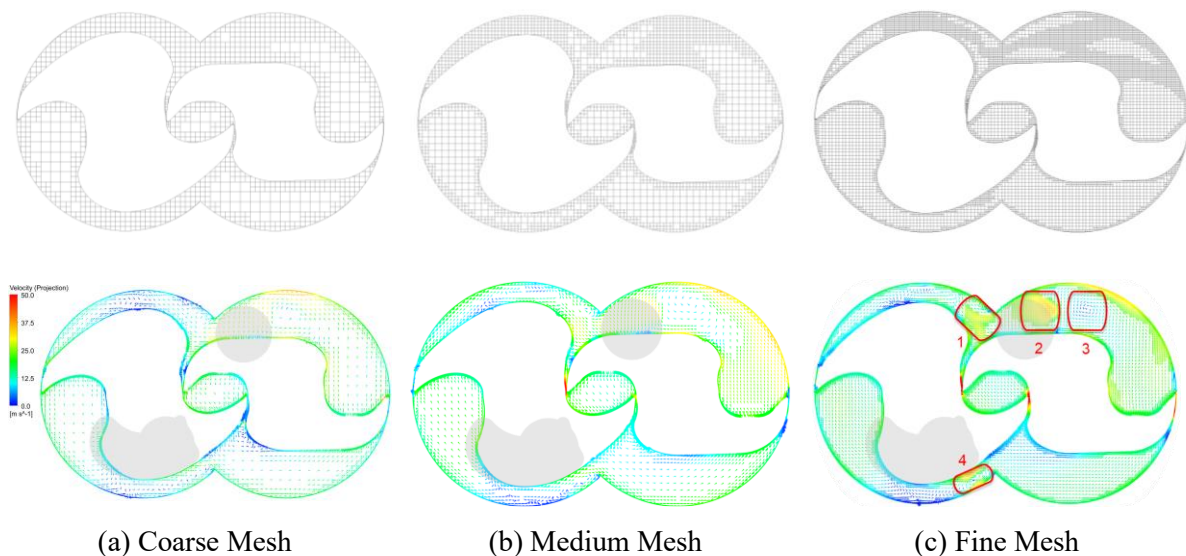


Figure 5-3 The mesh and velocity distribution results of varying mesh sizes.

The volume flow rate is also compared for every rotational cycle to check the convergence of the simulation. The inlet volume flow rate and outlet volume flow rate changing with the

rotation angle are shown in the Figure 5-4. The volume flow rate shows a repetitive trend after each 180 degree crank angle.

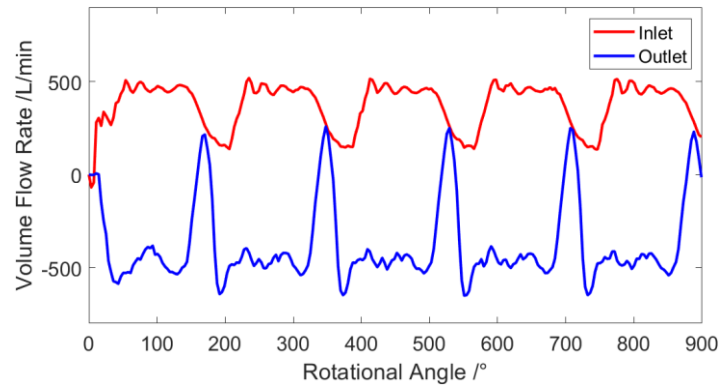


Figure 5-4 The Volume flow rate

Five cycles were calculated for the fine mesh case. To check the convergence accuracy, the inlet volume flow rate was calculated and compared for individual cycles. The volume flow rate and error compared with the experimental results are shown in the Table 5-4. The volume flow rate becomes stable after the cycle 1 and the error is around 3 % for the subsequent cycles which is a practically acceptable accuracy level.

Table 5-4 Cycle comparison

	Unit	Cycle1	Cycle2	Cycle3	Cycle4	Cycle5
Volume flow rate	L/min	384.2	372.3	370.8	372.2	371.5
Error	%	6.4	3.1	2.7	3.1	2.9

## 5.2.5 Study with varying fluids and operating conditions

To study the pressure and velocity variation inside the claw pump under different working conditions, four cases with different outlet pressures were simulated and compared with the experimental results. The working fluid is air. Other parameters are same as listed in Table 5-2. In addition, the case study with hydrogen as the medium was simulated to show the difference with the air.

### 5.2.5.1 Case study with air

The power was calculated based on the rotor torque as shown in equation 5-2.

$$P = \frac{2\pi n(T_{main} + T_{gate})}{60} \quad 5-2$$

The power and volume flow rate were calculated and listed in Table 5-5. The power consumption is increasing with the discharge pressure while the inlet volume flow rate is decreasing. The error between simulation and experiment changes from 2.88 % to -2.46 %. The volume flow rate is over predicted in the simulation Case1. The predicted volume flow rate decreases with the increase of the discharge pressure due to increased leakage flow for higher pressure difference. It is believed that the internal clearances reduce with the increase of the discharge pressure in the experiment due to the higher temperatures of the fluid. However, in simulation, the clearances are kept constant. The power measured from experiments is more than three times higher than the power calculated from simulation. The reason is that mechanical losses including timing gear, bearings, mechanical sealings are not considered in the simulation.

Table 5-5 Simulation results comparison

Variables	Unit	Case1	Case2	Case3	Case4
Discharge pressure	[bar]	1.01	1.11	1.21	1.31
Simulation power	[W]	90.2	102.1	144.3	199.5
Experiment power	[W]	300	445	600	600
Simulation inlet volume flow rate	[L/min]	371.4	320.6	287.2	261.8
Experimental inlet volume flow rate	[L/min]	361.0	321.1	288.6	268.4
Errors between simulation and experiment	[%]	2.88	-0.16	-0.49	-2.46

To study changes in the internal flow, 7 probes are set to monitor the pressure inside the chamber. Their positions are shown in Figure 5-5. P1 is set near the suction port and P7 is positioned near the discharge port. The interval between remaining probes is 60 degrees.

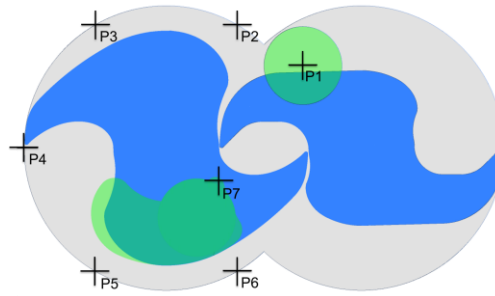


Figure 5-5 Location of the seven pressure monitor points

By picking up the valid pressure of each probe and connecting the pressure according to the rotational angle, the pressure- angle diagram was constructed as shown in Figure 5-6 (a). The pressure-volume diagram was constructed by matching the pressure with the volume. The suction process is between points A and B followed by the pressure drop process BC caused by the sudden increase of the chamber volume. Subsequently, the chamber volume remained constant between points C and D while the pressure increased as a result of the back leakage. The internal compression began at point D and finished at point E. this is followed by the discharge process from E to F. At point F, the pressure drops due to the sealing curve of the chamber changed to cycloid seal.

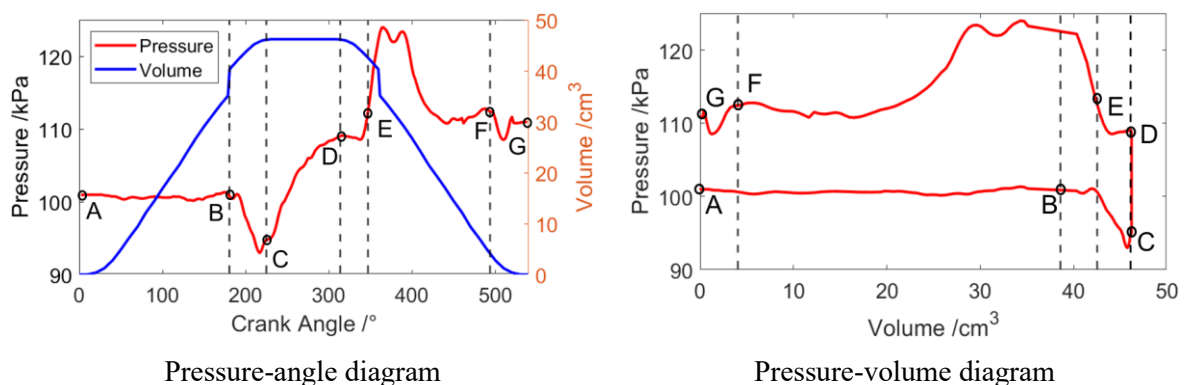


Figure 5-6 The Pressure variation with angle and volume

The pressure contour in the middle plane is shown in the Figure 5-7. The starting position is A where the suction started. The rotors return to the same position after 180 degrees as shown in the Figure 5-7 (a). The sealing curve between the upper and lower chambers is arc. The pressure of the gate rotor chamber is higher than the main rotor chamber despite the fact that two chamber are connected. This shown pressure variation within the same chamber. Pressure starts

to increase, and the main and gate rotor chamber start to separate from position C as shown in Figure 5-7 (b). The internal compression starts from position D as shown in Figure 5-7 (c). The pressure of the gate rotor chamber is higher than the main rotor chamber because of the volume difference. In this position, there are two types of sealing curves which are arc and cycloid. The sealing effect of cycloid is lower than the arc because the cycloid sealing is point – line meshing. The pressure contour at discharge position is shown in Figure 5-7 (d).

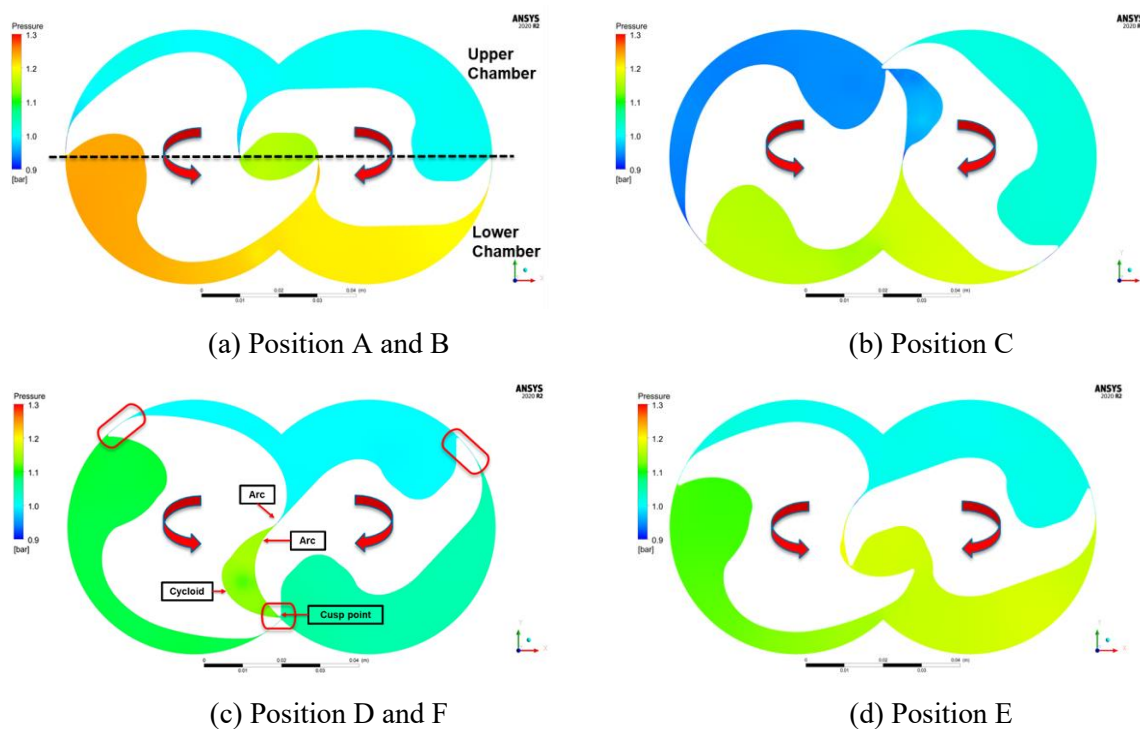


Figure 5-7 The gas pressure contour in the mid plane

The velocity vector distribution in the middle plane is shown in Figure 5-8. Both vortices and leakage flow can be tracked. The position of vortices are marked using red rectangle. Figure 5-8 shows strong vortices near the discharge port and the leakage flow at cycloid meshing area. Strong vortices are mainly produced after the meshing of cycloid and bears advantages and disadvantages. In one hand, vortices can lead to flow instabilities and undesirable flow patterns. In some cases, vortices can cause flow separation, which may result in reduced efficiency, increased drag, or other detrimental effects. Uncontrolled vortex shedding can induce vibrations and oscillations, causing structural fatigue in engineering systems. In another hand, vortices can enhance mixing and transport of fluids within a flow. They promote the exchange of momentum, heat, and mass between different regions, leading to improved mixing efficiency



in applications such as chemical reactions, combustion processes, and heat transfer. In this particular case, vortices near the discharge port can increase resistance to the flow and reduce the delivery of the compressor.

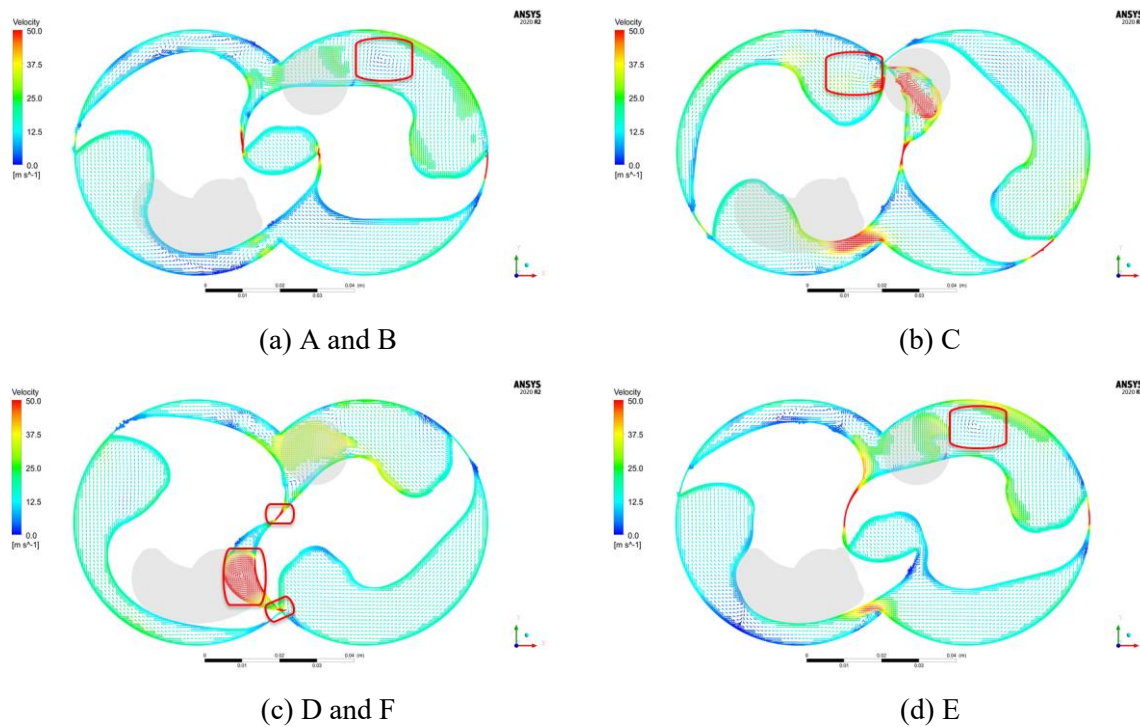
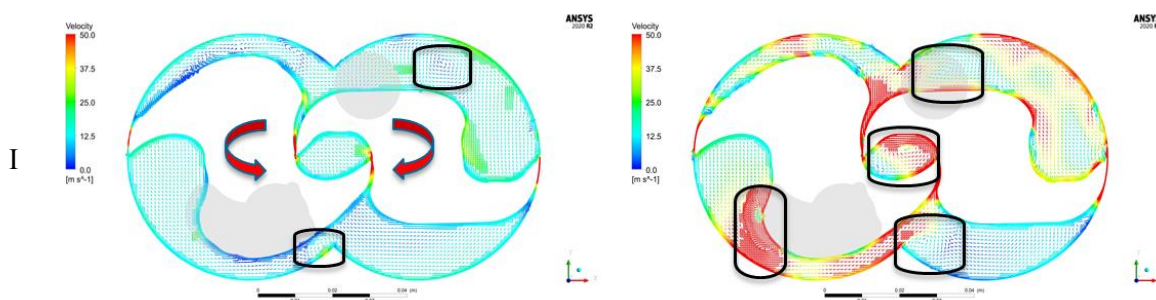


Figure 5-8 The velocity distribution in the middle plan

### 5.2.5.2 Case study with hydrogen

The velocity, temperature and pressure are compared with air and hydrogen as the working medium. The air and hydrogen properties are listed in Table 4-2. The density and the dynamics viscosity of air is around 14 times and 2 times higher than hydrogen respectively. The thermal conductivity and specific heat capacity of hydrogen is around 7 times and 14 times higher than of the air respectively.



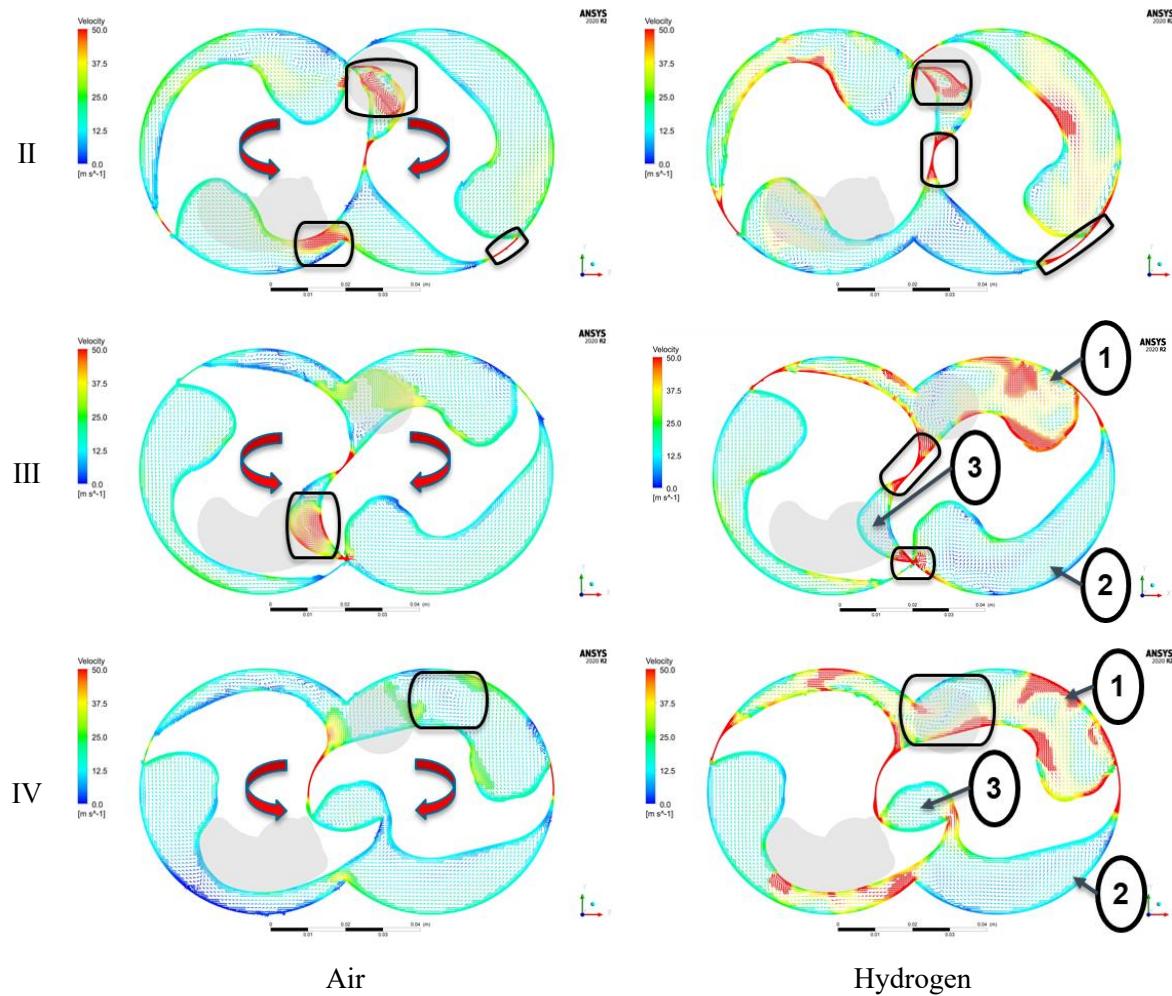


Figure 5-9 The velocity distribution comparison

The temperature under the 1.31 bar discharge pressure is compared as shown in Figure 5-9. The hydrogen case has higher range of velocities within the chamber than the air case. In the stage I of hydrogen case, high velocity can be observed near the discharge port and the interlobe clearance. The main vortices were generated near the suction port, blowhole area, discharge port and casing lower tip. The hydrogen case has higher velocity than the air case at the rotor to casing clearance and rotor to rotor clearance in the stage II. Strong velocity can be observed near the suction port. The direction of the fluid flow is from the gate to the main rotor. The stage III is compression process. In this position, there are three chambers observed at the start of the compressor. Strong vortices are observed in chamber 3 for air case. The leakage direction from chamber 3 to chamber 1 and chamber 2 is caused by the pressure difference. The stage IV is the discharge process. Chamber 2 and chamber 3 are connected when the discharge port is open. There may be leakage flow to the blowhole area which will add to the suction chamber. Hydrogen is more compressible than air. It has a lower molecular weight and a higher speed of

sound compared to air. As a result, pumping hydrogen requires consideration of its compressibility factor and the associated changes in volume and pressure, which may affect the pump performance and design requirements.

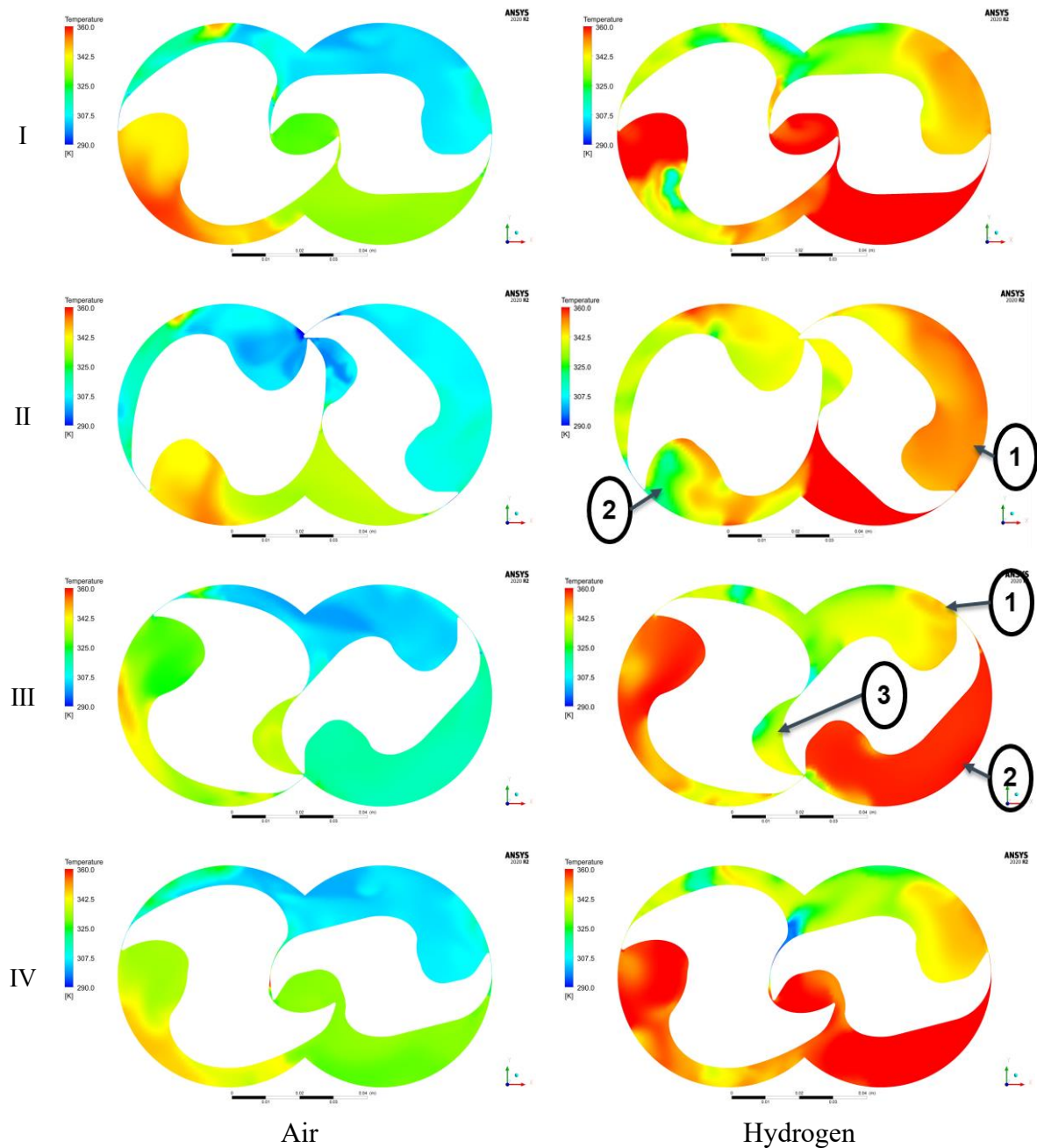
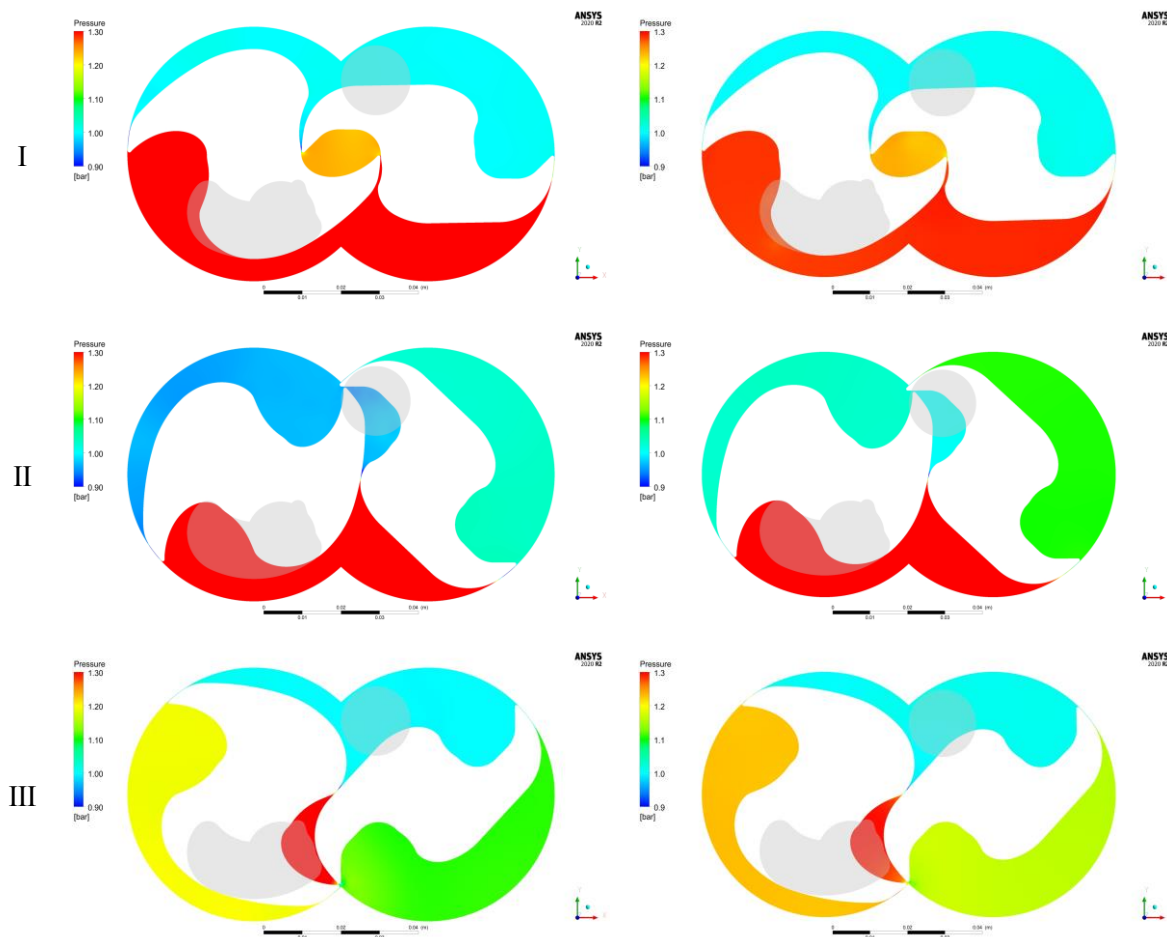


Figure 5-10 Comparison of the Temperature distribution in mid plane

The temperature under the 1.31 bar discharge pressure was compared as shown in Figure 5-10. The hydrogen case has higher temperatures in the chamber. The stage I is suction process. Th

upper chamber has lower temperature than the lower chamber. The temperature inside the chamber is not uniform. The hydrogen case has lower temperature near the discharge port because of the higher flow rate to the discharge port. Higher temperatures appear near the main rotor tip because of the leakage losses. The suction chamber temperature increased in the II stage because of the leakage. The compression starts from position III. Air case has higher temperature in the gate chamber while lower temperature for hydrogen case. The temperature within the chamber is more uniform after this stage. This can be observed in stage IV. Hydrogen has a higher thermal conductivity compared to air. This means that heat generated during compression can be more efficiently transferred within the pump and to the surroundings. Heat management, such as cooling systems, may need to be optimized for hydrogen pumping to prevent excessive temperature rise and ensure proper operation.



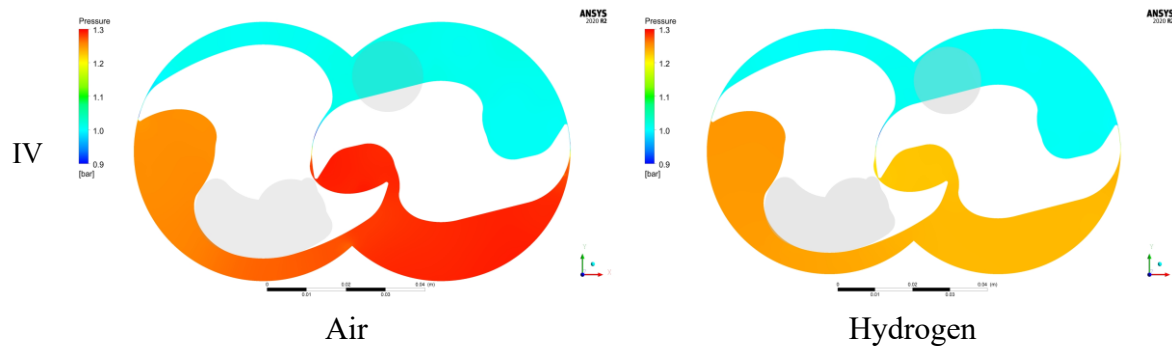


Figure 5-11 Comparison of the Pressure distribution in mid plane

The pressure distribution under the 1.31 bar discharge pressure was compared as shown in Figure 5-10. Similar pressure distribution for two cases in the stage I. Hydrogen case has higher pressure in the suction chamber compared to the air case in stage II. Hydrogen molecules are smaller and can leak through clearances more easily compared to air. The main rotor chamber pressure is higher than in the gate rotor chamber in both cases. In the stage III, the gate rotor chamber pressure is higher than in the main rotor chamber because of the leakage from the discharge port to the gate rotor chamber. The pressure variation can be observed in the main and gate chambers when two chambers are connected.

The inlet volume flow rate and power are compared in the Table 5-6. The hydrogen case has higher inlet volume flow rate and power, but the difference is negligible.

Table 5-6 Comparison of volume flow rate and power

Parameters	Unit	Air	Hydrogen
Inlet volume flow rate	[L/min]	261.8	264.7
Power	[W]	199.5	201.8

The cut-cell cartesian method was successfully tested for the claw-type pump case and provided useful data for improvement of the pump and performance optimisation.

### 5.2.6 Conclusion

In this chapter, the cut-cell cartesian mesh which was generated in the ANSYS Forte has been evaluated for numerical accuracy and feasibility for a complex hook and claw pump application. This open system allowed for greater reliability for the CFD simulation using cut-cell cartesian method for hook and claw rotor profile. The claw pump was simulated under different

discharge pressure and the inlet volume flow rate was compared to the experimental results. Additionally, two fluids air and hydrogen were analysed under 1.31 bar discharge pressure. the flow field data of velocity vectors, gas temperature and pressure contours were compared. The following conclusions can be drawn from these studies:

- The cut-cell cartesian mesh has been successfully implemented in the claw pump. Automatic mesh generation (AMG) method enables the simulation setup much simpler and adaptive mesh refinement (AMR) method enables to capture the velocity, temperature and pressure variation more clearly.
- For the claw pump under same working condition, the volume flow rate error was consistent after the first cycle and accuracy is around 3 %. Under different discharge pressures, the volume flow rate error is within 3 % compared with the experimental results.
- The P-theta diagram shows a pressure dip during the suction. It is suggested that to enlarge the inlet pressure to reduce the suction loss. The discharge port is suggested to open later after blow hole is disconnected with the discharge chamber.
- There is not much difference of the volume flow rate and power between the air case and hydrogen case.

### 5.3 The simulation of the Roots blower

The roots blower is used to compare the simulation results calculated by two solvers ANSYS CFX and ANSYS Forte which employed body-fitted mesh and cut-cell mesh respectively. This comparison can be helpful to further study the conservation and leakage model of the cut-cell Cartesian meshing.

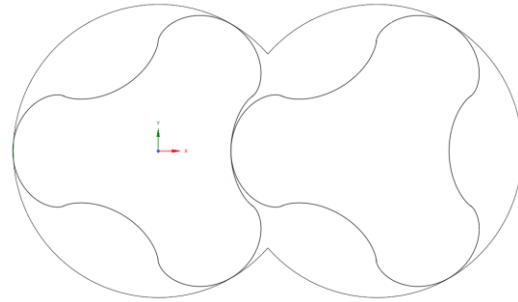
#### 5.3.1 Working conditions

The rotor geometry is shown in Table 5-7 and Figure 5-12. The roots blower analysed in this case study has a small wrap angle of 20°, which is different with the common straight Roots blower. This case is setup to investigate influence of the grid generation method on the low wrap angle machines.

Table 5-7 Rotor dimensions

Figure 5-12 Rotor profile

Item	Value
Rotor diameter/mm	160
Rotor length/mm	200
Center distance/m	120
Wrap angle/°	20
Clearances/mm	0.07
Rotor lobes	3/3



The operating conditions are listed in Table 5-8.

Table 5-8 Working conditions

Item	Value
Inlet pressure (Abs)/bar	1
Outlet pressure (Abs)/bar	3
Inlet temperature/K	300
Outlet temperature/K	375
Rotation speed/rpm	6000
Rotor lobes	3/3

### 5.3.2 Setup of the ANSYS Forte and ANSYS CFX models

Setting up a simulation starts by defining the computational mesh that will represent the geometry of the system. The 3D simulation model required for ANSYS Forte is surface geometry which was created by ANSYS SpaceClaim. The cut-cell cartesian mesh was automatically generated during the calculation. The clearances between the casing and rotor and rotors were handled by using gap refinement and gap model [101]. The mesh automatically generated in ANSYS Forte as shown in Figure 5-13 requires setting the material and the global mesh size.

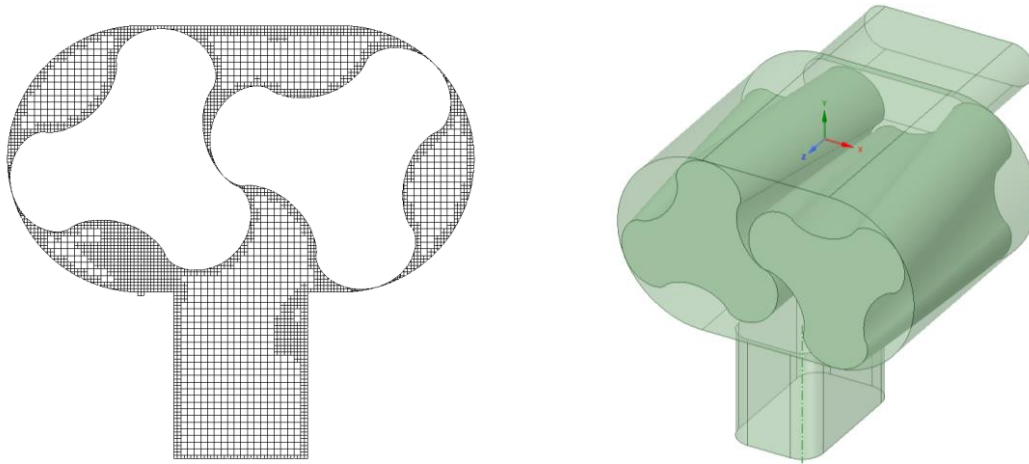


Figure 5-13 Cut-cell cartesian mesh from ANSYS Forte

The body-fitted mesh used for ANSYS CFX is generated by SCORG as shown in Figure 5-14. The process of grid generation with SCORG starts with profile definition, continues with generation of 2D meshes in cross sections along the rotor axis and finishes with connecting such meshes in a final 3D mesh. The process is explained in detail in the PhD thesis by Kovacevic [13]. The numerical mesh for ANSYS CFX is then created in SCORG together with the 3D geometry used in ANSYS forte for grid generation of cut-cartesian meshes.

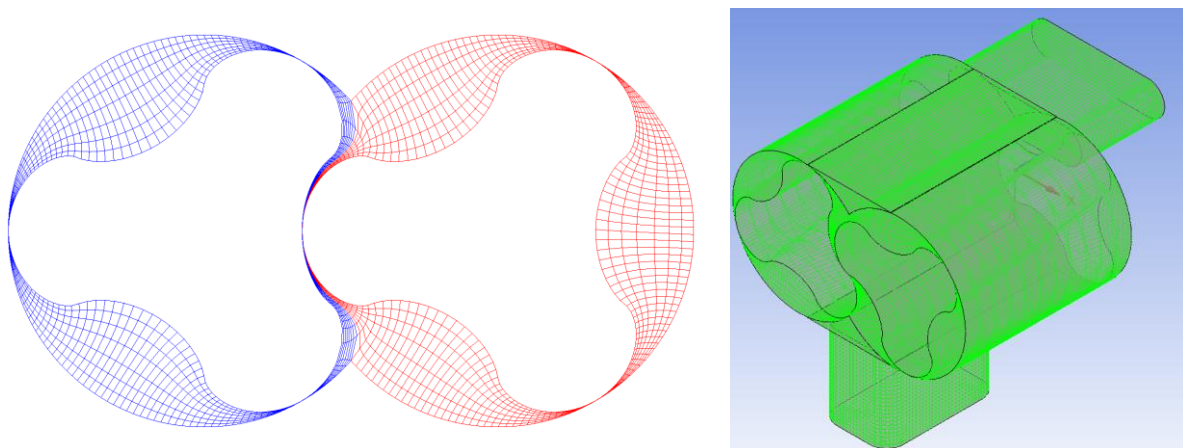


Figure 5-14 Body-fitted mesh for ANSYS CFX

All domains elements are listed in Table 5-9. The number of elements using for ANSYS Forte simulation is around 6 times comparing to ANSYS CFX. The reason could be because of automatically mesh refinement to capture results in important areas in ANSYS Forte based on



the solution. It is worth to mention that the setup of both mesh generation software follows the recommendation from the help manuals [104,105].

Table 5-9 Number of mesh for solver Forte and CFX

	<b>ANSYS Forte</b>	<b>ANSYS CFX</b>
<b>All Domains elements</b>	390000-400000	67497

### 5.3.2.1 Simulation controls

The governing equations are discretized with the respect to the spatial coordinates of the system, on a computational grid based on a control volume approach. In ANSYS CFX, the timestep is set in advance and fixed during the simulation. In ANSYS Forte, to provide time-accurate solutions, the equations are further discretized with respect to time following the operator-splitting method. The hydrodynamic time step is adaptively controlled to maximize the solution efficiency, accuracy, and stability. The numerical setup for ANSYS Forte and ANSYS CFX are shown in Table 5-10.

Table 5-10 Numerical setup for Forte and CFX

<b>Criteria</b>	<b>ANSYS Forte</b>	<b>ANSYS CFX</b>
Turbulence Model	k-epsilon	SST
Inlet boundary conditions	Inlet boundary	Opening
Outlet boundary condition	Inlet boundary	Opening
Turbulence numeric	First order	First order
Transient Scheme	Quasi-second upwind	Second order backward Euler
Time step/sec	2.78 E-6	5.55 E-5

The ANSYS CFX simulation was run in the Intel i5 6 cores computer. The running time is 10 hours. The same computer cannot be used for ANSYS Forte because this run exceeded the heartbeat limit (default is 30 mins) during the initial volume mesh creation. The CPU time could be long to solve this case if the calculation is done in serial mode or with only a few MPI cores. But ANSYS Forte has very good parallel scalability. For typical compressor calculations, ANSYS Forte can scale beyond 200 cores for parallel calculation. The ANSYS Forte was run in the Intel Xeon 16 nodes computer while the running duration is 133 hours. The ANSYS

Forte takes longer because the time step is smaller, and the number of cells in the mesh is much larger than the mesh calculated by ANSYS CFX. It is worth to point out that the operating condition from inlet 1 bar to outlet 3 bar is difficult for ANSYS CFX. The used solution was to gradually increase the discharge pressure to 2 bar and use the result file as initial conditions for 1 bar to 3 bar.

Table 5-11 Calculation time comparison of Forte and CFX

Solver	ANSYS Forte	ANSYS CFX
Total time/h	133	10
Number of iterations	20248	9000
Computer	Intel Xeon 16 cores	Intel i5 6 cores

### 5.3.3 Simulation results and discussion

The pressure, temperature, flow rate, torque and power are compared, and the results are shown in the Table 5-12. Two solvers have similar level of error between inlet and outlet mass flow rate.

Table 5-12 Numerical setup for Forte and CFX

Solver	ANSYS Forte	ANSYS CFX
Inlet MFR [kg/s]	0.3501	0.3219
Outlet MFR [kg/s]	-0.3245	-0.3014
Error between inlet and outlet	7.31%	6.39%

#### 5.3.3.1 Pressure and temperature

Three monitor points were set in the middle of the casing and along the casing. The variation of pressure at the point1 is shown in Figure 5-15. The pressure fluctuations have a similar trend between two solvers, but ANSYS Forte shows higher frequency oscillations which do not seem fully physical. That is because ANSYS Forte uses the gap model to calculate the flow in the gap clearance and the timestep in ANSYS CFX is 20 times higher than in ANSYS Forte.

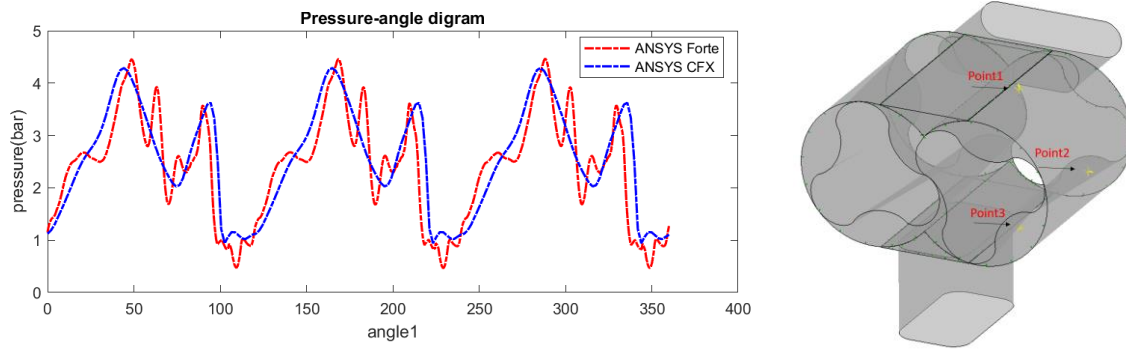


Figure 5-15 Pressure variation at Point1

The temperature at outlet is different for two solvers. ANSYS Forte predicts steady outlet temperature while ANSYS CFX predicts fluctuating temperature which has peak at 500 K as shown in Figure 5-16.

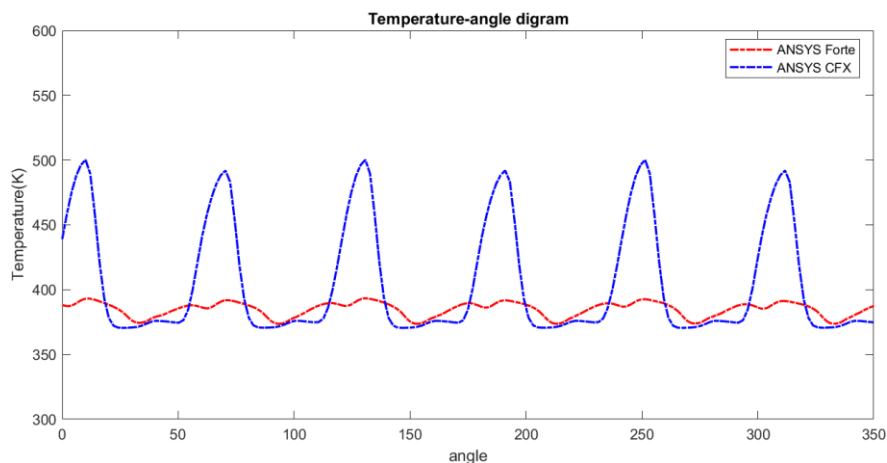


Figure 5-16 Temperature variation at outlet

### 5.3.3.2 Flow rate

The mass flowrate in the outlet port showed good agreement between two solvers. The average outlet flow rate for Forte and CFX are 0.329 kg/s and 0.335 kg/s respectively.

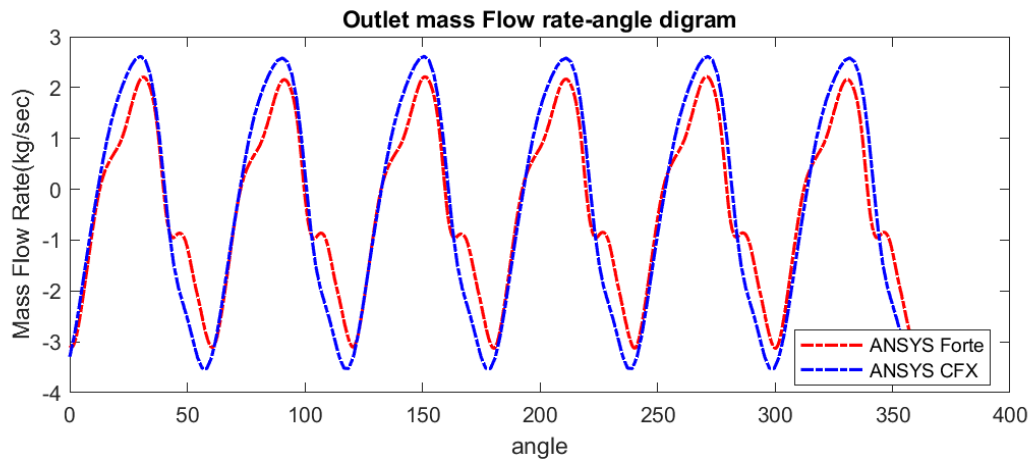


Figure 5-17 Inlet Mass flow rate

The average inlet flow rate for Forte and CFX are 0.351 kg/s and 0.325 kg/s respectively. Like outlet temperature, ANSYS CFX predicts higher maximum value.

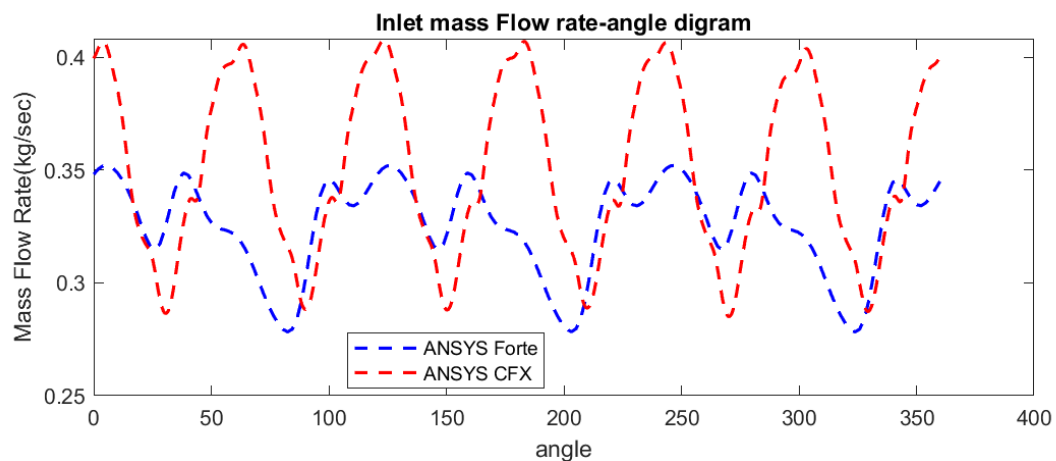


Figure 5-18 Outlet Mass flow rate

### 5.3.3.3 Torque and power

The torque is changing with the rotation angle and the trend are similar for both solvers while ANSYS Forte has significant oscillation.

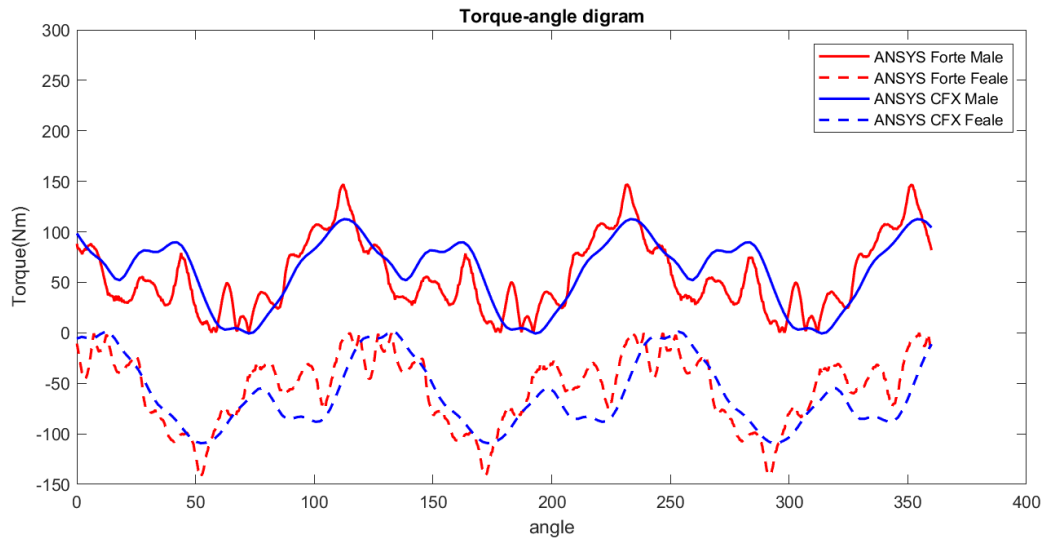


Figure 5-19 Torque

The same power trend as shown in Figure 5-20. The mean power for the ANSYS Forte and CFX are 70.14 W and 76.19 W respectively.

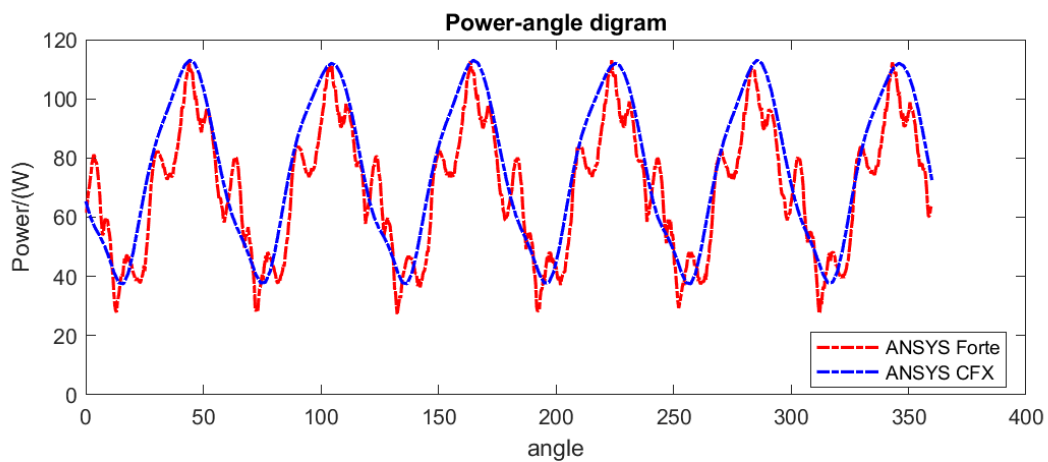
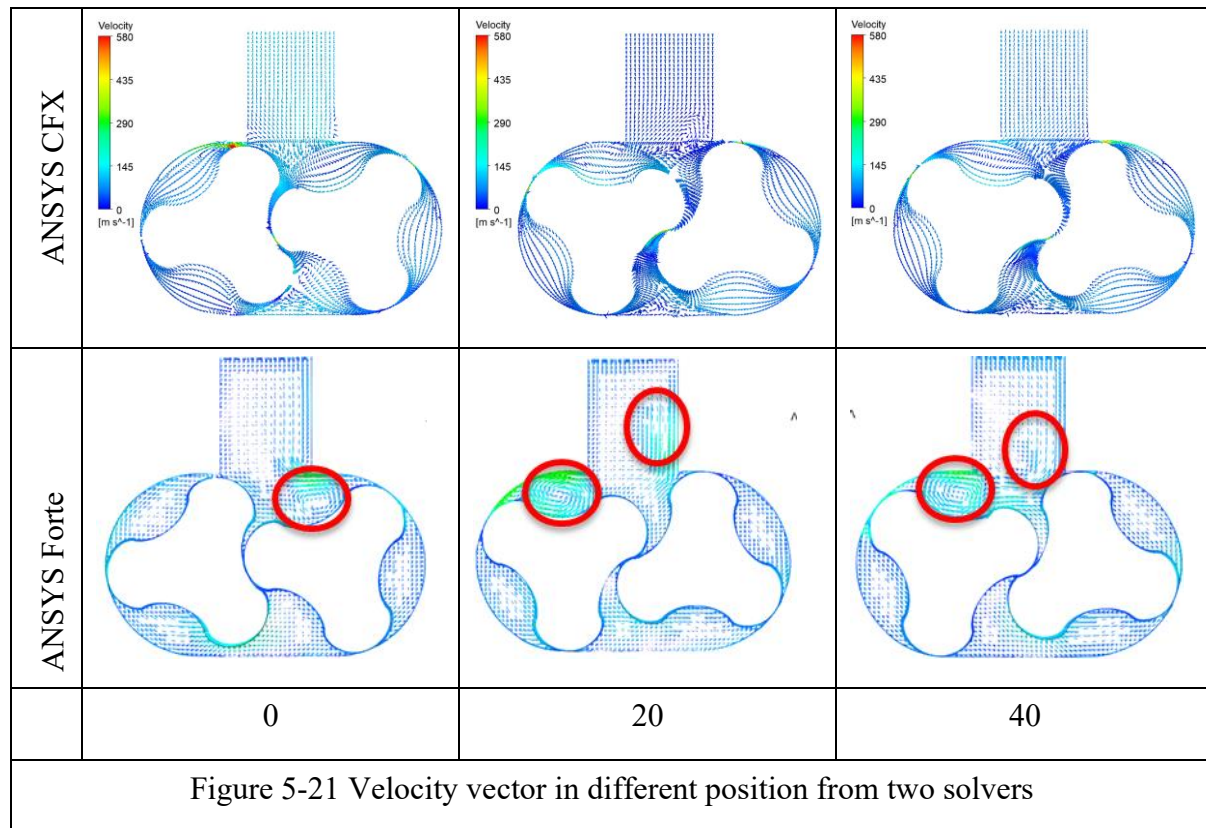


Figure 5-20 Power

#### 5.3.3.4 Velocity contour

Finally, the velocity vector from two solvers is compared as shown in the Figure 5-21. The velocity vortex is well captured in ANSYS Forte because of the mesh adaptation procedure automatically refined the regions where the velocity changed quickly.



### 5.3.4 Conclusion

Two different mesh methods cut-cell cartesian mesh and body-fitted mesh were calculated by two different CFD solvers ANSYS Forte and ANSYS CFX separately. ANSYS Forte can predict the same trend with ANSYS CFX regarding to the mass flow rate, torque, and power. However, the significant pressure and torque oscillation can be observed in ANSYS Forte which does not seem to be physical and is most probably caused by the technique use for modelling leakage gaps.

## 5.4 Analysis of the twin screw compressors

A commercial refrigeration twin screw compressor with intermediate helix angle was used for evaluation of suitability of using body fitted meshes for analysis of screw compressor as the test results were available for validation. The body fitted mesh generated by SCORG is utilized for the simulation of this compressor. The rotor geometrical parameters are shown in the Table 5-13. The male and female rotor configuration are 4 and 6 respectively. The wrap angles of the main and gate rotors are 300 degrees and 200 degrees respectively. The chamber volume reaches the maximum after 540 degree of the male rotor rotation and the discharge starts after

another 140 degrees. The radial and axial discharge ports have  $V_i$  1.6 and  $V_i$  4.3 respectively. There was no radial suction port, but the radial pressure relief valve is installed in the system. An oil return port is connected to the casing on the gate rotor side and the three direct oil injection ports are connected on the main rotor side casing. The CFD simulation was setup to compare with the experimental results which have been provided by the compressor manufacturer.

Table 5-13 Rotor Geometry

Parameters	Value	Parameters	Value
Axis distance [mm]	320	Lobe combination	4/6
Outer diameter [mm]	408	Radial/Axial $V_i$	1.6/4.3
Inner diameter [mm]	231	Lead [mm]	807/1121
Rotor length [mm]	673	Wrap angle [deg]	300/200
Compression end [deg]	140	Interlobe clearance [mm]	0.120
Helix angle [deg]	44.88	Radial clearance [mm]	0.275

The working fluid considered in this project are nitrogen and ammonia. The working conditions and properties of nitrogen and ammonia are listed in Table 5-14.

Table 5-14 Working conditions and fluid properties

Parameters	Value	Properties	Nitrogen	Ammonia
Speed [rpm]	3600	Molar Mass [kg kmol <sup>-1</sup> ]	29.013	17.027
P <sub>suc</sub> [bar]	3.55	Specific Heat Capacity [J kg <sup>-1</sup> K <sup>-1</sup> ]	743.31	2200
P <sub>dis</sub> [bar]	4.62	Dynamic Viscosity [kg m <sup>-1</sup> s <sup>-1</sup> ]	1.592x10 <sup>-5</sup>	9.04x10 <sup>-6</sup>
T <sub>suc</sub> [°C]	14.7	Thermal Conductivity [W m <sup>-1</sup> K <sup>-1</sup> ]	0.022925	0.02257
T <sub>dis</sub> [°C]	67.2	P <sub>oil</sub> [bar]	6.7	6.7
T <sub>oil</sub> [°C]	16.5	M <sub>oil</sub> [kg/s]	0.3559	0.3559

From the preliminary case study, there are following two phenomena that were necessary to explore.

- (1) The oil drag was underestimated

(2) There was around 15 % difference between the torque power and PV power which is calculated. PV power is determined by calculating the area enclosed by the pressure versus volume curve in the PV diagram.

Oil-free and oil-injection cases are studied using the same model to address the first phenomena. The setup of general oil-free and oil-injection cases in ANSYS CFX are listed in Table 5-15.

Table 5-15 The CFX setup

<b>Parameters</b>	<b>Oil-free</b>	<b>Oil-injection</b>
Turbulence Model	k-epsilon	SST
Advection scheme	High resolution	Upwind
Turbulence scheme	First order	First order
Transient scheme	First order	First order
Transient inner loop coefficients	5	5
Convergence criteria	1E-4	1E-4
Relaxation parameters	0.02	0.02

Seventeen cases were setup to match the oil injection condition in CFD with experiments and to analyse reasons for 15 % difference between the torque power and PV power observed by simulation and experiment.



Table 5-16 Comparison between PV power and Torque Power

No	Boundary conditions	PV Power [kW]	Torque Power [kW]
0	Experiment P_suc = 1.9 bar, P_dis = 3.6 bar	549.30	762.70
1	Case1 Oil Flow Rate, M_oil = 3.26 kg/s, Inlet	545.80	637.08
2	Case2 Oil Pressure, P_oil = 3.25 bar, T_oil = 40 C, Opening	523.40	612.99
3	Case3 Oil Flow Rate, Oil Initialisation with 0.01, Inlet	537.03	630.09
4	Case4 Oil Flow Rate, 5 * Oil Viscosity, Inlet	546.38	637.94
5	Case5 Oil Pressure & Flow Rate, P_oil = 3.25 bar, M_oil = 3.26 kg/s, Inlet	550.52	644.39
6	Case6 Oil Pressure, P_oil = 3.13 bar, Inlet	547.10	637.00
7	Case6_New0 Oil Pressure, P_oil = 4.0 bar, Opening	631.15	761.74
8	Case6_New1 Oil Pressure, P_oil = 3.6 bar, Opening	570.40	664.78
9	Case6_New2 Oil Pressure, P_oil = 3.425 bar, Opening	543.80	635.88
10	Case6_New3 Oil Pressure, P_oil = 3.5125 bar, Opening	553.41	644.17
11	Case6_New4 Oil Pressure, P_oil = 3.46875 bar, Opening	547.52	638.23
12	Case6_New2_vf Oil Pressure, P_oil = 3.425 bar, Opening, VF Function off	536.90	620.72
13	Case1_New Oil Flow Rate, M_oil = 3.26 kg/s, Inlet, Drag coefficient = 0.1	541.30	635.46

14	Case1_OilFree	Vi = 1.6, 3600 rpm, with oil return port	552.51	634.25
15	Case2_OilFree	Vi = 1.6, 3600 rpm, without oil return port	565.10	646.60
16	Case2_OilFree_N	Vi = 1.6, 3600 rpm, pressure condition of axial relief port	577.24	646.32
17	Case3_OilFree	Vi = 1.6, 1 rpm	414.03	406.85

The setup of all simulation cases is shown in Table 5-16. The results were compared with the experiment at  $P_{suc} = 1.9$  bar and  $P_{dis} = 3.6$  bar. The cases can be categorized to four groups: (1) Oil flow rate cases; (2) Oil pressure cases; (3) Oil free cases and (4) Other cases. The first two categories mean the ANSYS CFX setup of the oil return port boundary where can be set as oil flow rate condition or oil pressure condition as shown in Figure 5-22.

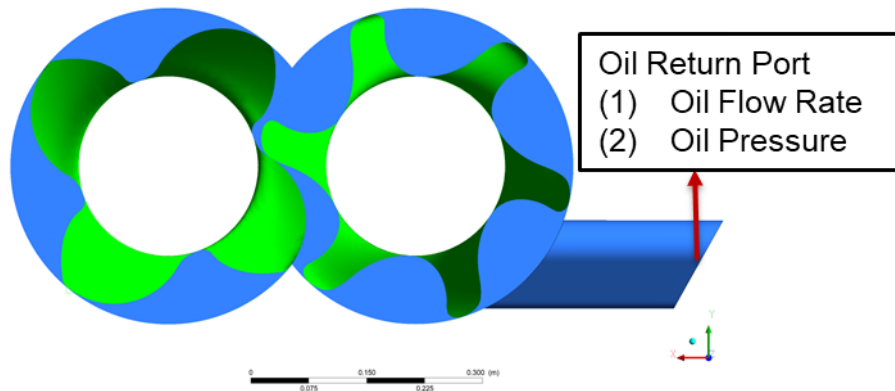


Figure 5-22 Boundary condition of oil return port

In order to find out if a local distribution of pressure within the working chamber affects the calculation of power, two methods are applied to the results from ANSYS CFX. One is called the torque power which was calculated from the pressure and drag forces distributed on the rotor. Another one is the PV power which was calculated by the pressure extracted from the probe located in the gate rotor interlobe. The PV integrated power of all calculated cases was compared with the experimental PV integrated power as shown in the Figure 5-23. The PV integrated power errors were within 2 %. However, the error between the torque power and the PV power reached 15 %. It was suspected that the local pressure maybe the reason that causes the higher torque power.

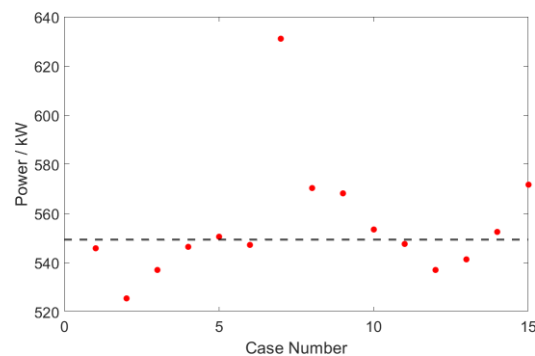


Figure 5-23 Integrated PV power

The oil flow rate cases and oil pressure cases were set to explore the underestimated oil drag power. The oil free cases were setup to study the difference between the PV power and torque power.

#### 5.4.1 Oil injection with flow rate boundary condition

The torque constitution is described in Figure 5-24. Rotor torque is caused by pressure and drag forces. Pressure can be divided into the oil pressure and air pressure. Drag forces can also be divided into the oil drag and air drag. Air pressure and air drag make up the air torque. Oil pressure and oil drag make up the oil torque.

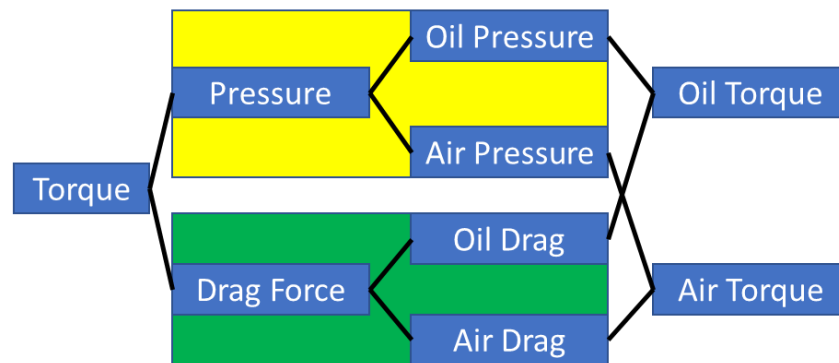
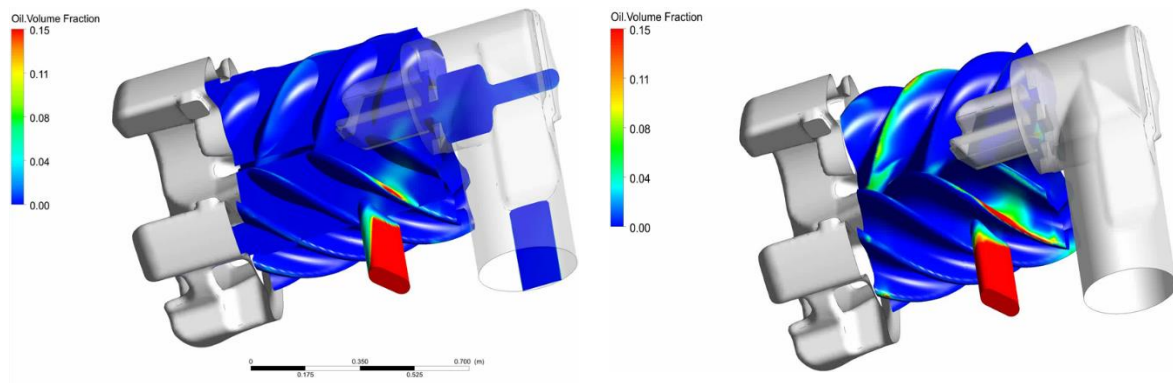


Figure 5-24 Torque constitution

Case 1 is the first case study. The simulation was run for 3600 timesteps which represents 10 rotations of the main rotor. The initial pressure dip was not observed compared with the experimental result. As this machine has the oil return port, it was suspected that this can be the pressure dip.

Case1\_New was set to increase centrifugal force influence, the inter-phase drag has been reduced to 0.1. More oil can be seen along the tip and end rotors. Compared with the Case1, the oil drag power increase from 2.7 kW to 4.15 kW and the torque power decreased from 637.1 kW to 635.5 kW.



(a) Oil Volume Fraction of Case 1

(b) Oil Volume Fraction of Case 1 New

Figure 5-25 Comparison of Oil Volume Fraction

Because the oil drag power is still low, the Case1\_New case was continued to 7200 more-time steps which means 20 rotations of the main rotor. The oil drag power was listed in the Table 5-17. The oil drag power is stable by increasing the time step from 3600 to 10800 and no significant accumulation of oil with longer simulation time was observed.

Table 5-17 Oil Drag Power

Case	Time Step	Oil Drag Power [kW]
Case1	3600	2.70
Case1_New	3600	4.15
Case1_New	10800	4.18

#### 5.4.2 Oil injection with pressure boundary condition

The purpose of the case study is to match the simulation results with the experiments in order to find the most appropriate ANSYS CFX setup to increase the accuracy of the simulation for the future case studies. All the oil pressure boundary cases were listed in the Table 5-18. The reasons of the setup of all the cases are explained here.

Table 5-18 The PV power and Torque Power

No	Boundary conditions	PV Power [kW]	Oil Flow Rate [kg/s]
0	Experiment P <sub>suc</sub> = 1.9 bar, P <sub>dis</sub> = 3.6 bar	549.30	3.26
6	Case6 P <sub>oil</sub> = 3.13 bar, Inlet	547.10	1.29

7	Case6_New0	P_oil = 4.0 bar, Opening	631.15	27.21
8	Case6_New1	P_oil = 3.6 bar, Opening	570.40	10.80
9	Case6_New2	P_oil = 3.425 bar, Opening	543.80	0.85
10	Case6_New3	P_oil = 3.5125 bar, Opening	553.41	6.74
11	Case6_New4	P_oil = 3.46875 bar, Opening	547.52	2.29

Case 2 – The initial dip in pressure was due to the bearing return being captured, but the oil flow rate was too low when compared to the measured data. Also, oil injection temperature was 40 °C while measured value is 49.8 °C. Case 6 was simulated using the same conditions with the experiment for the oil return port, the inlet boundary type was used here. The initial pressure dip was not obvious. The oil flow rate is 1.29 kg/s which is lower than the experiment. Hence Case6\_New cases were required to iteratively improve oil flow rate and retain pressure-volume results. Case6\_New0 used opening boundary type and higher oil pressure boundary condition which is 4 bar. The oil flow rate is 27.21 kg/s which is too high. The oil pressure needs to decrease to minimise the oil flow rate. Case6\_New1 used the averaged oil pressure of Case2 and Case6\_New0. The oil flow rate is 10.80 kg/s. Case6\_New2 used the averaged oil pressure of Case2 and Case6\_New1. The oil flow rate is 0.85 kg/s. The oil pressure needs to increase to rise the oil flow rate. Case6\_New3 used the averaged oil pressure of Case6\_New1 and Case6\_New2. The oil flow rate is 6.74 kg/s. Case6\_New4 used the averaged oil pressure of Case6\_New2 and Case6\_New3. The oil flow rate is 2.29 kg/s.

The oil flow rate was similar to the experimental oil flow rate which was achieved by adjusting the oil pressure of the oil return port. The PV power is also much closer to the experimental result. The P-theta diagram and PV diagram are compared in Figure 5-26. The pressure dip and the maximum pressure were captured well by 3D CFD simulation.

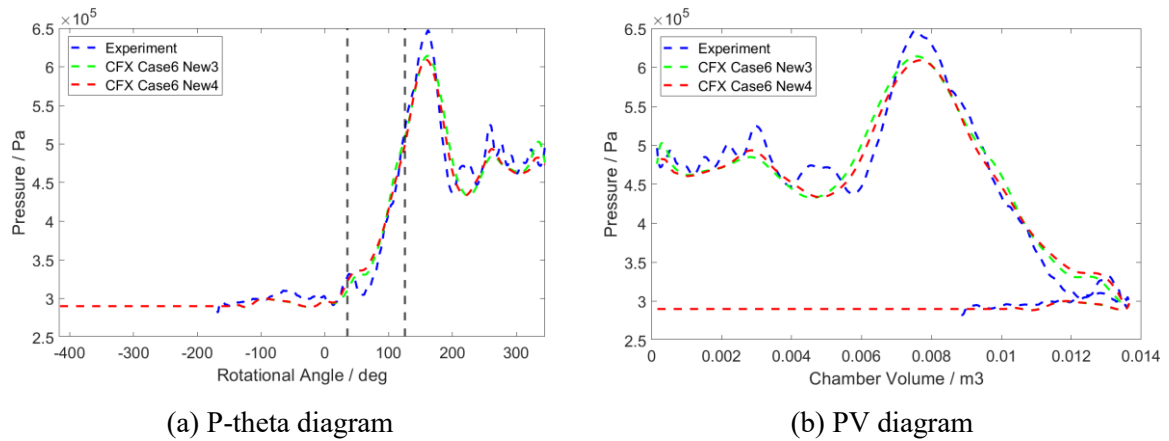


Figure 5-26 Pressure distribution

### 5.4.3 Oil free cases

Case1\_OilFree was setup to compare with the oil injected case in order to study the effect of the oil drag power. The dip pressure and rise pressure were captured here as shown in the Figure 5-27. The difference between the PV power and torque power is still exist which is in the same level with the oil injected cases as shown in Table 5-16.

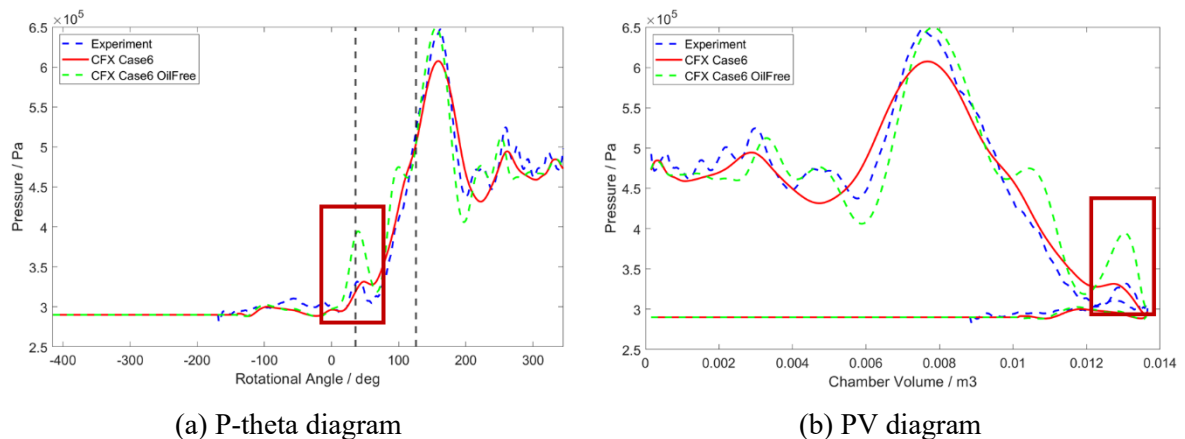


Figure 5-27 Oil Free Cases

The local pressure variation on both rotors is one of the dominant reasons for the 15% difference between the PV power and torque power. To a smaller extent the oil drag torque contributes which is by default included in the torque power. For example, 4.18 kW out of the 635.5 kW in Case1\_New. Figure 5-28 shows the pressure contour in the range between 280 kPa and 300 kPa.

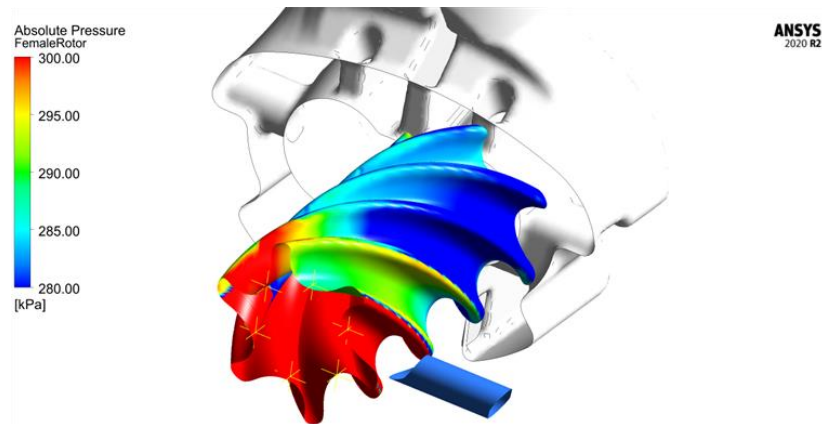


Figure 5-28 Pressure Variation along the rotor

#### 5.4.4 Other cases

Other cases were setup to study the effect of oil initialisation, oil viscosity, oil return power boundary condition and VF function.

Table 5-19 Other Cases

No	Boundary conditions	PV Power [kW]	Oil Flow Rate [kg/s]
3	Case3 Oil Flow Rate, Oil Initialisation with 0.01, Inlet	537.03	3.26
4	Case4 Oil Flow Rate, 5 * Oil Viscosity, Inlet	546.38	3.26
5	Case5 Oil Pressure & Flow Rate, P_oil = 3.25 bar, M_oil = 3.26 kg/s, Inlet	550.52	1.41/3.26
12	Case6_New2_vf Oil Pressure, P_oil = 3.425 bar, Opening, VF Function off	536.90	*

#### 5.4.5 PV power calculated at different rotor length positions

In the experiments, the pressure was monitored by the pressure transducer located in the root of the gate rotor as shown in theFigure 5-29. The distance between the pressure transducer and the discharge end rotor plane is 17 mm.

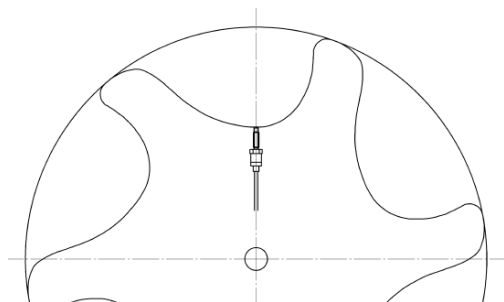




Figure 5-29 Position of pressure transducer

Similarly, the probe was set in the same position in the CFD case study. The pressure was extracted from the CFD case study and compared in the above section. Furthermore, to investigate the local pressure variation along the rotor, four probes with distance 50 mm, 100 mm, 150 mm and 200 mm to the discharge end plane were set at the gate rotor root as shown in Figure 5-30. It is apparently that probes P3, P4 and P5 cannot capture part of the discharge process. In this case, constant discharge pressure was added for the part which was not captured.

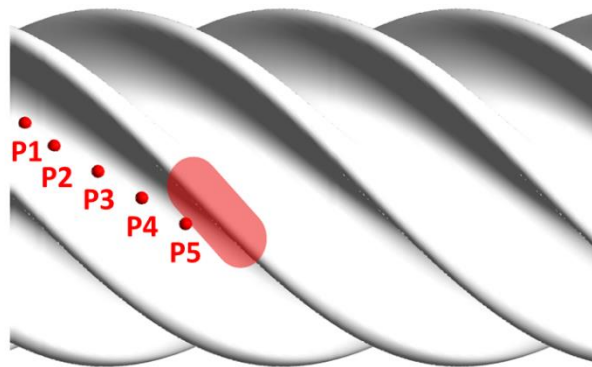


Figure 5-30 Position of probes

Then, pressure was extracted from different position probes and connected corresponding to rotational angle. Figure 5-31 shows the pressure diagrams of oil free  $V_i = 1.6$  Case. It can be seen from Figure 5-31 (a) that lower suction pressure was captured by probe P5 (at 200 mm position).

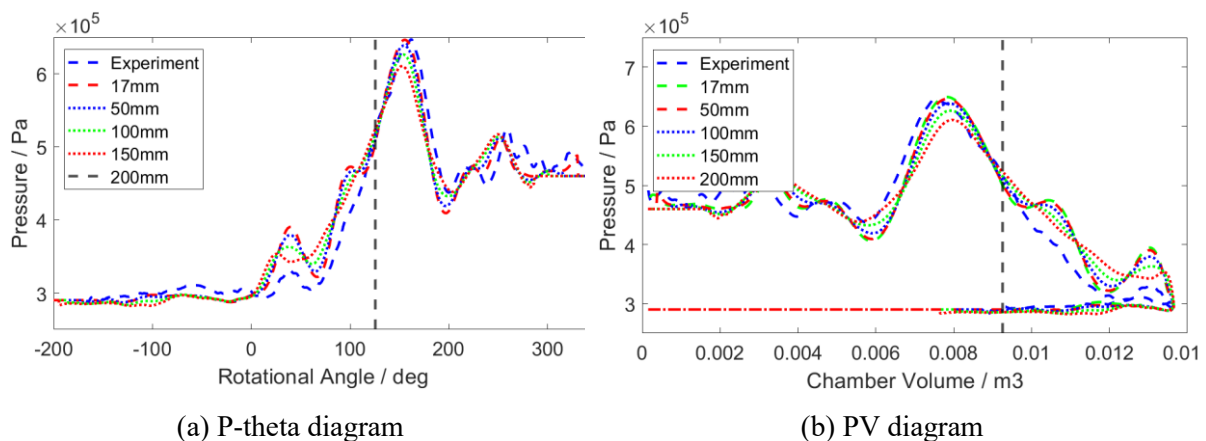
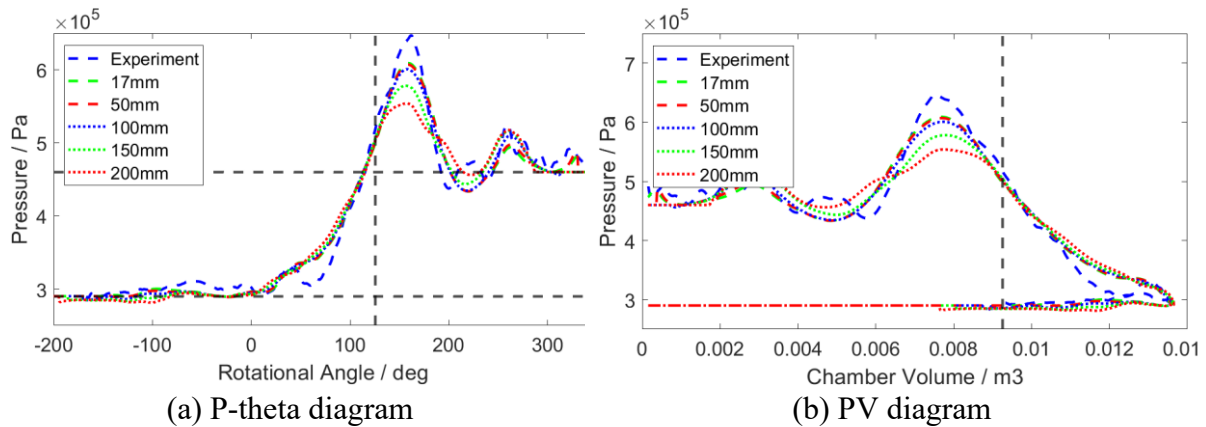


Figure 5-31 Oil free  $V_i = 1.6$ 

The pressure diagrams of Case6 New4 captured in five different positions are as shown in Figure 5-32.

Figure 5-32 Case6 New4  $V_i = 1.6$ 

The integrated PV power was calculated for the above two cases and listed in Table 5-20. PV power increased with the probe position increase. Maximum power difference is 8.9 kW between P1 and P2 in Case6 New4.

Table 5-20 PV Power and Torque Power

	Distance	Oil Free $V_i 1.6$	Case6_New4
Unit	mm	kW	kW
P1	17	571.72	547.52
P2	50	572.80	549.27
P3	100	571.66	552.23
P4	150	574.47	553.57
P5	200	576.34	556.40
Torque Power	*	656.83	638.23

#### 5.4.6 Investigation of the rotor torque power and PV power in CFD

The rotor torque was calculated using the working chamber rotor-to-rotor and rotor-to-casing contact points method. It is observed that the torque calculated using pressure from CFD oil-free case is higher. This section shows the results of CFD investigation into the effect of

pressure variation within chamber on calculated power. Oil free operation was considered to enable easier comparison of results.

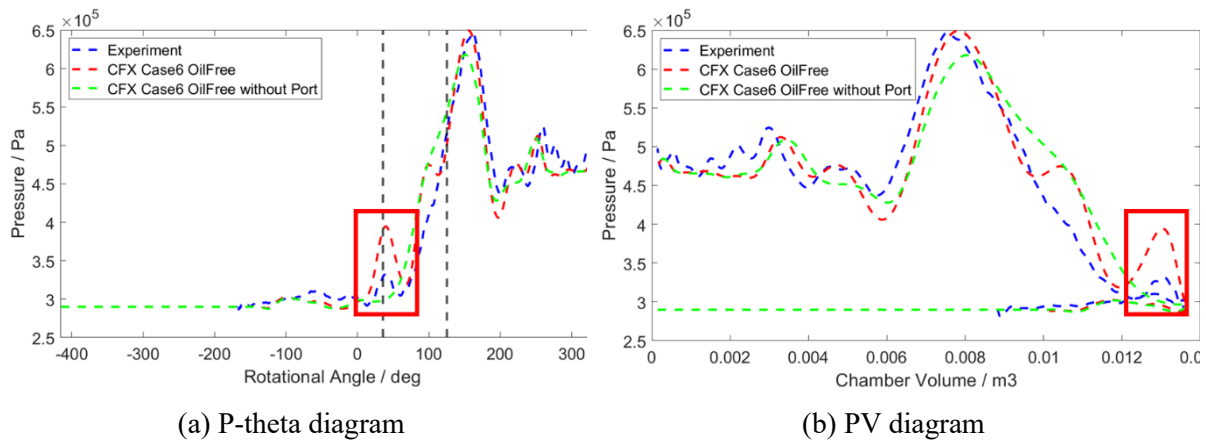


Figure 5-33 Oil free case comparison

As illustrated by Figure 5-33, the oil return line was shown to create significant variation in working chamber pressure due to leakage of fluid when compared to case without oil return port. However, the calculated power was very similar in both cases as shown in Table 5-21. The main rotor torque decreased 24.21 Nm while the Gate rotor torque is similar. Around 15 % difference between torque power and PV power.

Table 5-21 PV Power and Torque Power

	Main Torque/Nm	Gate Torque/Nm	Torque Power/kW	PV Power/ kW
Case1_OilFree	1514.35	-338.62	656.00	571.72
Case2_OilFree	1490.14	-337.52	646.60	565.10
Abs Difference	24.21	1.1	9.4	6.62

The pressure contour shows the impact of the oil return port in Figure 5-34. The oil return port act as a leakage gap and has effect to the local pressure distribution.

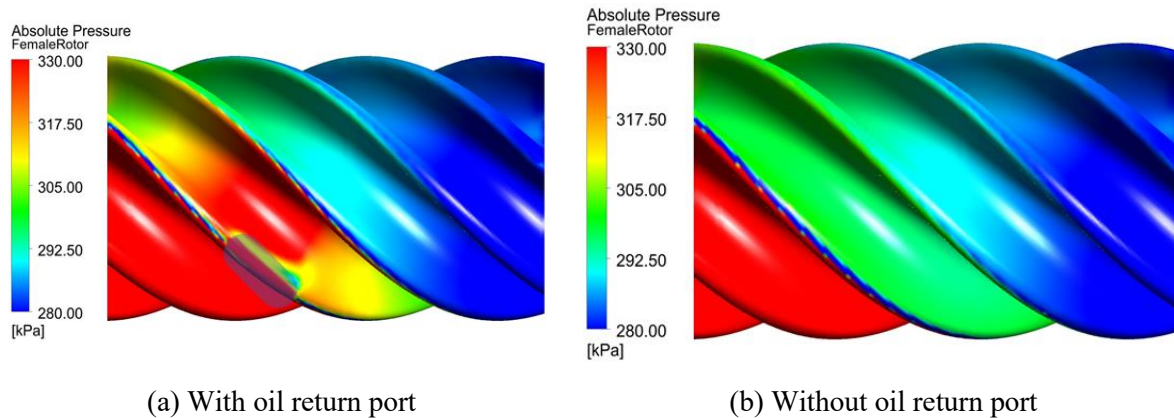


Figure 5-34 Pressure contour of oil free case

A low-speed case was calculated. The purpose of this simulation is to investigate the reason causing 15 % difference between torque power and PV power. The power difference was reduced to 2 % for low rotational speed of 1 rpm. The difference between Case2 oil-free and Case3 oil-free is only the rotational speed which are 3600 rpm and 1 rpm individually. The power calculated via P-V diagram and via rotor torque is then very close in Case3 Oil-free because there is less dynamic pressure variations within the same chamber. By changing the speed from 3600 rpm to 1 rpm. The main rotor torque decreased 526.02 Nm while the gate rotor torque decreased 136.31 Nm as shown in Table 5-22. Case2 oil-free new was set up by applying suction pressure boundary conditions on this axial relief face to see effect of ‘best case’ conditions. The torque power of Case2 oil-free new is same as case2 oil free. However, the PV power shows around 12 kW increase.

Table 5-22 PV Power and Torque Power of Oil free case

	Main Torque/ Nm	Gate Torque/ Nm	Torque Power/ kW	PV Power / kW
Case2_Oil-Free	1490.14	-337.52	646.60	565.10
Case2 Oil-Free New	1488.6	-338.74	646.32	577.24
Case3 Oil-Free	964.12	-201.21	414.03	406.85

The pressure contour of main and gate is shown in Figure 5-35. Case1 oil free and Case2 oil free both show the pressure variation near the suction port. The variation at suction port may because axial relief restriction. Case2 oil free new shows uniform pressure within chambers by applying suction pressure boundary conditions on this axial relief face.

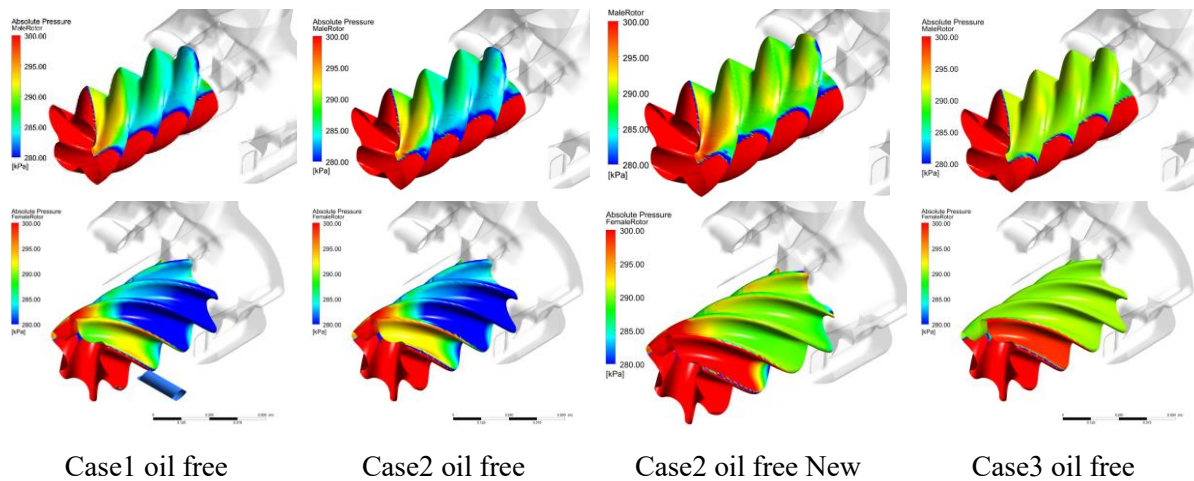


Figure 5-35 Pressure contour of oil free case

The above results suggest that the pressure variation within chamber is responsible for the higher rotor torque. In the last section, several different cases have been considered to investigate issues around the predicted power consumption of the compressor including accurate calculations of indicated power and oil drag losses. The simulations were carried out based on the operating conditions from experimental results ( $V_i = 1.6$ ,  $P_{suc} = 1.9$  bar,  $P_{dis} = 3.6$  bar) to evaluate, internal pressure distribution, performance parameters and oil drag losses so that the CFD model could be utilised to improve and re-design rotors for low  $V_i$  operation.

#### 5.4.7 Conclusion

In this study, a twin screw compressor with a typical helix angle was successfully simulated using body-fitted mesh generation method. The underestimated oil drag power and the approximate 15 % difference between torque power and PV power has also been explored successfully. Pressure variation within chamber is responsible for the higher rotor torque than PV power. In conclusion, by comparing the simulation results with the experimental results of twin screw machines with moderate helix angle, body-fitted method is capable for 3D CFD simulation of both oil-free and oil-injected screw compressors with an intermediate helix angle.

## 5.5 Analysis of a twin screw vacuum pump with large helix angle using Body-fitted mesh

The casing to rotor conformal and non-conformal grids were generated in SCORG™ and used with FLUENT® using User Defined Functions (UDF) developed by Basha [108]. The flow field and internal pressure were calculated for two different inlet relative pressures of -0.3 bar and -0.5 bar for conformal and non-conformal grids. Integral parameters of the vacuum pump such as the mass flow rate, rotor torque and indicated power are used for comparison.

### 5.5.1 Rotor geometry

To have large displacement capacity and excellent sealing result, twin screw vacuum pump rotors usually have large wrap angle which is normally more than 360 degree and large helix angle. The test twin screw vacuum pump profile is shown in Figure 5-36. The rotor profile is symmetrical and consists of arc curves and cycloid curves. The rotor configuration is a 1-1 type which is common for twin screw vacuum pump.

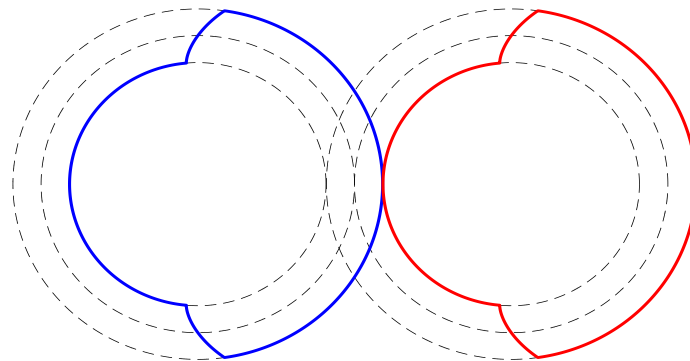


Figure 5-36 Twin screw rotor profile

The rotor configuration is shown in Table 5-23. The rotor length is 285 mm and the wrap angle is  $504^\circ$ . The outer circle diameter is 144mm and the inner circle diameter is 100 mm. The helix angle is  $62^\circ$ .

Table 5-23 Rotor configuration

<b>Rotor Configuration</b>	<b>Value</b>	<b>Rotor Configuration</b>	<b>Value</b>
Rotor combination	1by1	Wrap angle[° ]	504
Axis distance [mm]	122	Helix angle [° ]	62
Outer circle diameter [mm]	144	Radial gap [mm]	0.12
Rotor length [mm]	285	Interlobe gap [mm]	0.12

The axial inlet and outlet ports are used for the vacuum pump as shown in the Figure 5-37. In this case just simple ports were considered as the objective of the case study is to evaluate suitability of the grid generation method for large helix angle rotors. Five monitor points were positioned along the z-axis to show the pressure distribution.

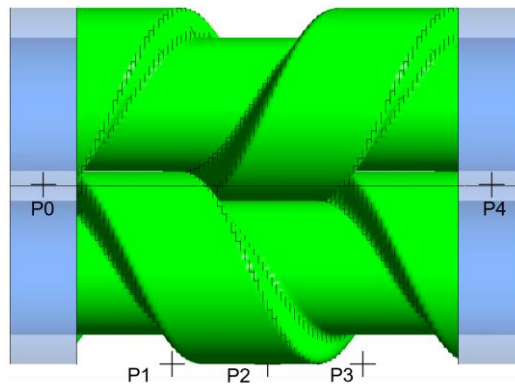


Figure 5-37 Monitor points

Figure 5-38 shows the chamber volume changing with the rotation angle. After one full rotation of the main rotor, a closed chamber is formed between two rotors and casing. And then, the formed chamber is transported to the outlet end and connect with the exhaust port after 144° of rotation. Finally, the chamber volume comes to 0 after another full rotation.

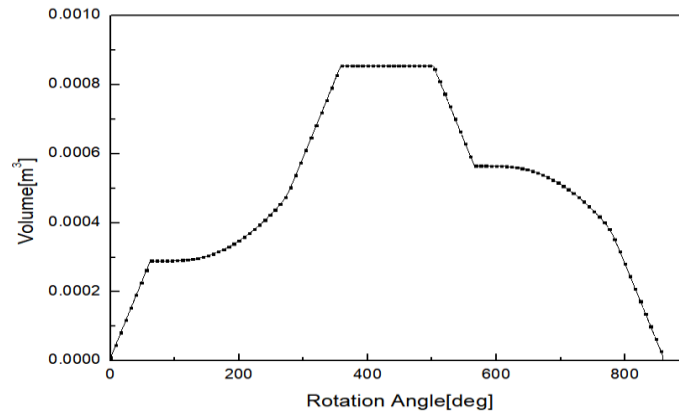


Figure 5-38 Volume angle curve

### 5.5.2 Grid generation for twin screw vacuum pump.

The grid of the fluid domain is generated by standalone software SCORG™ which is a tool for the design and CFD pre-processing of rotary twin screw machines.

Casing to rotor grid generation method has two benefits compared to the rotor to casing method, as explained by Sham and Kovacevic [60,73]. Firstly, the mesh in the interlobe region can be independently controlled which could improve accuracy of the prediction of leakage flows. Secondly, the method allows creation of a single computational domain with the structured grid. The setting of casing to rotor conformal mesh is shown in Table 5-24. The male rotor domain has 486720 vertices and 423360 cells.

Table 5-24 Fluid domain grid set-up

Variable	Value	Boundary Condition	Value
Circumferential division	400	K main and M main	10
Radial division	7	Relaxation factor	0.2
Angular divisions	60	Tolerance factor	20
Interlobe divisions	150	Radial bias factor	0.5
Axial gap [mm]	0.05	Interlobe smoothing factor	7

The male and female rotors have same number of vertices and cells. Each rotor domain has 272000 vertices and 235200 cells. Figure 5-39 shows the casing to rotor non-conformal mesh.



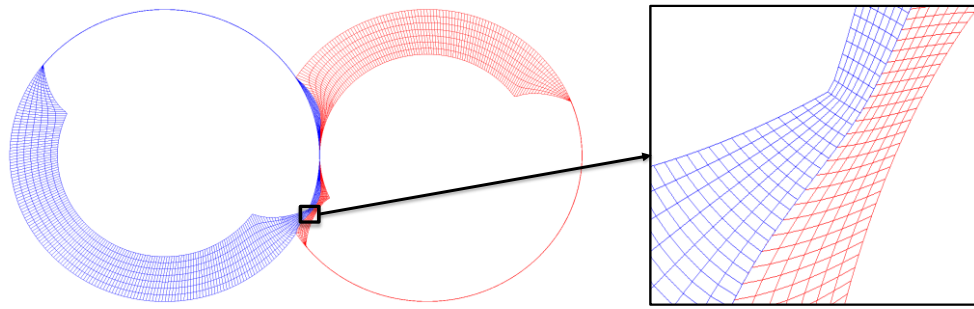


Figure 5-39 Mesh of casing to rotor non-conformal

Figure 5-40 shows the casing to rotor conformal mesh. The mesh is fully hexahedral and the interface between the O block is conformal. By using the casing to rotor grid generation method, it is possible to independently control grid refinement in the interlobe region thereby providing better accuracy in representation of the leakage gaps [60].

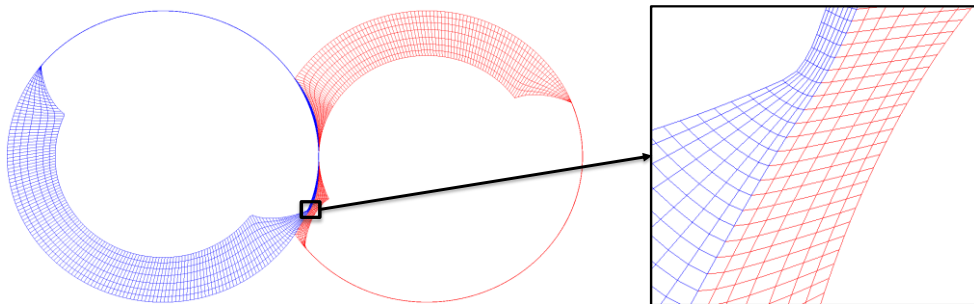


Figure 5-40 Mesh of casing to rotor conformal

Figure 5-41 shows the grid distribution on one rotor. All grid cells are hexahedral and the grid between the two rotor meshing regions is refined.

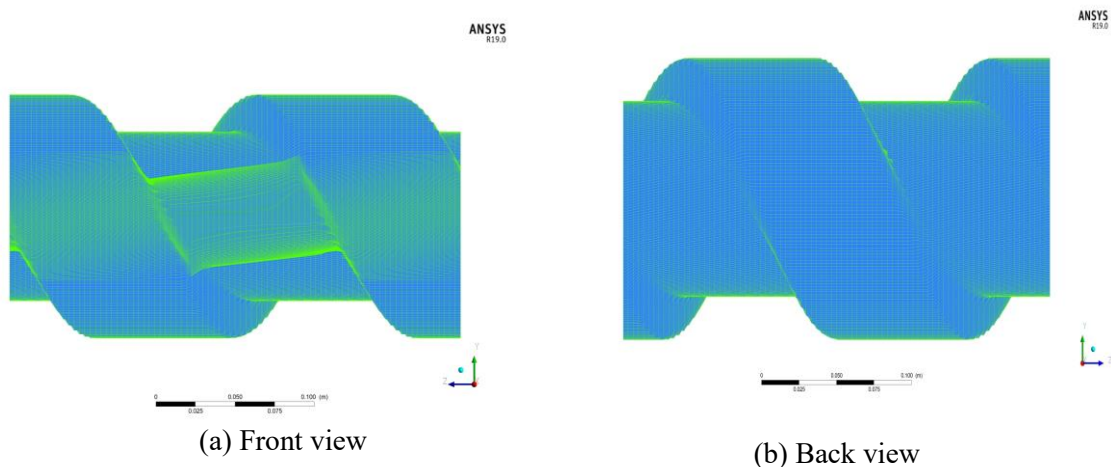


Figure 5-41 Grid distribution on the rotor

The aspect ratio and orthogonality of the conformal and non-conformal meshes are compared in Figure 5-42. For the non-conformal mesh, the aspect ratio is between 86.54 and 114.62 while for the conformal mesh is between 86.53 and 247.13. The high aspect ratio of the non-conformal mesh occurred when the cycloids mesh with each other. When the outer circle mesh with the inner circle, the aspect ratio is slightly better in the conformal mesh. For the non-conformal mesh, the orthogonality is between 13.07 and 35.63 while for the conformal mesh is between 5.9 and 35.98.

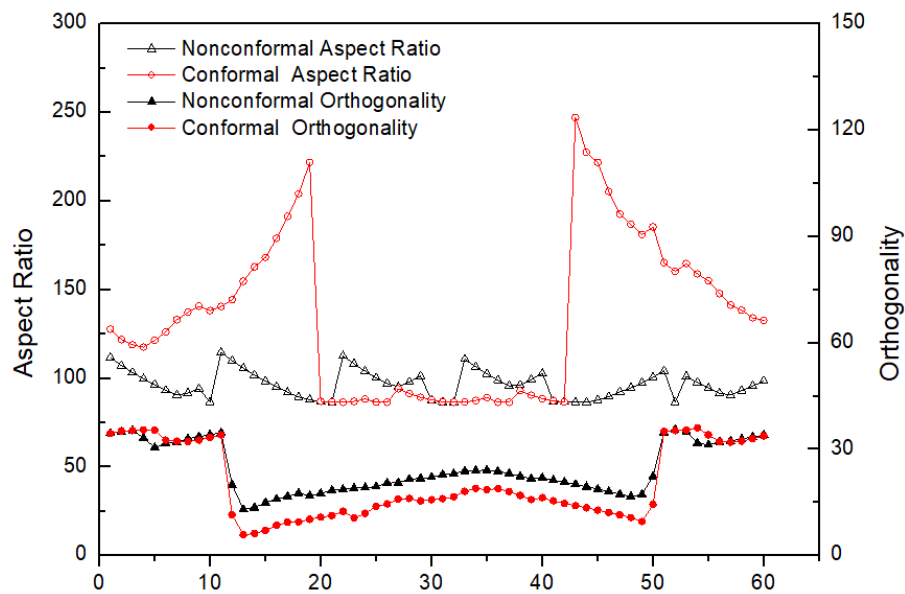


Figure 5-42 Comparison of the aspect ratio and orthogonality

### 5.5.3 Simulation

The fluid domain of the twin screw vacuum pump is firstly discretized using a standalone program SCORG™. The FLUENT® finite-volume method solver is used in PC with 4-core parallel calculation which was carried out on a on a Core™ i5 3.40GHz processor and 16 GB memory computer. The working fluid is air, and the speed of the rotor is 3500 rpm. Absolute pressure of -0.3 barg and -0.5 barg were specified at the suction while the discharge pressure was 1.0 bar. The mass flow rate indicated power and the interlobe pressure are calculated based on the results from the simulation.

Table 5-25 Working condition

Boundary Condition	Value
Fluid	Ideal-air
Operation speed [rpm]	3500
Suction pressure/barg	-0.3,-0.5
Discharge pressure/bar	1
Suction temperature/K	298

In FLUENT, the general solver setting is pressure-based transient flow. The turbulence model is k-omega SST. The Pressure-Velocity coupling scheme is SIMPLEC (SIMPLE-Consistent) algorithm. The under-relaxation factors for all parameters are 0.1. The convergence criteria for continuity, velocity, k and omega are  $1 \times 10^{-4}$  while the energy is  $1 \times 10^{-5}$ . The CFD simulation results are presented in the form of pressure-angle diagram, torque distribution, power, and mass flow rate. Figure 5-43 shows the pressure contour obtained in one time step of -0.5 barg inlet pressure. The pressure changed gradually from the inlet side to the outlet side.

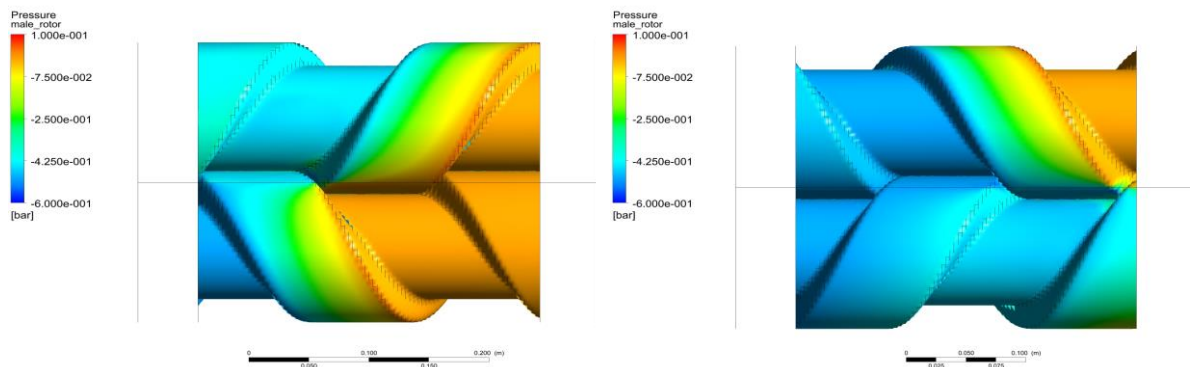
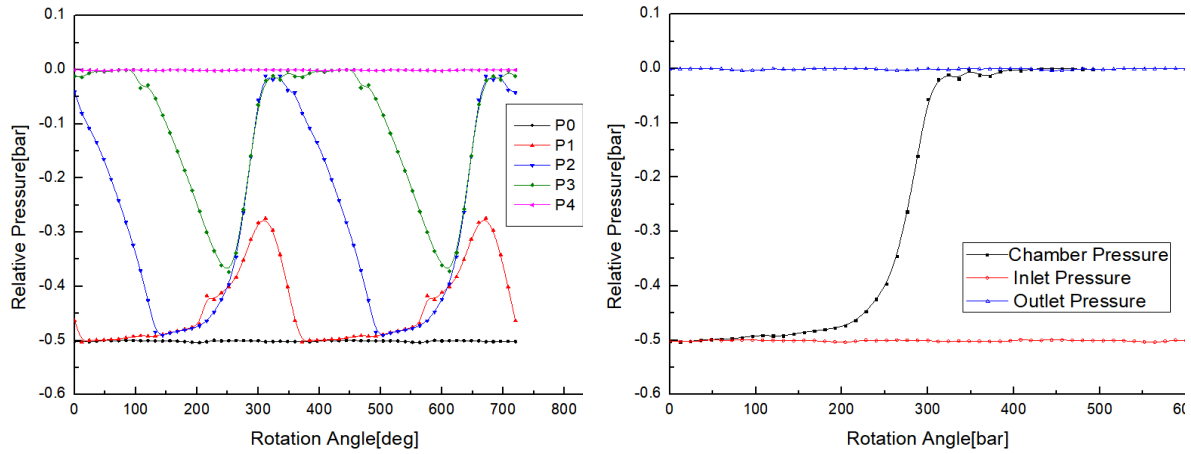


Figure 5-43 Pressure contour of -0.5 barg inlet pressure

Figure 5-44 shows the variation of pressure in the chamber with inlet pressure -0.5 barg at 3500rpm. As shown in Figure 5-44(a), P0 and P4 show the inlet pressure -0.5 barg and outlet pressure 0 barg respectively, and the pressure in the inlet port and outlet port are relatively steady. By connecting the pressure of P1, P2 and P3 monitor points, the pressure-angle diagram can be generated as shown in Figure 5-44(b). This pump does not have internal compression process. The pressure increase in the chamber is caused by the leakage from the high-pressure

side to the low-pressure side. Since the outlet port is fully opened and the pressure is not high, the outlet pressure fluctuations are relatively low compared with a twin screw compressor.

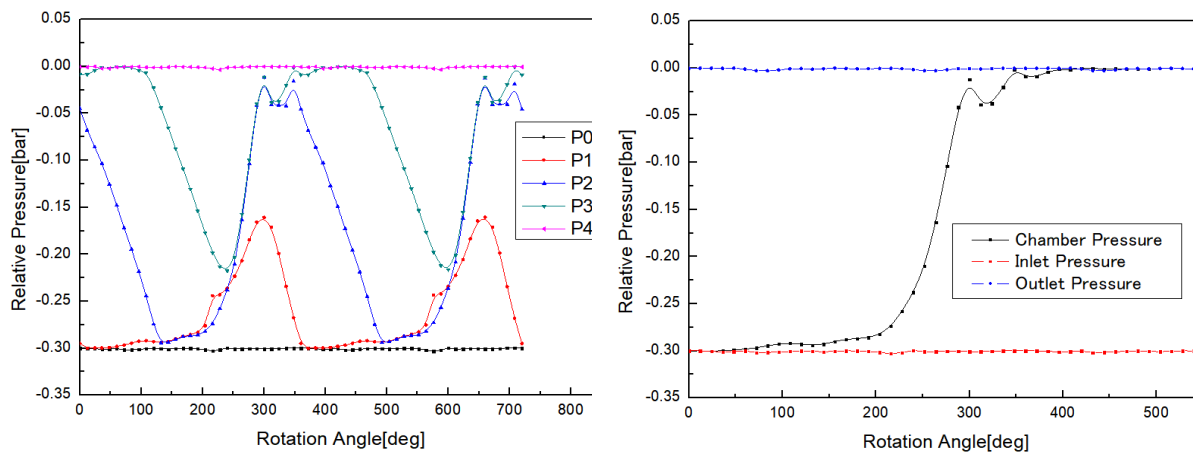


(a) Pressure distribution

(b) Chamber pressure

Figure 5-44 Pressure variation in the compression with -0.5 barg

Figure 5-45 shows the variation of pressure in the chamber with inlet pressure -0.3 barg at 3500 rpm.



(a) Pressure distribution

(b) Chamber pressure

Figure 5-45 Pressure variation in the compression with -0.3 bar.

The torque on each rotor is calculated from the surface pressure as shown in Figure 5-46(a). The torque distributed on the male and female rotors do not have much difference because of

the equal rotor profile of both rotors. The average torque on the male rotor of -0.5 barg inlet pressure is 5.88 Nm while the average torque of -0.3 barg is 3.54 Nm.

The indicated power can be calculated using equation 5-3.

$$P_i = 2\pi n(T_M + \frac{Z_1}{Z_2}T_G)/60 \quad 5-3$$

$Z_1$  and  $Z_2$  are the lobe number of male and female rotor respectively.  $T_M$  and  $T_G$  are the torque of the male and female rotor,  $n$  is the angular speed with units [radians /sec]. The power changing with the rotation angle is shown in Figure 5-46(b). The average power of -0.3 barg inlet pressure is 2590 W while the average power of -0.5 barg inlet pressure is 4319 W.

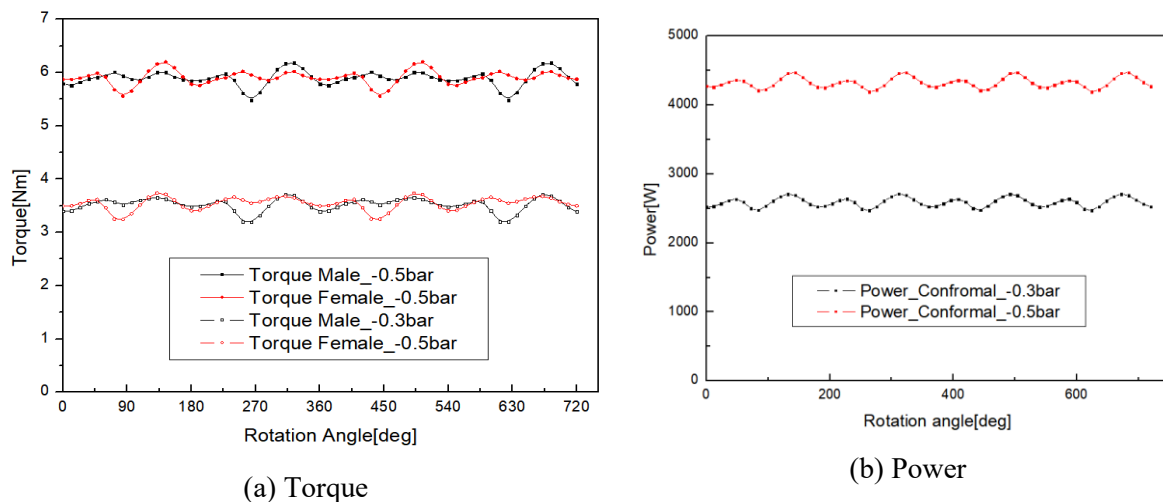


Figure 5-46 Comparison of torque and power

The variation of the mass flow rate with the rotation angle is shown in Figure 5-47. The average suction mass flow rate of -0.5 barg is 0.00416 kg/s and -0.3 barg is 0.03124 kg/s. Every vacuum pump has a point (usually very near atmospheric pressure) at which it can move the most air. The actual pumping speed decreases sharply with the vacuum degree as the developing vacuum resists the pump's efforts to move air.

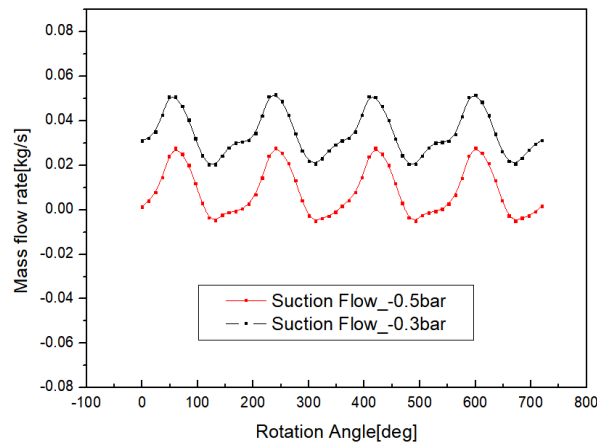


Figure 5-47 Comparison of the mass flow rate

#### 5.5.4 Conclusion

The aim of the study presented in this section was to explore the utilisation of body-fitted mesh for simulation of a twin screw vacuum pump with large helix angle. Working conditions of -0.3 bar(g) and -0.5 bar(g) suction pressure at 3500 rpm are simulated to obtain performance characteristics. With the open port vacuum pump, the pressure fluctuations in the outlet are small in comparison to a compressor. The torque distribution, power and mass flow rate values are relatively reasonable when compared with similar twin screw vacuum pumps. The developments in SCORG have allowed extension of the capability of calculation using ANSYS FLUENT with parallel processes which decrease the simulation time compared with ANSYS CFX. In this case, the helix angle is 62 degrees. When the helix angle is higher, it is difficult to generate high quality 3D meshes in the traditional way because of high skewness of numerical cells. In the future, the innovative grid generation method which generates numerical mesh in the normal plane of the pitch helix line will be implemented. It is expected that this implementation will have advantages for CFD calculation of twin screw vacuum pumps with large helix angle.

## 5.6 Analysis of a twin screw vacuum pump with large helix angle using Cut-cell cartesian mesh

Cycloid is widely used for twin screw vacuum pumps to increase cross section area. However, it is difficult to produce accurate mesh for this kind of rotor profile with large helix angle. In this study, the cycloid arc circle and Archimedes rotor profile is used in the twin screw vacuum pumps as shown in Figure 5-48. The main and gate rotors have same profile. The detailed of this rotor profile can be found in literature [31]. In section 5.3, cycloid is utilized for straight rotor and cut-cell cartesian method has been demonstrated to simulate the working process successfully. Twin screw vacuum pump normally has large helix angle and wrap angle to decrease leakage. The cusp points of the rotor profile and large helix angle of rotor geometry results in poor mesh quality when body fitted meshes are constructed. In this study, a cut-cell cartesian mesh is used for this geometry which has not been studied before.

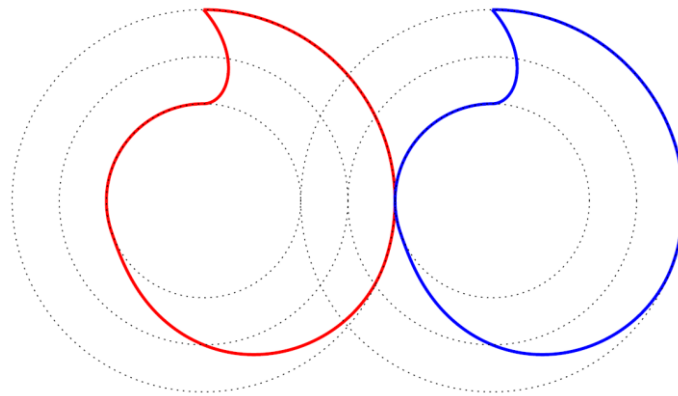


Figure 5-48 The twin screw vacuum pump rotor profile.

The rotor configuration is shown in Table 5-26. The twin screw vacuum pump used for the simulation has two sections with different pitch to enable internal compression. Total rotor length is 340 mm which consists of 200 mm rotor length with the pitch of 88mm and 140 mm rotor length with the pitch of 60mm. With variable rotor pitch, the sealing line length and leakage area could be reduced in the high-pressure side in order to improve performance for higher pressure ratio working conditions. The greater wrap angle would produce more chambers which could also be beneficial for higher pressure ratios. Discharge port plate is mounted at the end or the rotor end to increase volume index.

Table 5-26 Rotor configuration

Rotor Configuration	Value	Rotor Configuration	Value
Rotor combination	1by1	Wrap angle [°]	165.7
Axis distance [mm]	98	Helix angle [°]	87.7° and 82.3°
Outer circle diameter [mm]	130	Pitch [mm]	88 and 60
Rotor length [mm]	340	Gap [mm]	0.08

3D vacuum pump geometry is shown in Figure 5-49. Suction port is located at left hand side. The suction side of rotors has larger pitch than the discharge side of rotors.

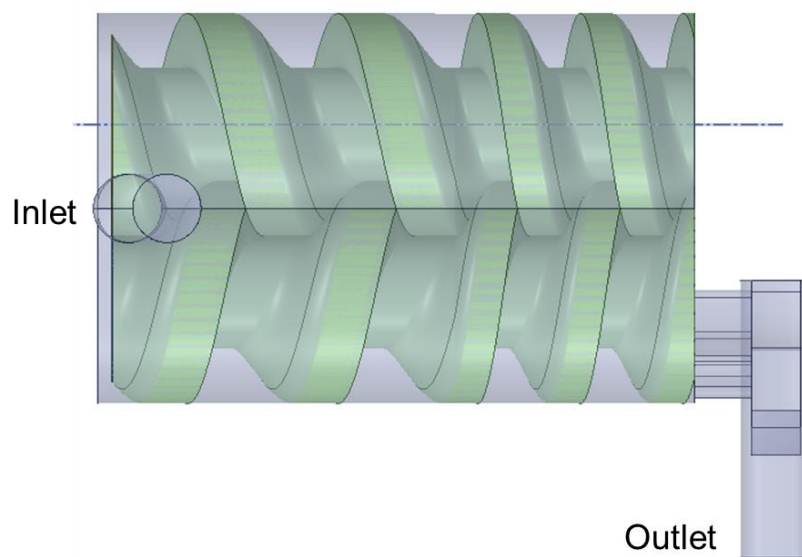


Figure 5-49 3D rotor geometry.

A schematic diagram of the dry twin screw vacuum pump test rig is shown in Figure 5-50. The oil free twin screw vacuum pump is driven by a motor. A torquemeter with an uncertainty of 0.1% reading is coupled between the motor and twin screw vacuum pump. The suction pressure in is measured by a PSG 500 pressure sensor. Its measurement range is from 0 Pa to 105 Pa and the accuracy is less than 2% of reading.



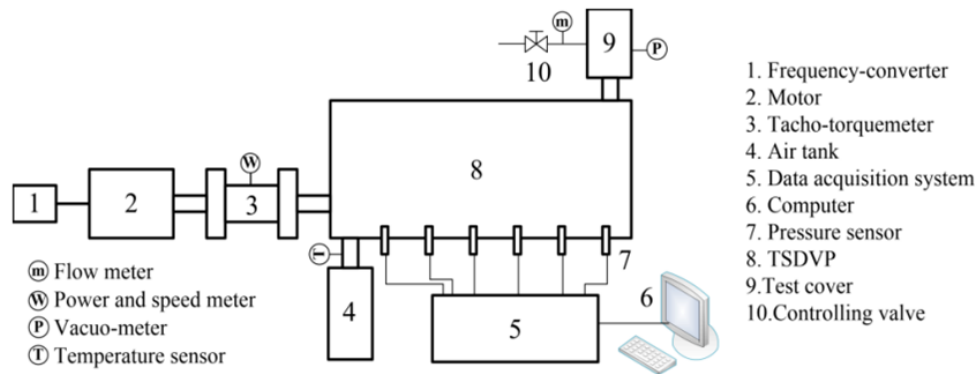


Figure 5-50 Schematic diagram of the test rig .

### 5.6.1 ANSYS Forte solver setup

The twin screw vacuum pump's operating condition specifications are listed in Table 5-27. This case study did not consider heat transfer, for example, between the casing wall and environment, the outlet wall and the environment and the rotors and chamber. All boundary walls were set as adiabatic. The inlet pressure is set as the 0.03 bar and outlet pressure is 1 bar. The external pressure ratio is 33.33. The global mesh size is set as 0.6 which produce sufficient mesh for this simulation.

Table 5-27 Operating conditions and solver setup parameters

Parameters	Value	Parameters	Value
Speed [rpm]	3000	Turbulence Model	k-epsilon
Suction Temperature [K]	300	Suction Pressure [bar]	0.03
Discharge Temperature [K]	300	Discharge Pressure [bar]	1
Global mesh size	0.6	Time steps size	1E-05

### 5.6.2 Mesh generation

Mesh density could be regulated by global mesh size, surface refinement control, gap feature control and solution adaptive mesh in ANSYS Forte. Figure 5-51 shows fine mesh at XY cross section. Three layers of mesh are generated along the casing and rotor wall. The cusp points and rotor boundary of the rotor profile are well captured.

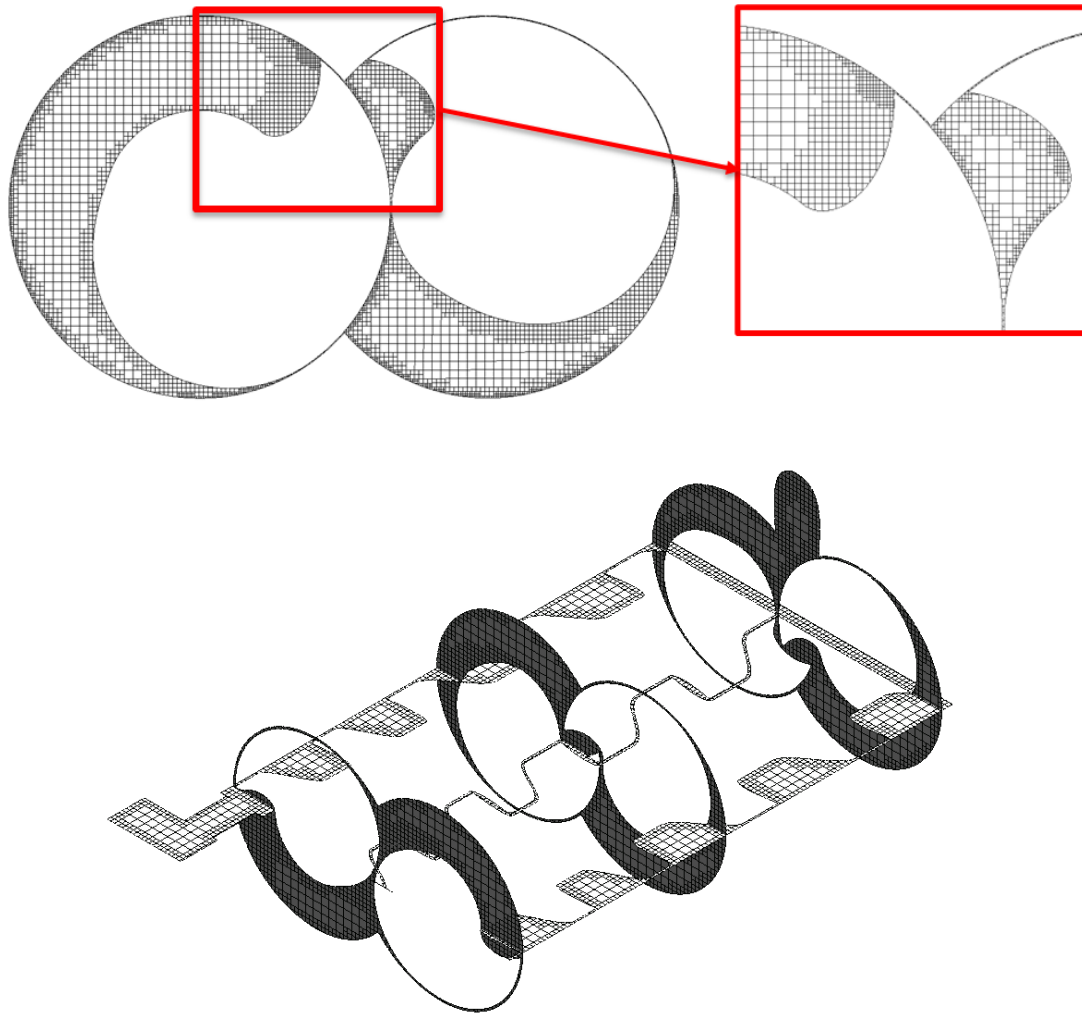


Figure 5-51 Mesh at XY AND XZ cross section.

In one aspect, the mesh generated using cut-cell cartesian method is always Hexahedral mesh, so the mesh quality is not a concern for this method. The number of the cells generated plays an important role to ensure the accuracy and stability of the simulation results. Fine mesh gives advantage to capture details of the flow features but would cause much lower simulation speed and deadlock in MPI communication which may be caused by the memory limitations. In another aspect, too small clearance between two rotors and rotor and casing would also cause the failure of the simulation. ANSYS Forte provides the tools to scale the rotor size and gap size scale factor could be used to compensate for the enlarged gaps.

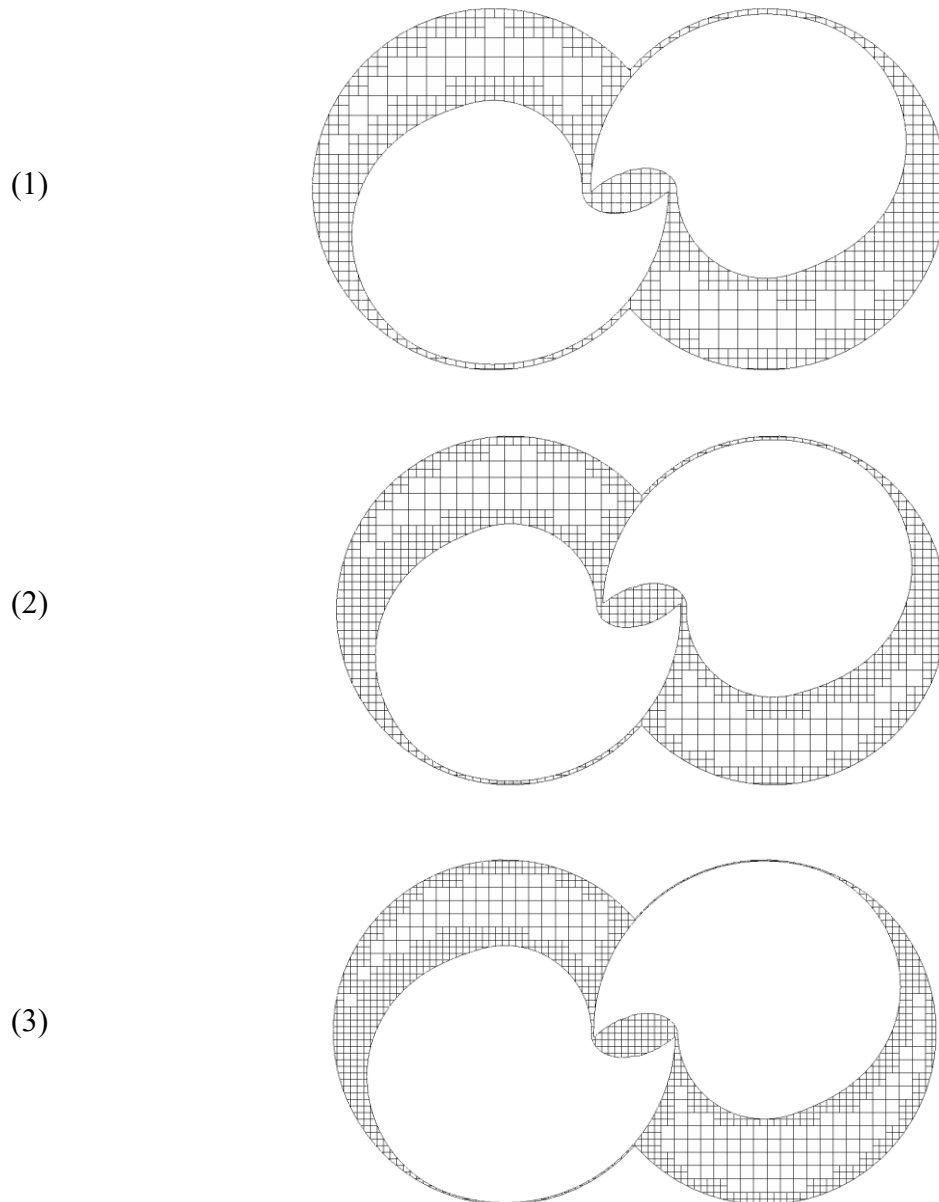


Figure 5-52 XY cross section of scaled rotor.

The rotor geometry was scaled with factor 0.997, 0.998 and 0.999 to compare the leakage flow. Figure 5-54 shows the scaled rotors with factor 0.998 and 0.999 comparing with the original rotors. The original gap size is 0.08 mm. With the scale factor, the gap changed to 0.275 mm, 0.21 mm and 0.145 mm for scale factor 0.997, 0.998 and 0.999 respectively. The gap between two rotors and the casing will not be meshed in the volume mesh. This physically large gap is desirable to model the flow leakage through them. To compensate for the under-resolution in the gap, a momentum sink term is applied in the gap model, which accounts for the wall shear stress and mass flow rate on the coarse grid. Both the gap size and the local fluid cell size are

considered as the input in the gap model. The gap size scale factor can be implemented to enlarge or reduce the physical gap sizes. The scaled gap size is then used as the input for the gap model in the pre-defined individual gap. This provides convenient option to adjust rotor gaps without changing the 3D CAD model. The setup of gap scale factor is shown in Figure 5-53.

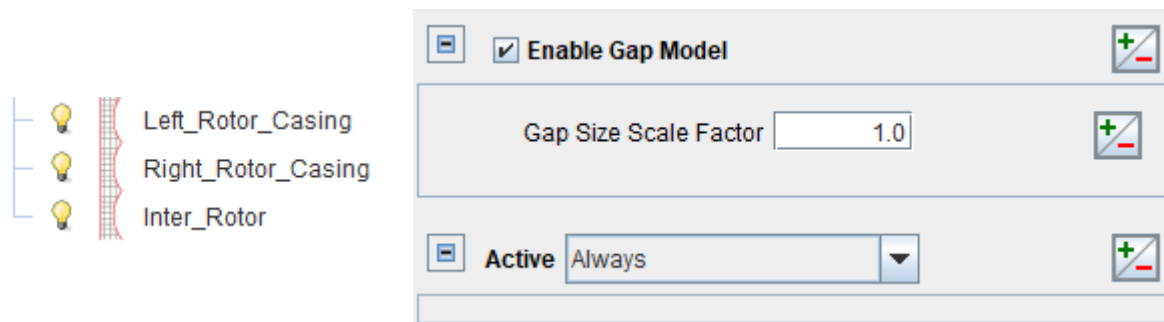


Figure 5-53 Set up of scale factor.

### 5.6.3 Results and discussion

The same boundary conditions are implemented for three different cases with scaled rotors. Figure 5-54 shows the pressure contour in XZ cross section. Figure 5-54 (1) shows the case with scale factor 0.997. The gap size of 0.275 mm leads to big amounts of leakage from high pressure at discharge side to low pressure side. The suction chamber and all vacuum pump chambers have same pressure around 0.6 bar. Figure 5-55 (2) shows the case with scale factor 0.998 which corresponds to 0.21 mm gap size. This case has much better sealing effect because of smaller gap size. Suction chamber and first vacuum pump chamber has approximately same pressure as 0.4 bar. Pressure shows gradually increasing to 1 bar after first vacuum pump chambers. The suction chamber pressure is still higher than the pre-defined suction pressure 0.03 bar. In the case of scale factor 0.999 and gap size of 0.145 mm, the sealing effect shows obvious improvement especially in the suction side. Suction chamber pressure is 0.12 bar. Pressure along rotor chambers increases gradually. Rotor scale factor could be increase to 0.9995 to further decrease the gap size but it is found the problem of deadlock in MPI communication would stop the simulation during the calculation. The leakage model in ANSYS Forte is used to compensate the larger model gap than physical gap to decrease leakage flow from high pressure side to low pressure side.

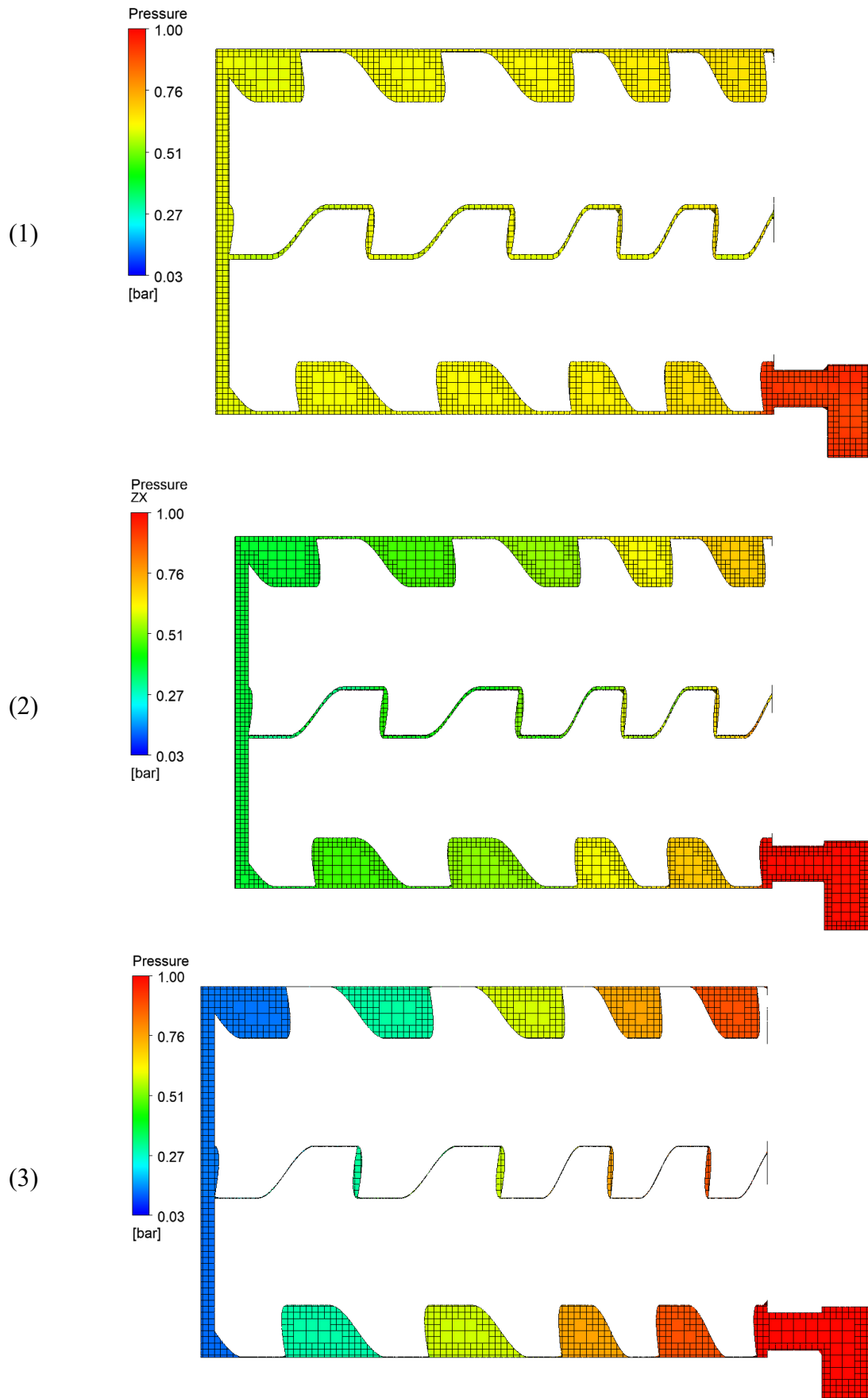


Figure 5-54 Pressure contour at YZ cross section of scaled rotor.

The averaged power and pump speed from CFD simulation were compared with experiments. The simulation and experimental results are shown in Table 5-28. The inlet volume flow during the experiment was controlled by the inlet valve and the suction pressure was achieved by throttling from the atmospheric pressure. The pump speed was calculated with the equation 5-4.

$$S_A = \frac{QP_{atm}}{p_A} \quad 5-4$$

The case with gap size 0.6 has the best agreement with the experiments. The power difference is around 4 % while the pump speed has 13.0 % difference. There are two facts which could lead to the higher difference. The gap size in simulation was 0.007 mm different than the cold clearance set in the experiment. Additionally, in the real experimental condition the discharge temperature reached 80 °C which causes expansion of rotors and the gap in running condition would be reduced. In the calculation that expansion was not taken in consideration. Another reason is that the casing with water cooling is not considered in the simulation. Higher chamber temperature would result in lower pump speed.

Table 5-28 Comparison between simulation and experimental results

Gap scale factor	Gap size/mm	Inlet pressure/Pa	Power/W	Pump speed/L/min
1	0.145	3000	1820	1003.1
0.8	0.116	3000	1900	1092.0
0.6	0.087	3000	2210	1164.7
Experiment	0.08	3100	2310	1338.7

Since the gap size of 0.145 mm is still higher than the physical design rotor gap size 0.08. The gap scale factor 0.8 and 0.6 are set up to compare with the original case with gap scale factor 1. The new gaps are 0.116 mm and 0.087 mm for 0.8 and 0.6 scale factors respectively. Three cases with gap scale factors 1, 0.8 and 0.6 are compared in Figure 5-55 to study the effect of the gap scale factors to the pressure distribution and volume flow rate. The lowest pressure of the suction chamber in three cases are 0.12 bar, 0.10 bar and 0.03 bar. Only in the third case,

the suction chamber has the same pressure with the inlet boundary condition 0.03 bar. The gap size is 0.087 mm with consideration of gap scale factor 0.6 gives good agreement with the real physical model.

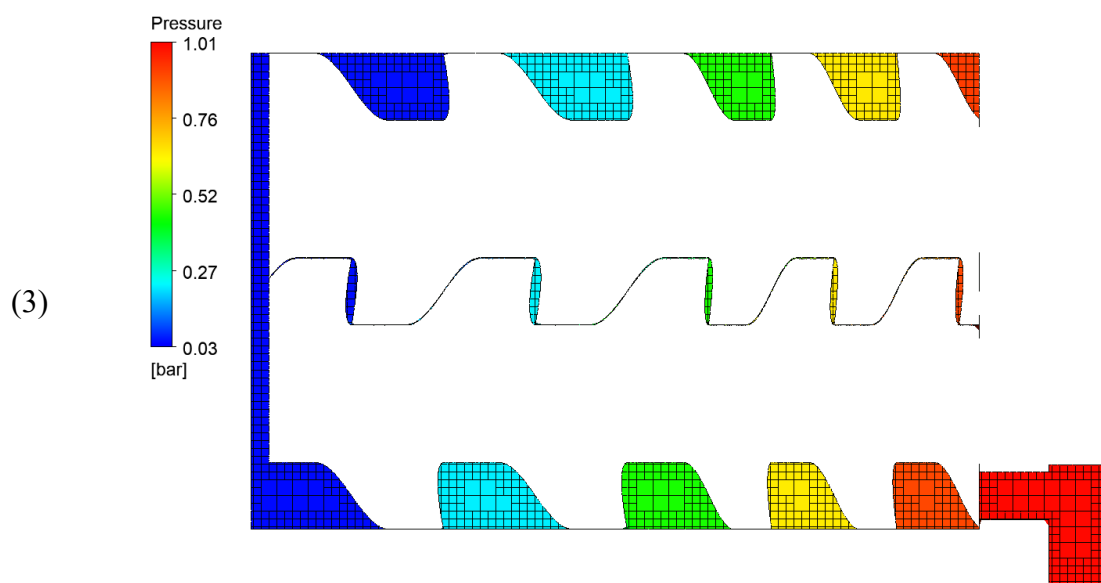
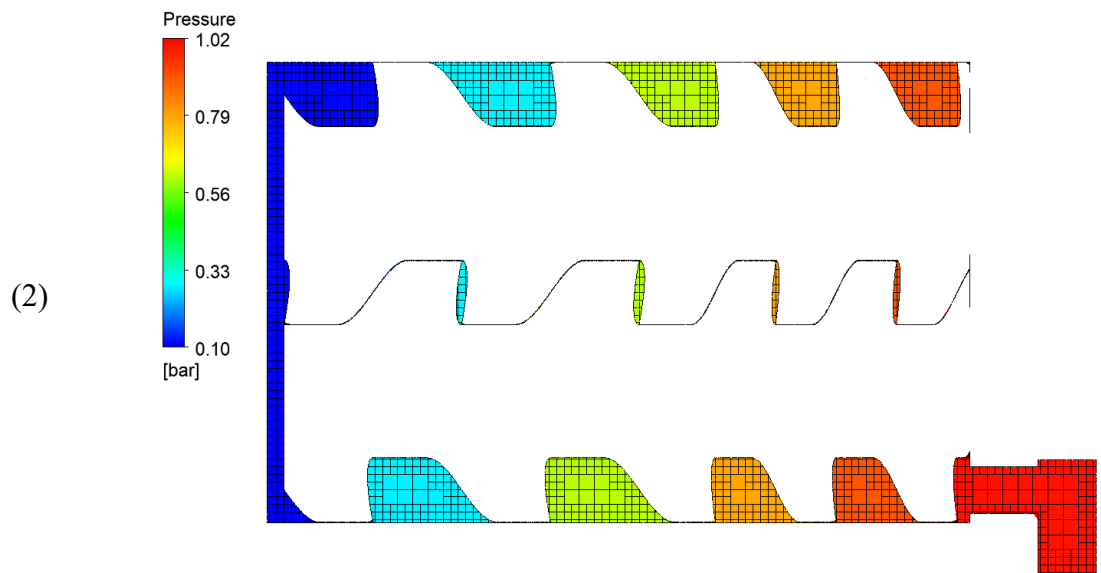
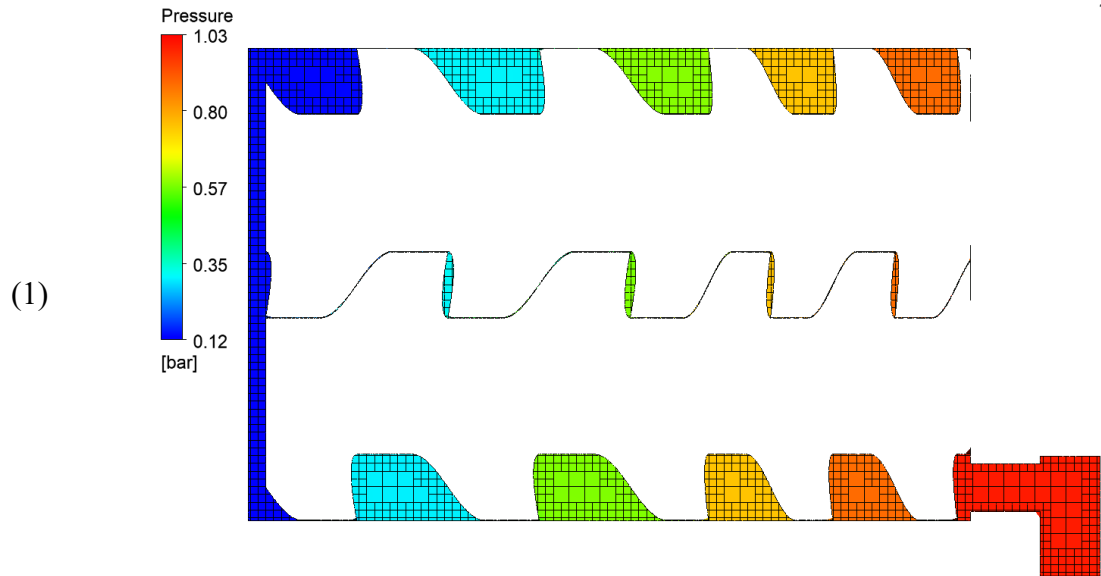




Figure 5-55 YZ cross section with different gap scale factors.

#### 5.6.4 Conclusion

In this case study, a typical large helix angle twin screw vacuum pump with cycloid rotor profile was simulated using cut-cell cartesian method. The simulation results of different geometry scale factor and gap scale factor cases are compared with experimental results at 33.33 pressure ratio operating conditions. It showed that cut-cell cartesian is capable of simulating the working process of the large helix angle twin screw machines.

The following conclusions can be made from the study:

- Successful simulation is restricted to physical gap and mesh resolution. Small gap and fine mesh would lead to deadlock in MPI communication. The reason could be the large curvature around the cusp point.
- Only RANS k-epsilon turbulence model is available in ANSYS Forte, which restrict the study for such high-pressure operating conditions.
- The leakage model built-in ANSYS Forte gives reasonable prediction of volume flow rate. The gap scale factor is a valid tool to adjust the gap in the model to match with the real running condition without update the CAD model.
- Pressure distribution along vacuum pump chambers is sensitive to model gap size and gap scale factor.

#### 5.7 Closure

In this chapter, five case studies have been presented using alternative grid generation methods aiming to demonstrate the feasibility of using cut-cell cartesian and body fitted mesh for different helix angle, including low, intermediate and large helix angles as shown in Figure 5-56.

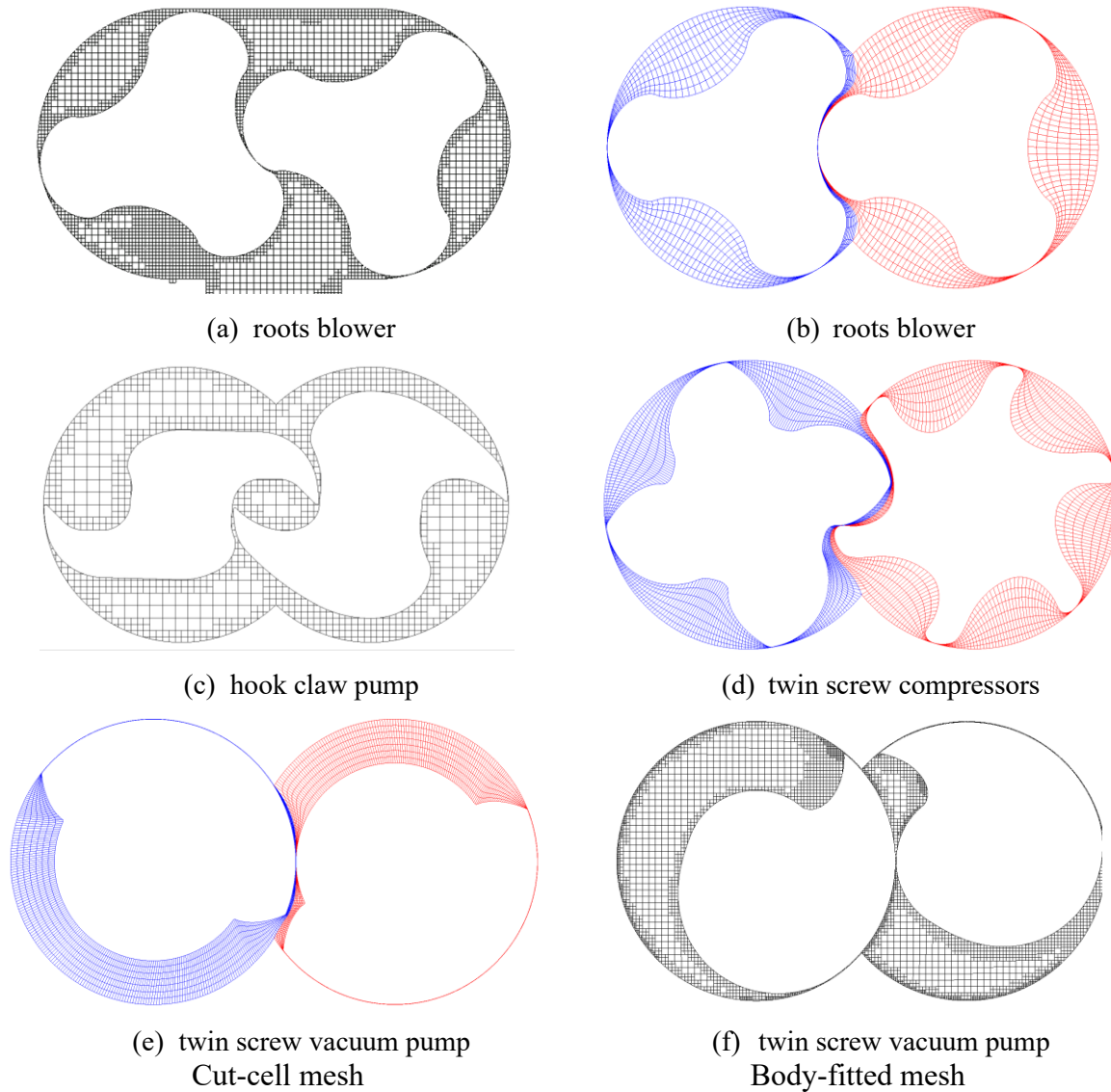


Figure 5-56 Comparison of analysed geometries

In the first case study, the hook claw pump with straight lobes was analysed using cut-cell cartesian method. The mesh independent study was conducted, and different operating conditions were simulated and compared with experimental results. It shows that cut-cell cartesian method is capable and reliable to predict the performance of the hook and claw pump which is difficult for body-fitted method because of the cusp point.

In the second case study, a roots blower with low helix angle is utilised for comparison of cut-cell cartesian mesh and body-fitted mesh which were solved using ANSYS Forte and ANSYS CFX respectively. ANSYS Forte can predict the same trend as ANSYS CFX regarding to the mass flow rate, torque, and power. However, the pressure torque oscillation can be observed

from ANSYS Forte simulation results indicating that there are issues with gap model definition in Ansys Forte.

Third case study presented the body-fitted mesh utilized for the simulation of an intermediate helix angle (44.88 degree) oil-injected twin screw compressor. It is demonstrated that the body-fitted mesh is capable of the simulation of intermediate helix angle.

The aim of the fourth case study was to explore the body-fitted mesh to be used for large helix angle (62 degree) twin screw vacuum pump. The developments in SCOGR have allowed extension of the capability of calculation using ANSYS FLUENT with parallel processes. When the helix angle is higher, it is difficult to generate high quality 3D meshes in the traditional way because the numerical cells become to skewness. It was proposed that an innovative grid generation method which generates numerical mesh in the normal plane of the pitch helix line will be developed. It is expected that this implementation will have advantages for application in modelling of twin screw vacuum pumps with large helix angle.

The last case study is the simulation of large helix angle twin screw vacuum pump using cut-cell cartesian mesh. The mesh scale factor and gap scale factor were explored to adjust the gap size and leakage flow. The method provides indicative results but tuning of gap model is require for each individual case.

# Chapter 6 Grid Generation in a normal plane for Screw Machines with Large Helix Angles

## 6.1 Introduction

The objective of creating numerical mesh in a plane normal to the helix of screw machines is to allow numerical cells to align with the main and leakage flow directions. This will reduce skewness of numerical cells and numerical diffusion and increase stability of CFD calculations. This method also opens possibility for generating numerical mesh for other types of positive displacement machines such as single screw compressor.

The advantages of normal rack domain decomposition are as follows; Firstly, the size and shape of numerical cells in clearances between rotors and casing can be refined by adjusting the density of nodes in a required sections and the alignment of the mesh to the main and leakage flows can be achieved. Secondly, orthogonality of the mesh can be more easily achieved. These advantages can contribute to more robust and efficient simulation of twin screw machines using several CFD solvers. Software SCORG was utilised as the platform for development of the normal grid generation method (NGGM). This chapter firstly generalizes the domain decomposition with emphasis on producing normal plane. Then it introduces the method which uses series of 2D numerical meshes in the planes normal to each of the rotors and rack to decompose the working domain in two sub-domains. Special treatment is required to provide conformal interface between two moving meshes and with the casing. This method will greatly benefit efficiency and accuracy and ease of performance calculation using several CFD solvers. In addition, it will allow generation of various different screw machine configurations like single screw machines or machines with conical rotors. The customized grid generation tool SCORG is utilised here as the platform to process the grid generation in the normal cross section. Several subroutines were programmed for the grid generation in the normal plane.

## 6.2 Fluid domain decomposition

Traditionally, the grid generation of the twin screw compressor fluid domain utilises 2D numerical meshes generated in the transverse plane to the rotor axis and forms 3D numerical

mesh by connecting appropriate vertices in consecutive transverse planes. This method is capable of generating numerical meshes for low and medium helix angles but causes issues with CFD calculation for screw machines with large helix angles due to the skewness of hexahedral cells. A different method using the normal rack to split the fluid domain is proposed in this chapter. It is more convenient if the main rotor and gate domains are cutting by their normal plane respectively, so the grids can be generated in the normal plane. This process makes the grid lines in coordinate directions nearly normal to each other which will reduce or completely remove skewness of the numerical cells which becomes particularly important in modelling leakage flows. The 2D cross sections is then combined to construct the full 3-D fluid domain representing the main and gate fluid domain.

### 6.2.1 Coordinate systems

The fluid domain of a screw rotor is helical type volume generated by the simultaneous revolving of the interlobe space around the rotor axis and translation along the axis. The fluid domain can be separated to two sub-domains using the surface of a normal rack. The outer boundary is the combination of the rack and the casing circle, and the inner boundary is the rotor profile boundary. The sub-domain around one interlobe of the main rotor coloured in green and the sub-domain in one interlobe of the gate rotor coloured in red are meshing with each other and the unique rack surface exists between these two domains as shown in Figure 6-1. The fluid domain between the rotors and casing is represented by several cross sections using the normal planes of the main rotor and gate rotor respectively. Then the normal rack and the casing will form the outer boundary of the fluid domain.

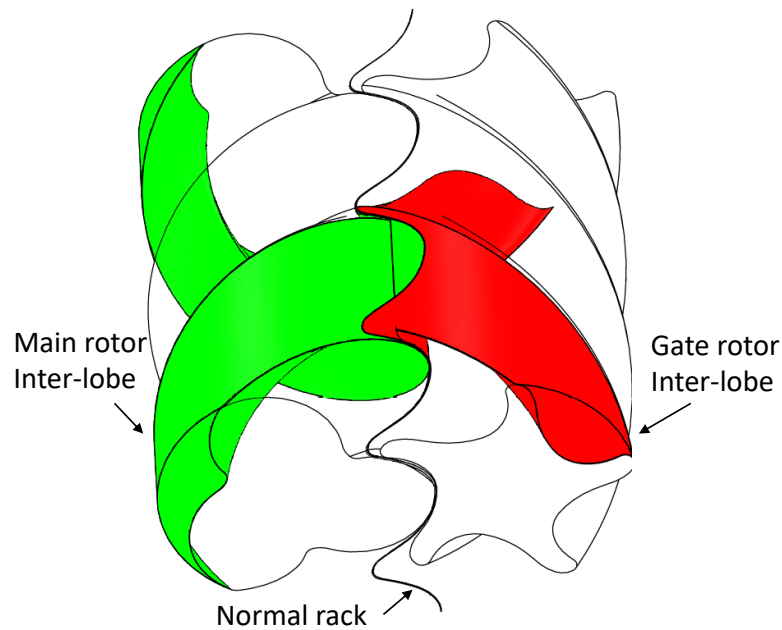


Figure 6-1 Two sub-domain between the rotors.

Figure 6-2 shows the flow chart of the subroutine for grid generation in normal plane. The original coordinates of the rotor and rack in the transverse planes are used as input. Normal coordinate systems of the main and gate rotor are defined for coordinate transformation.

To conduct the structure mesh between the inner and outer boundaries, the number of nodes distributed on the outer boundary should be same as number of nodes on the inner boundary. After the inner and outer boundaries of a physical sub-domain have been calculated in the normal plane and the same points distribute on the boundaries by a scanning function which is introduced to interpolate same number of points on the boundaries as shown in Figure 6-2 (a). Then the boundaries are mapped to a computational domain. As shown in Figure 6-2 (b), the outer boundary nodes are redistributed according to an arc-length based projection to determine the nodes to be placed on the casing. The redistribution can be controlled by the factor coefficient. Next procedure is to make the inverse transformation from the computational domain to the physical domain according to the new arc-length. The new distribution on the rack is based on previous distribution on the casing by calculation the intersections of the rotor and casing connecting line with the rack. Once the outer and inner boundaries are distributed same number of nodes, the interior nodes can be distributed in the sub-domain using algebraic transfinite interpolation. The standard transfinite interpolation and a more accurate ortho-transfinite interpolation can be employed here. Figure 6-2 (c) shows the distribution of the interior nodes in the normal plane. The spacing and boundary orthogonality could be

controlled. 3-D numerical mesh can be formed by connecting corresponding points in consecutive cross sections. The grid lines will be parallel to the helix line and thus orthogonal mesh will be produced.

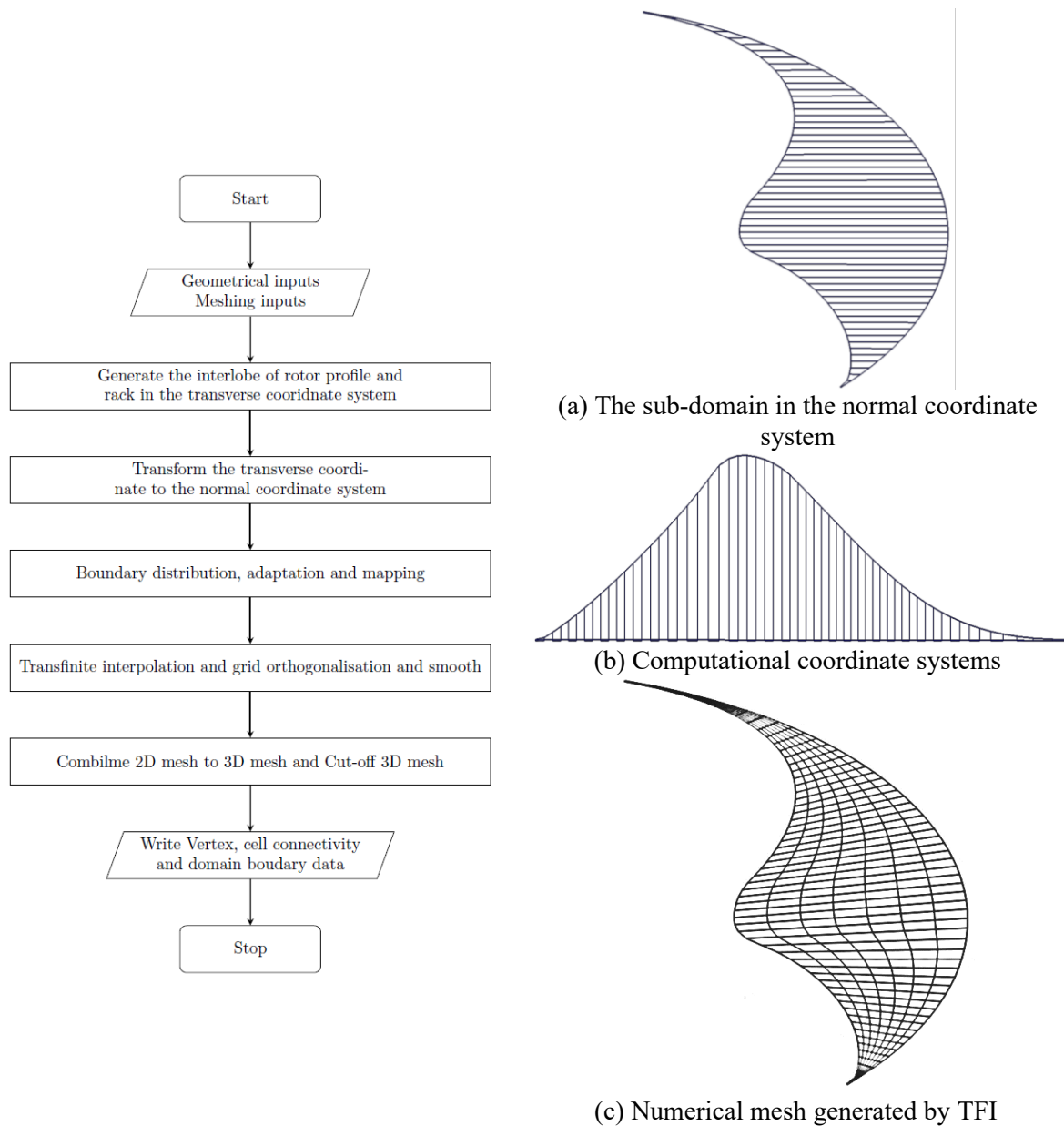


Figure 6-2 The flow chart of grid generation subroutine

The numerical grid of the fluid domain between casing and two rotors can be generated either in the transverse plane of the rotor or normal plane of the pitch helix line. The transverse plane and normal plane are as shown in Figure 6-3. The angle between normal plane and transverse is the helix angle  $90 - \beta$ .

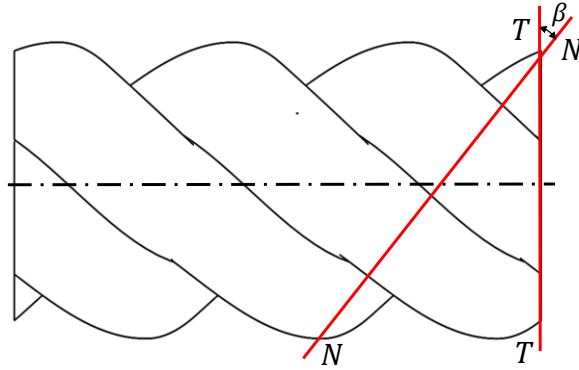


Figure 6-3 Transverse plane and normal plane.

One global coordinate system, two rotor coordinate systems, two rotor transverse coordinate systems are constructed as shown in Figure 6-4. The global coordinate system is  $S(X, Y, Z)$ . Two rotor transverse coordinate systems are  $S_1(X_1, Y_1, Z_1)$  and  $S_2(X_2, Y_2, Z_2)$ . Two rotor coordinate systems are  $S_{01}(X_{01}, Y_{01}, Z_{01})$  and  $S_{02}(X_{02}, Y_{02}, Z_{02})$ .

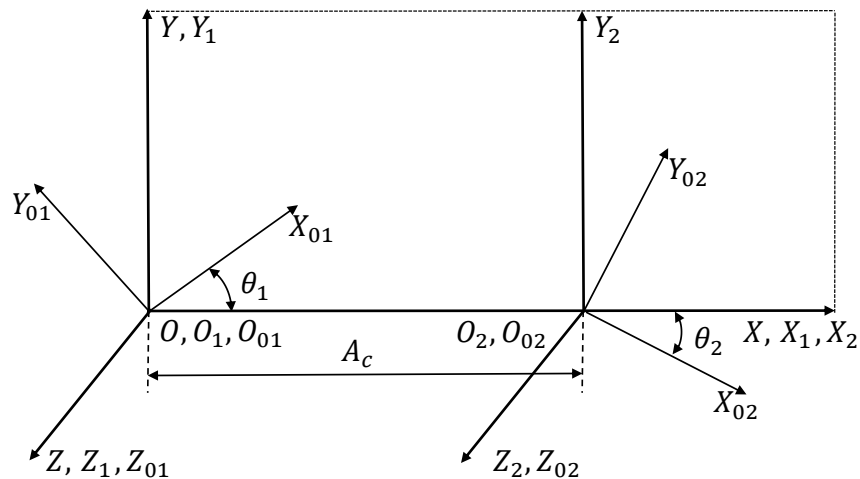


Figure 6-4 Global coordinate system.



The global coordinate system is  $S(X, Y, Z)$  with the origin in the centre of the main rotor on the discharge plane and the  $Z$ -axis along the rotor axis. The origin and unit vector are defined as shown in the Table 6-1.

Table 6-1 Unit vector of global coordinate system

	Origin	Unit vector
Global coordinate system	$\begin{bmatrix} X \\ Y \\ Z \end{bmatrix} = \begin{bmatrix} 0 \\ 0 \\ 0 \end{bmatrix}$	$\begin{bmatrix} i \\ j \\ k \end{bmatrix} = \begin{bmatrix} 1 & 0 & 0 \\ 0 & 1 & 0 \\ 0 & 0 & 1 \end{bmatrix}$

The main rotor coordinate  $S_1(X_1, Y_1, Z_1)$  is fixed in the centre of the main rotor and  $Z_1$ -axis is along the main rotor axis. The gate rotor coordinate  $S_2(X_2, Y_2, Z_2)$  is fixed in the centre of the gate rotor and  $Z_2$ -axis is along the gate rotor axis. The distance between these two coordinate systems was  $A_c$ . The origins and unit vectors of the rotor coordinate system are defined as shown in Table 6-2.

Table 6-2 Unit vector of rotor coordinate systems

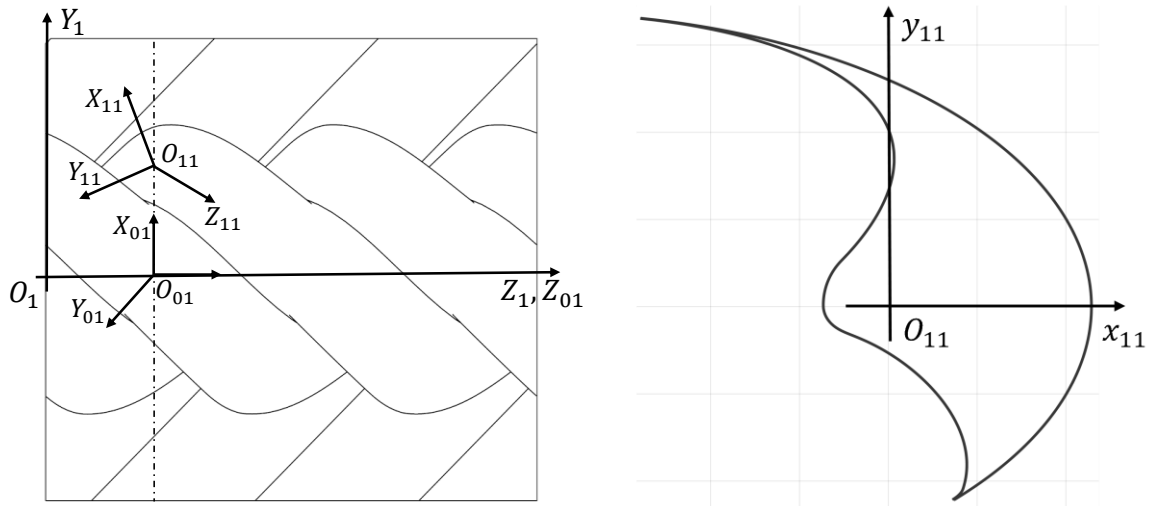
	Origin	Unit vector
Main rotor	$\begin{bmatrix} X_1 \\ Y_1 \\ Z_1 \end{bmatrix} = \begin{bmatrix} 0 \\ 0 \\ 0 \end{bmatrix}$	$\begin{bmatrix} i_1 \\ j_1 \\ k_1 \end{bmatrix} = \begin{bmatrix} i \\ j \\ k \end{bmatrix}$
Gate rotor	$\begin{bmatrix} X_2 \\ Y_2 \\ Z_2 \end{bmatrix} = \begin{bmatrix} A_c \\ 0 \\ 0 \end{bmatrix}$	$\begin{bmatrix} i_2 \\ j_2 \\ k_2 \end{bmatrix} = \begin{bmatrix} i \\ j \\ k \end{bmatrix}$

In the main rotor coordinate system  $S_1(X_1, Y_1, Z_1)$ , the main rotor transverse coordinate system  $S_{01}(X_{01}, Y_{01}, Z_{01})$  rotates around the  $Z_1$ -axis. In the gate rotor coordinate system  $S_2(X_2, Y_2, Z_2)$ , the gate rotor transverse coordinate system  $S_{02}(X_{02}, Y_{02}, Z_{02})$  rotates around the  $Z_2$ -axis. The origins and unit vectors of the rotor transverse coordinate system are defined as shown in the Table 6-3. The origin of main rotor transverse coordinate system is along the  $Z_1$  axis. The unit vectors are defined by rotating the main rotor coordinate system unit vector anticlockwise around the  $Z_1$  axis. The origin of the gate rotor transverse coordinate system is along the  $Z_2$  axis. The unit vectors are defined by rotating the gate rotor coordinate system unit vector clockwise along with the  $Z_2$  axis.

Table 6-3 Unit vector of rotor local transverse coordinate systems

	Origin	Unit vector
Main rotor	$\begin{bmatrix} X_{01} \\ Y_{01} \\ Z_{01} \end{bmatrix} = \begin{bmatrix} 0 \\ 0 \\ \frac{n_i}{N} \cdot L \end{bmatrix}$	$\begin{bmatrix} i_{01} \\ j_{01} \\ k_{01} \end{bmatrix} = \begin{bmatrix} \cos\left(\frac{n_i}{N} \cdot \Omega_1\right) & -\sin\left(\frac{n_i}{N} \cdot \Omega_1\right) & 0 \\ \sin\left(\frac{n_i}{N} \cdot \Omega_1\right) & \cos\left(\frac{n_i}{N} \cdot \Omega_1\right) & 0 \\ 0 & 0 & 1 \end{bmatrix} \begin{bmatrix} i_1 \\ j_1 \\ k_1 \end{bmatrix}$
Gate rotor	$\begin{bmatrix} X_{02} \\ Y_{02} \\ Z_{02} \end{bmatrix} = \begin{bmatrix} A_c \\ 0 \\ \frac{n_i}{N} \cdot L \end{bmatrix}$	$\begin{bmatrix} i_{02} \\ j_{02} \\ k_{02} \end{bmatrix} = \begin{bmatrix} \cos\left(\frac{n_i}{N} \cdot \Omega_2\right) & \sin\left(\frac{n_i}{N} \cdot \Omega_2\right) & 0 \\ -\sin\left(\frac{n_i}{N} \cdot \Omega_2\right) & \cos\left(\frac{n_i}{N} \cdot \Omega_2\right) & 0 \\ 0 & 0 & 1 \end{bmatrix} \begin{bmatrix} i_2 \\ j_2 \\ k_2 \end{bmatrix}$

In addition, the rotor normal coordinate systems were constructed in the rotor coordinate systems. The main rotor normal coordinate system is  $S_{11}(X_{11}, Y_{11}, Z_{11})$  which is defined in the main rotor coordinate system as shown in Figure 6-5. The  $Z_{11}$  axis is tangent to the main rotor pitch helix line in the origin  $O_{11}$  and the  $X_{11}Y_{11}$  plane is perpendicular to  $Z_{11}$  axis. The main rotor normal profile is defined in this coordinate system. The right picture shows the main rotor normal profile in the local normal coordinate system. The origins move along with the pitch helix line.

Figure 6-5 Main rotor local *coordinate* system.

The gate rotor normal coordinate system  $S_{12}(X_{12}, Y_{12}, Z_{12})$  is defined in the gate rotor coordinate system as shown in Figure 6-6. The  $Z_{12}$  axis is tangent to the helix line in the origin

$O_{12}$  and the  $X_{12}Y_{12}$  plane is perpendicular to  $Z_{12}$  axis. The gate rotor normal profile is defined in this coordinate system. The right picture shows the gate rotor normal profile in the local normal coordinate system.

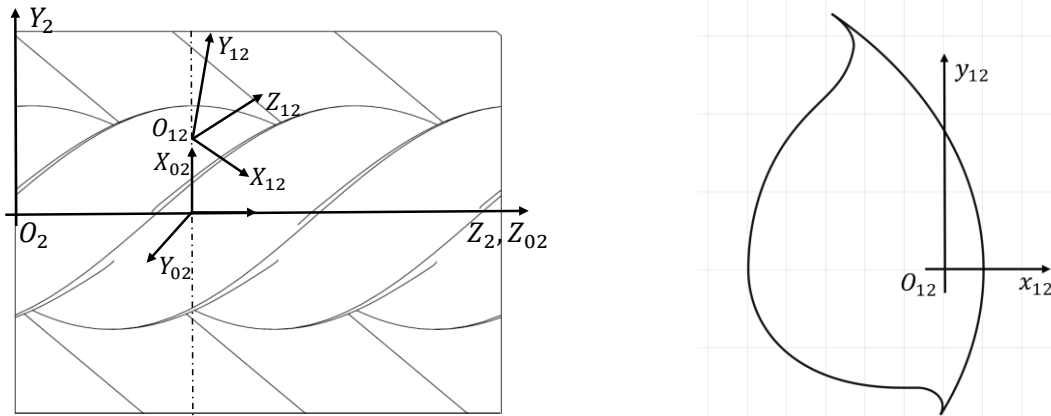


Figure 6-6 Gate rotor local coordinate system.

The origins and unit vectors of the main and gate rotor normal coordinate systems are defined as shown in the Table 6-4. The origins of the main rotor normal coordinate system are along the main rotor pitch helix line. The unit vectors are defined by rotating the main rotor transverse coordinate system unit vector clockwise along with the  $X_{01}$  axis. The origins of the gate rotor normal coordinate system are along the gate rotor pitch helix line. The unit vectors are defined by rotating the gate rotor transverse coordinate system unit vector anticlockwise along with the  $X_{02}$  axis.

Table 6-4 Unit vector of rotor local normal coordinate systems

	Origin	Unit vector
Main rotor	$\begin{bmatrix} X_{11} \\ Y_{11} \\ Z_{11} \end{bmatrix} = \begin{bmatrix} r_{p1} \\ 0 \\ 0 \end{bmatrix}$	$\begin{bmatrix} i_{11} \\ j_{11} \\ k_{11} \end{bmatrix} = \begin{bmatrix} 1 & 0 & 0 \\ 0 & \cos(\beta) & -\sin(\beta) \\ 0 & \sin(\beta) & \cos(\beta) \end{bmatrix} \begin{bmatrix} i_{01} \\ j_{01} \\ k_{01} \end{bmatrix}$
Gate rotor	$\begin{bmatrix} X_{12} \\ Y_{12} \\ Z_{12} \end{bmatrix} = \begin{bmatrix} r_{p2} \\ 0 \\ 0 \end{bmatrix}$	$\begin{bmatrix} i_{12} \\ j_{12} \\ k_{12} \end{bmatrix} = \begin{bmatrix} 1 & 0 & 0 \\ 0 & \cos(\beta) & \sin(\beta) \\ 0 & -\sin(\beta) & \cos(\beta) \end{bmatrix} \begin{bmatrix} i_{02} \\ j_{02} \\ k_{02} \end{bmatrix}$

The rack is the curve representing a rotor with infinite radius, which meshes with the main rotor profile and gate rotor profile simultaneously. The rack surface is generated by extruding rack curve along helix angle. Figure 6-7 shows the normal rack local coordinate

system  $S_{13}(X_{13}, Y_{13}, Z_{13})$ . The  $Z_{13}$  axis is along the extruding line and the  $X_{13}Y_{13}$  plane is perpendicular to  $Z_{13}$ -axis. The right picture shows the rack profile in the normal rack local coordinate system.

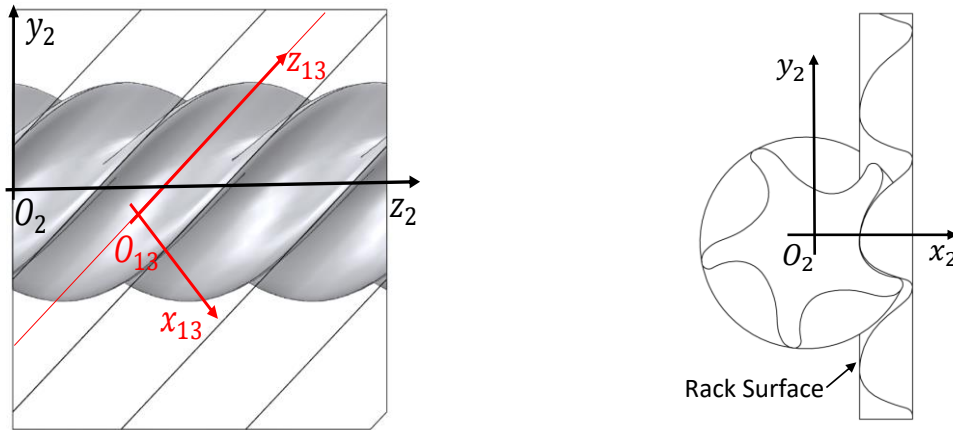


Figure 6-7 Local coordinate system of main rotor.

The origins and unit vector of the rack normal coordinate system are defined as shown in the Table 6-5. The origins of rack normal coordinate system are along the rack extruding line. The unit vectors are defined by rotating the main rotor coordinate system unit vector anticlockwise along with the  $X_{01}$  axis.

Table 6-5 Unit vector of rack normal coordinate system

	Origin	Unit vector
Rack Normal coordinate system	$\begin{bmatrix} X_{13} \\ Y_{13} \\ Z_{13} \end{bmatrix} = \begin{bmatrix} r_{p1} \\ r_{p1} \cdot \frac{n_i}{N} \cdot \Omega_1 \\ \frac{n_i}{N} \cdot L \end{bmatrix}$	$\begin{bmatrix} i_{13} \\ j_{13} \\ k_{13} \end{bmatrix} = \begin{bmatrix} 1 & 0 & 0 \\ 0 & \cos(\beta) & \sin(\beta) \\ 0 & -\sin(\beta) & \cos(\beta) \end{bmatrix} \begin{bmatrix} i_{01} \\ j_{01} \\ k_{01} \end{bmatrix}$

### 6.2.2 Normal rack and normal rotor profile

The detailed procedure of coordinates transforming from transfer plane to normal plane is explained in this section.

1. Input main rotor and gate rotor profile coordinates in rotor coordinate system  $S_1(X_1, Y_1, Z_1)$  and  $S_2(X_2, Y_2, Z_2)$ . Only one lobe of the main rotor and one interlobe of the gate rotor are considered for generation of the profile in the normal coordinate system. The main rotor profile starts from the fourth quadrant of the main rotor

coordinate system to the first quadrant while the gate rotor profile starts from the third quadrant to the second quadrant. The number of points for the main rotor profile and gate rotor profile are  $m_1$  and  $m_2$  respectively as defined in Table 6-6..

Table 6-6 The input rotor profile coordinates

	Position vector	Coordinate system
Main rotor	$(x_1(m_1), y_1(m_1), z_1(m_1))$	$S_1(X_1, Y_1, Z_1)$
Gate rotor	$(x_2(m_2), y_2(m_2), z_1(m_2))$	$S_2(X_2, Y_2, Z_2)$

The initial input rotor profile is shown in Figure 6-8

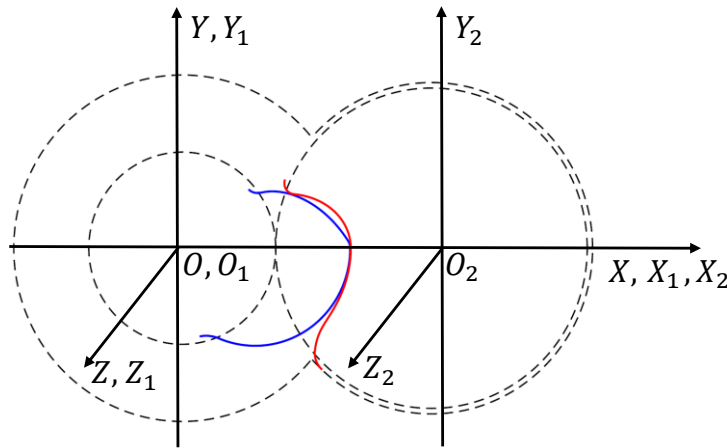


Figure 6-8 Input Profile.

2. The main rotor profile is transformed from lobe to interlobe as shown in Figure 6-9.

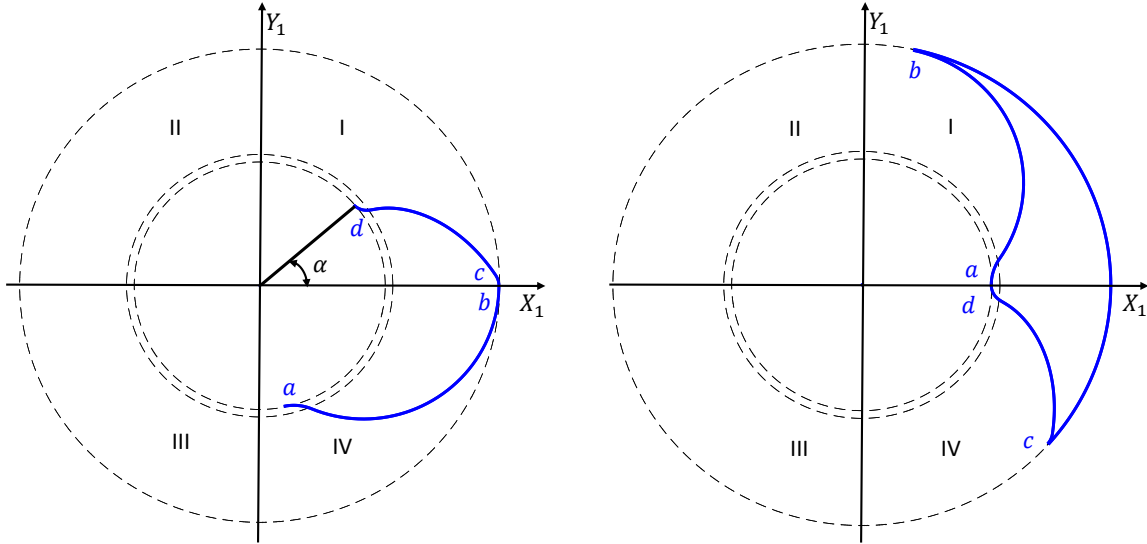


Figure 6-9 Main rotor profile transformation.

- Rotate the profile in the fourth quadrant  $ab$  anticlockwise for an angle  $2 \cdot \pi/Z_1$  by using equation 6.1
- Rotate the new profile clockwise with angle  $\alpha$  to the start position according to equation 6.2.

$$\begin{bmatrix} x'_1(ab) \\ y'_1(ab) \\ z'_1(ab) \end{bmatrix} = \begin{bmatrix} \cos\left(\frac{2 \cdot \pi}{Z_1}\right) & -\sin\left(\frac{2 \cdot \pi}{Z_1}\right) & 0 \\ \sin\left(\frac{2 \cdot \pi}{Z_1}\right) & \cos\left(\frac{2 \cdot \pi}{Z_1}\right) & 0 \\ 0 & 0 & 1 \end{bmatrix} \begin{bmatrix} x_1(ab) \\ y_1(ab) \\ z_1(ab) \end{bmatrix} \quad 6.1$$

$$\begin{bmatrix} x_1(cb) \\ y_1(cb) \\ z_1(cb) \end{bmatrix} = \begin{bmatrix} \cos(\alpha) & \sin(\alpha) & 0 \\ -\sin(\alpha) & \cos(\alpha) & 0 \\ 0 & 0 & 1 \end{bmatrix} \begin{bmatrix} x'_1(cb) \\ y'_1(cb) \\ z'_1(cb) \end{bmatrix} \quad 6.2$$

3. Generate numerical rack for the main and gate rotor separately in the rotor coordinate system according to equation 6.3 and 6.4. The rack coordinates have the same sequence with the rotor coordinates starting from the bottom to the top

$$\text{Main rotor rack} \quad \begin{bmatrix} xr_1 \\ yr_1 \\ zr_1 \end{bmatrix} = \begin{bmatrix} \cos(\theta_1) & -\sin(\theta_1) & 0 \\ \sin(\theta_1) & \cos(\theta_1) & 0 \\ 0 & 0 & 1 \end{bmatrix} \cdot \begin{bmatrix} x_1 \\ y_1 \\ z_1 \end{bmatrix} + \begin{bmatrix} 0 \\ r_{p1} \cdot \theta_1 \\ 0 \end{bmatrix} \quad 6.3$$

$$\text{Gate rotor rack} \quad \begin{bmatrix} xr_2 \\ yr_2 \\ zr_2 \end{bmatrix} = \begin{bmatrix} \cos(\theta_2) & \sin(\theta_2) & 0 \\ -\sin(\theta_2) & \cos(\theta_2) & 0 \\ 0 & 0 & 1 \end{bmatrix} \cdot \begin{bmatrix} x_2 \\ y_2 \\ z_2 \end{bmatrix} + \begin{bmatrix} 0 \\ r_{p2} \cdot \theta_2 \\ 0 \end{bmatrix} \quad 6.4$$

The relative position of rack with main and gate rotor interlobe is shown in Figure 6-10.

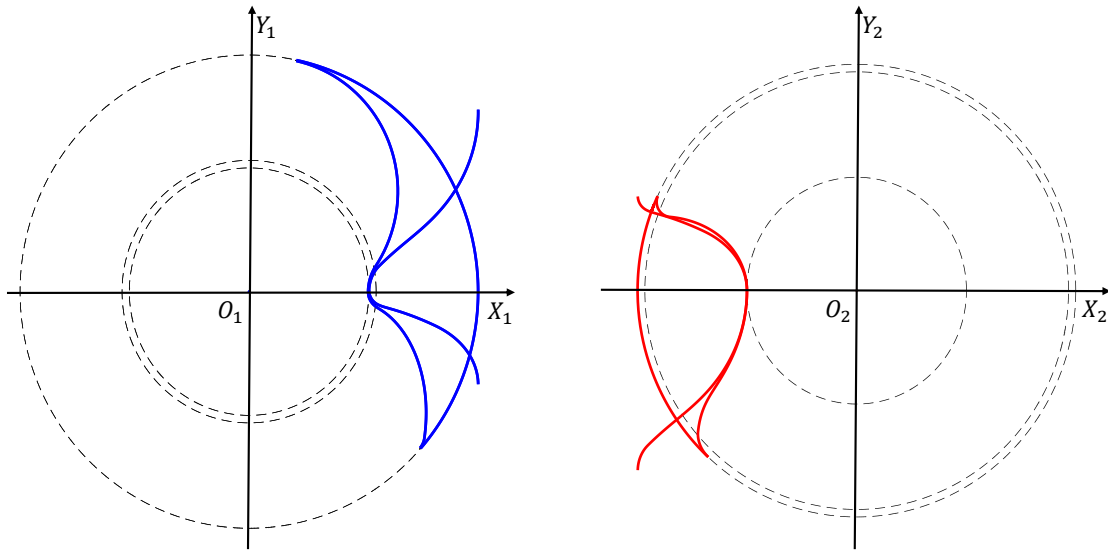


Figure 6-10 Rotor profile and rack relative position.

4. Transform the rotor profile from the rotor coordinate system to the rotor transverse coordinate system.
  - Define the number of cross sections along the  $z$  axis:  $n$ . The cross sections are defined at equal distances from each other. The corresponding position of the cross sections is defined by  $L/N \cdot n_i$  and the rotation angle of the profile is defined by  $\Omega_k/N \cdot n_i$ .
  - Transform the rotor profile from the rotor coordinate system to the rotor transverse coordinate system which is corresponding to the cross section by the equation 6.5 and equation 6.6.

$$\begin{bmatrix} x_{01} \\ y_{01} \\ z_{01} \\ 1 \end{bmatrix} = \begin{bmatrix} \cos\left(\frac{n_i}{N} \cdot \Omega_1\right) & -\sin\left(\frac{n_i}{N} \cdot \Omega_1\right) & 0 & 0 \\ \sin\left(\frac{n_i}{N} \cdot \Omega_1\right) & \cos\left(\frac{n_i}{N} \cdot \Omega_1\right) & 0 & 0 \\ 0 & 0 & 1 & \frac{n_i}{N} \cdot L \\ 0 & 0 & 0 & 1 \end{bmatrix} \cdot \begin{bmatrix} x_1 \\ y_1 \\ z_1 \\ 1 \end{bmatrix} \quad 6.5$$

$$\begin{bmatrix} x_{02} \\ y_{02} \\ z_{02} \\ 1 \end{bmatrix} = \begin{bmatrix} \cos\left(\frac{n_i}{N} \cdot \Omega_2\right) & \sin\left(\frac{n_i}{N} \cdot \Omega_2\right) & 0 & 0 \\ -\sin\left(\frac{n_i}{N} \cdot \Omega_2\right) & \cos\left(\frac{n_i}{N} \cdot \Omega_2\right) & 0 & 0 \\ 0 & 0 & 1 & \frac{n_i}{N} \cdot L \\ 0 & 0 & 0 & 1 \end{bmatrix} \cdot \begin{bmatrix} x_2 \\ y_2 \\ z_2 \\ 1 \end{bmatrix} \quad 6.6$$

5. Transform the main and gate rotor profiles from the rotor transverse coordinate systems to the related rotor normal coordinate systems. Here taking an example for main rotor profile.
  - The angle between one interlobe of main rotor profile is  $2\pi/Z_1$ . Divide this angle  $\theta = [-\pi/Z_1, \pi/Z_1]$  according to the number of points on the profile  $M$ . Rotate of  $\theta_1 \in [\alpha_1 + \theta, \alpha_m + \theta]$  for change in coordinates due to twist of main rotor profile in the transverse coordinate system. There are  $m$  cross sections are generated for defining the normal rotor profile.

$$\begin{bmatrix} x'_{01} \\ y'_{01} \\ z'_{01} \\ 1 \end{bmatrix} = \begin{bmatrix} \cos(\theta_1) & -\sin(\theta_1) & 0 & 0 \\ \sin(\theta_1) & \cos(\theta_1) & 0 & 0 \\ 0 & 0 & 1 & \frac{L}{\Omega_1} \cdot \theta \\ 0 & 0 & 0 & 1 \end{bmatrix} \cdot \begin{bmatrix} x_{01} \\ y_{01} \\ z_{01} \\ 1 \end{bmatrix} \quad 6.7$$

- Change in  $y_{01}$  for the intersection between the normal plane and the  $m$  cross section.

$$y_{01} = \frac{z'_{01}}{\tan(\beta)} \quad 6.8$$

- The rotor profile in the main rotor local normal plane.

$$y_{11} = \frac{y_{01}}{\cos(\beta)} \quad 6.9$$

$$x_{11} = \text{intep1}(x'_{01}, y'_{01}, y_{11})$$

- The casing profile in the main rotor local normal plane.

$$y_{11} = \frac{y_{01}}{\cos(\beta)} \quad 6.10$$

$$x_{11} = r_{o1} \cos\left(\arcsin\left(\frac{y_{11}}{r_{o1}}\right)\right)$$

6. Transform the transverse rack to the normal rack in rack normal coordinate systems  $S_{13}(x_{13}, y_{13}, z_{13})$  according to equation 4.11 and 4.12.

$$\begin{bmatrix} x_{rn1} \\ y_{rn1} \\ z_{rn1} \end{bmatrix} = [1 \quad \cos(\beta) \quad 1] \cdot \begin{bmatrix} x_{rt1} \\ y_{rt1} \\ z_{rt1} \end{bmatrix} \quad 6.11$$



$$\begin{bmatrix} x_{rn2} \\ y_{rn2} \\ z_{rn2} \end{bmatrix} = [1 \quad \cos(\beta) \quad 1] \cdot \begin{bmatrix} x_{rt2} \\ y_{rt2} \\ z_{rt2} \end{bmatrix} \quad 6.12$$

7. Transform normal rack form the rack normal coordinate systems  $S_{13}(x_{13}, y_{13}, z_{13})$  to the related rotor normal coordinate system. Firstly, define the normal rack origin in the rotor normal coordinate system. Secondly, get the relative x and y coordinates of the rack in the rotor normal local coordinate system. Finally, connect the origin and the relative coordinates. The procedures are as following:

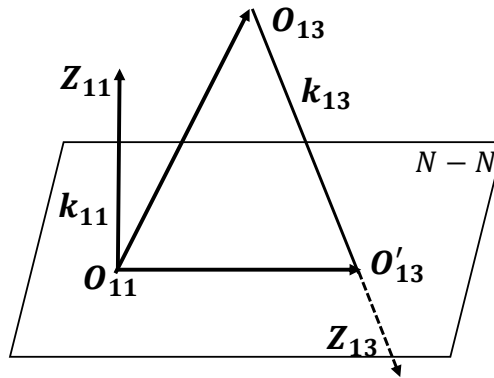


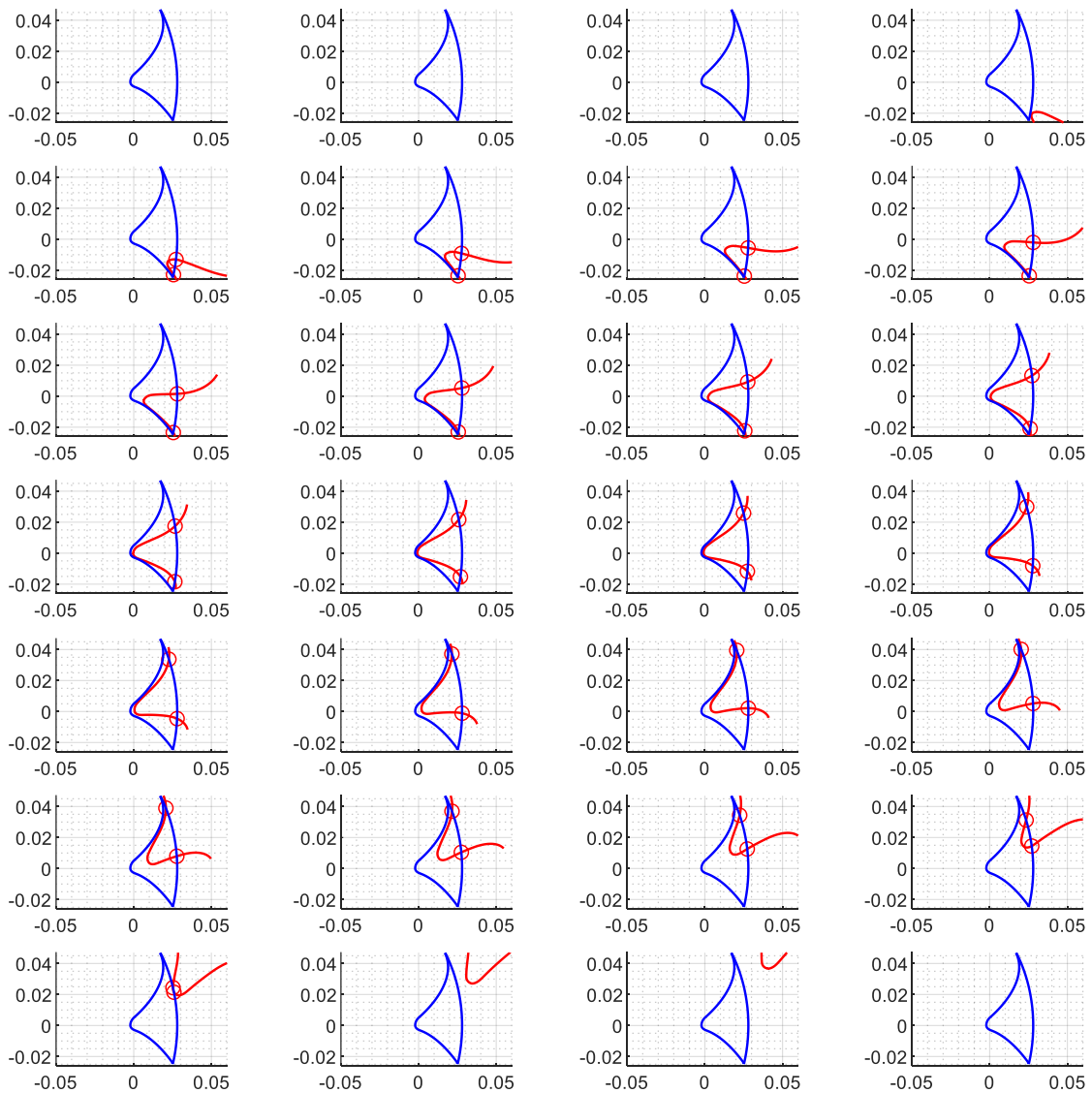
Figure 6-11 Line-plane intersection.

- Get the unit vector of the main rotor normal coordinate system unit vector  $\mathbf{k}_{11}$ .
- Get the unit vector of the rack normal coordinate system unit vector  $\mathbf{k}_{13}$ .
- The origin of the main rotor normal coordinate system is  $O_{11}$ .
- The origin of the rack in the main rotor normal coordinate system is  $O_{13}$ .
- The origin of the rack in the main rotor normal coordinate system is  $O'_{13}$ .
- So  $\mathbf{O}_{13}\mathbf{O}'_{13} = s \cdot \mathbf{k}_{13}$  which satisfied the relation  $\mathbf{k}_{11} \cdot (\mathbf{O}_{11}\mathbf{O}_{13} + \mathbf{O}_{13}\mathbf{O}'_{13}) = 0$ . Then the  $s$  can be calculated. Then the origin of the normal rack in the main rotor normal coordinate can be obtained.
- Get one rack vector  $O_{13}P(x_{13}, y_{13})$  in the rack normal coordinate system. Project  $O_{13}P$  to rotor normal coordinate system to get the relative position.

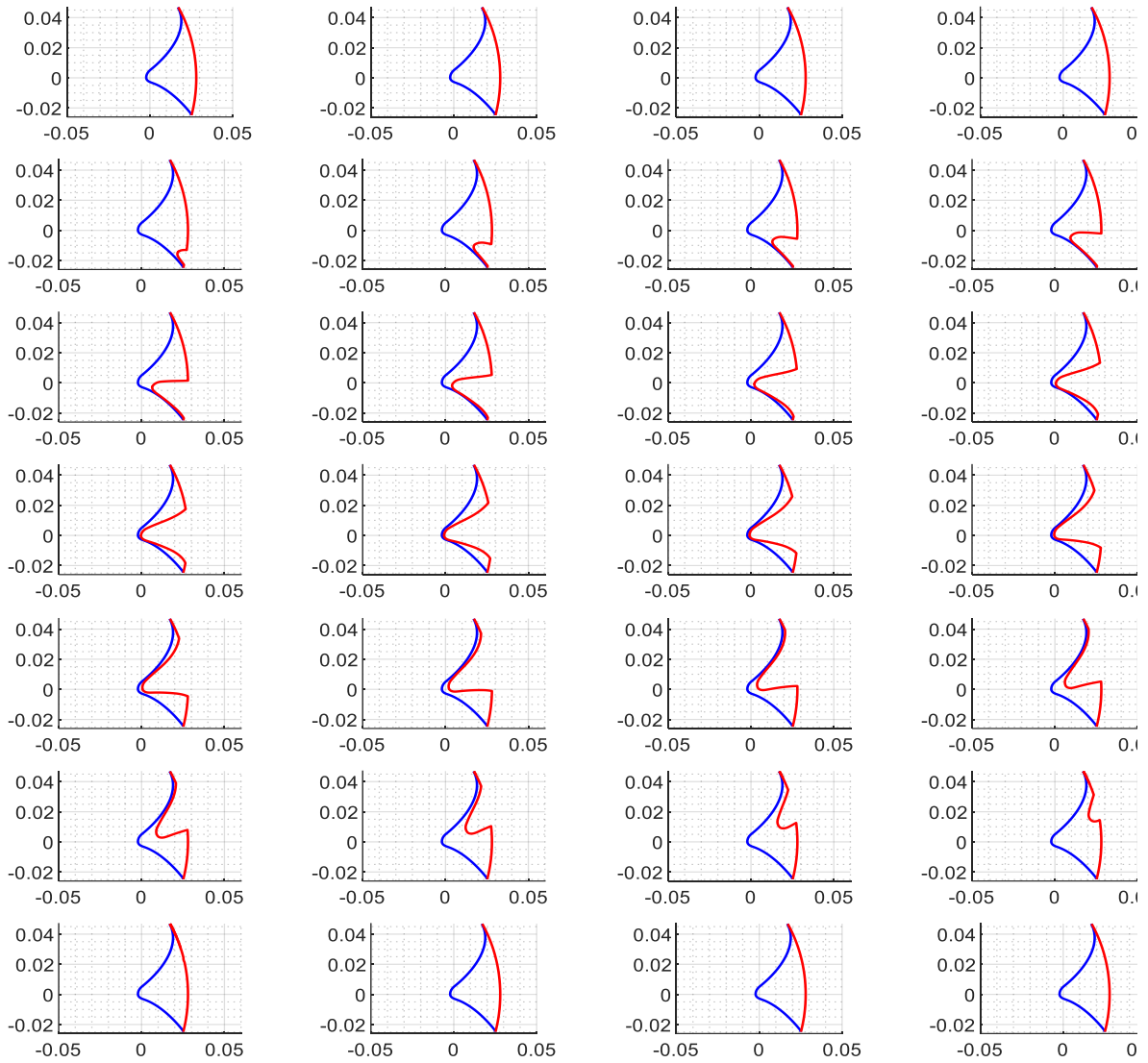
$$\begin{cases} P_x(n) = \frac{\mathbf{O}_{13}\mathbf{P} \cdot \mathbf{i}_{11}}{|\mathbf{i}_{11}|} \\ P_y(n) = \frac{\mathbf{O}_{13}\mathbf{P} \cdot \mathbf{j}_{11}}{|\mathbf{j}_{11}|} \end{cases}$$

- The normal rack position vector in the rotor normal coordinate system can be obtained by the origin  $O'_{13}$  and relative position  $(P_x(n), P_y(n))$ .
8. Repeat the step 2 to step 5 to get the rotor profile and rack in all N cross sections. Then the four boundaries can be obtained by connecting rotor profile and rack.

The normal sub-domain of main and gate rotor was at first visualized in MATLAB and the data files contained the coordinates of the sub-domain. The Figure 6-12 shows the relative position between the main rotor profile and the rack. Figure 6-12(a) shows the rack cut the casing to get the outer boundary. The rotor profile boundary of the main and gate rotor profile coordinates keeps the same in their own rotor normal coordinate systems. The same number of points are generated in the inner boundary and outer boundary.



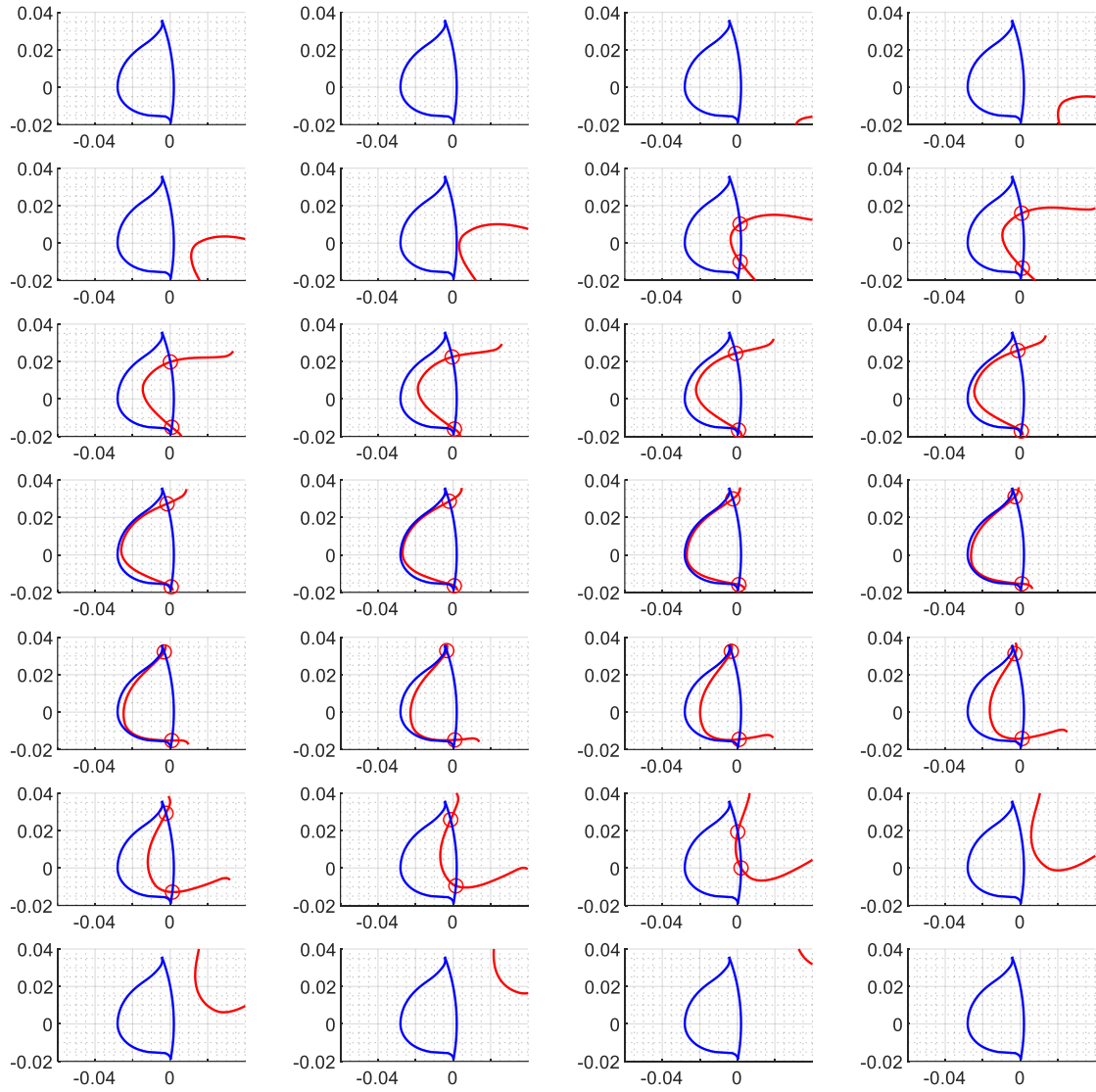
(a)



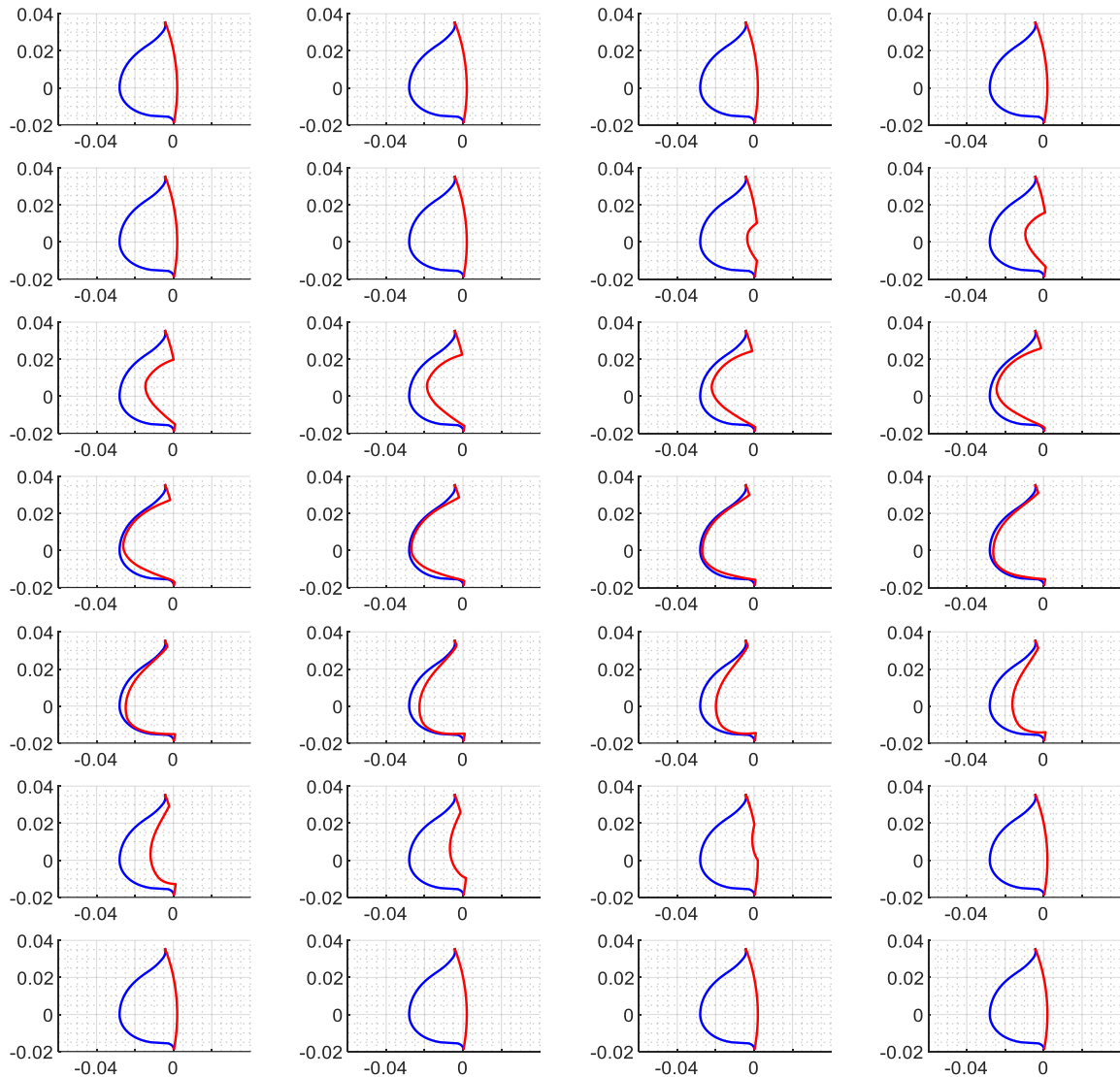
(b)

Figure 6-12 The main rotor sub-domain and rack in LNCS.

Figure 6-13(b) shows the relative position of the gate rotor profile and the rack. The rack cut the casing to get the outer boundary. The MATLAB program was translated to FORTRAN to perform the same procedure in SCORG. In the next section, the subroutine used for the grid adaptation and interpolation are studied in detail.



(a)



(b)

Figure 6-13 The gate rotor sub-domain and rack in LNCS.

### 6.3 Algebraic Grid generation

In the previous section, the global coordinate system, rotor coordinate systems, rotor transverse local coordinate systems, rotor normal local coordinates and rack normal coordinate system are defined. The rotor profiles and rack defined in this coordinate systems are used for coordinate transformation. In addition, the interlobe of the main and gate rotors are defined in both the rotor transverse coordinate systems and rotor normal coordinate systems. In this section, the grid generation method is implemented on the defined interlobe. The grid generation process of screw machine is performed in the Cartesian coordinate system introduced above and starts

from the process of replacing the working chamber with a set of grid points. The decomposition of the flow region between the casing and two rotors consists of dividing the region into a series of 2D cross sections. The boundaries are discretised according to the rotor geometry and flow characteristics.

### 6.3.1 Outer boundary regularisation

As mentioned previously, in the normal plan the coordinate system origin is located at the pitch circle and the sub-domain is one interlobe. The inner boundary of this sub-domain is the rotor profile in the normal plane and outer boundary of this sub-domain is the combination of an ellipse and normal rack. In this case, the rotor configure combination is 3/5. Number of divisions along helix line is 60 and number of divisions along the main rotor sub-domain interlobe ellipse is 60 while along the gate rotor sub-domain interlobe ellipse is 36. All the coordinate generation, transformation and adaptation of the domain boundaries are implemented in the rotor normal local coordinate system.

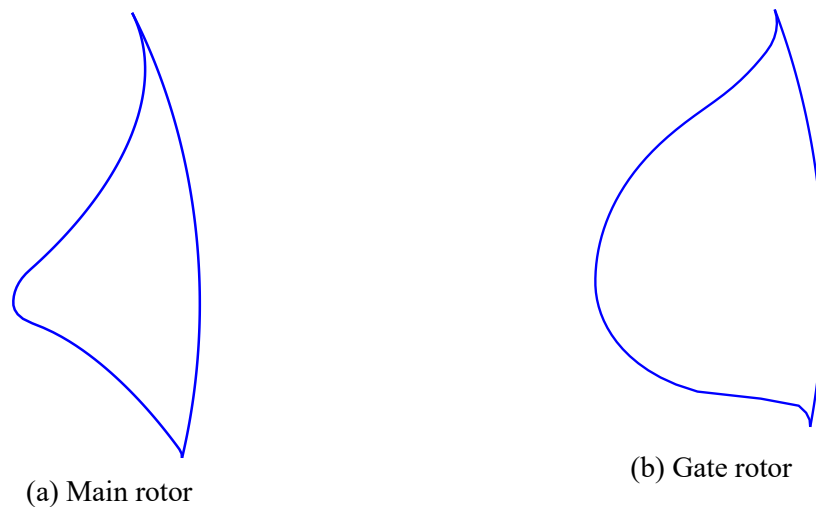


Figure 6-14 The sub-domain coordinate in the normal plane

To make the transformation from physical coordinate to computational coordinate, the outer boundaries and inner boundaries needed to firstly be transferred from the normal plane to the transverse plane. Subsequently, the outer boundaries were transferred from the ellipse to the circle and also the origin needs to be moved to the centre of the origin according to the helix angle in the outer circle. The next step is the adaptation of the rotor profiles and mapping on the outer circle according to Appendix B.

After the inner and outer boundaries of a physical sub-domain have been calculated and the same points distribute on the boundaries by a scanning function which is introduced to interpolate same number of points on the boundaries. Then the boundaries have to be mapped to a computational domain in which the outer boundary nodes are redistributed according to an arc-length based projection to determine the nodes to be placed on the casing. The redistribution can be controlled by the factor coefficient. The detailed of this redistribution process can be referenced in the book [58].

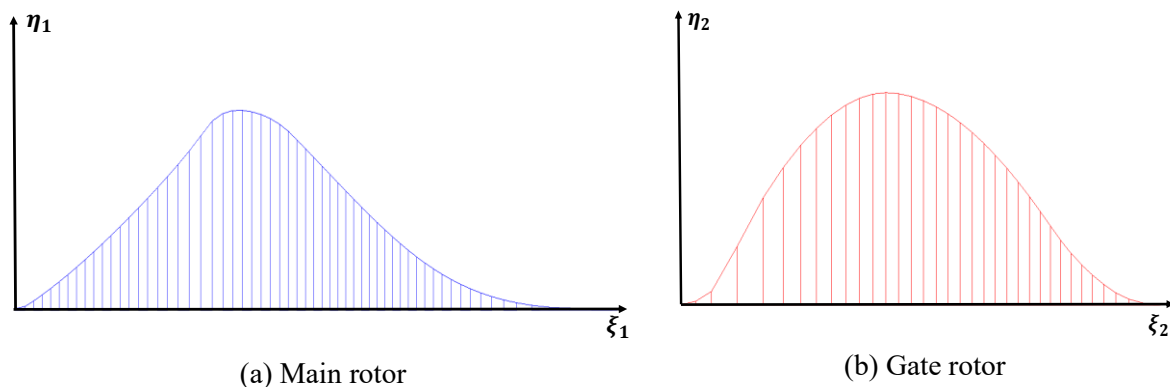


Figure 6-15. Computational coordinate systems

Next procedure is to make the inverse transformation from the computational domain to the physical domain using the new arc-length. At the same time, the coordinates need to be transformed back from the transvers plane to normal plane then the casing is transformed from circle to ellipse and the centre needs to be transformed back to the origin of the normal plane. The new distribution on the rack is based on the previous distribution on the casing by calculation the intersections of the rotor and casing connecting line with the rack. These crossed points are the new distributions on the rack curve as shown in Figure 6-16.

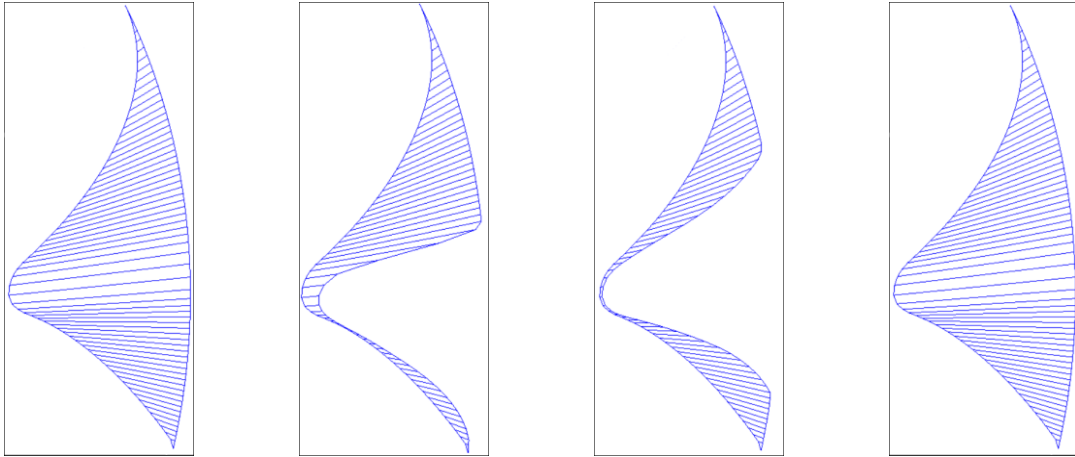


Figure 6-16 Transform the casing form circle to ellipse.

### 6.3.2 Transfinite interpolation

The interior nodes distribution was calculated through transfinite interpolation. Figure 6-17 shows the distribution of the interior nodes in the normal plane. The spacing and boundary orthogonality can be controlled through selection of control parameters. 3-D numerical mesh can be formed by connecting corresponding points in consecutive cross sections. The grid lines will go parallel to the helix line and thus orthogonal mesh will be produced. A series of 2D numerical meshes are generated in the planes normal to each of the rotor's helix line. The 2D cross sections is then combined to construct the full 3D fluid domain representing the main and gate fluid domain.

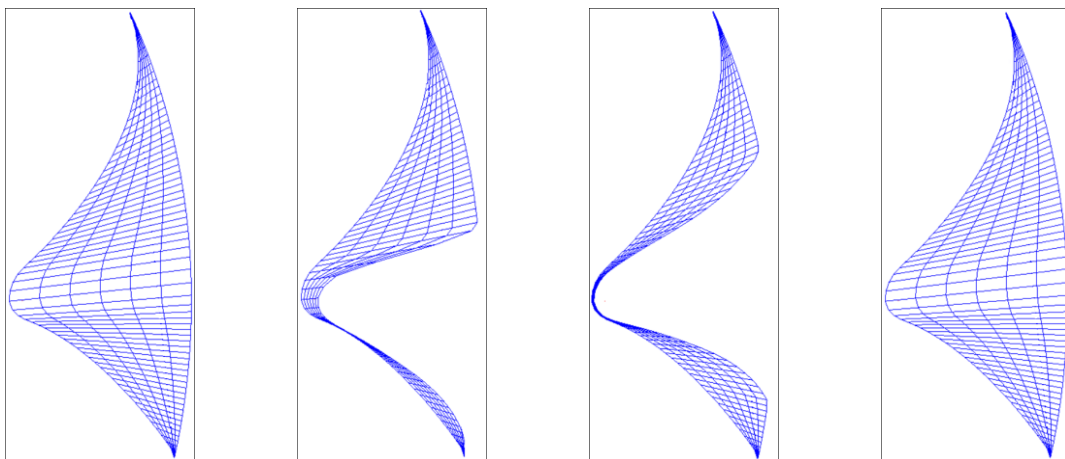


Figure 6-17 Numerical mesh generated by TFI



### 6.3.3 3D mesh generation

The screw machine rotor geometry is described by the boundary and internal points in a sequence of rotor cross sections. Numerical mesh is then formed by connecting these points in consecutive 2D cross sections. Based on the methodology developed in the last section, this procedure was integrated with the SCORG according to the flow chart shows in the Figure 6-18 which gives the main subroutines and the procedure to get the rotor to casing mesh, casing to rotor conformal mesh and casing to rotor non-conformal mesh. The parameters for mesh generation are firstly defined from subroutine names. Then original rotor profile and rack are generated through subroutine profile. Complete rotor file for all angles of rotation is generated by subroutine 'rot'. A normal rack is then calculated, and smoothing connection of casing and rack are defined by subroutine rack. Three different types of mesh can be generated depends on the connection at the interface of main and gate rotor which are rotor to casing mesh, casing to rotor conformal mesh and casing to rotor non-conformal mesh. This depends on the value of the parameter krot. Here, casing to rotor non-conformal mesh method is selected. In this method, point distribution in the computational and physical domains are calculated through subroutine distrBackground. At this stage, the initial mesh of the fluid domain is generated. Further grid adaptation and transfinite interpolation is implemented to smooth grid distribution and connection through subroutine TFImesh. After that, Final mesh files with mesh coordinates are exported. The main program has two main functions which are boundary regularization and transfinite interpolation which are also used in the normal grid generation method. Only rotor to casing mesh method is used in the Normal Grid Generation Method (NGGM).

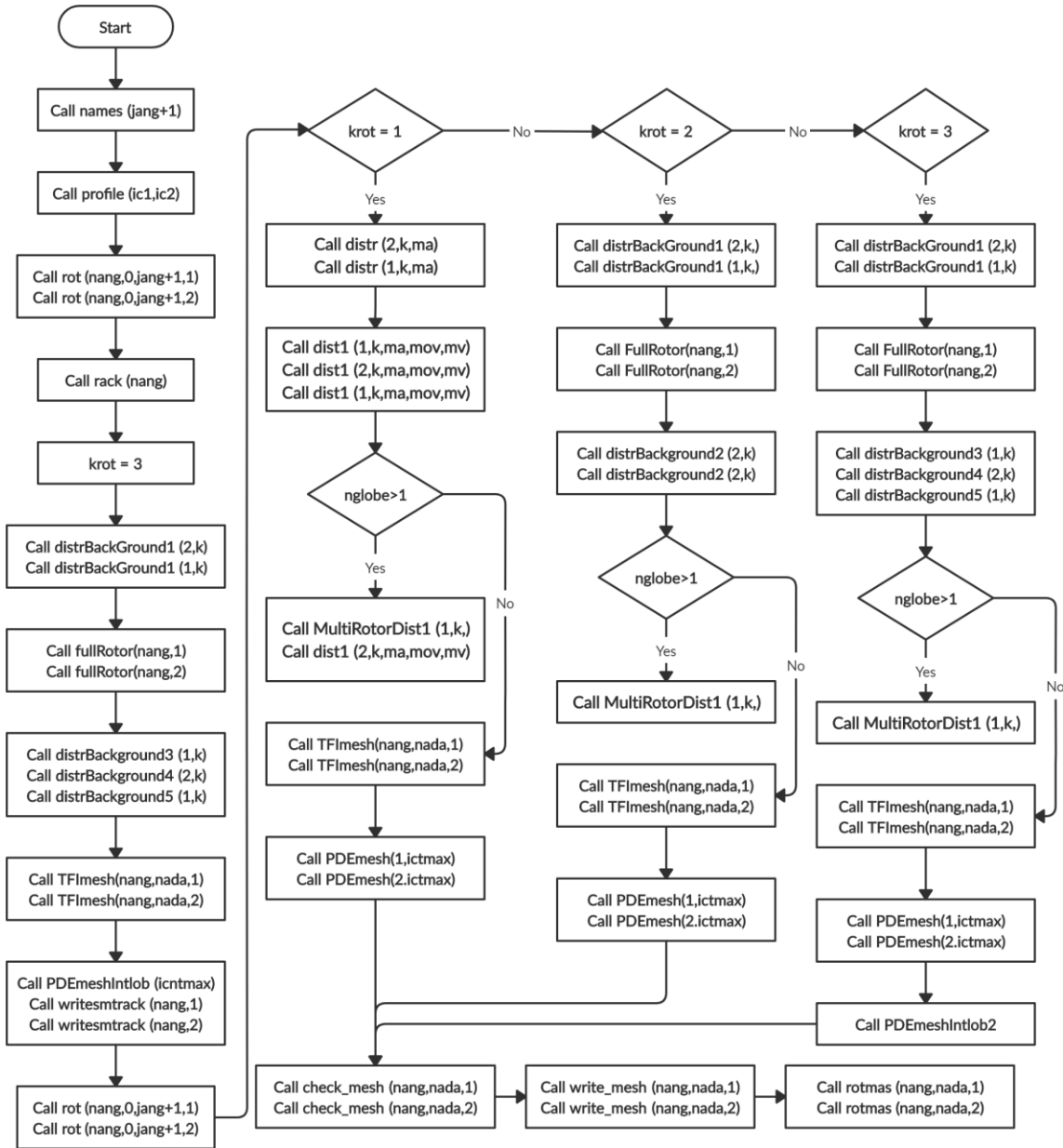


Figure 6-18 Flow chart of grid generation.

With implementing above procedures in SCROG, one interlobe 3D mesh of main and gate rotors are generated and displayed in ANSYS CFX. As shown in Figure 6-19, the numerical mesh in each cross section was aligned with helix direction.

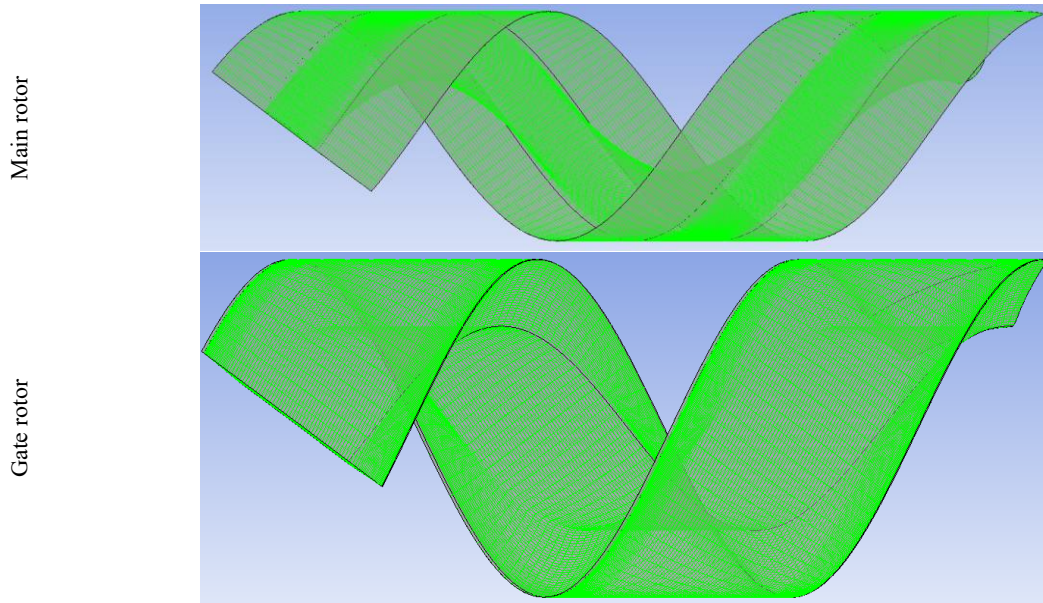


Figure 6-19 3D mesh of one interlobe.

The last step was to combine every interlobe and cut rotor end as illustrated by Figure 6-20. However, it was challenging to maintain total number of mesh same when mesh is moving and cutting rotor end. Therefore, this remains as an avenue for future examination.

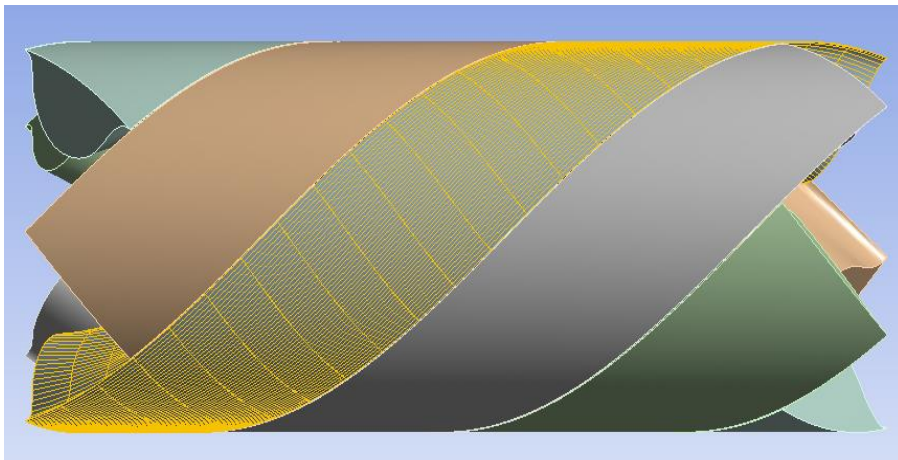


Figure 6-20 3D mesh of one rotor.

## 6.4 Summary

Algebraic grid generation is widely used for discretization of the working domain for screw machines. This chapter presents the new development of an algebraic grid generation algorithm which uses the normal rack to decompose the fluid domain into two sub-domains. Several subroutines were written to generate the 2D numerical mesh according following the same principles as integrates in SCORG. A series of 2D numerical meshes are generated in the planes

normal to each of the rotors' helix line. The 2D cross sections are then combined to construct the interlobe 3D fluid domain representing the main and gate fluid domain. However, time limitation and challenges to define a method to cut cells at rotor ends while retaining a constant number of cells in the mesh did not allow the process of generating 3D mesh to be completed which remains a task for future work.

# Chapter 7 Summary and Recommendation for Future Work

## 7.1 Conclusions of the research

The aim of the study presented in this thesis was to explore the suitability of the grid generation method for the calculation of twin-screw machines with large helix angles and to propose alternative methods which could improve accuracy and extend application. A summary of the research and recommendations for future work are proposed here.

- The cut-cell cartesian mesh generated in ANSYS Forte has been evaluated for numerical accuracy and conservation for an adiabatic compression and expansion process in a simple piston cylinder. Furthermore, the cut-cell cartesian mesh has been successfully implemented in the complex hook and claw pump. Automatic mesh generation (AMG) method enables the simulation setup much simpler and adaptive mesh refinement (AMR) method enables to capture the velocity, temperature, and pressure variation more clearly.
- Cut-cell cartesian mesh generation method for CFD analysis of twin screw compressors have been compared with a low helix angle Roots blower. Both methods are suitable for this application.
- The performance of the single lobed twin screw vacuum pump is obtained using the conformal casing-to-rotor body-fitted numerical mesh generated by SCORG. The helix angle of the rotors is 62 degree. The performance prediction is obtained in ANSYS Fluent for the transient 3D CFD calculations.
- The cut-cell cartesian has been implemented to large helix angle hook and claw vacuum pump. The built-in function of the mesh scale factor and gap scale factor have been studied to adjust the gap size. The downside of this method is the limitation to model small gap size and generation of a fine mesh suitable for simulation.
- New development of an algebraic grid generation algorithm which uses the normal rack to decompose the fluid domain into two sub-domains has been proposed. A series of 2D numerical meshes are generated in the planes normal to each of the rotors helix line.

The 2D cross sections is then combined to construct the full 3D fluid domain representing the main and gate fluid domain. This process makes the grids aligning with the main and leakage flow direction which can reduce numerical diffusion and the skewness of the grids in order to increase the stability of the CFD calculation. Unfortunately, it was not possible to complete the generation process since it was difficult to devise a method to cut these hexahedral cells in the axial plane and this development is recommended for future work.

## 7.2 Recommendations for future work

The stability and accuracy of prediction of screw machines with large helix angle are likely to be much improved through flow aligned mesh. Innovative grid generation method in normal planes perpendicular to the helix line in the pitch circle was proposed but have not been fully applied. The remained difficulty is to cut the mesh beyond the rotor end plane and maintain the constant number of cells which is required for retaining conservativeness of body fitted mesh. It is expected that further development will be conducted to generate 3D mesh from 2D normal planes for the CFD simulation of twin screw machines with large helix angle. This method also opens possibility for generating numerical mesh for single screw machines.

The cut-cell cartesian was explored to check its capability of mass conservation, calculation accuracy, mesh scale factor and leakage model (gap scale factor). It is also worthy to further investigate the cut-cell cartesian method by simulating the gap flow instead of utilising gap model for twin screw machines with large helix angle. In addition, in the case of leakage model in ANSYS Forte, machine learning could provide possibility to adapt leakage coefficient during the simulation.

## References

1. Brown, R.N. *Compressors Selection and Sizing*, Second Edition ed.; Gulf Publishing Company: 1997.
2. <https://www.howden.com/en-gb/products/compressors/oil-free-screw-compressor-package>. Howden Product Range, . Available online: <https://www.howden.com/en-gb/products/compressors/oil-free-screw-compressor-package> (accessed on
3. Schey, O.; Ellerbrock, H. Comparative Performance of a Powerplus Vane-Type Supercharger and an N.A.C.A. Roots-Type Supercharger. 1932.
4. Tran-The, V.; Do-Anh, T. A Tooth Profile Design for Roots Rotors of Vacuum Pump. In Proceedings of the Proceedings of the International Conference on Advances in Computational Mechanics 2017, Singapore, 2018//, 2018; pp. 1003-1016.
5. Sun, S.-K.; Jia, X.-H.; Xing, L.-F.; Peng, X.-Y. Numerical study and experimental validation of a Roots blower with backflow design. *Engineering Applications of Computational Fluid Mechanics* **2018**, *12*, 282-292, doi:10.1080/19942060.2017.1419148.
6. Cai, Y.; Yao, L. Comparison Analysis and Verification on Spur and Helical Three-lobe Rotors with Novel Tooth Profile in Roots Blower. *DEStech Transactions on Engineering and Technology Research* **2016**.
7. Wang, P.Y.; Fong, Z.H.; Fang, H.S. Design constraints of five-arc Roots vacuum pumps. *Proceedings of the Institution of Mechanical Engineers, Part C: Journal of Mechanical Engineering Science* **2002**, *216*, 225-234, doi:10.1243/0954406021525151.
8. Xing, L.; Feng, J.; He, Z.; Peng, X. Analysis and development of a roots-type air compressor with fixed internal compression for fuel cell system. *Proceedings of the Institution of Mechanical Engineers, Part A: Journal of Power and Energy* **2021**, 095765092110300, doi:10.1177/09576509211030031.
9. Theofanidis, K.; Lu, Y.; Kovacevic, A. CFD analysis on the effect of discharge port geometry of the hook and claw vacuum pumps. *IOP Conference Series: Materials Science and Engineering* **2021**, *1180*, 012063, doi:10.1088/1757-899x/1180/1/012063.
10. Stosic, N.; Smith, I.K.; Kovacevic, A.; Mujic, E. Development of Water Lubricated Compressor-Expander for Fuel Cell Application. In Proceedings of the Volume 5: Energy Systems Analysis, Thermodynamics and Sustainability; NanoEngineering for Energy; Engineering to Address Climate Change, Parts A and B, 2010; pp. 875-881.
11. Tu, J.; Yeoh, G.-H.; Liu, C. *Computational Fluid Dynamics A Practical Approach*, Third Edition ed.; Elsevier: 2018.
12. Peric, M. A finite volume method for the prediction of three-dimensional fluid flow in complex ducts. Imperial college, London, August 1985.
13. Kovačević, A. Three-Dimensional Numerical Analysis for Flow Prediction in Positive Displacement Screw Machines. City University London, 2002.
14. OpenFOAM. Available online: <https://www.openfoam.com/> (accessed on 2022).
15. ANSYS. Available online: <https://www.ansys.com/> (accessed on 2022).

16. SIEMENS. Available online: <https://www.plm.automation.siemens.com> (accessed on 2022).
17. SIEMERICS. <https://www.simerics.com/pumplinx/>. Available online: (accessed on 2022).
18. CONVERGECFD. Available online: <https://convergecf.com/> (accessed on 2022).
19. COMSOL. Available online: <https://www.comsol.com/> (accessed on 2022).
20. Owen, S.J. A survey of unstructured mesh generation technology. *IMR* **1998**, *239*, 267.
21. Rane, S.R. Grid Generation and CFD Analysis of Variable Geometry Screw Machines. PhD Thesis, City University London, 2015.
22. Sadrehaghghi, I. *Mesh Generation in CFD*; 2020.
23. Bianchi, G.; Rane, S.; Kovacevic, A.; Cipollone, R. Deforming grid generation for numerical simulations of fluid dynamics in sliding vane rotary machines. *Advances in Engineering Software* **2017**, *112*, 180-191, doi:10.1016/j.advengsoft.2017.05.010.
24. Li, J.; Jia, X.; Wu, Z.; Peng, X. The cavity profile of a diaphragm compressor for a hydrogen refueling station. *International Journal of Hydrogen Energy* **2014**, *39*, 3926-3935, doi:10.1016/j.ijhydene.2013.12.152.
25. Zhang, Q.; Feng, J.; Zhang, Q.; Peng, X. Performance prediction and evaluation of the scroll-type hydrogen pump for FCVs based on CFD–Taguchi method. *International Journal of Hydrogen Energy* **2019**, *44*, 15333-15343, doi:10.1016/j.ijhydene.2019.04.019.
26. Feng, J.; Xing, L.; Wang, B.; Wei, H.; Xing, Z. Effects of Working Fluids on the Performance of a Roots Pump for Hydrogen Recirculation in a PEM Fuel Cell System. *Applied Sciences* **2020**, *10*, 8069, doi:10.3390/app10228069.
27. Xing, L.; Feng, J.; Chen, W.; Xing, Z.; Peng, X. Development and Testing of a Roots Pump for Hydrogen Recirculation in Fuel Cell System. *Applied Sciences* **2020**, *10*, 8091, doi:10.3390/app10228091.
28. He, Y.; Xing, L.; Zhang, Y.; Zhang, J.; Cao, F.; Xing, Z. Development and experimental investigation of an oil-free twin-screw air compressor for fuel cell systems. *Applied Thermal Engineering* **2018**, *145*, 755-762, doi:10.1016/j.applthermaleng.2018.09.064.
29. Gu, P.; Xing, L.; Wang, Y.; Feng, J.; Peng, X. A multi-objective parametric study of the claw hydrogen pump for fuel cell vehicles using taguchi method and ANN. *International Journal of Hydrogen Energy* **2020**, doi:10.1016/j.ijhydene.2020.11.186.
30. Hsieh, C.-F.; Hwang, Y.-W.; Fong, Z.-H. Study on the tooth profile for the screw claw-type pump. *Mechanism and Machine Theory* **2008**, *43*, 812-828, doi:10.1016/j.mechmachtheory.2007.06.011.
31. Lu, Y.; Guo, B.; Geng, M.F. Study on Design of Rotor Profile for the Twin Screw Vacuum Pump with Single Thread Tooth. In Proceedings of the IOP Conference Series: Materials Science and Engineering, 2015.
32. Stosic, N.; Rane, S.; Kovacevic, A.; Smith, I.K. Screw Rotor Profiles of Variable Lead Vacuum and Multiphase Machines and Their Calculation Models. In Proceedings of the Volume 6A: Energy, 2016.
33. YuRen, W. Novel design methods of rotor and cutter profiles for the twin screw compressor. PhD Thesis, National Chung-Cheng University, Taiwan, 2007.
34. Zaytsev, D.; Infante Ferreira, C.A. Profile generation method for twin screw compressor rotors based on the meshing line. *International Journal of Refrigeration* **2005**, *28*, 744-755, doi:10.1016/j.ijrefrig.2004.12.006.



35. N. Stosic; Hanjalic, K. Development and optimization of screw machines with a simulation model-Part2 thermodynamic performance simulation and design optimization. *Journal of Fluids Engineering* **1997**, 119.
36. Stos'ic', N.; Hanjalic', K. Development and Optimization of Screw Machines With a Simulation Model—Part I: Profile Generation. *Journal of Fluids Engineering* **1997**, 119, 659-663, doi:10.1115/1.2819295.
37. Bianchi, G.; Rane, S.; Kovacevic, A.; Cipollone, R.; Murgia, S.; Contaldi, G. Numerical CFD simulations on a small-scale ORC expander using a customized grid generation methodology. *Energy Procedia* **2017**, 129, 843-850, doi:10.1016/j.egypro.2017.09.199.
38. Kovacevic, A.; Rane, S.; Stosic, N.; Jiang, Y.; Lowry, S.; Furmanczyk, M. Influence of approaches in CFD solvers on performance prediction in screw compressors. **2014**.
39. Kovacevic, A.; Stosic, N.; Mujic, E.; Smith, I.K. CFD Integrated Design of Screw Compressors. *Engineering Applications of Computational Fluid Mechanics* **2014**, 1, 96-108, doi:10.1080/19942060.2007.11015185.
40. Rane, S.; Kovačević, A. Application of numerical grid generation for improved CFD analysis of multiphase screw machines. *IOP Conference Series: Materials Science and Engineering* **2017**, 232, doi:10.1088/1757-899x/232/1/012017.
41. Arjeneh, M.; Kovacevic, A.; Rane, S.; Manolis, M.; Stosic, N. Numerical and Experimental Investigation of Pressure Losses at Suction of a Twin Screw Compressor. *IOP Conference Series: Materials Science and Engineering* **2015**, 90, doi:10.1088/1757-899x/90/1/012006.
42. Wu, H.; Huang, H.; Zhang, B.; Xiong, B.; Lin, K. CFD Simulation and Experimental Study of Working Process of Screw Refrigeration Compressor with R134a. *Energies* **2019**, 12, 2054, doi:10.3390/en12112054.
43. Zhang, W.; Jiang, Q.; Bois, G.; Li, H.; Liu, X.; Yuan, S.; Heng, Y. Experimental and Numerical Analysis on Flow Characteristics in a Double Helix Screw Pump. *Energies* **2019**, 12, doi:10.3390/en12183420.
44. Nguyen, T.L.; Wu, Y.R. A Novel Rotor Profile Generation Method for Claw-Type Vacuum Pumps Based on Sealing Line. *Applied Mechanics and Materials* **2019**, 894, 34-40, doi:10.4028/[www.scientific.net/AMM.894.34](http://www.scientific.net/AMM.894.34).
45. Wang, J.; Song, Y.; Jiang, X.; Cui, D.; Qu, Y. An analytical model of claw rotor profiles and working process model with the mixing process for claw vacuum pumps. *Vacuum* **2015**, 114, 66-77, doi:10.1016/j.vacuum.2014.12.029.
46. Stosic, N.; Smith, I.K.; Kovacevic, A. *Screw Compressor Geometry\_Mathematical Modeling and Performance Calculation*; Springer 2005.
47. Peng, X.; Xing, Z.; Li, L.; Shu, P. Thermodynamic analysis of the rotary tooth compressor. *Proceedings of the Institution of Mechanical Engineers, Part A: Journal of Power and Energy* **2005**, 216, 321-327, doi:10.1243/09576500260251165.
48. Demirdžić, I.; Perić, M. Finite volume method for prediction of fluid flow in arbitrarily shaped domains with moving boundaries. *International Journal for Numerical Methods in Fluids* **1990**, 10, 771-790, doi:<https://doi.org/10.1002/flid.1650100705>.
49. Hosain, M.L.; Fdhila, R.B. Literature Review of Accelerated CFD Simulation Methods towards Online Application. *Energy Procedia* **2015**, 75, 3307-3314, doi:10.1016/j.egypro.2015.07.714.
50. Thompson, J.F.; Bharat. Hand book of grid genertion.

51. Frymier Jr, P.D.; Hassan, H.; Salas, M. Navier-Stokes calculations using Cartesian grids. I-Laminar flows. *AIAA journal* **1988**, *26*, 1181-1188.
52. Johnson, M.W. A novel Cartesian CFD cut cell approach. *Computers & Fluids* **2013**, *79*, 105-119, doi:10.1016/j.compfluid.2013.03.011.
53. Pracht, W.E. Calculating three-dimensional fluid flows at all speeds with an Eulerian-Lagrangian computing mesh. *Journal of Computational Physics* **1975**, *17*, 132-159, doi:[https://doi.org/10.1016/0021-9991\(75\)90033-9](https://doi.org/10.1016/0021-9991(75)90033-9).
54. Hirt, C.W.; Amsden, A.A.; Cook, J.L. An arbitrary Lagrangian-Eulerian computing method for all flow speeds. *Journal of Computational Physics* **1974**, *14*, 227-253, doi:[https://doi.org/10.1016/0021-9991\(74\)90051-5](https://doi.org/10.1016/0021-9991(74)90051-5).
55. Stosic, N.; Smith, I.K.; Kovacevic, A. Optimisation of screw compressors. *Applied Thermal Engineering* **2003**, *23*, 1177-1195, doi:10.1016/s1359-4311(03)00059-0.
56. Kovacevic, A. Boundary adaptation in grid generation for CFD analysis of screw compressors. *International Journal for Numerical Methods in Engineering* **2005**, *64*, 401-426, doi:10.1002/nme.1376.
57. Kovacevic, A.; Stosic, N.; Smith, I.; Mujic, E. Clearance management in multifunctional screw machines. *IMEchE, Fluid Machinery Group - International Conference on Compressors and their systems 2005* **2005**, 437-446.
58. Kovacevic, A.; Stosic, N.; Smith, I. *Screw Compressors-Three dimensional computational fluid dynamics and solid fluid interaction*; Springer-Verlag: New York, 2006.
59. Jasak, H. Error analysis and estimation for the finite volume method with applications to fluid flows. PhD Thesis, Imperial College London, United Kingdom, 1996.
60. Rane, S.; Kovacevic, A. Algebraic generation of single domain computational grid for twin screw machines. Part I. Implementation. *Advances in Engineering Software* **2017**, *107*, 38-50, doi:10.1016/j.advengsoft.2017.02.003.
61. Voode, J.V.; Vierendeels, J.; Dick, E. A grid generator for flow calculations in rotary volumetric compressors. In Proceedings of the European Congress on Computational Methods in Applied Sciences and Engineering, Finland 2004.
62. Voorde, J.V.; Vierendeels, J. A grid manipulation algorithm for ALE calculations in screw compressors. In Proceedings of the 17th AIAA Computational Fluid Dynamics Conference, Toronto, Ontario Canada, 2005.
63. Lu, Y.; Kovacevic, A.; Read, M. Numerical study on screw machines with large helix angles. In Proceedings of the IOP Conference Series: Materials Science and Engineering, Dortmund, 2018.
64. Lu, Y.; Kovacevic, A.; Read, M.; Basha, N. Numerical Study of Customised Mesh for Twin Screw Vacuum Pumps. *Designs* **2019**, *3*, doi:10.3390/designs3040052.
65. Rinder, L. Screw rotor profile and method for generating. 1987.
66. Litvin, F.L.; Fuentes, A. *Gear Geometry and Applied Theory*, 2 ed.; New York: Cambridge university press, 2004.
67. Stosic, N. On gearing of helical screw compressor rotors. *Proceedings of the Institution of Mechanical Engineers, Part A: Journal of Power and Energy* **1998**, *212*, 587-594.
68. Stosic, N.; Hanjalic, K. General Method for Screw Compressor Profile Generation. In Proceedings of the International Compressor Engineering Conference at Purdue, West Lafayette, Indiana, USA, 1996.

69. Wu, Y.; Fong, Z. Optimization design of an explicitly defined rack for the generation of rotors for twin-screw compressors. *Mechanism and Machine Theory* **2009**, *44*, 66-82, doi:10.1016/j.mechmachtheory.2008.02.013.
70. Rane, S.; Kovacevic, A.; Stosic, N.; Kethidi, M. Grid deformation strategies for CFD analysis of screw compressors. *International Journal of Refrigeration* **2013**, *36*, 1883-1893, doi:10.1016/j.ijrefrig.2013.04.008.
71. Rane, S.; Kovačević, A.; Stošić, N. Analytical Grid Generation for accurate representation of clearances in CFD for Screw Machines. *IOP Conference Series: Materials Science and Engineering* **2015**, *90*, doi:10.1088/1757-899x/90/1/012008.
72. Rane, S.; Kovacevic, A.; Stosic, N.; Kethidi, M. CFD grid generation and analysis of screw compressor with variable geometry rotors. In Proceedings of the 8th International Conference on Compressors and their Systems, 2013; pp. 601-612.
73. Kovacevic, A.; Rane, S. Algebraic generation of single domain computational grid for twin screw machines Part II – Validation. *Advances in Engineering Software* **2017**, *109*, 31-43, doi:10.1016/j.advengsoft.2017.03.001.
74. Kennedy, S.; Wilson, M.; Rane, S. Combined Numerical and Analytical Analysis of an Oil-free Twin Screw Compressor. *IOP Conference Series: Materials Science and Engineering* **2017**, *232*, doi:10.1088/1757-899x/232/1/012080.
75. ANSYS *ANSYS CFX*, v17.2; ANSYS Inc.: 2017.
76. Vierendeels, J. Introduction to CFD analysis in positive displacement machines. In Proceedings of the 10th international conference on compressors and their systems, London, 2017.
77. Casari, N.; Fadiga, E.; Pinelli, M.; Suman, A.; Ziviani, D. CFD Simulations of Single- and Twin-Screw Machines with OpenFOAM. *Designs* **2020**, *4*, 2, doi:10.3390/designs4010002.
78. Hsieh, C.-F.; Zhou, Q.-J. Fluid analysis of cylindrical and screw type Roots vacuum pumps. *Vacuum* **2015**, *121*, 274-282, doi:10.1016/j.vacuum.2015.04.037.
79. Sun, S.H.; Kovacevic, A.; Bruecker, C.; Leto, A.; Singh, G.; Ghavami, M. Numerical and Experimental Analysis of Transient Flow in Roots Blower. *IOP Conference Series: Materials Science and Engineering* **2018**, *425*, doi:10.1088/1757-899x/425/1/012024.
80. Kovacevic, A.; Rane, S.; Stosic, N. Modelling of Multiphase Twin Screw Machines. In *New Technologies, Development and Application*; Lecture Notes in Networks and Systems; 2019; pp. 18-32.
81. Rane, S.; Kovacevic, A.; Stosic, N.; Stupple, G. Analysis of water evaporation in twin screw compressors using eulerian multiphase approach in CFD. In Proceedings of the 24th International Compressor Engineering Conference at Purdue, 2018.
82. Gu, P.; Xing, L.; Wang, Y.; Feng, J.; Peng, X. Transient flow field and performance analysis of a claw pump for FCVs. *International Journal of Hydrogen Energy* **2020**, doi:10.1016/j.ijhydene.2020.09.154.
83. Dong, K.; Liu, G.; Yang, Q.; Zhao, Y.; Li, L.; Gao, Z. Flow field analysis and performance study of claw hydrogen circulating pump in fuel cell system. *International Journal of Hydrogen Energy* **2021**, doi:10.1016/j.ijhydene.2021.08.014.
84. Rowinski, D.H.; Li, Y.; Bansal, K. Investigations of Automatic Meshing in Modeling a Dry Twin Screw Compressor. In Proceedings of the 24th International Compressor Engineering Conference, Purdue, 2018.

85. Rowinski, D.; Nikolov, A.; Brümmer, A. Modeling a dry running twin-screw expander using a coupled thermal-fluid solver with automatic mesh generation. *IOP Conference Series: Materials Science and Engineering* **2018**, *425*, doi:10.1088/1757-899x/425/1/012019.
86. Yan, D.; Kovacevic, A.; Tang, Q.; Rane, S. Numerical investigation of cavitation in twin-screw pumps. *Proceedings of the Institution of Mechanical Engineers, Part C: Journal of Mechanical Engineering Science* **2017**, doi:10.1177/0954406217740927.
87. Yan, D.; Kovacevic, A.; Tang, Q.; Rane, S.; Zhang, W. Numerical modelling of twin-screw pumps based on computational fluid dynamics. *Proceedings of the Institution of Mechanical Engineers, Part C: Journal of Mechanical Engineering Science* **2016**, *231*, 4617-4634, doi:10.1177/0954406216670684.
88. Kovacevic, A.; Stosic, N.; Smith, I. Grid aspects of screw compressor flow calculations. In Proceedings of the ASME Congress, Orlando, Florida, 05-10 November 2000, 2000.
89. Andres, R.; Hesse, J.; Babic, H. CFD Simulation of a Twin Screw Expander including Leakage Flows. In Proceedings of the 23rd International Compressor Engineering Conference at Purdue, West Lafayette, Indiana, USA, 2016.
90. Spille-Kohoff, A.; Hesse, J.; Andres, R. Grid generation and CFD simulation for positive displacement machines. In Proceedings of the NAFEMS World Congress Stockholm, Sweden, 2017.
91. Tuo, J.; Guo, B.; Wu, R.; Zhang, Y.; Chen, X. Study on the performance prediction of dry twin screw vacuum pump. *IOP Conference Series: Materials Science and Engineering* **2018**, *425*, doi:10.1088/1757-899x/425/1/012029.
92. Jünemann, T.; Brümmer, A. Optimisation of screw spindle vacuum pumps with variable rotor pitch regarding load-lock operation. *IOP Conference Series: Materials Science and Engineering* **2018**, *425*, doi:10.1088/1757-899x/425/1/012028.
93. Huck, C.; Bruemmer, A. Thermodynamical operation behaviour of screw vacuum pumps with Cycloid- and Quimby-toothed rotors. In Proceedings of the Dortmund conference, 2014.
94. Li, D.; He, Z.; Wu, W.; Xing, Z. Study on the Quimby-tooth rotor profile for dry screw vacuum pumps. *Proceedings of the Institution of Mechanical Engineers, Part E: Journal of Process Mechanical Engineering* **2022**, *236*, 1947-1957, doi:10.1177/09544089221081334.
95. CFX-Berlin *TwinMesh*, 2014.
96. Xing, Z.; Peng, X.; Shu, P. Development and application of a software package for the design of twin screw compressors. In Proceedings of the International Compressor Engineering Conference at Purdue, West Lafayette, Indiana, USA, 2000.
97. Ferziger, J.H.; Peric, M. *Computational Methods For Fluid Dynamics*; Springer: 2002.
98. Trulio, J.G.; Trigger, K.R. *NUMERICAL SOLUTION OF THE ONE-DIMENSIONAL LAGRANGIAN HYDRODYNAMIC EQUATIONS*; United States, 1961; p. Medium: ED; Size: Pages: 95.
99. Demirdžić, I.; Issa, R.I.; Lilek, Ž. Solution Method for Viscous Flows at all Speeds in Complex Domains. In Proceedings of the Conference on Numerical Methods in Fluid Mechanics, Wiesbaden, 1990; pp. 89-98.
100. ANSYS. *Fluent Theory Manual*; 2021 R1.

101. Holmes, B. CFD Analysis and ANSYS solutions for Positive Displacement Machines. In Proceedings of the 5th Short Course & Forum on Computational Fluid Dynamics in Rotary Positive Displacement Machines, London, September 2021.
102. Liu, K.; Haworth, D.C. Large-Eddy Simulation for an Axisymmetric Piston-Cylinder Assembly With and Without Swirl. *Flow, Turbulence and Combustion* **2010**, *85*, 279-307, doi:10.1007/s10494-010-9292-1.
103. P. K. Senecal, K.J.R., E. Pomraning, T. Yang and M. Z. Dai. A New Parallel Cut-Cell Cartesian CFD Code for Rapid Grid Generation Applied to In-Cylinder Diesel Engine Simulations. In Proceedings of the SAE International by Univ of California Berkeley, 2007.
104. ANSYS. Forte Tutorials. **2021 R1**.
105. PDMAnalysis. SCORG Help Manual. Available online: <http://pdmanalysis.co.uk/> (accessed on 2022).
106. Zhao, Y.; Liu, Y.; Liu, G.; Yang, Q.; Li, L.; Gao, Z. Air and hydrogen supply systems and equipment for PEM fuel cells: a review. *International Journal of Green Energy* **2021**, 1-18, doi:10.1080/15435075.2021.1946812.
107. Zhang, Q.; Feng, J.; Wen, J.; Peng, X. 3D transient CFD modelling of a scroll-type hydrogen pump used in FCVs. *International Journal of Hydrogen Energy* **2018**, *43*, 19231-19241, doi:10.1016/j.ijhydene.2018.08.158.
108. Basha, N.; Kovacevic, A.; Rane, S. User defined nodal displacement of numerical mesh for analysis of screw machines in FLUENT. *IOP Conference Series: Materials Science and Engineering* **2019**, *604*, doi:10.1088/1757-899x/604/1/012012.
109. Wu, Y.; Fong, Z. Rotor Profile Design for the Twin-Screw Compressor Based on the Normal-Rack Generation Method. *Journal of Mechanical Design* **2008**, *130*, 8, doi:10.1115/1.2839003.
110. Thompson, J.F.; Soni, B.K.; Weatherill, N.P. *Handbook of Grid Generation*, First Edition ed.; CRC Press: Boca Raton, 1999.

# Appendix

## Appendix A. Profile and rack generation

There are three different mathematical rotor profiles generation methods, namely, generation from given main rotor profile curve; generation from a meshing line; generation from a specifying rack on the transverse or normal plane.

Generally speaking, the coordinate systems do not coincide for profile generation. For twin screw compressors, the male rotor and female rotor has parallel and intersecting axes and for the compressor rotor and its formed hobbing tool are equivalent to a pair of meshing crossed helical gears with nonparallel and nonintersecting axes. In these two cases, the coordinate transformation can be based on the application of homogeneous coordinates and 4X4 matrices that describe separately rotation about a fixed axis and displacement of one coordinate system with respect to the other. The matrices can be used to conduct coordinate transformation of the two fixed coordinate systems and the fixed coordinate and rotational coordinate.

### A.1 Coordinate transformation

The coordinate system of non-parallel and non-intersecting axes is illustrated by Figure A.1. The shortest distance between the two axes is  $C$  and the angle between them is  $\Sigma$ . Consider coordinate system  $S_1(X_1, Y_1, Z_1)$  and  $S_2(X_2, Y_2, Z_2)$  that are rigidly connected to male rotor and female rotor respectively. But the coordinate system  $(X_{01}, Y_{01})$  rotates around  $Z_1$  with the male rotor and the coordinate system  $(X_{02}, Y_{02})$  rotates around  $Z_2$  with the female rotor.

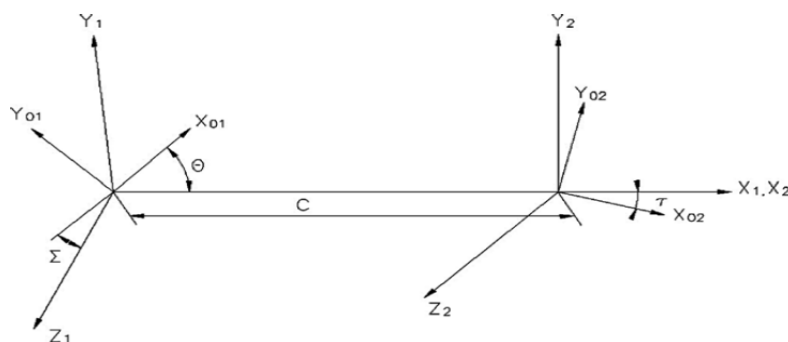


Figure A.1 Coordinate systems with non-parallel and non-intersecting shafts

With the coordinate systems showed in A.1, the coordinate transformation in transition from  $S_1$  to  $S_2$  is based on the matrix equation:

$$\mathbf{r}_2 = \mathbf{M}_{21}\mathbf{r}_1 = \mathbf{M}_{2p}\mathbf{M}_{pf}\mathbf{M}_{f1}\mathbf{r}_1 \quad \text{A.1}$$

Where  $\mathbf{r}_1$  and  $\mathbf{r}_2$  are the generating and generated surface respectively.  $\mathbf{M}_{2p}$  and  $\mathbf{M}_{f1}$  are anti-clockwise rotational matrices and clockwise rotational matrices around the Z axis.  $\mathbf{M}_{pf}$  is a translational matrix. Here these matrices are as defined in equation A. 2

$$\mathbf{r}_1 = \begin{bmatrix} x_1 \\ y_1 \\ z_1 \\ 1 \end{bmatrix}, \mathbf{r}_2 = \begin{bmatrix} x_2 \\ y_2 \\ z_2 \\ 1 \end{bmatrix}, \mathbf{M}_{pf} = \begin{bmatrix} 1 & 0 & 0 & -C \\ 0 & \cos(\Sigma) & -\sin(\Sigma) & 0 \\ 0 & \sin(\Sigma) & \cos(\Sigma) & 0 \\ 0 & 0 & 0 & 1 \end{bmatrix}$$

$$\mathbf{M}_{2p} = \begin{bmatrix} \cos(\tau) & -\sin(\tau) & 0 & 0 \\ \sin(\tau) & \cos(\tau) & 0 & 0 \\ 0 & 0 & 1 & 0 \\ 0 & 0 & 0 & 1 \end{bmatrix}, \mathbf{M}_{f1} = \begin{bmatrix} \cos(\theta) & -\sin(\theta) & 0 & 0 \\ \sin(\theta) & \cos(\theta) & 0 & 0 \\ 0 & 0 & 1 & 0 \\ 0 & 0 & 0 & 1 \end{bmatrix} \quad \text{A. 2}$$

## A.2 Rack generation

The rack is the curve representing a rotor with infinite radius. Namely, 3D rotors and rack are unique surfaces. They do not change when the cutting plane changes. Only if they are cut with the particular plane, they can potentially form either transverse or normal 2D projections of rotors and rack. As shown in Figure A.2, the main rotor profile and gate rotor profiles are both generated from the rack and the main rotor with three lobes is able to mesh with the gate rotors with five lobes or seven lobes. The rack can be defined in the transverse plane system which is called transverse rack and in the normal plane system which is called normal rack. Yu-ren[109] proposed normal-rack generation method (NRGM) to design all the tangent continuous profile segments explicitly in the normal section to generate the conjugated rotors which can be utilised for various lobe combinations, centre distances even the different helix angles.

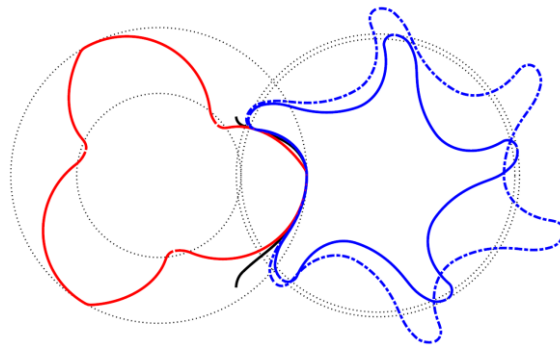


Figure A.2 Rotor profiles of 3/5 and 3/7 with the same rack profile

As illustrated by Figure A.3, the transverse plane is marked with T-T and the normal plane is marked with N-N. The transverse plane is perpendicular to the rotor shaft. Usually, the rotor profiles are generated in the transverse plane. As the definition of the normal plane, it is perpendicular to the rotor surface in the pitch circle points and changes along the helical line. The angle between the transverse plane and normal plane is helix angle  $90 - \beta$ . For grid generation, if the transverse plane is used for the grid generation, then the transverse plane is unique for both rotors and rack. However, if the normal plane is used for grid generation, in that case each rotor will have a series of its own normal planes and the rack will have own normal plane.

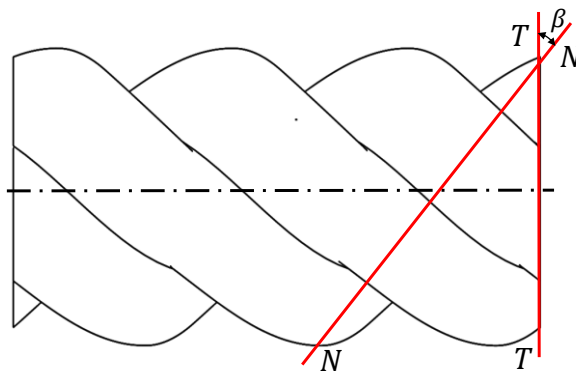


Figure A.3 Transverse plane and normal plane

The transverse rack profile can be obtained. The rack surface between two rotors can be generated by stretching the transverse rack which is shown in Figure A.4.



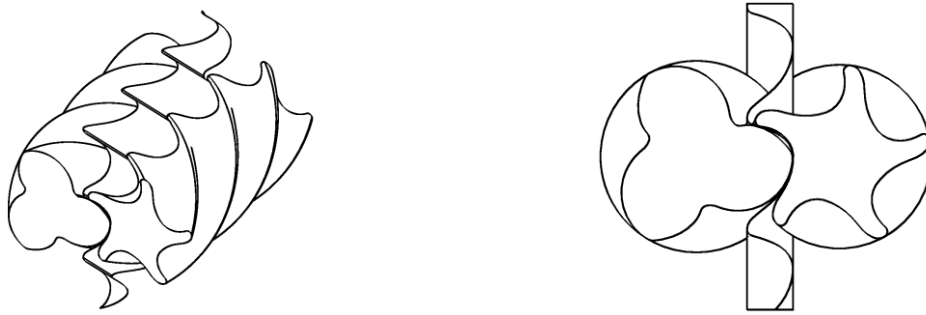


Figure A.4 Rack surface.

### A.3 Derivation of meshing equation

In the meshing condition, the rotation angle of the main rotor for which the rotors and rack are in contact at meshing points can be solved either numerically or directly permits the introduction of a variety of primary arc curves and effectively constitutes a general procedure. The procedure of deducing the general meshing condition starts with a generating surface  $r_1(t, \theta)$ . The generated surface  $r_2(t, \theta, \tau)$  can be obtained with the meshing condition. Where  $t$  is a profile parameter, while  $\theta$  and  $\tau$  are motion parameters. According to the transformational matrices, the rack and gate rotor profile can be developed from the main rotor profile and also the main and gate rotor profiles can be generated from rack with meshing condition.

#### A.3.1 Meshing condition of crossed helical rotors

The envelope method is a basis for the generation of a screw compressor rotor profile and the hobbing tool for rotor manufacture. The method states that two surfaces are in mesh if each generates or envelops the other under a specified relative motion. The procedure of derivation of meshing equation starts with a generating surface  $r_1(t, \theta)$  and generated surface  $r_2(t, \theta, \tau)$

$$\begin{aligned}
\mathbf{r}_1 &= \begin{bmatrix} x_1 \\ y_1 \\ z_1 \\ 1 \end{bmatrix} = \begin{bmatrix} x_{01} \cos(\theta) - y_{01} \sin(\theta) \\ x_{01} \sin(\theta) + y_{01} \cos(\theta) \\ p_1 \theta \\ 1 \end{bmatrix} \\
\mathbf{r}_2 = \mathbf{M}_{pf} \mathbf{r}_1 &= \begin{bmatrix} 1 & 0 & 0 & -C \\ 0 & \cos \Sigma & -\sin \Sigma & 0 \\ 0 & \sin \Sigma & \cos \Sigma & 0 \\ 0 & 0 & 0 & 1 \end{bmatrix} \begin{bmatrix} x_1 \\ y_1 \\ z_1 \\ 1 \end{bmatrix} \\
&= \begin{bmatrix} x_1 - C \\ y_1 \cos \Sigma - z_1 \sin \Sigma \\ y_1 \sin \Sigma + z_1 \cos \Sigma \\ 1 \end{bmatrix}
\end{aligned} \tag{A.3}$$

According to the envelop method, the meshing equation which determines meshing between the surfaces  $\mathbf{r}_1$  and  $\mathbf{r}_2$  can be written as equation A.4:

$$f(t, \theta, \tau) = \frac{\partial \mathbf{r}_1}{\partial \tau} \cdot \left( \frac{\partial \mathbf{r}_1}{\partial t} \times \frac{\partial \mathbf{r}_1}{\partial \theta} \right) \tag{A.4}$$

Insertion of previous expressions into the meshing equation gives equation A.5:

$$\begin{aligned}
& [C - x_1 + (p_1 - p_2) \cot \Sigma (x_1 \frac{\partial x_1}{\partial t} + y_1 \frac{\partial y_1}{\partial t})] + p_1 [p_1 \theta \frac{\partial y_1}{\partial t} + (p_2 \\
& - C \cot \Sigma \frac{\partial x_1}{\partial t})] = 0
\end{aligned} \tag{A.5}$$

### A.3.2 Meshing of screw rotors

Screw machine rotors have parallel axes, so the required meshing condition can be obtained by setting  $\Sigma = 0$ . The meshing condition for a screw machine rotor simplified generate from equation A.5 is:

$$\frac{dy_{01}}{dx_{01}} (ky_{01} - \frac{C}{i} \sin \theta) + kx_{01} + \frac{C}{i} \cos \theta \tag{A.6}$$

Where  $i = Z_2/Z_1$  and  $k = 1 + 1/i$ .

Once getting the meshing angle, the meshing profile equations of the gate rotor in the transverse plane can be calculated according to equation A.1

$$\begin{aligned} x_{02} &= x_{01} \cos(k\theta) + y_{01} \sin(k\theta) - C \cos\left(\frac{\theta}{i}\right) \\ x_{02} &= -x_{01} \sin(k\theta) + y_{01} \cos(k\theta) + C \cos\left(\frac{\theta}{i}\right) \end{aligned} \quad \text{A.7}$$

Rack coordinates can be calculated from A.7 if the gear ratio  $i$  tends to infinity:

$$\begin{aligned} x_{02} &= x_{01} \cos(\theta) + y_{01} \sin(\theta) \\ x_{02} &= -x_{01} \sin(k\theta) + y_{01} \cos(k\theta) + r_{1w}\theta \end{aligned} \quad \text{A.8}$$

Conversely, if the generating profiles are given on the rack  $\mathbf{r}_{tr}(\theta)$ , the main rotor profile and gate rotor profile can be calculated respectively as equation A.9.

$$\begin{aligned} x_{01} &= x_{0r} \cos(\theta) - (y_{0r} - r_{1w}\theta) \sin(\theta) \\ x_{01} &= x_{0r} \sin(\theta) - (y_{0r} - r_{1w}\theta) \cos(\theta) \\ x_{02} &= x_{0r} \cos(\theta) - (y_{0r} - r_{2w}\theta) \sin(\theta) \\ x_{02} &= x_{0r} \sin(\theta) - (y_{0r} - r_{2w}\theta) \cos(\theta) \end{aligned} \quad \text{A.9}$$

The meshing condition is obtained from equation A.6:

$$\theta = [y_r - \frac{\partial x_{0r}}{\partial y_{0r}}(r_{jw} - x_{0r})]/r_{jw}, j = 1,2 \quad \text{A.10}$$

#### A.4 Calculation of meshing angle

As showed in equation A.10, the rack meshing condition  $\theta$  can be solved directly. This is the advantage of the rack generation procedure. But for equation A.5 and equation A.6, the numerical method should be used to calculate the meshing angle. A graphical presentation of

the meshing condition given in Figure A.5 confirms that the Willis gearing condition, which states that the normal of both the rotors and the rack at their contact point pass through the pitch point.

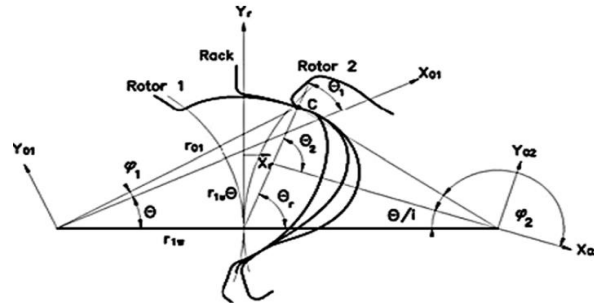


Figure A.5 Willis meshing condition

For the given rotor coordinates  $x_{01}$  and  $y_{01}$ ,  $\tan \theta_1 = -\frac{dy_{01}}{dx_{01}} \tan \theta_1 = -\frac{dy_{01}}{dx_{01}} \tan \theta_1 = -\frac{dy_{01}}{dx_{01}}$ .

Let  $\varphi$  be a profile angle at the contact point given as  $\tan \varphi_1 = \frac{y_{01}}{x_{01}}$ . Let  $\theta$  be the meshing condition. Then the relation between these three angles required for calculation of the meshing condition  $\theta$  is obtained as:

$$\frac{\sin(\theta_1 + \theta)}{r_{01}} = \frac{\sin(\theta_1 - \varphi)}{r_{1w}} \quad \text{A.11}$$

## Appendix B. Algebraic approach for Grid Generation of Twin Screw Rotors

### B.1 Coordinate transformation of the interlobe rotor space

To construct the hexahedral structured mesh, the physical domain needs to be transformed to computational domain. The coordinates of the physical domain are given in  $x\_y$  coordinate system while the computational coordinate is  $\xi\_eta$  as shown in Figure B.1. The main rotor sub-domain from tip to tip form an interlobe space which can be mapped from physical region  $X^n$  onto a computational domain  $\Xi^n$ . Inner boundary of the sub-domain is the rotor profile, and the outer boundary is formed by combining the casing circle with the rack curve. *Kovačević* has developed a unique two parameter unidirectional boundary adaptation procedure to be applied for screw rotor profiles that helps in achieving a regular distribution in the transformed space. These procedures have been briefly described below in two parts: Rotor boundary adaptation and Outer boundary regularisation and form key elements in the algebraic grid generation.

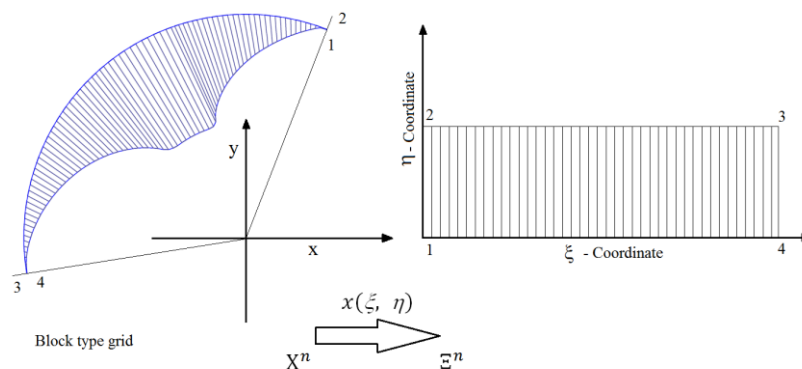


Figure B.1 Coordinate transformation from physical region to computational region[21]

### B.2 Outer boundary regularisation

The number of nodes distributed on the casing and the rack curves should be same as number of nodes on the rotor so that structured distribution is achieved between the two boundaries. The requirement of the outer boundary distribution is that it should produce regular cells for a given distribution on inner boundary. After the step of rotor profile adaptation, the nodes on

rotor profile are fixed. They essentially rotate as the rotor turns. But nodes on the casing circles and the rack curve are not fixed. They essentially slide on these curves taking a new position with every rotor turn such that the distribution is always regular.

If the arc length scale on inner boundary is used as a criterion for node distribution of the outer boundary, then it is not assured that the cells created will be regular. This is because the aspect ratio between the clearance gap and the core rotor is too large. *Kovacevic* has formulated a special procedure of regularisation of the outer boundary applicable for twin screw rotors.

Suppose that the points distributed on the boundaries are represented in index notation with respect to the physical coordinate system as  $\mathbf{r}_{i,j}(x,y)$ . Points on the inner boundary are  $\mathbf{r}_{i,j=0}(x,y)$  and points on the outer boundary are  $\mathbf{r}_{i,j=1}(x,y)$ . Additionally, if the outer boundary is considered as a full circle instead of a combination with the rack curve then the point distribution is  $\mathbf{r}_{i,j'=1}(x,y)$  as shown in Figure B.2.

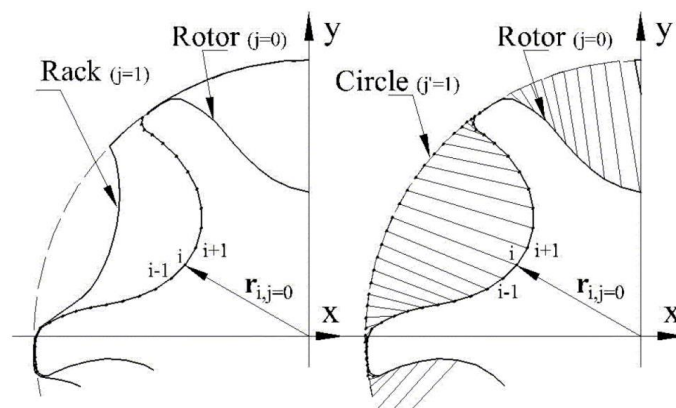


Figure B.2 Point distribution on inner boundary and outer circle.

Based on arc length distribution on the rotor,

$$\mathbf{r}_{i,j'=1}(x,y) = \mathbf{r}_{i,j=0} \frac{S_i}{S_l} \quad \text{B. 1}$$

The procedure of outer boundary adaptation starts with a transformation from physical region  $X^2$  onto a computational domain  $\Xi^2$  in which the outer circular boundary becomes a straight line along the  $x$  coordinate. The transformation is represented by equation B. 2.

$$x_{i,j=0} = x_{i-1,j=0} + c \cos \alpha_{ac}$$

$$x_{i,j'=0} = x_{i,j=0}$$

$$h_{i,j=0} = h_{i-1,j=0} + c \cos \alpha_{ac}$$

$$h_{i,j'=0} = 0$$

B. 2

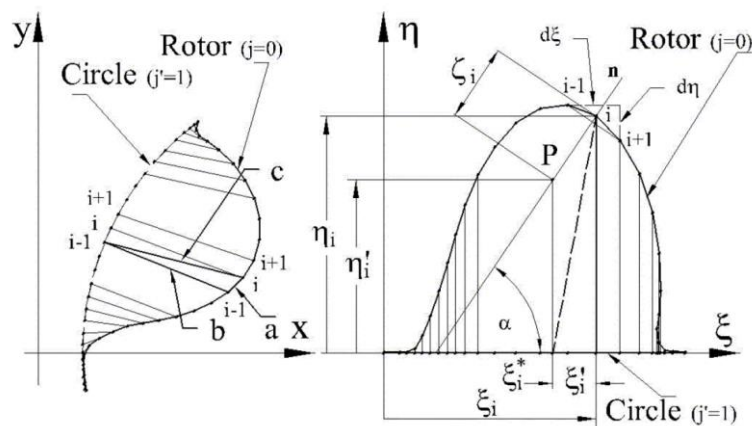


Figure B.3 Transformation of interlobe region to computational domain.

The B.3 shows the physical region  $X^2$  of one interlobe space and the computational coordinate system  $(x, h)$  with the transformed coordinates of both, the rotor and the outer circle.

Consider point  $i$  in the physical domain. The lengths  $a$ ,  $b$  and  $c$  are:

$$a = \sqrt{(x_i - x_{i-1})_{j=0}^2 + (y_i - y_{i-1})_{j=0}^2},$$

$$b = \sqrt{(x_{i-1,j=0} - x_{i-1,j'=1})^2 + (y_{i-1,j=0} - y_{i-1,j'=1})^2},$$

$$c = \sqrt{(x_{i,j=0} - x_{i-1,j'=1})^2 + (y_{i,j=0} - y_{i-1,j'=1})^2}$$

B.3

and the angle  $\alpha_{ac}$  between  $a$  and  $c$  is determined by the cosine law

$$\cos \alpha_{ac} = \frac{a^2 + b^2 - c^2}{2 a b},$$

The outer circle is a straight line along  $x$  coordinate and the  $h$  coordinate is the distribution of the rotor profile points. On the outer circle the  $h$  coordinate is zero for all the points. Right and left boundaries are produced as vertical lines in the transformed space. The equations B.4 and B.5 are then used to regularise the cells in  $(x, h)$  by recalculating the  $x$  coordinates on the outer circle.

A control point **P** is introduced into the system as shown in B.3. The point is located at a distance  $z_i$  on the normal at point  $i$ . The angle of this normal with  $x$  axis is

$$\tan \alpha = \frac{dx}{dh}, \quad \text{at } j = 0 \quad \text{B.4}$$

Coordinates of point **P** are  $(x_i^*, h_i')$  and  $x_i^*$  is the required new distribution on the outer circle.

$$\begin{aligned} x_i^* &= x_i - x_i' \\ h_i' &= h_i - x_i \cos \alpha \end{aligned} \quad \text{B.5}$$

Where  $x_i'$  is the projection of  $z_i$  on  $x$  axis and  $(x_i, h_i)$  are the coordinates of point  $i$ .

$h_i'$  and  $z_i$  are related by the parameter  $k_i$ ,

$$\begin{aligned} k_i &= \frac{h_i'}{z_i}, \quad 0 \leq k_i \leq \text{¥} \\ x_i^* &= x_i - h_i \frac{\cos \alpha}{k_i \sin \alpha} \end{aligned} \quad \text{(D.1)}$$



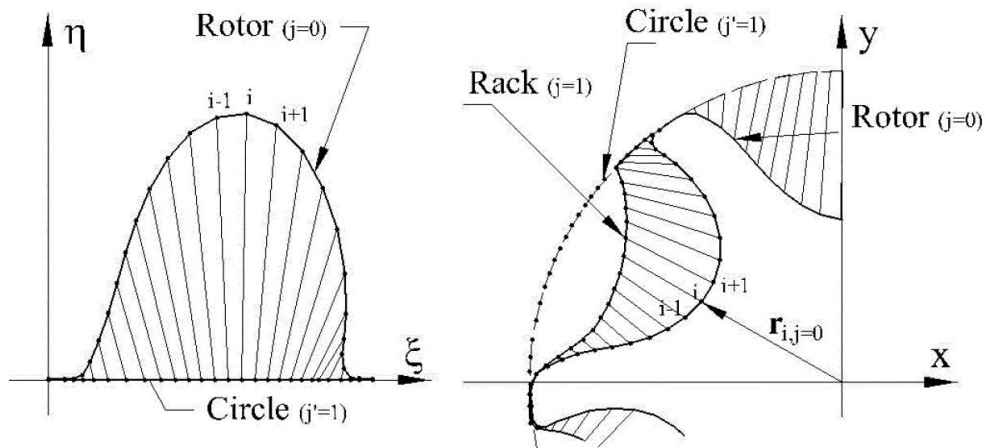


Figure B.4 Regularised distribution on the outer boundary.

The inverse transformation of  $x$  coordinates to the circle in the physical domain is with the arc-length factor as in equation B.6.

$$\mathbf{r}^*_{i,j'=1}(x, y) = \mathbf{r}_{i,j'=1} \frac{x_i^*}{x_I^*} \quad \text{B.6}$$

The rack points at ( $j = 1$ ) are obtained by linear interpolation between corresponding points on the outer circle ( $j' = 1$ ) and the rotor ( $j = 0$ ). This distribution is also regular as shown in Figure B.4.

### B.3 Transfinite interpolation

Once the outer and inner boundaries are distributed the same number of nodes, the interior nodes can be distributed in the sub-domain using algebraic transfinite interpolation. The standard transfinite interpolation and a more accurate ortho-transfinite interpolation[110] can be employed here. The quality can be further improved by smoothing the numerical mesh. The mesh generated by this way is more consistent and have lower aspect ratios[13].

## Appendix C. Mesh quality evaluation standard

The high mesh quality is the premise of an accurate 3-D CFD simulation results. Using a mesh of adequate geometrical mesh quality is an important part of controlling discretization error. For different mesh generation software and CFD software, the criteria of the mesh quality are different. The significant measures of mesh quality are identified through a number of factors such as cell aspect ratio, orthogonality expansion factor and wrap angle.

Here, the grid quality criteria of most popular grid generation software and CFD software are concluded for the evaluation of the generated grid.

Currently, the most popular grid generation software for twin screw machines are SCORG™ and TwinMesh. SCORG is a tool for the design and CFD pre-processing of rotary twin screw machines. The main functionality is to construct deforming grids in the rotor domain of a twin screw machine. TwinMesh™ is a software developed by CFX Berlin Software GmbH, which generates high-quality hexahedral meshes for each time step automatically to represent the continuously changing fluid volumes of the inter-lobe chambers.

SCORG has introduced several tools for inspection of the 2D grids so that some corrections and improvements are done before any solver calculations.

Aspect ratio is defined for each 2D cell based on the edge lengths as shown in Figure C. 1. A maximum It is recommended to have low number of cells exceeding the 200.

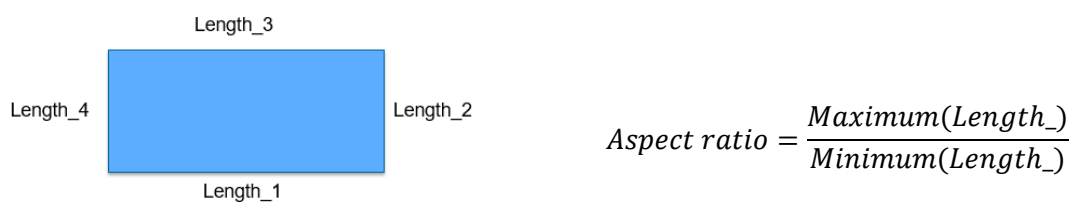
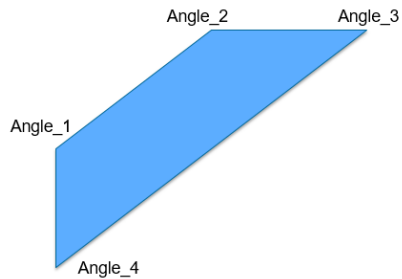


Figure C. 1 Aspect ratio

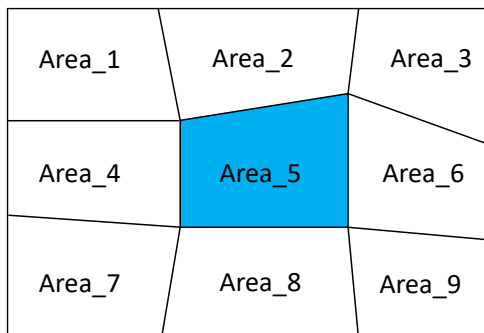
Orthogonality is an important characteristic of the cell and indicates a deviation from the ideal cubic structure. In SCORG orthogonality has been defined as shown in Figure C.2. The recommended value of the orthogonality is no more than 15 degree.



$$\text{Orthogonality} = \text{Max}(\text{Absolute}(\text{Angle}_i - 90^\circ))$$

Figure C.2 Orthogonality

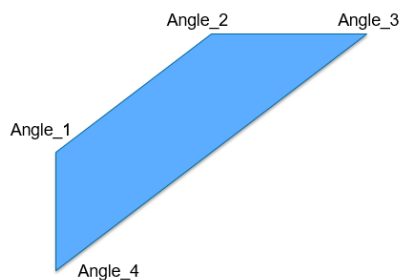
Expansion factor is an evaluation criterion concerning the stability of the flow solver. SCORG defined expansion factor for the 2D mesh based on face area of all the neighbouring cell. The equation is represented below. The recommended value of the expansion factor is less than 10.



$$\text{Expansion Factor}(\text{Area}_5) = \frac{\text{Maximum}(\text{Area}_i)}{\text{Minimum}(\text{Area}_i)}$$

Figure C.3 Expansion Factor

Minimum face angle is calculated for each cell of the 2D mesh and is available for inspection. Values below 15 degrees should be avoided.



$$\text{Minimum face angle} = \text{Min}(\text{Angle}_i)$$

Figure C.4 Face angle

1. Min angle: Quality is determined based on the minimum element angle the recommended min angle value is less than 18°.

2. Aspect ratio: Quality is determined based on the aspect ratio of cells which is recommended less than 1000.
3. Volume change: Quality is determined based on the growth ratio from one cell to its neighbour cells. The recommended value is less than 10.
4. Determinant: Quality is determined based on its determinant. Negative values indicate a negative element face which value is recommended less than 0.05.

Various forms of these measures are presented during different stages of the simulation process (for example, mesh generation, physics pre-processing, solution, and so on). It is important to realize, however, that the most relevant form of the orthogonality, expansion and aspect ratio measures is intimately related to the discrete approximations employed by the field solver being used. Moreover, acceptable ranges for the values of these measures also depend heavily upon the discretization used.

The discussion that follows focuses on the measures that are relevant to the CFX-Solver.

#### 1) Mesh orthogonality (acceptable range $>20^\circ$ )

The concept of mesh orthogonality relates to how close the angles between adjacent element faces or adjacent element edges are to some optimal angle (for example,  $90^\circ$  for quadrilateral faced elements and  $60^\circ$  for triangular faces elements). The most relevant measure of mesh orthogonality for the CFX-Solver is illustrated below. It involves the angle between the vector that joins two mesh (or control volume) nodes (s) and the normal vector for each integration point surface (n) associated with that edge. Significant orthogonality and non-orthogonality are illustrated at ip1 and ip2, respectively.

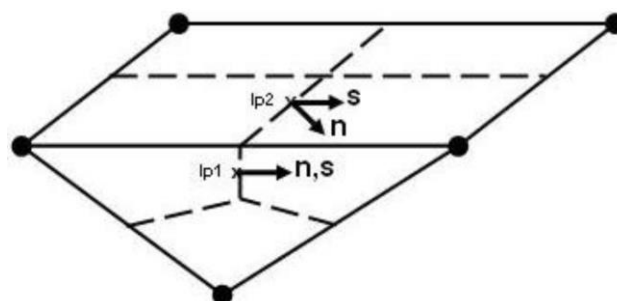


Figure C.5 Orthogonality angle

#### 2) Mesh aspect ratio (acceptable rang $<100$ )

The concept of the mesh aspect ratio relates to the degree that mesh elements are stretched. The most relevant measure of aspect ratio for the CFX-Solver is illustrated below. It involves the ratio of the maximum to minimum integration point surface areas in all elements. Nodal (that is, control volume) values are calculated as the maximum of all element aspect ratios that are adjacent to the node. In clearance regions solver ANSYS CFX can still work with Aspect ratio about 1000 with double precision calculations.

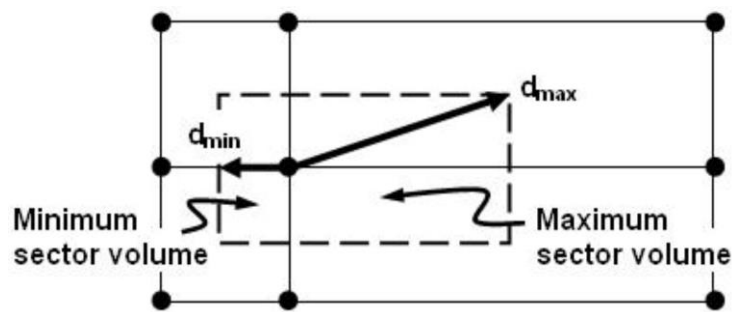


Figure C.6 Mesh Aspect ratio

### 3) Mesh expansion (acceptable range $<20$ )

The concept of mesh expansion relates to rate of change in the magnitude of adjacent element face areas or volumes.

The most relevant measure of mesh expansion for the CFX-Solver is illustrated below. It involves the ratio of the maximum to minimum distance between the control volume node and the control volume boundaries. Because this measure is relatively expensive to calculate for arbitrarily shaped control volumes, an alternative formulation, the ratio of maximum to minimum sector volumes, is used.

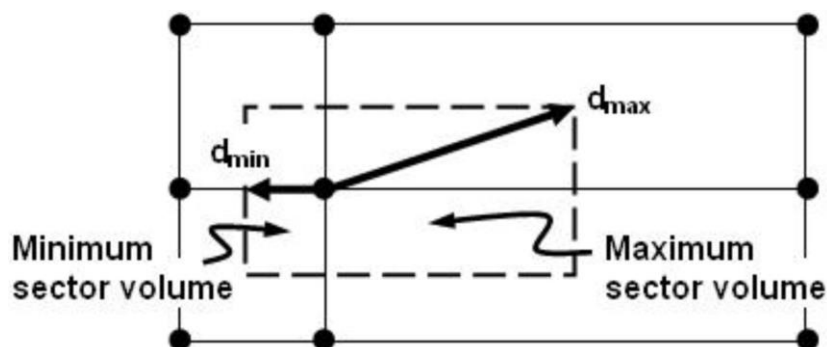


Figure C.7 Mesh expansion

